Computational Analysis of Fluid Interfaces Influenced by Soluble Surfactant

Computergestützte Analyse von fluiden Grenzflächen unter dem Einfluss löslicher Tenside

Am Fachbereich Maschinenbau an der Technischen Universität Darmstadt
zur Erlangung des akademischen Grades Doktor-Ingenieur (Dr.-Ing.)
genehmigte Dissertation vorgelegt von **Chiara Pesci** aus Suzzara

Tag der Einreichung: 11.04.2019
Tag der mündlichen Prüfung: 09.07.2019

Referent: Prof. Dr. Dieter Bothe
Korreferent: Prof. Dr. Martin Oberlack

TECHNISCHE
UNIVERSITÄT
DARMSTADT

Institut für Mathematische
Modellierung und Analysis
Fachbereich Mathematik

Computational Analysis of Fluid Interfaces Influenced by Soluble Surfactant

Computergestützte Analyse von fluiden Grenzflächen unter dem Einfluss löslicher Tenside

Am Fachbereich Maschinenbau an der Technischen Universität Darmstadt
zur Erlangung des Grades eines Doktor-Ingenieurs (Dr.-Ing.) genehmigte

DISSERTATION

vorgelegt von Chiara Pesci aus Suzzara

Referent: Prof. Dr. Dieter Bothe
Korreferent: Prof. Dr. Martin Oberlack

Tag der Einreichung: 11.04.2019

Tag der mündlichen Prüfung: 09.07.2019

Darmstadt 2019

D 17

Abstract

This work presents novel insights about the influence of soluble surfactants on rising bubbles obtained by direct numerical simulation (DNS). Surfactants are amphiphilic compounds which accumulate at fluid interfaces and significantly modify the respective interfacial properties, influencing also the overall dynamics of the flow. Since these interfaces are moving, continuously deforming and expanding, the local time-dependent interfacial coverage is the most relevant quantity. With the aid of DNS, local quantities, like the surfactant distribution on the bubble surface, can be accessed for a better understanding of the physical phenomena occurring close to the interface. However, the description and the simulation of such processes poses severe challenges. The core part of the physical model consists of the description of the surfactant transport in the bulk and on the deformable interface. The solution procedure is based on an arbitrary Lagrangian–Eulerian (ALE) interface-tracking method. The existing framework was enhanced to describe a wider range of physical phenomena. After a thorough validation of the latest numerical developments, the DNS of single rising bubbles in contaminated solutions is compared to experimental results. The full velocity transients of the rising bubbles, especially the contaminated ones, are correctly reproduced by the DNS. The simulation results are then studied to gain a better understanding of the local bubble dynamics under the effect of soluble surfactant.
As an outlook, the mathematical and numerical models have been further extended to describe the influence of surfactant on the mass transfer from the bubble to the liquid phase. Two different models are studied; the first where the species and the surfactant transport are solved independently, and the second one where the hindrance effect of surfactant on mass transfer is taken into account. Preliminary simulation results are presented and discussed.

Zusammenfassung

Diese Arbeit präsentiert neue Erkenntnisse über den Einfluss von löslichen Tensiden auf aufsteigende Einzelblasen, die durch direkte numerische Simulation (DNS) erhalten wurden. Tenside sind amphiphile Substanzen, die sich an Fluidgrenzflächen ansammeln und die Grenzflächeneigenschaften signifikant verändern, wodurch auch die Gesamtdynamik der Strömung beeinflusst wird. Da sich diese Fluidgrenzflächen bewegen, sich kontinuierlich verformen und ausdehnen, ist die lokale zeitabhängige Grenzflächenbelegung die relevanteste Größe. Mit Hilfe von DNS können lokale Größen wie die Tensidverteilung auf der Blasenoberfläche zum besseren Verständnis der physikalischen Phänomene in der Nähe der Grenzfläche berechnet werden. Dennoch stellt die Beschreibung und Simulation solcher Prozesse eine große Herausforderung dar. Der Kern des physikalischen Modells besteht aus der Beschreibung des Tensidtransports im Bulk und auf der verformbaren Grenzfläche. Das Lösungsverfahren basiert auf einer Arbitrary Lagrange-Eulerian (ALE)-Interface-Tracking Methode. Die bestehende Methodik wurde erweitert, um ein breiteres Spektrum an physikalischen Phänomenen zu beschreiben. Nach einer gründlichen Validierung der neuesten numerischen Entwicklungen wird die DNS von aufsteigenden Einzelblasen in kontaminierten Lösungen mit experimentellen Ergebnissen verglichen. Die zeitabhängigen Geschwindigkeiten der aufsteigenden Blasen, insbesondere die der kontaminierten, werden durch die DNS korrekt wiedergegeben. Die Simulationsergebnisse werden dann im Detail analysiert, um ein besseres Verständnis der lokalen Blasendynamik unter der Wirkung von löslichem Tensid zu erhalten.
Im Sinne eines Ausblicks wurden die mathematischen und numerischen Modelle weiter ausgebaut, um den Einfluss von Tensiden auf den Stoffübergang von der Blase in die Flüssigphase zu beschreiben. Zwei verschiedene Modelle werden verwendet; ein erstes, bei dem die Spezies und der Tensidtransport unabhängig voneinander gelöst werden, und ein zweites, bei dem die hinderliche Wirkung von Tensiden auf den Stoffaustausch berücksichtigt wird. Vorläufige Simulationsergebnisse werden vorgestellt und diskutiert.

Publications

Some ideas, results and figures have appeared previously in the publications below.

Journal papers and book chapters

[97] A. Weiner, J. Timmermann, **C. Pesci**, J. Grewe, M. Hoffmann, M. Schlüter, and D. Bothe, *Experimental and numerical investigation of reactive species transport around a small rising bubble*, Chemical Engineering Science: X, 1:100007, 2019.

[73] **C. Pesci**, A. Weiner, H. Marschall, and D. Bothe, *Computational analysis of single rising bubbles influenced by soluble surfactant*, Journal of Fluid Mechanics, 856:709-763, 2018.

[72] **C. Pesci**, H. Marschall, V. Ulaganathan, T. Kairaliyeva, R. Miller, and D. Bothe, *Experimental and Computational Analysis of Fluid Interfaces Influenced by Soluble Surfactant*, in *Transport Processes at Fluidic Interfaces*, ser. Advances in Mathematical Fluid Mechanics, D. Bothe and A. Reusken, Eds., Springer International Publishing, AG Cham, 2017, ch. 15.

[71] **C. Pesci**, K. Dieter-Kissling, H. Marschall, and D. Bothe, *Finite Volume/Finite Area Interface Tracking method for two-phase flows with fluid interfaces influenced by surfactant*, in *Progress in colloid and interface science*, M. T. Rahni, M. Karbaschi, and R. Miller, Eds., CRC Press, Taylor & Francis Group, 2015, ch. 18.

Conference contributions

- 8th International Berlin Workshop on Transport Phenomena with Moving Boundaries, 25th - 26th October 2018, Berlin, Germany, *Computational analysis of single rising bubbles influenced by soluble surfactant*
- 5th ESI OpenFOAM Conference, 17th - 19th October 2017, Wiesbaden, Germany, *Computational analysis of single rising bubbles influenced by soluble surfactant*
- 12th OpenFOAM Workshop, 24th - 27th July 2017, Exeter, UK, *Computational Analysis of single rising bubbles influenced by soluble surfactant*, winner of the Best Presentation Award
- 11th OpenFOAM Workshop, 26th - 30th June 2016, Portugal, *Direct Numerical Simulation of fluid interfaces influenced by soluble surfactant*

- International Conference on Multiphase Flows, 22nd - 27th May 2016, Firenze, Italy, *Finite Volume / Finite Area Interface-Tracking method for two-phase flows with soluble surfactants and mass transfer*
- 6th International Workshop on Bubble & Drop Interfaces, 6th - 10th July 2015, Potsdam-Golm, Germany, *Direct Numerical Simulation of a single rising bubble under the influence of surfactant*
- Advanced Course on Dynamics of Bubbly Flows, CISM, 8th - 12th June 2015, Udine, Italy, *Computational analysis of fluidic interfaces influenced by soluble surfactant*

Co-supervised thesis

[81] M. Steinhausen. *Numerical simulation of single rising bubbles influenced by soluble surfactant in the spherical and ellipsoidal regime.* Master thesis, TU Darmstadt, 2018.

[50] J.A. Kleinkemper, *A comparative study of different mesh types for transport processes near gas bubbles regarding accuracy, stability, and run time.* Bachelor thesis, TU Darmstadt, 2018.

[37] M. Hartmann. *Description of Marangoni-induced flow patterns through photo-switchable surfactants by means of Direct Numerical Simulation using OpenFOAM.* Master thesis, TU Darmstadt, 2016.

Contents

Chapter 1

Introduction

1.1 Motivation

Surfactants are amphiphilic compounds which accumulate at fluid interfaces and significantly modify the respective interfacial properties, influencing also the overall dynamics of the flow. In general, a surfactant molecule contains a hydrophobic group (tail) and a hydrophilic group (head). See, for instance, the molecular structure of the surface active agent dodecyldimethylphosphine oxide ($C_{12}DMPO$) in figure 1.1.

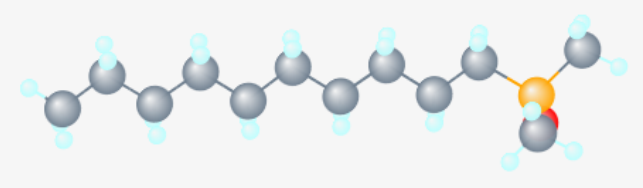

Figure 1.1: Representation of a surfactant molecule: Dodecyldimethylphosphine oxide, chemical formula $C_{14}H_{31}OP$, also known as $C_{12}DMPO$; figure from [34].

The hydrophobic group tends to leave the water phase. Thus, the surfactant molecules accumulate at the interface between water and gaseous or oil phase with their tails extending towards the gas phase while the hydrophilic head remains in the water. Usually, surfactants are classified according to the polar head group, i.e. non-ionic surfactants having no charged groups in their heads, and ionic surfactants carrying a net positive (cationic) or negative charge (anionic). The surfactant molecules, distributing on the interface, have the effect of reducing the surface tension between the two phases. A schematic representation of this effect is given in figure 1.2, where a surface tension reduction is depicted in correspondence of the area where the surfactant concentration is higher.
Surfactants find application in many industrial processes acting as, for instance, detergent, emulsifier, wetting or foaming agents, and dispersant. They may be also encountered in the system as contaminants. In chemical engineering, surfactants are present in most multiphase contactors, either as contaminants or added on purpose to change the way how phases interact. In the design of these industrial apparatuses knowing how the gas and the liquid phases interact is fundamental to predict as accurately as possible its performances. The sought information are usually the average bubble size in the bubble swarm, the contact area and time, and the gas hold-up, i.e. the amount of gas retained in the column at a given time. All these factors

influence the efficiency of the mass transfer in the column, and the better the predictions are, the more performant the reactor can be designed. Nevertheless, the simulation of the full scale problem is not possible, but a scale-down strategy can be employed.

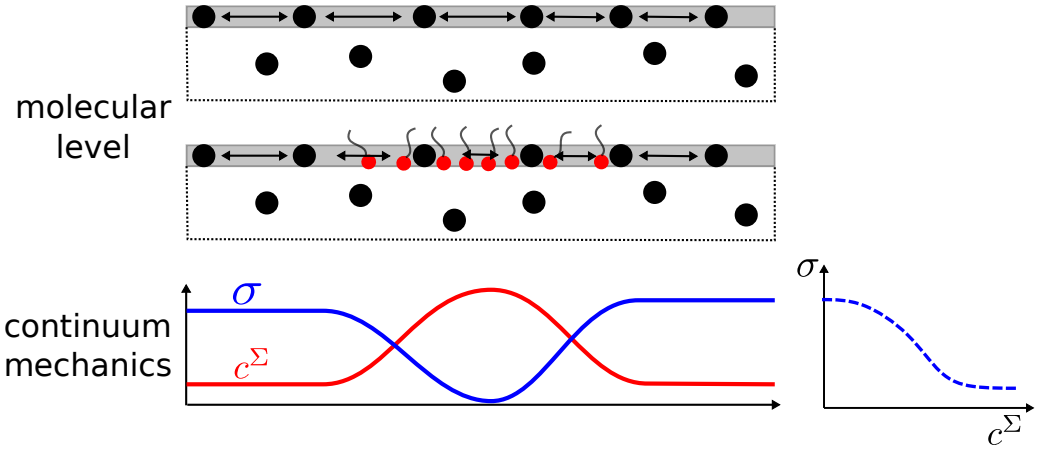

Figure 1.2: Sketch to visualize the effect of surfactant on the surface tension at a liquid/gas interface. The surface tension is lower where the surfactant concentration is higher.

The problem complexity is reduced to the point which can be studied with precise and reliable numerical models, i.e. direct numerical simulations (DNS). This implies that the meter-sized problem is reduced to a centimetre-sized problem where the bubble-bubble interaction problem may be addressed, and then to the millimetre-sized problem where a single bubble rising into a liquid solution is considered. Once the smallest scale problem is solved, the inverse path up to the industrial scales can be followed with the aid of correlations, for instance. If surfactants are present in the system, the level of complexity of the problem is even higher. In fact, the most challenging but also most astonishing property of surfactants is that even traces of it, which are modifying cohesion forces on a molecular level, can cause a tremendous change in the macroscopically observed, sometimes meter-sized, flow patterns; see for instance figure 1.3 where on the left a bubble swarm under the influence of methyl isobutyl carbinol (MIBC) is shown. Already 10 ppm of MIBC have a significant effect on the bubble size and distribution, on the void fraction and on the flow pattern.

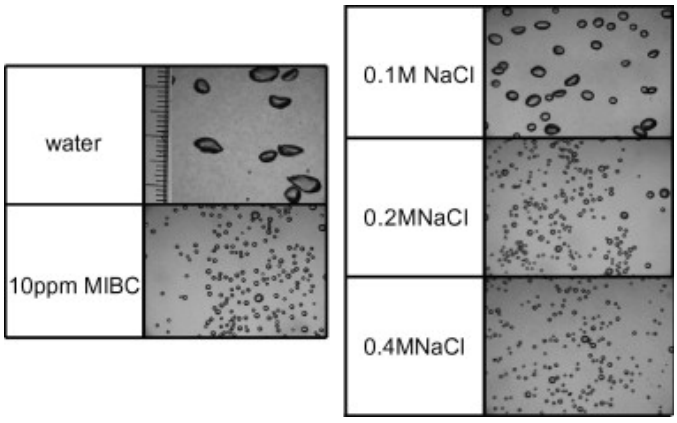

Figure 1.3: Bubble swarm under the influence of methyl isobutyl carbinol (MIBC) and sodium chloride (NaCl); figure reproduced from [31, figure 7] with permission of the copyright owner.

Another example of industrial application can be froth flotation, where a so-called frother is used to separate hydrophobic from hydrophilic particles. The frother is surface active and renders the particles in question hydrophobic. The particles can then attach to air bubbles, which rise to the surface of the floatation cell and form a froth (or foam) that can be removed. The efficiency of flotation cells is determined by the probability of bubble-particle collisions, and therefore by the interaction of gas, liquid, particles, and frother. Also the example of froth flotation demonstrates how complex a system involving surfactants can be.

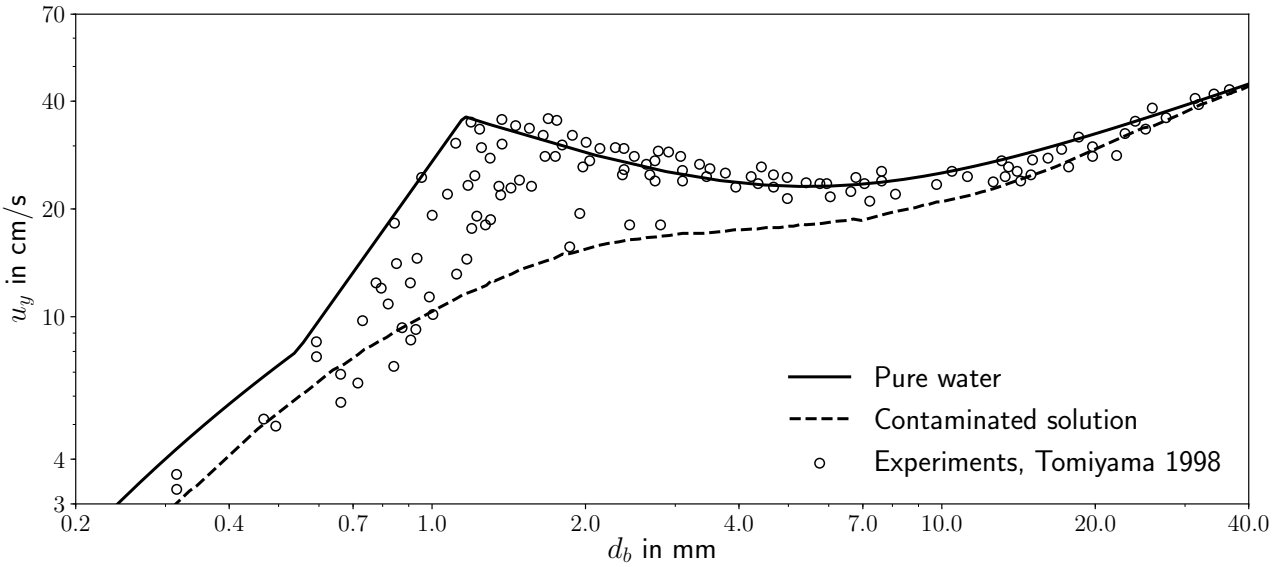

Figure 1.4: Experimental and calculated rise velocities for an air bubble rising in water; figure based on data from [88]. Lines computed according the correlations reported in the reference.

But also systems as simple as a single air bubble rising in tap water may be determined by the presence of a surfactant. Experiments have shown that bubbles rising in purified water can reach terminal velocities that are two times higher than in tap water; see [14, figure 7.3, page 172] or the more recent [88] from which figure 5 is reproduced here in figure 1.4. This demands that the used materials must be well determined in order to obtain reliable and reproducible results. Also the modelling and the simulation of single bubbles rising in contaminated water is a challenging task.

The flow around the bubble is strongly affected by the presence of surfactants. Trailing vortexes in the wake of the bubble appear at much lower Reynolds numbers for contaminated bubbles ($\mathrm{Re} > 20$, [60, 98]) than for clean ones ($\mathrm{Re} > 600$); see, for instance, figure 1.5. The flow field around the bubble determines the bubble rise velocity and path, leading to terminal velocities for contaminated bubbles that are up to two times smaller than for uncontaminated ones [14]; see also the exemplifying velocity profiles in figure 1.5. Figure 1.5 shows the typical velocity profiles for clean and contaminated bubbles, too. These profiles will be discussed in more details later in this chapter.

Regarding the bubble path, figure 1.6 reproduced from [83] shows the influence of surfactant on the bubble path. While the bubble rises along an helical path in pure water, in contaminated solution the width of the helix may increase (b), progressively decrease (c), or the motion may even switch from helical to zig-zag (d).

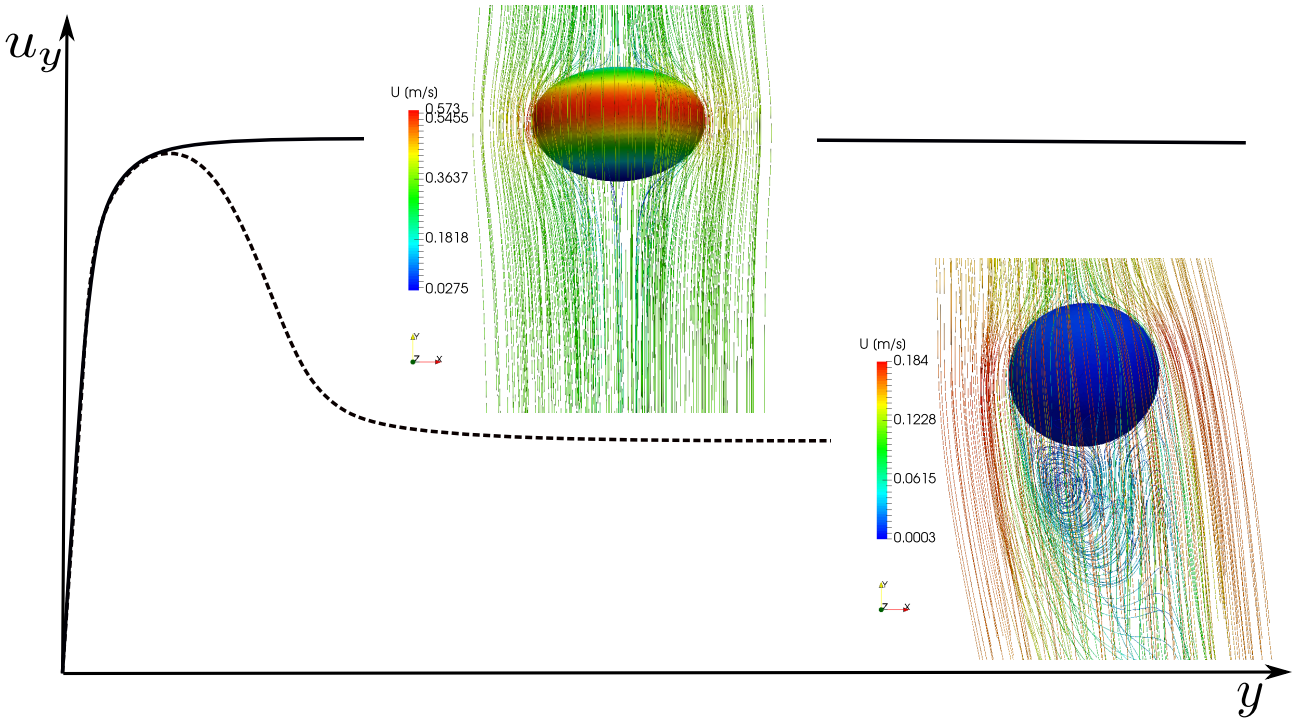

Figure 1.5: Example of rise velocity profiles for a bubble rising in pure water (continuous line) and in a contaminated solution (dashed line) with respective flow field around the bubble.

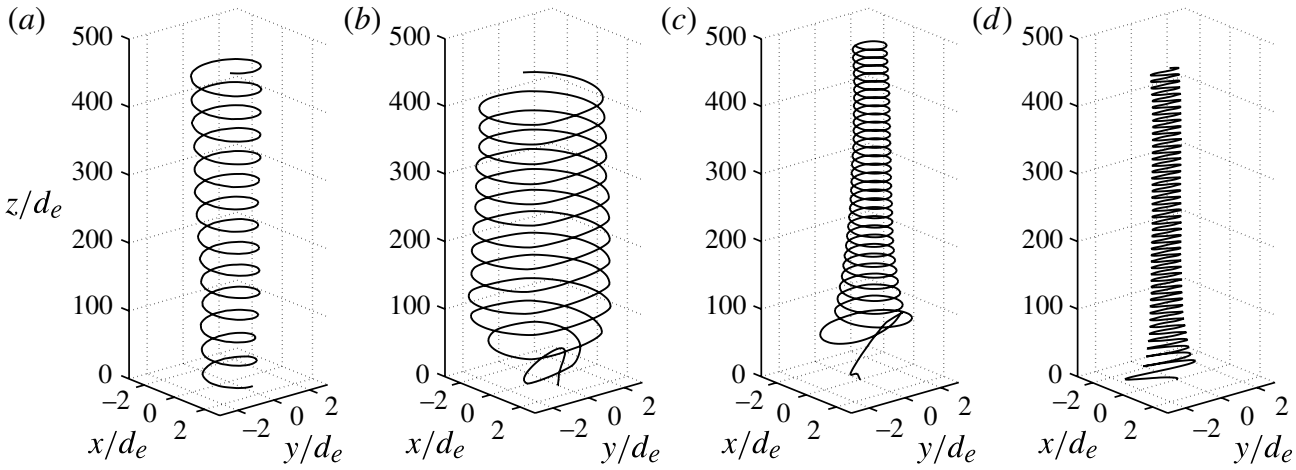

Figure 1.6: Bubble trajectories under the influence of surfactant, (a) 0 ppm, (b) 25 ppm, (c) 75 ppm, (d) 150 ppm of 1-Pentanol. Figure reproduced from [83, figure 3] with permission of the copyright owner.

Not only the type of trajectory that the bubble follows but also its position in the column is affected by the presence of surfactant. As reported in the study by Takagi et al. [84], bubbles rising in laminar Poiseuille flow, instead of heading towards the wall of the channel, they will follow a more rectilinear path in the centre of the column, if traces of contaminants are present; see figure 1.7 reproduced from [84].

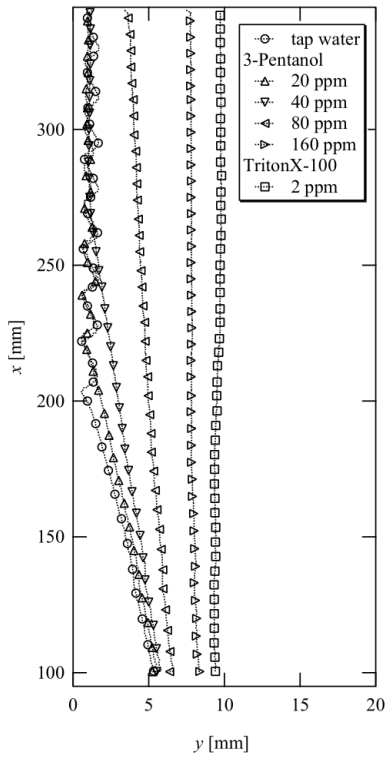

Figure 1.7: Bubble trajectories in laminar Poiseuille flow. Figure reproduced from [84, figure 5] with permission of the copyright owner.

In addition, one has to deal with deformable interfaces; see, for instance, figure 1.8 where the bubble shapes from experiments at different heights in the channel are reported. While the bubble is rising, it is deforming towards an ellipsoidal shape. If the system is contaminated, under certain circumstances, the bubble then decelerates and the shape goes back to a spherical one.
Finally, the transport of surfactant is a typical high Péclet number problem. This problem stems from the fact that the transport of any quantity close to the bubble surface is advection-dominated and thin species boundary layers form. These extremely thin layers pose a highly challenging task for the numerics. Moreover, if mass transfer from the gas to the liquid phase is considered, not only this process but also the influence of surfactant on it has to be modelled.

The motivations for this work can be summarized in the list below:

1. a general interest in the surfactant effects on bubble motion, due to their presence in numerous industrial applications, as reported above;

2. access local data which are not available from experiments and gain a better understanding of the dynamic behaviour of rising bubbles;

3. being able to describe quantitatively the surfactant effects on single rising bubbles would allow to make predictions on the larger scales;

4. the interest of industrial applications lies in the possibility to obtain predictions as accurately as possible to design, for instance, more efficient contactors saving resources. This problem includes also considering the effects of surfactant on mass transfer processes.

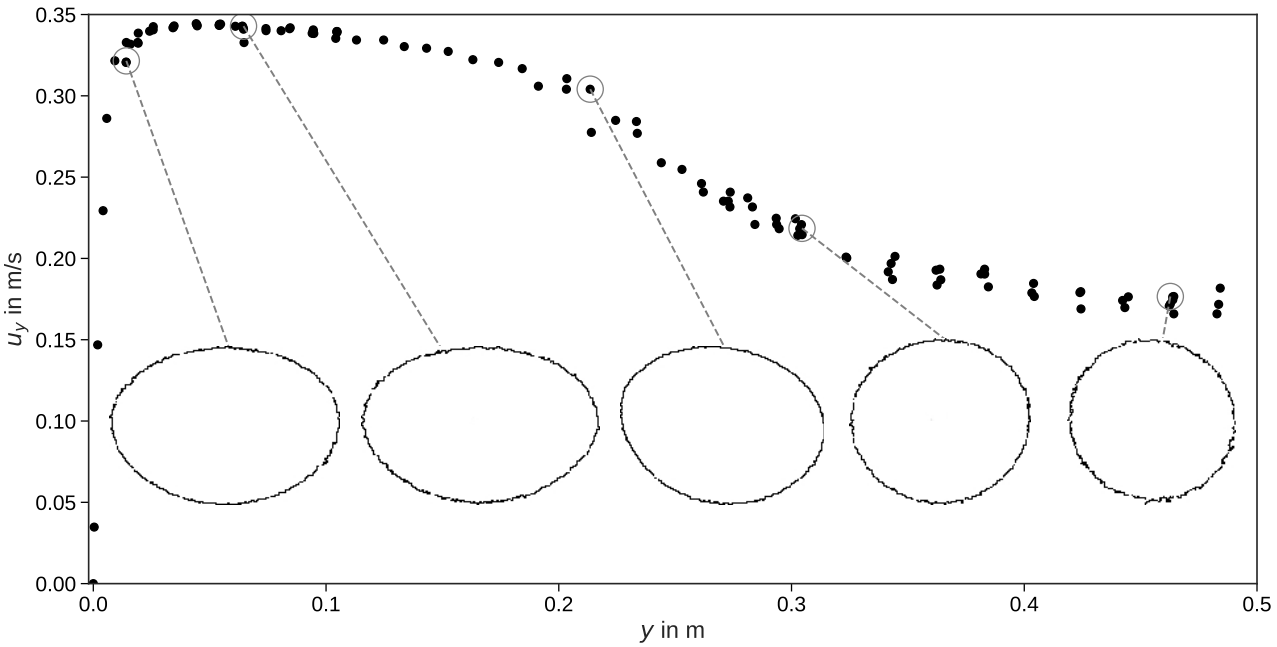

Figure 1.8: Example of shape deformation during the bubble rise. Air bubble rising in a contaminated solution with C_{12}DMPO; rise velocities from [72]; corresponding bubble shapes after image post-processing courtesy of Dr. Marcel Krzan, Polish Academy of Sciences.

1.2 State of the art

From now on the focus will be on single rising bubbles. Historically, the problem of rising bubbles has been intensively studied both experimentally and numerically, but due to its complexities, it is still open to discussion.
Levich's *Physicochemical Hydrodynamics* [57] is one of the first textbooks containing a theoretical treatment of surface forces resulting from an inhomogeneous distribution of a surface-active substance on the interface of a rising bubble, and it also describes in much greater detail some of the basic concepts outlined hereafter. Bubbles rising in a pure liquid are characterized by a mobile interface, meaning that the fluid elements forming the gas-liquid interface are movable and can be deformed or displaced. Therefore, the velocity gradients present in the liquid around a rising bubble are smaller than those around a solid body, and less energy is dissipated in the liquid. Consequently, under the same driving force, bubbles rise faster than solid particles. If impurities are present in the surrounding liquid, however, the observed rise velocity varies somewhere between the one of particles with a fully mobile and fully immobile or rigid interface. This observation gave rise to the idea of a partially immobilized interface, which is

useful to derive simplified models to account for the influence of surfactants, but which can be misleading sometimes. It is important to clarify that the inhomogeneous surfactant distribution causes additional surface specific forces which in turn change the flow pattern around a rising bubble. The surfactant itself cannot render a fluid particle (partially) rigid.
The molecules of the surface active substance, present in the liquid bulk phase, accumulate at the gas-liquid interface and lower the surface tension. The process of accumulation is characterized by two steps (see [13], section 4 and the reference therein and figure 2.2): (1) the exchange of molecules between a surface and a subsurface layer, which is only a few molecule diameters in width, and (2) the transfer of molecules from the bulk liquid into the subsurface layer. The first step is called adsorption and the latter (bulk) mass transfer. In this work, cases of diffusion-controlled (or fast) adsorption are mainly considered, meaning that the diffusive transport of surfactant molecules from the bulk into the subsurface layer is much slower than their adsorption such that the surfactant concentrations in surface and subsurface layer are always locally in equilibrium. The other limiting case, the so-called kinetically-controlled (or slow) adsorption occurs when the diffusive transport of surfactant molecules from the bulk into the subsurface layer is much faster than the adsorption. In the latter case, the adsorption of molecules is the limiting step.
Because the interface of a rising bubble is mobile and constantly entrained by the surrounding bulk liquid, the adsorbed surfactant is transported to the rear of the bubble, where it accumulates. As a consequence, there is a region in the rear part with high surfactant concentration and lowered surface tension, while the upper part stays almost uncontaminated and the surface tension is unchanged. In the transition zone between contaminated and uncontaminated interface segments, strong gradients of surfactant concentration and surface tension result. These surface tension gradients lead to additional, so-called Marangoni forces, acting from points of low towards points of high surface tension. These tangential interface forces have to be balanced by shear forces in the liquid phase. The arising viscous forces act against the Marangoni forces from the top to the bottom and, hence, add to the overall drag force.

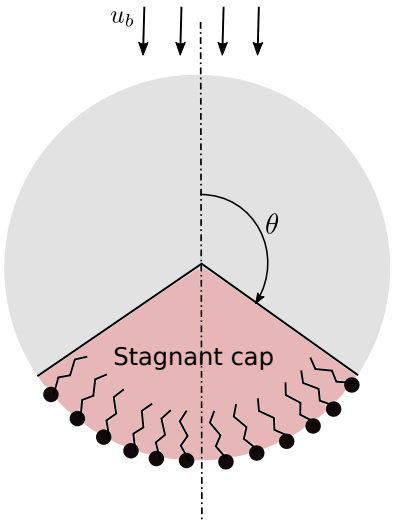

Figure 1.9: Schematic representation of the stagnant cap model.

The described mechanisms and experimental observations led Davis and Acrivos [16] to propose a mathematical model which incorporates the idea of a “stagnant cap”. The interface is divided

at a certain polar angle in two segments rotationally symmetric around the rise direction, one fully covered with surfactant and one completely clean; see figure 1.9. The contaminated cap is stagnant, meaning that the velocity at the interface is zero in a reference frame moving with the bubble center, and the shear stress at the cap is equal to the surface tension gradient. The clean bubble front instead is characterized by zero shear stress. The dividing angle is often referred to as stagnant cap angle θ. Such a clear separating circle is a strong idealization, assuming that the transition zone from a fully contaminated to an uncontaminated surface is small compared to the bubble size.

A variety of theoretical and numerical studies based on the stagnant cap concept have appeared in the last decades, e.g. [38, 29, 58, 99, 100, 36, 69, 32, 21, 23]. One drawback of stagnant cap based models is that dynamic effects cannot be easily included, especially when the assumption of symmetry is violated, as it occurs in most applications. In fact, experiments show that the bubble motion is highly transient, especially after the bubble release. Sam et al. [77] describe the typical transient rise of single bubbles under the influence of different surface active agents (frothers) as a three-stage process that has then been observed several times in experiments, e.g. in [54, 55, 83]. After releasing the bubble, it accelerates until a maximum terminal velocity is reached; in the second stage, the rise velocity starts to reduce until, given sufficient time, a plateau is reached. The constant plateau velocity defines the third stage. Interestingly, the first and second stages depend on the liquid bulk concentration of the surfactant, but the plateau velocity in the third stage seems to be fully determined by the surfactant type alone. Furthermore, the authors observed in their experiments that all investigated bubbles (bubble diameter $d_b < 3mm$), after an initial deformation to an ellipsoidal shape, were almost spherical at the top of the column. Also, an influence of the frother concentration on the bubble path was reported: for bubbles showing path instability, the oscillation frequency decreased from the bottom to the top of the column with increasing frother concentration. Even in the case of large bubbles, the path at the column top was rectilinear, in contrast with the path instabilities observed for clean bubbles. Later, this effect was also observed in the experimental work by Takagi et al. [84] (see figure 5 in the reference or its reproduction in section 1.1, figure 1.7). Since the work of Mougin and Magnaudet [64], it is known that helical and zig-zag trajectories of bubbles in the spherical and ellipsoidal regime are associated with pairs of rotating or symmetric vortices in the bubble wake. Sometimes during the initial acceleration, a transition from zig-zag to helical paths can be observed. The reverse transition, from helical to zig-zagging, was only reported recently by Tagawa et al. [83] for contaminated systems. The authors infer that a similar transition between different wake structures may happen. A strong surfactant influence on wake structure, path and shape was also visualized and comprehensively studied by Huang and Saito [43, 42]. The possible impact of Marangoni forces on lift and drag was deduced from the bubble motion. All previously mentioned experimental results contribute to the partial understanding and description of processes occurring on the reactor scale, for instance why the gas hold-up in flotation cells increases from the bottom to the top. However, to fully understand the transient behaviour of contaminated systems, complementary local field information of surfactant concentration, velocity, and pressure at the interface and in the liquid bulk is necessary, which is currently only accessible via DNS.

Early numerical studies assuming rotational symmetry [29, 58, 85] were only able to find a qualitative agreement with the previously described experimental observations, presumably because of too many limiting assumptions in the mathematical model. But also more sophisticated, fully three-dimensional DNS solving the coupled problems of two-phase hydrodynamics and

surfactant transport in the bulk and on the interface [62, 87, 90, 3] could only partially reproduce and explain the typical three-stage process. As it will be shown in the following chapters, this is mainly due to the studied parameter range. The authors study Péclet numbers (Pe) below 10^3 (calculated with the kinematic viscosity of the bulk liquid and the molecular diffusivity of the dissolved surfactant in the bulk). The Péclet number is a measure for the ratio of convective to diffusive transport of a dilute species. For real systems, instead, Pe ranges from 10^4 to 10^7. High values of Pe are associated with thin boundary layers forming along the bubble surface, which determine the surfactant transfer, and hence, the ad- and desorption. The boundary layer width is approximately three to four orders of magnitude smaller than the bubble size [95], which is why it is extremely demanding to resolve it in a DNS.
Regarding the mass transfer problem in presence of surfactants, it is well known that a strong reduction in the mass transfer occurs if surfactants are introduced in the system; see, for instance, the experimental and numerical works in [86, 74, 78, 39, 35, 32, 47, 41]. Nevertheless, in the experimental works there is always the limitation on accessing local data, while in the numerical works the simplifications in the surfactant modelling and the difficulty of treating high Péclet number problems pose severe limitations on the range of applicability of the methods.

1.3 Objectives of this research

This work focuses on the investigation of the surfactant effects on rising bubbles. The main objectives of this work are

- to gain a deep understanding on how the surfactants are modifying not only the interfacial properties between gas and liquid phases but also the indirect effects on the flow around the bubble, the rise velocity and the path. To accomplish this task, Direct Numerical Simulations (DNS) of single bubbles rising in a contaminated solution are performed. This requires
  - extending the existing numerical method
  - validation and verification of the numerical model
  - comparison with experimental results
- set the basis to investigate the influence of surfactant on mass transfer, in view of the scale-up strategy described before.

An ALE Interface Tracking approach [67, 46, 90, 91] is used, combined with a recently introduced subgrid-scale model and related method [95] for the surfactant transfer, which allows to study realistic systems and to find a good agreement with experimental results. In the present work, only non-ionic surfactants are considered. The results for a single rising bubble influenced by different amounts of soluble surfactant are discussed. Local and global quantities are presented which explain how the surfactant distribution in the bulk and on the interface is related to the macroscopically observed bubble motion, and examine thoroughly different contributions to the overall drag and lift forces. It is the author's intention to provide detailed information which could lead to better scale-reduced models accounting for the influence of contamination in bubbly flows.
During the last part of this research, the focus is moved to consider the influence of surfactant on mass transfer process, ideally from a rising bubble. In detail, while the gas bubble is rising,

for instance, an oxygen or a carbon dioxide bubble, the gas phase is dissolving in the liquid phase. This mass transfer process is affected by the presence of surface active agents accumulating at the bubble interface mainly in two ways. First, the flow field around the bubble is completely different in presence of surfactant and this affects the species distribution around the bubble and the species transfer itself. Second, the surfactant molecules accumulating on the bubble surface form a sort of barrier for the molecules of species transferred from the gas to the liquid phase. This second effect is denoted as hindrance effect. Experiments [78, 39] have shown that the mass transfer is drastically reduced when the liquid phase is contaminated by surfactants and that a hindrance effect caused by the presence of the surfactant molecules on the interface occurs. Nevertheless, more sophisticated mathematical and numerical models are necessary to correctly reproduce the physics of mass transfer under the effects of surfactants. Within this work, only preliminary results will be presented which take into account both the surfactant effects on mass transfer described above for a single rising bubble.

The manuscript follows the structure reported below. In chapter 2 an overview of the mathematical model is given. In detail, the equations of motion, the transport equations for the transferred species and their closure are reported. Additionally, the modelling of the sorption processes and of the influence of the surfactant on the mass transfer are presented. Chapter 3 follows, where the main ideas regarding the equation discretization and the solution algorithm are outlined. In chapters 4 and 5 the validation and verification test cases are reported. To begin with, a newly implemented surface interpolation scheme is validated via comparison with an analytical solution, and the hydrodynamics of single bubbles rising in pure water is validated against experimental results. Afterwards, the two source terms for the limiting sorption mechanisms are first validated against analytical solutions. It follows the validation of the subgrid-scale model for species transfer and the validation for single rising bubbles under the effects of surfactant. Then in the verification chapter it is checked that the various sorption models implemented deliver physical and reasonable results. In chapter 6 the results for single rising bubbles in contaminated solutions are presented and compared to experimental data. Moreover, preliminary results for mass transfer under the effects of surfactant are reported. Finally, in chapter 7 the main findings of this work are summarized and suggestions for future work are outlined. In the appendix, space is given to technical details such as the derivation of the balance equations and the description of the surface mesh quality checks performed by a newly introduced utility to verify the quality of the surface meshes for the finite area method.

Chapter 2

Mathematical model

The description of two-phase flows employed here falls under the continuum mechanical modelling strategy. The system is described by the balances for the conserved quantities, e.g. mass and momentum. The mathematical model for two-phase flows employs a sharp interface representation, meaning that the interface is represented as a surface of zero thickness with unknown time-dependent shape and location. Moreover, it is assumed that the interface does not hold any mass (inertia).
Consider a fluid domain Ω containing two immiscible fluids, separated by a deformable interface. The interface, $\Sigma(t)$, separates the domain into two sub-domains, $\Omega^+(t)$ and $\Omega^-(t)$, corresponding to the two bulk phases. The presence of surfactant in the denser phase and on the interface is taken into account. Under the hypothesis of incompressible Newtonian fluids, isothermal conditions and absence of phase change, the governing equations are based on the conservation of mass, momentum, and surfactant molar mass. For the latter, the additional assumption of negligible inertia of the adsorbed surfactant on the interface is fundamental.

2.1 Two-phase flow hydrodynamics

The velocity and the pressure fields are obtained from the standard two-phase Navier-Stokes equations for incompressible Newtonian fluids.
Let $V(t)$ be a control volume inside the fluid domain Ω, with $\mathbf{n}$ being the outer unit normal to $V(t)$. The boundary of the control volume is denoted by $\partial V(t)$, and it is moving with velocity $\mathbf{w}$. In the integral formulation, mass and momentum balances in the moving control volume $V(t)$ read

$$\frac{d}{dt}\int_{V(t)} \rho \, dV + \int_{\partial V(t)} \rho(\mathbf{v}-\mathbf{w})\cdot\mathbf{n} \, dS = 0, \tag{2.1}$$

$$\frac{d}{dt}\int_{V(t)} \rho\mathbf{v} \, dV + \int_{\partial V(t)} \rho\mathbf{v}\otimes(\mathbf{v}-\mathbf{w})\cdot\mathbf{n} \, dS - \int_{\partial V(t)} \mathbf{S}\cdot\mathbf{n} \, dS - \int_{V(t)} \rho\mathbf{b} \, dV = 0, \tag{2.2}$$

where $\mathbf{v}$ is the barycentric velocity, p the pressure, ρ the density, $\mathbf{S}$ the stress tensor and $\mathbf{b}$ the body forces, i.e. $\mathbf{b} = \mathbf{g}$ being the gravitational force. The stress tensor $\mathbf{S}$ can be decomposed in viscous, $\mathbf{S}^{\text{visc}} = \mu\left(\nabla\mathbf{v} + (\nabla\mathbf{v})^{\mathsf{T}}\right)$, and pressure, $-p\mathbf{I}$, contributions, where μ is the dynamic viscosity. The derivation of the balance equation is outlined in Appendix A.1.
Consider the case where the control volume intersects the interface between the two phases; see figure 2.1. The intersection between the interface and the control volume $\Sigma(t) \cap V(t)$ is

denoted as $S(t)$, with the boundary curve $\partial S(t)$ and the outer unit normal $\mathbf{m} \perp \mathbf{n}_\Sigma$ to $\partial S(t)$. Moreover, we assume that the control volume is co-moving with the fluid, that is $\mathbf{w} = \mathbf{v}$. Under this assumption, the local formulation of equations (2.1) and (2.2) can be easily derived. See appendix A.2 for the main steps of the derivation of the equations in local form.

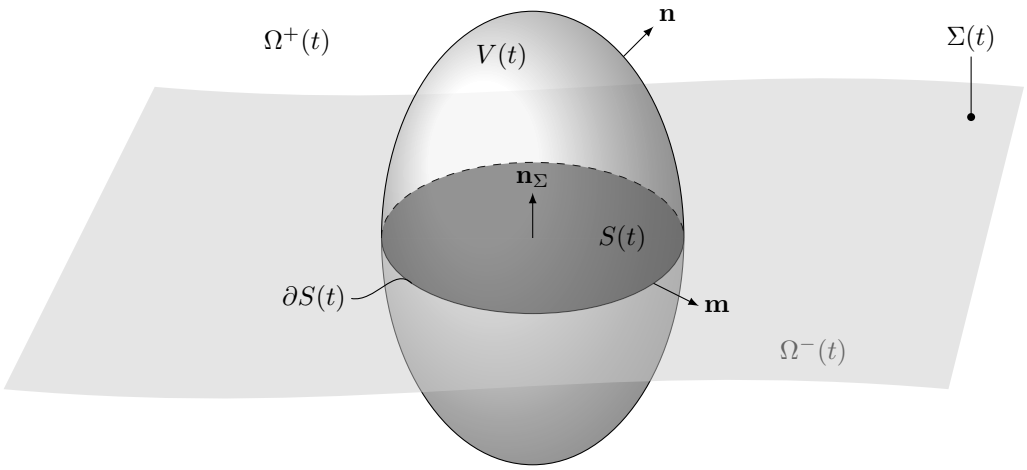

Figure 2.1: Domain representation for two-phase flows system.

The resulting local balance equations for mass and momentum read

$$\partial_t \rho + \nabla \cdot (\rho \mathbf{v}) = 0 \quad \text{in } \Omega(t) \setminus \Sigma(t), \tag{2.3}$$

$$\left[\!\left[\rho(\mathbf{v} - \mathbf{v}^\Sigma)\right]\!\right] \cdot \mathbf{n}_\Sigma = 0 \quad \text{on } \Sigma(t), \tag{2.4}$$

$$\partial_t(\rho \mathbf{v}) + \nabla \cdot (\rho \mathbf{v} \otimes \mathbf{v}) = \nabla \cdot \mathbf{S} + \rho \mathbf{b} \quad \text{in } \Omega(t) \setminus \Sigma(t), \tag{2.5}$$

$$\left[\!\left[\rho \mathbf{v} \otimes (\mathbf{v} - \mathbf{v}^\Sigma)\right]\!\right] \cdot \mathbf{n}_\Sigma + \left[\!\left[p\mathbf{I} - \mathbf{S}^{\text{visc}}\right]\!\right] \cdot \mathbf{n}_\Sigma = \sigma \kappa \mathbf{n}_\Sigma + \nabla_\Sigma \sigma \quad \text{on } \Sigma(t), \tag{2.6}$$

where $\mathbf{v}^\Sigma$ is the interface velocity with $\mathbf{v}^\Sigma = \mathbf{v}_{|\Sigma}$[1] and κ the surface curvature defined as $\kappa = -\nabla_\Sigma \cdot \mathbf{n}_\Sigma$, with $\nabla_\Sigma \cdot$ representing the surface divergence[2]. The symbol σ denotes the surface tension. In contaminated systems, the surface tension depends on the local concentration of surfactant on the interface $\sigma = \sigma(c^\Sigma)$; see section 2.2.2 for the various surface tension equations of state. The notation $[\![\cdot]\!]$ stands for the jump of a physical quantity across the interface, where the jump of ϕ is defined as

$$[\![\phi]\!](t, \mathbf{x}) = \lim_{h \to 0+} \left(\phi(t, \mathbf{x} + h\mathbf{n}_\Sigma) - \phi(t, \mathbf{x} - h\mathbf{n}_\Sigma)\right), \quad \mathbf{x} \in \Sigma(t). \tag{2.7}$$

According to the hypothesis of no phase change and no interfacial slip introduced above ($\mathbf{v}^\Sigma = \mathbf{v}_{|\Sigma}$), equations (2.4)-(2.6) reduce to

$$[\![\mathbf{v}]\!] = 0 \quad \text{on } \Sigma(t), \tag{2.8}$$

$$\mathbf{v} \cdot \mathbf{n}_\Sigma = \mathbf{v}^\Sigma \cdot \mathbf{n}_\Sigma = V_\Sigma \quad \text{on } \Sigma(t), \tag{2.9}$$

$$\left[\!\left[p\mathbf{I} - \mathbf{S}^{\text{visc}}\right]\!\right] \cdot \mathbf{n}_\Sigma = \sigma \kappa \mathbf{n}_\Sigma + \nabla_\Sigma \sigma \quad \text{on } \Sigma(t). \tag{2.10}$$

The system of equations governing the hydrodynamic problem is completed by the initial con-

[1] The notation $\cdot_{|\Sigma}$ denotes the trace of a quantity defined in $\overline{\Omega}^\pm$ on the interface.

[2] The surface gradient of a quantity $\phi(\mathbf{x})$ is defined as: $\nabla_\Sigma \phi(\mathbf{x}) = \nabla \phi(\mathbf{x}) - \mathbf{n}_\Sigma(\mathbf{x})(\nabla \phi(\mathbf{x}) \cdot \mathbf{n}_\Sigma(\mathbf{x}))$ at $\mathbf{x} \in \Sigma$, where ϕ is extended to a neighbourhood of Σ as a differentiable function. Then, the surface divergence of a vector $\mathbf{f}$ is defined as $(\nabla_\Sigma \cdot \mathbf{f})(\mathbf{x}) = \text{tr}(\nabla_\Sigma \mathbf{f})(\mathbf{x})$.

dition in $\Omega^{\pm}$ and the boundary condition on $\partial\Omega$ according to

$$\mathbf{v}(0,\mathbf{x}) = \mathbf{v}_0(\mathbf{x}) \quad \text{for } \mathbf{x} \in \Omega^{\pm}(t=0), \tag{2.11}$$

$$\Sigma(t=0) = \Sigma_0, \tag{2.12}$$

$$\mathbf{v}(t,\mathbf{x}) = \mathbf{v}_\Omega \quad \text{for } \mathbf{x} \in \partial\Omega(t). \tag{2.13}$$

2.2 Species transfer and surfactant transport

The species transport equation in integral form for the moving control volume $V(t)$ reads

$$\frac{d}{dt}\int_{V(t)} c_i \, dV = -\int_{\partial V(t)} c_i(\mathbf{v}-\mathbf{w})\cdot\mathbf{n}\, dS - \int_{\partial V(t)} \mathbf{j}_i\cdot\mathbf{n}\, dS + \int_{V(t)} r_i \, dV, \tag{2.14}$$

where c_i is the molar concentration of the transported species (mol/m^3), $\mathbf{j}_i$ the diffusive molar mass fluxes and r_i the source term due to chemical reactions; see appendix A for an outline of the derivation.
In case the transferred species is a surfactant species, additional terms in the transport equation appear due to the presence of surfactant on the interface. In fact, surfactants ad- and desorb on/from the interface via a sorption mechanism. The integral balance of surfactant molar mass for a moving control volume $V(t)$ in absence of chemical reactions (or any other source term)[3], see appendix A or [9, 3, 82] for a derivation, reads

$$\begin{aligned}\frac{d}{dt}\left[\int_{V(t)} c\, dV + \int_{S(t)} c^{\Sigma}\, dS\right] = &-\int_{\partial V(t)} c\,(\mathbf{v}-\mathbf{w})\cdot\mathbf{n}\, dS - \int_{\partial V(t)} \mathbf{j}\cdot\mathbf{n}\, dS \\ &- \int_{\partial S(t)} c^{\Sigma}\left(\mathbf{v}^{\Sigma}-\mathbf{w}\right)\cdot\mathbf{m}\, dl - \int_{\partial S(t)} \mathbf{j}^{\Sigma}\cdot\mathbf{m}\, dl,\end{aligned} \tag{2.15}$$

where c is the molar concentration of surfactant in the bulk (mol/m^3), c^{Σ} is the molar surface concentration of surfactant on the interface (mol/m^2), and $\mathbf{j}$ and $\mathbf{j}^{\Sigma}$ are the diffusive fluxes in the bulk phase and on the interface, respectively. Note that the surfactant species is present only in the denser phase and on the interface.
The local formulation of equations (2.14) and (2.15) can be derived as recorded in appendix A.2. The species transport equation in local form reads

$$\partial_t c_i^{\pm} + \nabla\cdot\left(c_i^{\pm}\mathbf{v} + \mathbf{j}_i^{\pm}\right) = r_i^{\pm} \quad \text{in } \Omega^{\pm}(t), \tag{2.16}$$

$$\left[\!\left[c_i(\mathbf{v}-\mathbf{v}^{\Sigma}) + \mathbf{j}_i\right]\!\right]\cdot\mathbf{n}_{\Sigma} = 0 \quad \text{on } \Sigma(t). \tag{2.17}$$

These equations are completed by initial and boundary conditions in both phases. Moreover, the source term and the diffusive fluxes need to be modelled; see section 2.2.1.
In local formulation the equations for surfactant transport in the bulk phase and on the interface read

$$\partial_t c + \nabla\cdot(c\mathbf{v} + \mathbf{j}) = 0 \quad \text{in } \Omega^{+}(t), \tag{2.18}$$

$$\partial_t^{\Sigma} c^{\Sigma} + \nabla_{\Sigma}\cdot\left(c^{\Sigma}\mathbf{v}^{\Sigma} + \mathbf{j}^{\Sigma}\right) = s^{\Sigma} \quad \text{on } \Sigma(t), \tag{2.19}$$

[3] Usually the surfactant species is not reacting in the bulk phase. Moreover, if we consider liquid/gas systems, the surfactant species is not transferred to the disperse phase, i.e. partitioning phenomena can be neglected. In case of liquid/liquid systems, e.g. water/oil, partitioning [75] has to be taken into account.

where the sorption term s^Σ satisfies

$$s^\Sigma + [\![c(\mathbf{v} - \mathbf{v}^\Sigma) + \mathbf{j}]\!] \cdot \mathbf{n}_\Sigma = 0 \quad \text{on } \Sigma(t), \tag{2.20}$$

and equation (2.19) can be seen as a dynamic boundary condition for equation (2.18). Assuming no relative motion between the fluid and the interface, i.e. when there is no phase change, equation (2.20) becomes

$$s^\Sigma + [\![\mathbf{j} \cdot \mathbf{n}_\Sigma]\!] = 0 \quad \text{on } \Sigma(t). \tag{2.21}$$

The initial and boundary conditions for the surfactant transport equations in the bulk and on the interface read

$$c(0, \mathbf{x}) = c_0(\mathbf{x}) \quad \text{for } \mathbf{x} \in \Omega^+(0), \tag{2.22}$$

$$c(0, \mathbf{x}) = 0 \quad \text{for } \mathbf{x} \in \Omega^-(0), \tag{2.23}$$

$$c^\Sigma(0, \mathbf{x}) = c_0^\Sigma \quad \text{for } \mathbf{x} \in \Sigma(0). \tag{2.24}$$

The systems of equations (2.16) - (2.17) and (2.18) - (2.24) are not closed, i.e. additional relations are needed to determine the diffusive fluxes and the source terms as functions of the primitive variables.

2.2.1 Species transport problem closure

2.2.1.1 Diffusive fluxes

The species are assumed to be diluted in the bulk phases, thus, the diffusive fluxes are modelled via Fick's law, i.e.

$$\mathbf{j}_i^\pm = -D_i^\pm \, \nabla c_i^\pm \quad \text{in } \Omega^\pm(t). \tag{2.25}$$

2.2.1.2 Species transfer

As stated by equation (2.17), the species fluxes at the interface must be continuous and no phase change occurs. Moreover, the concentration ratio between disperse and continuous phase at the interface is prescribed by Henry's law,

$$\frac{c_i^-|_\Sigma}{c_i^+|_\Sigma} = H_i \quad \text{at } \Sigma(t); \tag{2.26}$$

see [8]. In presence of surfactant this condition holds only under certain circumstances, as it will be discussed in section 2.3.2.

2.2.1.3 Source term

In presence of chemical reactions, the source term r_i is going to be modelled with respect to the reaction type taking place. For instance, the simplest chemical reaction that could occur is a first-order decay reaction. In this case, the reactive source term reads

$$r_i = -k \, c_i, \tag{2.27}$$

where k represents the reaction rate constant. Other chemical reactions could be considered, but they are not part of the scope of this work.

2.2.2 Surfactant transport problem closure

2.2.2.1 Diffusive fluxes

Under the assumption of dilute surfactant concentration both in the liquid phase and on the interface[4], the surfactant diffusive fluxes are modelled via Fick's law, i.e.

$$\mathbf{j} = -D\ \nabla c \quad \text{in } \Omega^+(t), \tag{2.28}$$

$$\mathbf{j}^\Sigma = -D^\Sigma\ \nabla_\Sigma c^\Sigma \quad \text{on } \Sigma(t). \tag{2.29}$$

Furthermore, homogeneous Neumann conditions for the diffusive fluxes at the outer domain boundary are assumed, i.e.

$$\mathbf{j} \cdot \mathbf{n} = 0 \quad \text{on } \partial\Omega(t). \tag{2.30}$$

2.2.2.2 Sorption process and surface tension equation of state

A constitutive equation for the sorption source term s^Σ in equation (2.15) is required. To model this term two limiting situations can be considered: diffusion-controlled (fast) sorption and kinetically-controlled (slow) sorption [63].
When a new interface between a surfactant solution and a gaseous phase (or another fluid) is created, a finite time is required to reach a local equilibrium state between the surfactant concentration on the interface c^Σ and the bulk concentration c. The dynamic adsorption behaviour can be described as a two-step process [13] as depicted in figure 2.2:

1. *adsorption process*, i.e. the transfer of surfactant molecules between the interface layer and the sub-surface layer (the layer immediately adjacent to the interface with a thickness of a few molecule diameters). The bulk concentration value in this sub-surface layer is referred to as $c_{|\Sigma}$

2. *bulk mass transfer process* (diffusion process for anionic surfactant), i.e. the exchange of molecules between the sub-surface layer and the bulk phase.

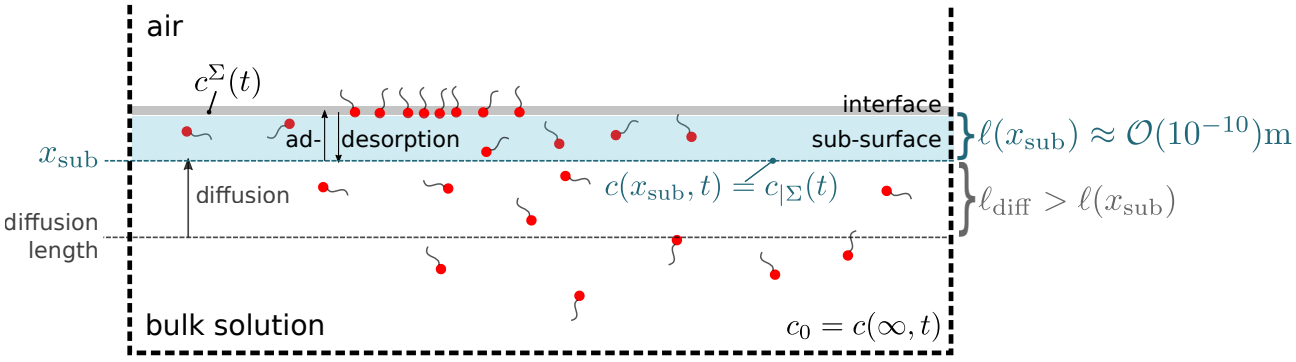

Figure 2.2: Schematic representation of the dynamic ad- and desorption mechanism. Surfactant molecules are adsorbed to the interface from the sub-surface layer. Diffusion supplies new molecules from the bulk solution to the sub-surface. Figure bases on [13, figure 8].

[4] In case of multicomponent surfactant systems, the interface can be significantly covered by surfactants and cross-effects between the surfactant species should be considered. These effects can be accounted for using the interfacial Maxwell–Stefan equations, cf. [19].

When surfactant molecules are adsorbed from the solution to the freshly generated surface ($c^\Sigma = 0$), the concentration first decreases in the sub-surface layer. Then the sub-surface concentration tends to be restored by diffusion from the bulk solution to the sub-surface.
In case of diffusion-controlled adsorption, diffusion is the dominant mechanism responsible for establishing adsorption equilibrium. The adsorption process is much faster than the diffusive transport from the bulk to the sub-surface layer. Under these circumstances, the surface concentration c^Σ is always in equilibrium with the sub-surface concentration $c(x_{\text{sub}}, t) = c_{|\Sigma}(t)$ which changes as diffusion occurs. On the other hand, if the adsorption or desorption rate at the interface is slow or comparable to the diffusion rate between the bulk solution and the sub-surface, c^Σ is not necessarily at local equilibrium with $c(x_{\text{sub}}, t)$. This situation occurs when there is a certain activation energy barrier to be overcome in order to transfer molecules from the sub-surface to the interface. To describe this process, a model considering both diffusion and adsorption/desorption steps is necessary.
Thus, the transfer rate in the two limiting conditions will be determined in two different ways:

- diffusion-controlled (fast) sorption (recall equation (2.21) which always holds, independently from the sorption mechanism):

$$s^\Sigma_{\text{fast}} = -\left[\!\left[\mathbf{j} \cdot \mathbf{n}_\Sigma\right]\!\right] = -\mathbf{j}^+ \cdot \mathbf{n}_\Sigma + \mathbf{j}^- \cdot \mathbf{n}_\Sigma, \tag{2.31}$$

  Note that only one of the two terms will be non-zero if the surfactant is only soluble in one of the bulk phases, say $s^\Sigma_{\text{fast}} = -\mathbf{j}^+ \cdot \mathbf{n}_\Sigma$. As described above, in the case of fast (as compared to diffusive transport) sorption, the ad- and desorption rates are locally equilibrated, i.e.

$$s^{\text{ads}}\left(c_{|\Sigma}, c^\Sigma\right) = s^{\text{des}}\left(c^\Sigma\right). \tag{2.32}$$

  This equality leads to a local relationship between c^Σ and $c_{|\Sigma}$, which needs to be accounted for in the numerical solution. In case of fast sorption, the interfacial surfactant mass balance can be viewed as a dynamic boundary condition for the surfactant bulk transport, coupling the Dirichlet- and the Neumann-data of the bulk concentration field. The numerical method needs to map this into a discretized form.

- kinetically-controlled (slow) sorption:

$$s^\Sigma_{\text{slow}} = s^{\text{ads}}\left(c_{|\Sigma}, c^\Sigma\right) - s^{\text{des}}\left(c^\Sigma\right), \tag{2.33}$$

  where $s^{\text{ads}}\left(c_{|\Sigma}, c^\Sigma\right)$ describes the rate of adsorption and $s^{\text{des}}\left(c^\Sigma\right)$ the desorption rate. Here the adsorption/desorption step is presented by means of a kinetic expression to account for the presence of the energy barrier and the lack of local equilibrium between c^Σ and $c_{|\Sigma}$. Note that the rate of adsorption is a function of the bulk concentration near the interface and the concentration of the adsorbed species, while the desorption rate is usually assumed to be a function of the surface concentration only.

Starting point of the concrete sorption modeling is the Gibbs-Duhem equation for dilute surfactant concentrations in a solution with a surfactant mixture. In the considered isothermal case, this reads as

$$d\sigma = -\sum_{i=1}^{N} c_i^\Sigma d\mu_i^\Sigma, \tag{2.34}$$

where μ_i^Σ is the (model-based) surface chemical potential of species i. In case of local adsorption/desorption equilibrium, $\mu_i = \mu_i^\Sigma$ and, hence, the Gibbs-Duhem equation becomes

$$d\sigma = -\sum_{i=1}^{N} c_i^\Sigma d\mu_i, \tag{2.35}$$

known as the Gibbs adsortion equation. Since the bulk concentration of the surfactants can be considered dilute, the chemical potential is given by

$$\mu_i(T, p, x_1, ..., x_N) = g_i(T, p) + RT \ \ln x_i, \tag{2.36}$$

where $g_i(T, p)$ is the Gibbs free energy of the pure constituent i at the temperature and the pressure of the mixture, and $x_i = c_i/c_{\text{tot}}$ is the bulk molar fraction of species i. For simplicity, a single surfactant system is considered. Then, the Gibbs' adsorption equation (2.35) simplifies to

$$d\sigma = -c^\Sigma d\mu. \tag{2.37}$$

Introducing (2.36) into equation (2.37), the relationship between the bulk molar fraction x, the concentration of the adsorbed form c^Σ and the change of surface tension $d\sigma$ is obtained as

$$d\sigma = -RTc^\Sigma d(\ln x). \tag{2.38}$$

With equation (2.38) and a surface concentration isotherm $c^\Sigma = f(c)$, one can derive the corresponding surface tension equation of state. At this point, to describe the relationship between the surfactant bulk concentration, the concentration of the adsorbed species c^Σ and the surface tension $\sigma(c^\Sigma)$, the equilibrium state, i.e. the diffusion-controlled (fast) sorption, is considered. A generally accepted assumption in literature is that the relationship between $c^\Sigma(t)$ and $\sigma(c^\Sigma(t))$ is the same as at equilibrium.

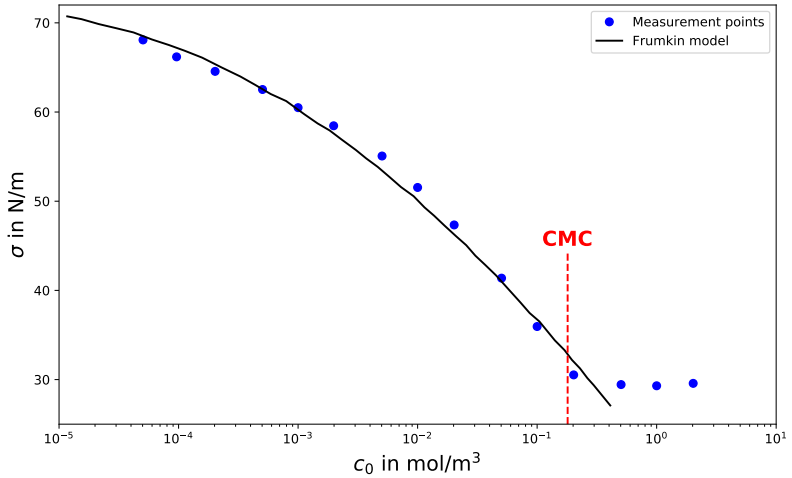

Figure 2.3: Typical surface tension plot with respect to the surfactant bulk concentration. Data extracted from [25, figure 2.3] for Triton X100, experimental data obtained with emerging bubble shape method; theoretical curve computed with Frumkin model.

Moreover, it is important to underline that all the sorption models presented in the following sections are valid under the hypothesis that the initial bulk concentration is smaller than the

critical micelle concentration (CMC), i.e. the concentration of surfactants above which micelles form. For $c_0 < CMC$, the surface tension changes strongly with the concentration of surfactant. After reaching the CMC, the surface tension remains essentially constant because only the monomeric form of the surfactant contributes to the surfactant activity or chemical potential and, hence, to the surface tension reduction. This behaviour is depicted in figure 2.3, where the dots represent the output of a typical surface tension measurement and the black line corresponds to a surface tension equation of state. As can be seen from figure 2.3, above the CMC, the model is not able to describe the surface tension changes.

2.2.2.3 Diffusion-controlled sorption (fast)

Fast sorption processes are characterized by quasi-instantaneous sorption. In the following paragraphs, a collection of sorption models for single component systems is recalled [13, 52], starting from the classical ones such as Henry, Langmuir and Frumkin models to close with more recent ones such as reorientation and aggregation models. A detailed description of the latter, more elaborate models can be found in [63] and [27].
To determine the equilibrium adsorption parameters in the adsorption isotherm reported below, experiments are needed. In particular, by applying a surface tension equation of state to surface tension measurement data $\sigma(c^\Sigma)$, the best-fit equilibrium adsorption parameters are found.

Henry model The simplest way to describe the sorption process is to apply the Henry model, where a linear relationship between the surfactant bulk concentration c and the concentration of the adsorbed one c^Σ is assumed. Thus, the relation between these two quantities reads

$$c^\Sigma = Kc, \tag{2.39}$$

where K is the Henry constant[5]. K not only represents a measure of the surface activity of the surfactant, but also the thickness of the bulk solution which contains as much surfactant as the interface with c^Σ. The corresponding equation of state for the surface tension becomes

$$\sigma = \sigma_0 - RTc^\Sigma, \tag{2.40}$$

where σ is the surface tension in N/m, R is the universal gas constant with $R = 8.3144$ J/(mol K) and T is the absolute temperature of the system in Kelvin. In the Henry model, interactions between molecules are not considered, the model is only applicable in case of low surface coverage, i.e. small values of c^Σ, and it has the drawback that there is no limit on c^Σ. In fact, experiments show that the interface has a certain capacity and it can hold only a limited amount of surfactant molecules.

Langmuir model The Langmuir adsorption isotherm takes partially into account the interactions between molecules at the interface by means of the Langmuir equilibrium constant a_L, expressed in mol/m^3, and the maximum number of adsorbed molecules per area c^Σ_∞. The adsorption isotherm reads as

$$c^\Sigma = c^\Sigma_\infty \frac{c/a_L}{1 + c/a_L}. \tag{2.41}$$

The Langmuir equilibrium constant corresponds to a situation in which half of the surface is covered by surfactant, that is $c^\Sigma = c^\Sigma_\infty/2$. Thus, at low concentrations $c/a_L << 1$, this

[5]Considering the molar concentration fields $[c^\Sigma] = \text{mol/m}^2$, $[c] = \text{mol/m}^3$, then $[K] = \text{m}$.

constant can be related to the Henry constant K through the relation $K = c_\infty^\Sigma / a_L$. To judge if a concentration is low or high, the reference concentration is given by a_L. Hence, the value of $1/a_L$ provides a useful measure of the surfactant activity, as also K does. The larger the value of $1/a_L$, the more surface active the surfactant and the better its ability in reducing the surface tension.
The Langmuir surface equation of state follows as

$$\sigma = \sigma_0 + RT\ c_\infty^\Sigma\ \ln\left(1 - \frac{c^\Sigma}{c_\infty^\Sigma}\right), \tag{2.42}$$

or, equivalently,

$$\sigma = \sigma_0 - RT\ c_\infty^\Sigma\ \ln\left(1 + \frac{c}{a_L}\right). \tag{2.43}$$

With increasing chain length of the hydrophobic part of the surfactant (e.g. for fatty acids), the Langmuir model fails to predict the surface tension and the concentration of the adsorbed form of the surfactant. Deviations are due to interaction between the adsorbed molecules.

Frumkin model The starting point of this model is the Langmuir one, but with an additional term considering solute-solvent interactions at a non-ideal surface which affect c^Σ. As a result, the so-called Frumkin isotherm reads as

$$b\ c = \frac{c^\Sigma \omega}{1 - c^\Sigma \omega}\ e^{-2ac^\Sigma \omega}, \tag{2.44}$$

where b is the Frumkin equilibrium adsorption constant, $[b] = \mathrm{m}^3/\mathrm{mol}$, $\omega = 1/c_\infty^\Sigma$ is the partial molar surface area, $[\omega] = \mathrm{m}^2/\mathrm{mol}$, and a here is a dimensionless constant that describes the intermolecular interactions between the adsorbed molecule, in other words a is a measure of the non-ideality of mixing in the interface layer. For this adsorption isotherm, the surface tension is given as

$$\sigma = \sigma_0 + \frac{RT}{\omega}\ \left[\ln\left(1 - c^\Sigma \omega\right) + a\ \left(c^\Sigma \omega\right)^2\right], \tag{2.45}$$

or, using the maximum surface coverage c_∞^Σ, as

$$\sigma = \sigma_0 + RTc_\infty^\Sigma\ \left[\ln\left(1 - \frac{c^\Sigma}{c_\infty^\Sigma}\right) + a\ \left(\frac{c^\Sigma}{c_\infty^\Sigma}\right)^2\right]. \tag{2.46}$$

Note that equations (2.45) and (2.46) are identical to the Langmuir equation of state in case $a = 0$.

Reorientation model This model admits the existence of molecules of surfactant in two states, state 1 and 2, in the adsorption layer. Thus we need to consider two molar areas of an adsorbed molecule, ω_1 and ω_2, with the assumption $\omega_1 > \omega_2$. ω_1 is the molar area required at an empty interface and ω_2 is the minimum area needed at a covered interface. The relations between the molar areas and surface concentrations fields of the two states are described by

$$c^\Sigma = c_1^\Sigma + c_2^\Sigma, \tag{2.47}$$

$$\omega c^\Sigma = \omega_1 c_1^\Sigma + \omega_2 c_2^\Sigma. \tag{2.48}$$

The model involves the ratio between surface concentrations in the two possible adsorption states of the molecules calculated through the generalized Joos' adsorption equation:

$$\frac{c_1^\Sigma}{c_2^\Sigma} = e^{(\omega_1-\omega_2)/\omega} \left(\frac{\omega_1}{\omega_2}\right)^\alpha e^{-(\sigma_0-\sigma)(\omega_1-\omega_2)/(RT)}, \tag{2.49}$$

where the coefficient α is usually taken as equal to zero. The associated surface equation of state and the relative adsorption isotherm are

$$\sigma = \sigma_0 + \frac{RT}{\omega} \ln\bigl(1 - c^\Sigma\omega\bigr), \tag{2.50}$$

$$bc = \frac{c_2^\Sigma\omega}{\bigl(1 - c^\Sigma\omega\bigr)^{\omega_2/\omega}}, \tag{2.51}$$

where b is still the adsorption constant as in the Frumkin model. For $\omega_1 = \omega$ this model falls back into the Langmuir model with $b = 1/a$, where a is the Langmuir equilibrium constant.
It has been shown that the reorientation model is superior to the Langmuir and Frumkin ones especially for surfactants with small mutual interaction at the interface, for instance molecules with a rather large molar area demand.

Aggregation model This model has been developed to contain only one molar area ω_1 of an adsorbed surfactant at a covered interface, as the Langmuir and Frumkin models, but including a critical surface adsorption concentration c^Σ_{crit} and a non-dimensional surface adsorption number n. The mean molar area can be obtained from a weighted average that involves the molar area of the adsorbed molecule and the current and critical adsorption concentrations:

$$\omega = \omega_1 \frac{1 + n\bigl(\frac{c^\Sigma}{c^\Sigma_{\text{crit}}}\bigr)^{n-1}}{1 + \bigl(\frac{c^\Sigma}{c^\Sigma_{\text{crit}}}\bigr)^{n-1}}. \tag{2.52}$$

Then, the adsorption isotherm and the surface equation of state for the aggregation model read as

$$bc = \frac{c^\Sigma\omega}{\left[1 - c^\Sigma\omega\Bigl(1 + \bigl(\frac{c^\Sigma}{c^\Sigma_{\text{crit}}}\bigr)^{n-1}\Bigr)\right]^{\omega_1/\omega}}, \tag{2.53}$$

$$\sigma = \sigma_0 + \frac{RT}{\omega} \ln\left[1 - c^\Sigma\omega\Bigl(1 + \Bigl(\frac{c^\Sigma}{c^\Sigma_{\text{crit}}}\Bigr)^{n-1}\Bigr)\right]. \tag{2.54}$$

Here it can already be anticipated that the implementation and the use of this model may be problematic for the presence of the critical concentration in the surface tension equation of state. In fact, from experiments [26] it is known that c^Σ_{crit} is much smaller than c^Σ, thus the argument of the logarithm may become quickly negative and make the simulation stop. This aspect is discussed further in section 5.1.

2.2.2.4 Kinetically-controlled sorption (slow)

In case of slow sorption processes, i.e. in presence of a kinetic barrier, the surfactant transfer from the sublayer to the interface is slower than the diffusive transport. The barrier can be due to sterical hindering, spatial reorientation or conformational changes accompanying the adsorption process. In this case, a kinetic modelling of the transfer process is needed.

Henry model For the Henry isotherm, the net rate of the reversible adsorption reads:

$$s^{\Sigma}_{\text{slow}} = \kappa^{\text{ads}} c_{|\Sigma} - \kappa^{\text{des}} \frac{c^{\Sigma}}{c^{\Sigma}_{\infty}}. \tag{2.55}$$

The first term on the right-hand side represents the rate of adsorption and the second one is the desorption rate. Here $c_{|\Sigma}$ is the concentration profile in the sub-surface[6]. The parameters k^{ads} and k^{des} describe the rate constants for the adsorption and desorption processes[7]. The corresponding surface equation of state is still (2.40).

Langmuir model The net rate of surfactant adsorption in the Langmuir sorption model reads:

$$s^{\Sigma}_{\text{slow}} = \kappa^{\text{ads}} c_{|\Sigma} \left(1 - \frac{c^{\Sigma}}{c^{\Sigma}_{\infty}}\right) - \kappa^{\text{des}} \frac{c^{\Sigma}}{c^{\Sigma}_{\infty}} \tag{2.56}$$

where the two constants for adsorption and desorption can be related to the Langmuir equilibrium constant for fast sorption:

$$\frac{1}{a} = \frac{\kappa^{\text{ads}}}{\kappa^{\text{des}}}. \tag{2.57}$$

The corresponding surface tension equation of state is still equation (2.43) or (2.42).

2.3 Surfactant effects on species transport

The modelling of the surfactant effects on mass transfer is, partly, an open topic. The easiest way to approach this problem is to consider the transport of surfactant and chemical species as the transport of two independent quantities. Thus, the presence of a surface active agent in the system will affect only indirectly the mass transfer mechanism. In other words, the surfactant modifies the interfacial properties between gas and liquid phases, e.g. lowering the surface tension. Since the surfactant concentration usually is non homogeneous, this has also a huge impact on the flow field near the interface. The mass transfer problem is then seeing a modified flow field which will also strongly influence the species transfer itself.
A more sophisticated model would have to include direct effects of the surfactant on the species transfer at the interface if present. Some studies have already been done in this direction; see, for instance, [4]. The idea here is that the surfactant species is hindering the mass transfer mechanism. The molecules of surfactant are accumulating on the gas-liquid interface constituting a sort of barrier for the mass transfer, and the mass transfer will be reduced; see figure 2.4. Nevertheless, to quantify the reduction in mass transfer due to this effect is not an easy task. It is also not clear how small/big is this reduction/hindrance with respect to the global reduction in mass transfer observed due to the modification of the flow field. A first modelling attempt is outlined in section 2.3.1 and it will be described in detail in an upcoming publication [10].

[6] This quantity is a bulk concentration, thus its physical unit is $[c_{|\Sigma}] = \text{mol/m}^3$.
[7] The physical units of the two constant are $[k^{\text{ads}}] = \text{m/s}$ and $[k^{\text{des}}] = \text{mol/(m}^2\text{s)}$.

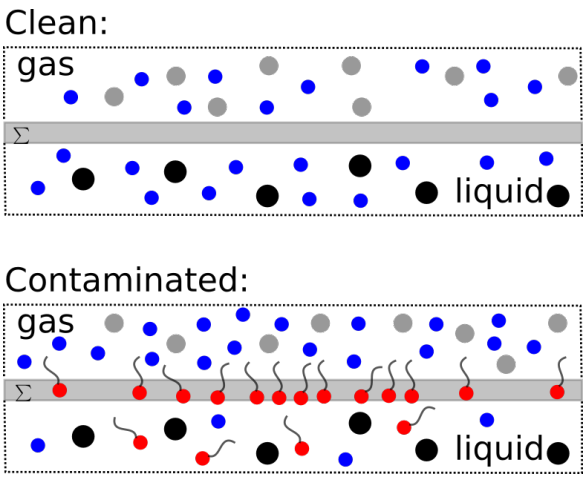

Figure 2.4: Sketch to visualize the hindrance effect due to the presence of surfactant on the gas-liquid interface. The transferred species molecules are depicted in blue, the surfactant molecules in red, the gas and the liquid molecules in gray and black, respectively.

2.3.1 Hindrance effect

Consider a thin layer around the interface. One can think of the mass transfer process from one phase to the other as a two-step process: the molecules first go from one phase to the interface and then from the interface to the other phase. This picture is valid for any species i. It can be a surfactant or any other substance. The one-sided mass transfer can be written as the balance between ad- and desorption from one bulk phase to the interface:

$$\dot{m}_i^{\pm,\Sigma} = s_{i,\pm}^{\mathrm{ad}} - s_{i,\pm}^{\mathrm{de}}; \tag{2.58}$$

see figure 2.5 for a graphical interpretation.

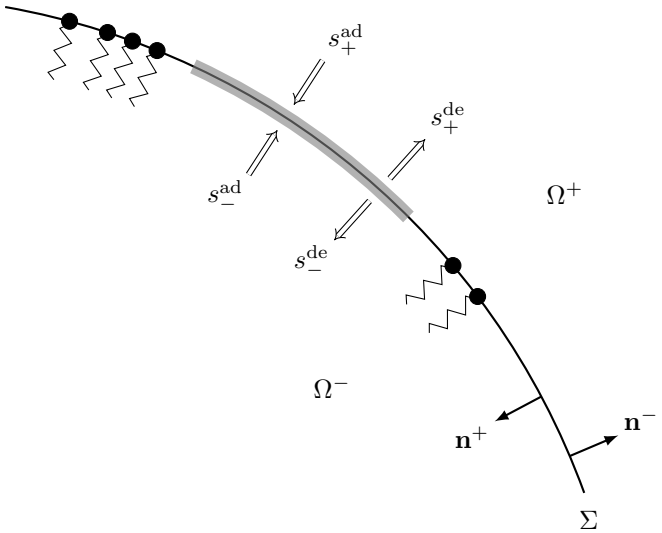

Figure 2.5: Sketch representing the mass transfer at the gas-liquid interface in the presence of surfactant.

Under the hypothesis of *quasi-stationarity*, a reduced form of the surface mass balance can be written as

$$\dot{m}_i^{+,\Sigma} + \dot{m}_i^{-,\Sigma} = 0. \tag{2.59}$$

A preliminary expression for $\dot{m}_i^{+,\Sigma}$ has been derived based on the works of Bothe [4, 5] and Bothe and Dreyer [7]. The reduced mass flux then reads

$$\dot{m}^{+,\Sigma} = \overline{k} \exp\left(-\frac{\sigma_0 - \sigma}{RTc_\infty^\Sigma}\right)\left(c_i^+ - \frac{c_i^-}{H_i}\right), \tag{2.60}$$

where c_i indicates the molar concentration of the species i, H_i its Henry constant and $\overline{k}$ is a constant collecting the desorption constants from each side and other terms; see appendix B.

2.3.2 Boundary conditions at the interface with hindrance effect

Close to the gas-liquid interface, the boundary condition for the transferred species is derived from (2.59) stating the continuity of the fluxes and it reads

$$D^- \frac{\partial c_i^-(y,t)}{\partial y}\bigg|_\Sigma = D^+ \frac{\partial c_i^+(y,t)}{\partial y}\bigg|_\Sigma, \tag{2.61}$$

where y in this case is a local coordinate normal to the interface. In general, Henry's law is not valid if surfactant is present on the interface and constitutes a barrier for the mass transfer. In this case, according to (2.60), the fluxes at the interface read

$$D_i^\pm \frac{\partial c_i^\pm(y,t)}{\partial y}\bigg|_\Sigma = k_{\text{eff}}\left(c_i^+ - \frac{c_i^-}{H}\right)\bigg|_\Sigma, \tag{2.62}$$

where k_{eff} can be defined as hindrance coefficient and reads

$$k_{\text{eff}} = \overline{k} \exp\left(-\frac{\sigma_0 - \sigma}{RTc_\infty^\Sigma}\right). \tag{2.63}$$

Note that for $k_{\text{eff}} \to \infty$, equation (2.61) still holds, but, since the mass transfer rate stays finite as $k_{\text{eff}} \to \infty$, we obtain

$$c_i^+ - \frac{c_i^-}{H} = 0, \tag{2.64}$$

i.e. Henry's law. The parameter $\overline{k}$ should be provided from experiments. In [39], a procedure to measure the reduction factor is suggested. The authors perform a series of experiments to determine the liquid side mass transfer coefficient at a free gas-liquid interface with and without contaminants. Based on the species (oxygen in their work) mass balance in the liquid phase under an unsteady-state condition, the volumetric mass transfer coefficient is determined. It has been observed that the liquid-side mass transfer coefficient decreases with increasing surfactant concentration until a plateau is reached when the surfactant concentration is equal or higher than the CMC.

2.4 Summary of the governing equations

In table 2.1 a summary of the equations constituting the full mathematical model for two-phase flows under the influence of surfactant, and, possibly, in presence of mass transfer from the gas phase to the liquid phase is given.

Table 2.1: Summary of the governing equations.

Hydrodynamics	
Mass	$\partial_t \rho + \nabla \cdot (\rho \mathbf{v}) = 0 \quad \text{in } \Omega(t) \setminus \Sigma(t)$
Momentum	$\partial_t (\rho \mathbf{v}) + \nabla \cdot (\rho \mathbf{v} \otimes \mathbf{v}) = \nabla \cdot \mathbf{S} + \rho \mathbf{b} \quad \text{in } \Omega(t) \setminus \Sigma(t)$
	$\mathbf{v} \cdot \mathbf{n}_\Sigma = \mathbf{v}^\Sigma \cdot \mathbf{n}_\Sigma = V_\Sigma \quad \text{on } \Sigma(t)$
	$[\![\mathbf{v}]\!] = 0 \quad \text{on } \Sigma(t)$
	$\left[\!\left[p\mathbf{I} - \mathbf{S}^{\text{visc}} \right]\!\right] \cdot \mathbf{n}_\Sigma = \sigma \kappa \mathbf{n}_\Sigma + \nabla_\Sigma \sigma \quad \text{on } \Sigma(t)$
	$\mathbf{v}(0, \mathbf{x}) = \mathbf{v}_0(\mathbf{x}) \quad \text{for } \mathbf{x} \in \Omega^\pm(t = 0)$
	$\Sigma(t = 0) = \Sigma_0$
	$\mathbf{v}(t, \mathbf{x}) = \mathbf{v}_\Omega \quad \text{for } \mathbf{x} \in \partial\Omega(t)$
Surfactant transport	
Bulk transport	$\partial_t c + \nabla \cdot (c\mathbf{v} + \mathbf{j}) = 0 \quad \text{in } \Omega^+(t)$
	$\mathbf{j} = -D \, \nabla c \quad \text{in } \Omega^+(t)$
	$c(0, \mathbf{x}) = c_0(\mathbf{x}) \quad \text{for } \mathbf{x} \in \Omega^+(0)$
Surface transport	$\partial_t^\Sigma c^\Sigma + \nabla_\Sigma \cdot \left(c^\Sigma \mathbf{v}^\Sigma + \mathbf{j}^\Sigma \right) = s^\Sigma \quad \text{on } \Sigma(t)$
	$s^\Sigma + [\![\mathbf{j} \cdot \mathbf{n}_\Sigma]\!] = 0 \quad \text{on } \Sigma(t)$
	$\mathbf{j}^\Sigma = -D^\Sigma \, \nabla_\Sigma c^\Sigma \quad \text{on } \Sigma(t)$
	$c^\Sigma(0, \mathbf{x}) = c_0^\Sigma \quad \text{for } \mathbf{x} \in \Sigma(0)$
Species transfer	
Bulk transport	$\partial_t c_i^\pm + \nabla \cdot \left(c_i^\pm \mathbf{v} + \mathbf{j}_i^\pm \right) = r_i^\pm \quad \text{in } \Omega^\pm(t)$
	$[\![\mathbf{j}_i]\!] \cdot \mathbf{n}_\Sigma = 0 \quad \text{on } \Sigma(t)$
	$\mathbf{j}_i^\pm = -D_i^\pm \, \nabla c_i^\pm \quad \text{in } \Omega^\pm(t)$
	$c_i^+|_\Sigma = c_i^-|_\Sigma / H_i$
	$c(0, \mathbf{x}) = c_0(\mathbf{x}) \quad \text{for } \mathbf{x} \in \Omega^+(0)$
	$c(0, \mathbf{x}) = 0 \quad \text{for } \mathbf{x} \in \Omega^-(0)$

Chapter 3

Numerical model

3.1 Hydrodynamics and mesh motion

The solution procedure is based on the Arbitrary Lagrangian-Eulerian (ALE) Interface Tracking method, originally presented by Hirt et al. [40], further developed by Muzaferija and Perić [67] and extended by Tuković and Jasak [91]. Collocated Finite Volume / Finite Area methods are applied to solve the transport equations on unstructured meshes of general topology with moving mesh support. The interface is represented by a computational surface mesh (boundary mesh) advected in a semi-Lagrangian manner under the enforcement of jump conditions at the interface, whereas the volume mesh is updated through automatic mesh motion with Laplacian smoothing in order to preserve a high mesh quality. The interface divides the computational domain into two disconnected sub-domains. The coupling between the two is enforced by the boundary conditions for pressure and velocity at $\Sigma(t)$ derived from the jump conditions (2.8) to (2.10). The governing equations are discretized in time using a second-order backward scheme known also as Gear's method [30]. The two fluid domains $\Omega^{\pm}(t)$ are discretized by a finite number of convex polyhedral control volumes V_P; see figure 3.1.

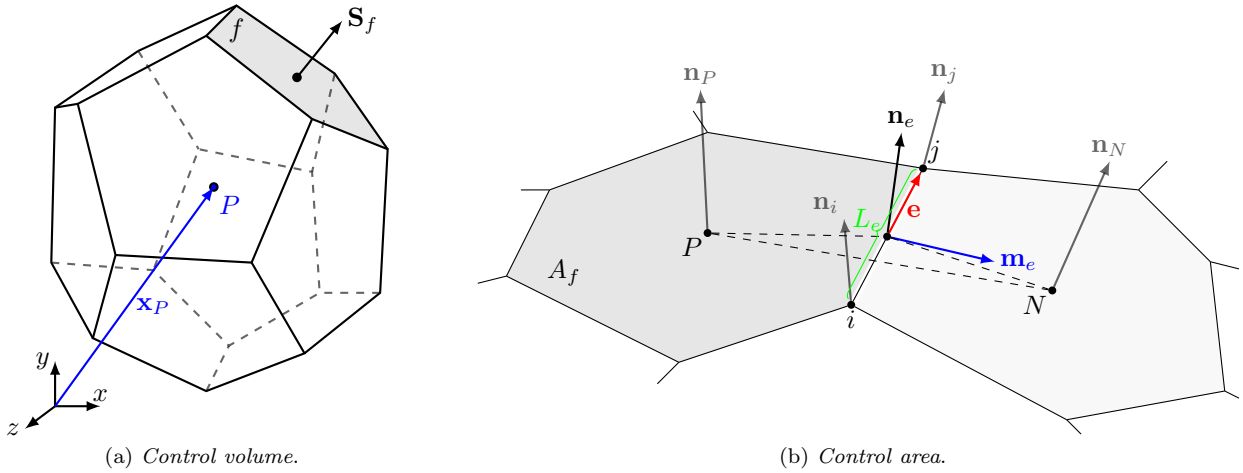

(a) *Control volume.* (b) *Control area.*

Figure 3.1: Sketches to introduce the FV/FA nomenclature.

The centroid of the control volume is denoted by P, and the one of the neighbouring cell by N. The cell faces f are of polygonal shape with area S_f and area normal vector $\mathbf{S}_f$. In analogy to

the volume discretization, the interface $\Sigma(t)$ is subdivided into polygonal control areas[1]. The centre of a control area is again denoted by P and the neighbouring one by N. The two control areas are separated by the edge e, characterized by the edge vector $\mathbf{e}$, length L_e and bi-normal $\mathbf{m}_e$ (perpendicular to both $\mathbf{e}$ and the edge normal vector $\mathbf{n}_e = (\mathbf{n}_1 + \mathbf{n}_2)/2$).
The pressure-velocity coupling is solved applying the iterative pressure implicit with splitting of operators (PISO) algorithm [44]. A modified version of the Rhie-Chow interpolation suggested in [91] is employed to prevent decoupling of pressure and velocity. A detailed description of the flow field solution and the mesh motion can be found in [91, 71].

3.1.1 Moving reference frame

For the simulation of single rising bubbles, a moving reference frame (MRF) that follows the bubble centre during its rise is employed. The presence of a non-inertial reference frame with the origin located in the centre of the bubble is taken into account via a correction in the momentum equation, i.e. $\rho\mathbf{a}_{\mathrm{MRF}}$ is added to the momentum equation. The boundary condition at the outer boundary also has to be corrected to account for the moving reference. The inlet velocity is set to minus the bubble rise velocity, i.e. $-\mathbf{u}_{\mathrm{b}}^n$ computed according to equation (3.5) below.
The idea behind the moving reference frame is to apply a proportional-derivative (PD) controller to keep the bubble in the centre of the domain; see page 159 in the reference [76], and [91]. The acceleration of the moving reference frame is computed from the resulting velocity variation in a time step Δt. In detail, let $\mathbf{c}_{\mathrm{b}}^0$ be the initial position of the bubble centre (set-point in control theory). The process variable, i.e. the variable we want to control, is the bubble centre $\mathbf{c}_{\mathrm{b}}$. The controller output is going to be the change in the bubble centre position $\Delta\mathbf{c}_{\mathrm{b}}$, which we want to minimize:

$$\Delta\mathbf{c}_{\mathrm{b}} = \lambda_P \left(\mathbf{c}_{\mathrm{b}}^n - \mathbf{c}_{\mathrm{b}}^0\right) + \lambda_D \frac{\mathbf{c}_{\mathrm{b}}^n - \mathbf{c}_{\mathrm{b}}^{n-1}}{\Delta t}, \tag{3.1}$$

where λ_P and λ_D are the non-negative proportional and derivative coefficients, respectively. The change in the bubble centre velocity is updated according to

$$\Delta\mathbf{u}_{\mathrm{b}} = \frac{\Delta\mathbf{c}_{\mathrm{b}}}{\Delta t} = \mathbf{u}_{\mathrm{b}}^{n-1} + \lambda_P \frac{\mathbf{c}_{\mathrm{b}}^n - \mathbf{c}_{\mathrm{b}}^0}{\Delta t} + \lambda_D \frac{\mathbf{c}_{\mathrm{b}}^n - \mathbf{c}_{\mathrm{b}}^{n-1}}{\Delta t^2}. \tag{3.2}$$

Rearranging the terms in equation (3.2), one obtains the relation implemented in the solver which reads

$$\Delta\mathbf{u}_{\mathrm{b}} = \lambda'_P \left(\mathbf{c}_{\mathrm{b}}^n - \mathbf{c}_{\mathrm{b}}^0\right) + \lambda'_D \frac{\mathbf{c}_{\mathrm{b}}^n - \mathbf{c}_{\mathrm{b}}^{n-1}}{\Delta t}, \tag{3.3}$$

where the parameters $\lambda'_P = \lambda_P/\Delta t$ and $\lambda'_D = \lambda_D/\Delta t$ can be set by the user. From the change in the velocity, the acceleration of the moving reference frame is computed, i.e.

$$\mathbf{a}_{\mathrm{MRF}} = \frac{\Delta\mathbf{u}_{\mathrm{b}}}{\Delta t}. \tag{3.4}$$

Then, the bubble centre velocity is updated according to

$$\mathbf{u}_{\mathrm{b}}^n = \mathbf{u}_{\mathrm{b}}^{n-1} + \Delta\mathbf{u}_{\mathrm{b}}. \tag{3.5}$$

[1]The computational surface mesh can be seen as the boundary of the volume mesh, that is the faces approximating the interface belong to the boundary cells of the volume mesh.

3.1.2 Pressure-velocity coupling at the interface

The coupling between the two phases at the interface is forced via boundary conditions derived from the equations (2.8) to (2.10). In figure 3.2 an overview of the boundary conditions at the interface and at the outer domain for velocity and pressure is given.

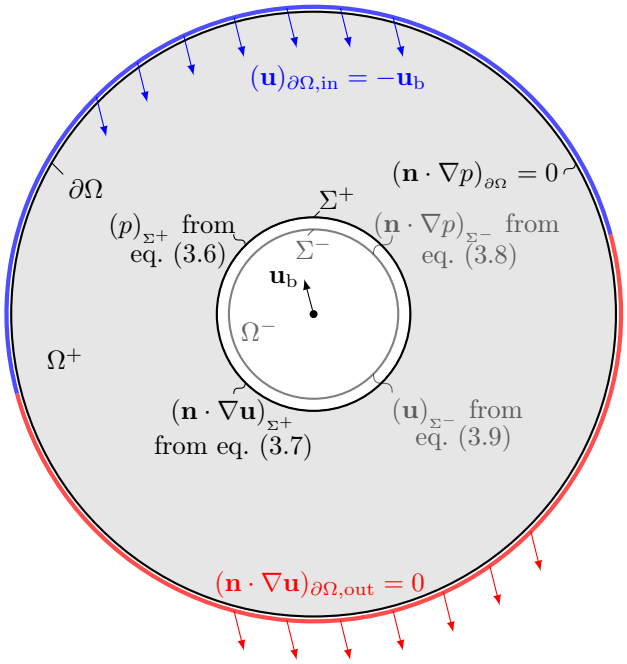

Figure 3.2: Overview of the boundary conditions for velocity and pressure.

At the interface, the following boundary conditions are applied[2],

$$p^+ = p^- - 2(\mu^+ - \mu^-)\nabla_S\cdot\mathbf{u} - \sigma\kappa \quad \text{on } \Sigma^+(t), \tag{3.6}$$

$$(\mathbf{n}\cdot\nabla\mathbf{u})^+ = \frac{\nabla_S\sigma}{\mu^+} + \frac{\mu^- - \mu^+}{\mu^+}\,\mathbf{n}\cdot(\nabla_S\mathbf{u}) + \frac{\mu^-}{\mu^+}\,\left[(\mathbf{I}-\mathbf{nn})\cdot(\mathbf{n}\cdot\nabla\mathbf{u})^-\right] - \mathbf{n}\,(\nabla_S\cdot\mathbf{u}) \quad \text{on } \Sigma^+(t), \tag{3.7}$$

$$\mathbf{n}^-\cdot(\nabla p)^- = -\frac{\rho^-}{\rho^+}\mathbf{n}^+\cdot(\nabla p)^+ - \rho^-\mathbf{n}^-\cdot\left(\frac{D\mathbf{u}}{Dt}\right)^- - \rho^-\mathbf{n}^+\cdot\left(\frac{D\mathbf{u}}{Dt}\right)^+ + \mu^-\mathbf{n}^-\cdot(\Delta\mathbf{u})^- + \rho^-\frac{\mu^+}{\rho^+}\mathbf{n}^+\cdot(\Delta\mathbf{u})^+ \quad \text{on } \Sigma^-(t), \tag{3.8}$$

$$\mathbf{u}^- = \mathbf{u}^+ \quad \text{on } \Sigma^-(t). \tag{3.9}$$

Equation (3.6) is derived from the force balance at the interface (2.10), taking the normal component of it to the interface. Equation (3.7) is derived considering the force balance at the interface (2.10) in tangential direction. Equation (3.8) is obtained considering that the jump of the momentum equation (2.5) across the interface must be equal to zero. Taking the normal component of this jump equation gives (3.8). To conclude, equation (3.9) states the continuity of the velocity across the interface according to equations (2.8) and (2.9). The kinematic

[2] A discussion about the possibility to use the surface operators in equation (3.7) is still open.

condition (3.9) is not directly implemented because of flux conservation requirements, but the velocity is split into tangential and normal component, and the conditions (3.10), (3.11) are applied. More details can be found in [91]. For each face constituting the interface on side Σ^-:

$$(\mathbf{u}^+)_t = (\mathbf{u}^-)_t, \tag{3.10}$$

while the normal component is calculated from the condition of zero net mass flux:

$$(\mathbf{u}^-)_n = \frac{\dot{V}^-}{S^-}\mathbf{n}^- \quad \text{on } \Sigma^-(t), \tag{3.11}$$

where $\dot{V}^- = \dot{V}^+$ is the volumetric flux across each face of Σ^-.

3.2 Equation discretization

Equations in the bulk and on the interface are discretized by means of Finite Volume (FV) and Finite Area (FA) methods, as anticipated above. Common to both bulk and interface equation discretization is the fact that the diffusion terms can be decomposed into orthogonal and non-orthogonal contributions, treating the first one implicitly and the second one explicitly; see [90].
Equations in the bulk and on the interface are solved with a Preconditioned Bi-conjugate Gradient (PBiCG) linear solver, with a Diagonal Incomplete-LU preconditioner (DILU) and tolerances of 10^{-6} for pressure and velocity, and 10^{-12} for the concentrations.

3.2.1 Finite Volume method

A Finite Volume method is applied to discretize the transport equations in the liquid phase. The transported quantity ϕ can be either the momentum, the species molar concentration c_i or the surfactant molar concentration c, from equations (2.2), (2.14) and (2.15) (in V(t)), respectively.
The fully discretized general transport equation in the control volume V_P reads

$$\frac{3\phi_P^n V_P^n - 4\phi_P^o V_P^o + \phi_P^{oo} V_P^{oo}}{\Delta t} + \sum_f F_f \phi_f^n = \sum_f D_f \left(\nabla\phi\right)_f^n \cdot \boldsymbol{S}_f + s_P V_P, \tag{3.12}$$

where $F_f = \boldsymbol{S}_f \cdot (\boldsymbol{u} - \boldsymbol{w})_f$ is the relative face flux. We denote the discrete velocity as $\boldsymbol{u}$ to distinguish between the discrete and the continuous quantity. The superscripts n, o and oo represent values evaluated at the new time instance t^n and the two previous time instance $t^o = t^n - \Delta t$ and $t^{oo} = t^o - \Delta t$. The discretized field is defined in the cell centres P as ϕ_P. Then, as required by the discretization of the diffusive and convective terms, the quantities $(\nabla\phi)_f$ and ϕ_f have to be interpolated to the faces centres.

3.2.2 Finite Area method

Applying the Finite Area method to the integral form of the surfactant transport equation on the interface (equation (2.15) on S(t)) or for any scalar quantity ϕ^Σ, the discretized equation

for the control surface S_P reads

$$\frac{3(\phi_P^S)^n(S_P)^n - 4(\phi_P^S)^o(S_P)^o \; + \; (\phi_P^S)^{oo}(S_P)^{oo}}{\Delta t} + \sum_e (F_e^S \phi_e^{S,n}) = \sum_e D_e^\Sigma \left(\nabla_S \phi^S\right)_e^n \cdot (\boldsymbol{m}_e L_e) \; + \; s_P^S S_P \tag{3.13}$$

with the relative edge flux $F_e^S = (\boldsymbol{m}_e L_e) \cdot (\boldsymbol{u} - \boldsymbol{w})_{||}$ and ∇_S representing the discrete counterpart of the surface gradient operator ∇_Σ. The quantity ϕ^S denotes the discretized counterpart of the continuous interface quantity ϕ^Σ in the face centre ϕ_P^S or interpolated to the edge centre ϕ_e^S. The term s_P^S is the discrete source term which can be split in explicit $s_{P,\text{exp}}^S$ and implicit $s_{P,\text{imp}}^S$ parts, respectively. In case of surfactant transport and in presence of *fast* sorption processes, the source term appears only in an explicit form.
The interpolation of the face-centred value ϕ_P^S to the edge-centred value ϕ_e^S is a delicate step and can be the source of numerical errors. In the following paragraph, a new edge interpolation scheme is introduced and in section 4.1 the comparison between the various surface discretization schemes with different edge interpolation methods is reported.

The surface operators available in the Finite Area library in *foamExtend* are

- gradient: *Gauss linear* or *leastSquares*
- divergence: *Gauss linear*

with *linear* being the only interpolation scheme effectively used if the Gauss discretization method is employed. From a preliminary test on these schemes, see section 4.1.2, emerged that the linear interpolation (from the face centre to the edge centre) was introducing relatively high errors. Thus, a new edge interpolation scheme based on the least squares gradient has been derived and implemented. This new edge interpolation scheme will be referred to as *least squares edge interpolation* scheme.

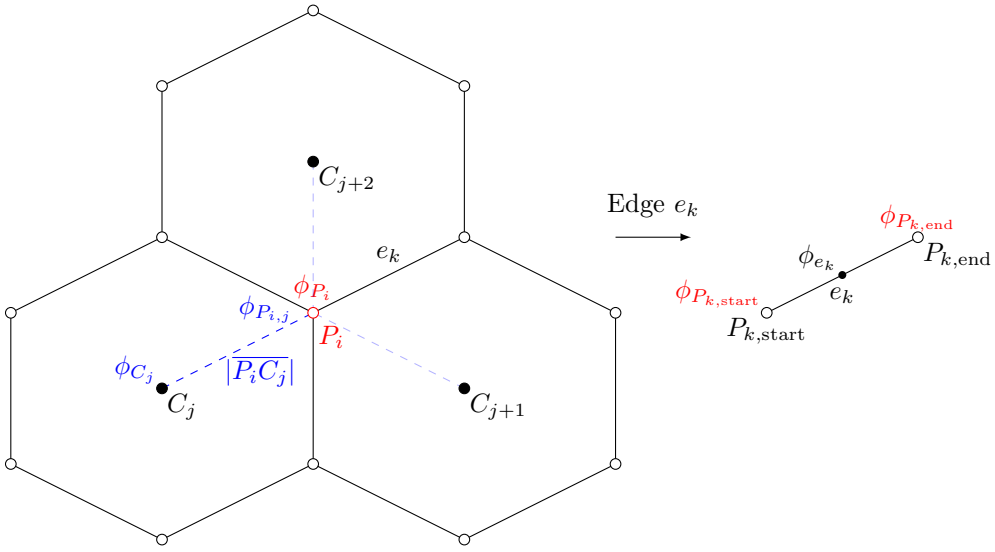

Figure 3.3: Least squares edge interpolation scheme, sketch of the numerical stencil.

The idea behind the *least squares* edge interpolation scheme is the following:

1. Consider the surface point P_i and all the faces with face centres C_j sharing the point P_i. For each face centred value ϕ_{C_j}, its interpolated value to the point P_i is computed using a least squares approach; cf. figure 3.3. Each face centre value interpolated to the point P_i reads
$$\phi_{P_{i,j}} = \phi_{C_j} + \overline{P_i C_j} \cdot \left(\nabla_\Sigma^{LS} \phi_{C_j}\right). \tag{3.14}$$

2. The interpolated field in P_i is then the average of the various $\phi_{P_{i,j}}$ computed according to equation (3.14) and weighted by the inverse distance between the point P_i and the face centres C_j, i.e.
$$\phi_{P_i} = \frac{\sum_j \phi_{P_{i,j}} / |\overline{P_i C_j}|}{\sum 1/|\overline{P_i C_j}|}. \tag{3.15}$$

3. The edge centre value is calculated as the mean between the values in the two points limiting the edge, i.e.
$$\phi_{e_k} = \frac{\phi_{P_{k,\text{start}}} + \phi_{P_{k,\text{end}}}}{2}. \tag{3.16}$$

The new interpolation scheme is tested and validated in section 4.1, where the numerical errors are also investigated with respect to the mesh topology.

3.2.3 Surfactant sorption process

Equation (3.13) is completed by the modelling of the sorption source term. In the system considered in this work only one surfactant species is present, while in [19, 18] the methodology and the results for multicomponent surfactant systems in free-surface flows were presented. The modelling of sorption processes has been introduced in section 2.2.2 and it differs considerably for fast and slow sorption. Common to both types is the evaluation of the surface tension as a function of the concentration of the adsorbed surfactant.

- For diffusion controlled (fast) sorption processes, the ad- and desorption rates are locally equilibrated, as stated in equation (2.32). This equality leads to an additional local relationship between c^Σ and the bulk concentration close to the interface $c_{|\Sigma}$, say
$$c^\Sigma = f(c_{|\Sigma}). \tag{3.17}$$
Various sorption models $f(c_{|\Sigma})$ are available to describe this relation; see section 2.2.2 and [71] for the full range of models implemented. From the sorption model, the value of
$$c_{|\Sigma} = f^{-1}\left(c^\Sigma\right) \quad \text{at } \Sigma \tag{3.18}$$
is taken as a Dirichlet boundary condition for the surfactant bulk equation (2.18). After the solution of the bulk equation with this Dirichlet data, the source term for the surface concentration equation is computed from the transmission condition (2.20) as
$$s^\Sigma = \boldsymbol{j} \cdot \boldsymbol{n}_\Sigma = -D(\nabla c \cdot \boldsymbol{n})_\Sigma =: s^\Sigma_{\text{fast}}. \tag{3.19}$$
In this way, the Neumann data from the new bulk field is transferred to the interfacial molar mass balance. Then the surface transport equation (2.19) is solved to obtain the new surface concentration field of the surfactant species.

- For kinetically controlled (slow) sorption processes, Henry and Langmuir models are available. The source term s^{Σ} is given directly by the adopted sorption model, as a balance between adsorption and desorption rates, see (2.33), i.e.

$$s^{\Sigma} = s^{\text{ads}}\left(c_{|\Sigma}, c^{\Sigma}\right) - s^{\text{des}}\left(c^{\Sigma}\right) =: s^{\Sigma}_{\text{slow}}. \tag{3.20}$$

  In this case, the coupling between the interface and the bulk flow is achieved by enforcing the discretized boundary condition (2.20) as a Neumann boundary condition for the bulk equation, i.e.

$$\mathbf{n} \cdot \nabla c = -\frac{s^{\Sigma}}{D} \quad \text{at } \Sigma. \tag{3.21}$$

After solving the interface and bulk surfactant transport equations, the surface tension $\sigma = \sigma(c^{\Sigma})$ is updated according to the sorption model chosen.

3.2.4 Temporal discretization

The temporal discretization introduces the time step Δt. The time step cannot be chosen arbitrarily, but it has to fulfil two conditions:

- Courant–Friedrichs–Lewy (CFL) condition

$$Co = \frac{u\Delta t}{\Delta x} \leq 1. \tag{3.22}$$

  Once the grid resolution Δx has been fixed, the time step size has to fulfil equation (3.22). In case of implicit solvers, a Courant number higher than unity may be tolerated, but this is not the limiting condition on the time step size for the problem under investigation.

- The time step size must be sufficiently small to fulfil the more restrictive criterion for the interface numerical stability [91], i.e.

$$\Delta t < \sqrt{\frac{\rho^{+} \min\left(l_{PN}\right)^3}{2\pi\sigma}}, \tag{3.23}$$

  with $\min\left(l_{PN}\right)$ being the minimum distance between two face centres on the interface; see figure 3.1b.

3.2.5 Spatial resolution requirements

Within the DNS framework, where all the scales of the motion and of the species transport need to be resolved, the correctness of the solution of the transport equations depends on the spatial discretization, too. Simple formulas can give a good estimate of the necessary grid resolution to correctly approximate the amount of transported quantity from one control volume/area to the other (cf. equations (3.24) and (3.26) below).
To characterize the flow, the following dimensionless numbers are used: the Reynolds number is used to predict the flow pattern, being defined as the ratio between inertial and viscous forces, $\text{Re} = uL/\nu$, where u is the velocity, L the characteristic length, ν the kinematic viscosity. The Schmidt number is used to characterize flows in which both momentum and mass diffusion processes occur. The Schmidt number is computed as the ratio between viscous and molecular

diffusion rates, $\mathrm{Sc} = \nu/D$, where D is the molecular diffusivity. To describe the species or surfactant transport, the dimensionless number considered is the Péclet number, defined as $\mathrm{Pe} = \mathrm{Re} \cdot \mathrm{Sc} = uL/D$. The Péclet number quantifies the ratio between advective and diffusive characteristic times, τ_{adv}, τ_{diff}. For the cases under investigation in this work, i.e. single rising bubbles, the Reynolds number varies around $\mathrm{Re} \approx 10^2$ and the Péclet number around $\mathrm{Pe} \approx 10^7$ (computed for the transported species).
Considering first the hydrodynamic problem, this Reynolds number suggests that the transport of momentum is dominated by convection in stream-wise direction. Thus a hydrodynamic boundary layer forms around the bubble surface. The average hydrodynamic boundary layer thickness δ_{h} around medium sized bubbles (see page 441 in [57]) can be estimated as

$$\delta_{\mathrm{h}} = \frac{d_{\mathrm{b}}}{\sqrt{2\mathrm{Re}}}, \tag{3.24}$$

where d_{b} is the bubble diameter. For the bubbles under investigation relation (3.24) predicts $\delta_{\mathrm{h}} \approx 10^{-5}$ m. Best practice guidelines suggest that an acceptable spatial discretization provides three to five cells in the boundary layer; cf. [96, table 4] where it can be seen that the error in the average gradient at the interface drops below 3% if there are at least four cells within the boundary layer.
The spatial discretization in normal direction is not the only constraint that has to be taken into account. Since the two phases are coupled at the interface explicitly, also the surface mesh discretization plays an important role. In the work by M. Steinhausen [81, chapter 3] the guidelines to create suitable computational grids for single rising bubble cases are listed. The analysis on the mesh requirements is performed based on the fulfilment of the transmission conditions at the interface derived from the force balance (2.10).
Consider now the species or surfactant transport problem in the liquid phase. The species transport along the bubble interface is mainly governed by two transport processes, namely advection in streamwise direction and diffusion in interface normal direction. As above, for the given Reynolds and Péclet numbers, the species transport is dominated by convection, leading to a very thin concentration boundary layer around the bubble. To estimate the species boundary layer thickness, the global Sherwood number Sh, is introduced. The Sherwood number describes the ratio between the amount of transferred species and the species quantity transported by pure diffusion ($\mathrm{Sh} = k_l L/D$, where k_l is the mass transfer coefficient, L a characteristic length and D the species diffusion coefficient). The Sherwood number can also be expressed as a function of Reynolds and Schmidt numbers, or simply as a function of the Péclet number. To compute the global Sherwood number, the correlation reported in [8] from [68] is used, which reads

$$\mathrm{Sh} \approx 2 + \frac{0.232\mathrm{Pe}^{1.72}}{1 + 0.205\mathrm{Pe}^{1.22}}. \tag{3.25}$$

The species boundary layer thickness relates to the Sherwood number according to

$$\delta_s \approx \frac{d_{\mathrm{b}}}{\mathrm{Sh}}, \tag{3.26}$$

which for the bubbles under investigation gives $\delta_s \approx 10^{-6}$ m. Thus, the numerical grid to correctly approximate species/surfactant transport problems has to be roughly 10 times finer than the necessary grid to resolve the hydrodynamic length scales.
In case of under-resolved grids, the species or surfactant transport will be under- or over-estimated. In case of surfactant transport, this error is affecting the sorption mechanism, too.

In fact, the sorption source term within the fast sorption mechanism is proportional to the gradient of the surfactant molar concentration at the interface. A higher or smaller gradient at the interface would result in unphysical concentrations on the interface.
A fully resolved DNS for the species transport is not feasible due to the high computational costs[3]. In previous studies, for instance in [15], this issue was faced using a very fine grid on the axisymmetric case with bubbles of fixed shape, i.e. with a non-deformable interface. Moreover, the hydrodynamic problem was solved only in the liquid phase. This approach is not suitable for the study of the initial transient of the bubble rise and the effect of surfactant on it. An effective solution to the thin species boundary layer problem is the use of a subgrid-scale (SGS) model, a by now standard approach in mass transfer problems, [8, 95], to approximate the surfactant boundary layer in the vicinity of the bubble. This approach is described in details in section 3.3.

3.3 Implicit SGS model for advection-dominated class of problems

The main idea behind the SGS model is to employ an appropriate model-function to compute the numerical (SGS) fluxes on all cell faces of an interface cell. These SGS fluxes are used to correct the numerical fluxes to accurately predict the species transport close to the interface, even if the concentration boundary layer is fully embedded in a single cell layer. The approach described in this section and which appeared in [73] is based on the latest development of the SGS model presented in [95], although here the transport equation is solved implicitly to improve the numerical stability and to allow for larger time steps. In [95] the transport equations are solved explicitly with a direct modification of diffusive fluxes and concentration values at the required faces. Since here the solution is implicit, i.e. the fluxes contain the unknown variable $(c_f)^n$, $(\nabla c)_f^n$, the diffusion coefficient and the advective term are modified as described in section 3.3.1. It has been shown in [95] that the SGS model can reduce the mesh resolution requirements near the interface by a factor of ten or more. In addition, if the SGS model is used to approximate the surfactant transport close to the interface, the corrected numerical fluxes are coupled to the sorption process. Note that this model applies both for species and surfactant transport problems.
Applying the SGS model to a species bulk transport results in the following discretized transport equation (from (3.12)) solved with locally modified diffusion coefficients and advection flux field:

$$\frac{3c_P^n V_P^n - 4c_P^o V_P^o + c_P^{oo} V_P^{oo}}{\Delta t} + \sum_f \phi_f^{\mathrm{SGS}} c_f = \sum_f D_f^{\mathrm{SGS}} \mathbf{S}_f \cdot (\nabla c)_f \,. \tag{3.27}$$

The derivation of ϕ^{SGS} and D^{SGS} is reported in section 3.3.1.

3.3.1 Implicit SGS model description

The SGS model for advection-dominated transport is based on a simplified 2D problem formulation of the species advection-diffusion equation (2.13). Consider the species transport in the vicinity of a bubble surface. Close to the interface Σ, a situation as sketched in figure 3.4 is encountered.

[3] As shown by the test case in section 4.4.2, the resolution of the species boundary layer ($\mathrm{Sc} = 10^7$) requires a computational grid with 22 times more cells (1.6 million cells rather than 75000) than the case solved with an SGS model.

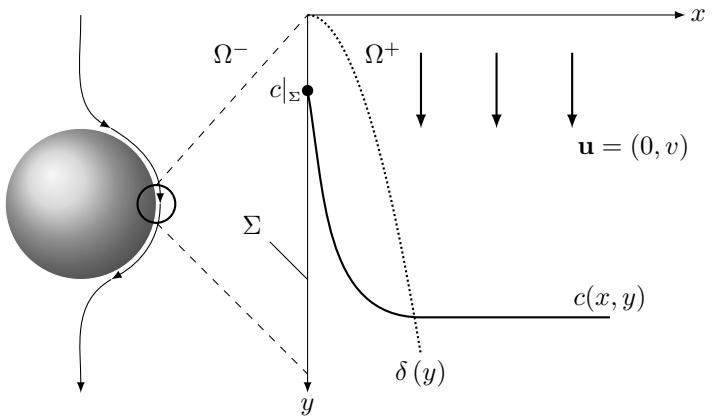

Figure 3.4: Simplified 2D model for species transport close to the bubble surface, figure based on [95].

For high Péclet numbers, constant species concentration in the gas phase (the diffusivity in the gas phase is much higher than the one in the liquid phase) and a fully developed and quasi-stationary boundary layer, equation (2.13) can be reduced to

$$v\frac{\partial c}{\partial y} = D\frac{\partial^2 c}{\partial x^2} \quad \text{for } x \geq 0 \text{ and } y \geq 0 \tag{3.28}$$

with the boundary conditions

$$c(x, y = 0) = c_\infty, \quad c(x \to \infty, y > 0) = c_\infty, \quad c(x = 0, y > 0) = c|_\Sigma. \tag{3.29}$$

Note that the assumptions to derive (3.28) may not be always fulfilled in case of rising bubbles. However, the aim is to derive a family of suitable, physically motivated functions that can be exploited to reconstruct the concentration profile in the boundary layer normal to the interface. The problem (3.28)-(3.29) has an analytical solution, describing the species distribution normal to the interface for a given boundary layer thickness $\delta(y)$,

$$c(x, y) = c|_\Sigma + (c_\infty - c|_\Sigma)\ \text{erf}\left(\frac{x}{\delta(y)}\right) \tag{3.30}$$

with $\delta(y) = \sqrt{4Dy/v}$. The physical profile derived from the local substitute problem is adopted to compute the fluxes over the faces in the interface cells. The free model parameter δ is computed iteratively to be consistent with the cell centred concentration value. The computation of the SGS model parameter is reported in section 3.3.2.
Consider now the discretized species transport equation in the liquid phase (3.12), and reported here in a condensed form,

$$\frac{3c_P^n V_P^n - 4c_P^o V_P^o + c_P^{oo} V_P^{oo}}{\Delta t} + \sum_f F_f^{\mathrm{A}} = \sum_f F_f^{\mathrm{D}}, \tag{3.31}$$

where $F_f^{\mathrm{A}} = \phi_f c_f^n$ and $F_f^{\mathrm{D}} = D_f\,(\nabla c)_f^n \cdot \boldsymbol{S}_f$ are the advective and diffusive species fluxes, respectively. Recall from section 2.2 that this equation is completed by the initial condition

$$c(t = 0, \boldsymbol{x}) = c_0, \quad \boldsymbol{x} \in \Omega^+(t = 0) \tag{3.32}$$

and the Dirichlet boundary condition imposed at the bubble surface,

$$c(t, \boldsymbol{x}) = c_D(t), \quad \boldsymbol{x} \in \Sigma(t), \tag{3.33}$$

where c_D is the Dirichlet value imposed at Σ. In case of surfactant transport and fast sorption, the Dirichlet boundary condition reads

$$c(t, \boldsymbol{x}) = f^{-1}\left(c^{\Sigma}(t, \boldsymbol{x})\right), \quad \boldsymbol{x} \in \Sigma(t). \tag{3.34}$$

as outlined in section 2.2.2 and equation (3.18). When applying the SGS model, the goal is to correctly represent the species distribution around the interface, even if the concentration boundary layer is completely contained in the first cell layer (i.e. when the DNS cannot resolve the boundary layer). To achieve this, a correction of the *diffusive* and *advective* species fluxes is introduced on the first cell faces normal to Σ to counteract the otherwise over- or underestimated numerical fluxes.

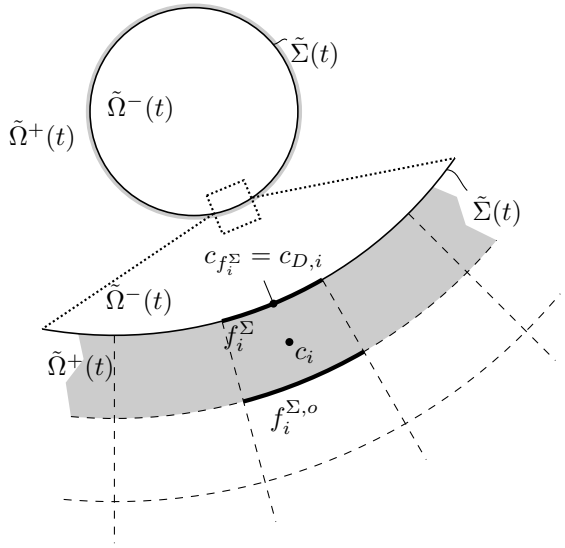

Figure 3.5: 2D sketch for the SGS model with enlarged view of the region near the interface. $\widetilde{\Omega}^{\pm}(t)$, $\widetilde{\Sigma}(t)$ are the discretized counterpart of $\Omega^{\pm}(t)$, $\Sigma(t)$.

3.3.1.1 Diffusion

The diffusive species fluxes F_f^{D} at the faces f_i^{Σ} and $f_i^{\Sigma,o}$ belonging to Σ and opposite to Σ, respectively, are considered; see figure 3.5 for the notation. The desired numerical diffusive fluxes at the relevant faces f_i^{Σ}, $f_i^{\Sigma,o}$ from now on indicated as f_i^* are computed as

$$F_{f_i^*}^{\mathrm{D,num}} = -D_{f_i^*} S_{f_i^*} \left(\partial_n c\right)_{f_i^*}^{\mathrm{num}}, \tag{3.35}$$

where $D_{f_i^*}$ is a corrected diffusion coefficient to counteract the numerical effects of the under-resolved species boundary layer. To derive an expression for $D_{f_i^*}$ we use the diffusive fluxes coming from the SGS modelling

$$F_{f_i^*}^{\mathrm{D,SGS}} = -D S_{f_i^*} \left(\partial_n c\right)_{f_i^*}^{\mathrm{SGS}}, \tag{3.36}$$

where D is the molecular diffusivity and $(\partial_n c)_{f_i^*}^{\mathrm{SGS}}$ is provided by the SGS model; see section 3.3.2 for the analytical expression. The goal is to compute $D_{f_i^*}$ such that the numerical diffusive fluxes, coming from the standard discretization, equal the SGS-fluxes,

$$F_{f_i^*}^{\mathrm{D,num}} \stackrel{!}{=} F_{f_i^*}^{\mathrm{D,SGS}}. \tag{3.37}$$

Thus, the following condition is imposed,

$$D_{f_i^*} \left(\partial_n c\right)_{f_i^*}^{\mathrm{num}} \stackrel{!}{=} D \left(\partial_n c\right)_{f_i^*}^{\mathrm{SGS}}, \tag{3.38}$$

to get an expression for the modified diffusion coefficients to be substituted in the discretized transport equation,

$$D_{f_i^*} = D \frac{\left(\partial_n c\right)_{f_i^*}^{\mathrm{SGS}}}{\left(\partial_n c\right)_{f_i^*}^{\mathrm{num}}}. \tag{3.39}$$

To simplify the notation, from now on $D_{f_i^*}$ will be addressed as D^{SGS}, where D^{SGS} contains the modified local values from the SGS model in the required faces. For the other faces the standard molecular diffusivity is kept. In case the estimated boundary layer thickness is more than 1000 times larger than the first cell width, the SGS correction is not applied to avoid non-physical diffusive fluxes; see section 3.3.2 for the exception handling.

3.3.1.2 Advection

The SGS correction of the advective species fluxes F_f^{A} is necessary only at the first cell faces opposite to Σ, $f_i^{\Sigma,o}$ because the velocity normal to the interface in a moving reference frame is zero. The aim would be to correct directly the concentrations with the prescribed value from the SGS model $c_{f_i^{\Sigma,o}}^{\mathrm{SGS}}$. However, this cannot be done within an implicit framework, thus the advective fluxes are corrected to match the prescribed SGS concentration. The numerical fluxes are computed as

$$F_{f_i^{\Sigma,o}}^{\mathrm{A,num}} = c_{f_i^{\Sigma,o}}^{\mathrm{num}} \phi_{f_i^{\Sigma,o}}, \tag{3.40}$$

where $c_{f_i^{\Sigma,o}}^{\mathrm{num}}$ is the concentration value interpolated to the face centre and $\phi_{f_i^{\Sigma,o}}$ is a modified advective flux.
The species fluxes computed with the SGS face value are

$$F_{f_i^{\Sigma,o}}^{\mathrm{A,SGS}} = c_{f_i^{\Sigma,o}}^{\mathrm{SGS}} \phi_{f_i^{\Sigma,o}}^{\mathrm{num}} \tag{3.41}$$

where $c_{f_i^{\Sigma,o}}^{\mathrm{SGS}}$ is provided by the SGS model. Enforcing the SGS fluxes to be equal to the numerical ones

$$F_{f_i^{\Sigma,o}}^{\mathrm{A,num}} \stackrel{!}{=} F_{f_i^{\Sigma,o}}^{\mathrm{A,SGS}}, \tag{3.42}$$

gives the equality

$$c_{f_i^{\Sigma,o}}^{\mathrm{num}} \phi_{f_i^{\Sigma,o}} \stackrel{!}{=} c_{f_i^{\Sigma,o}}^{\mathrm{SGS}} \phi_{f_i^{\Sigma,o}}^{\mathrm{num}} \tag{3.43}$$

from which one can compute the corrected advective fluxes as

$$\phi_{f_i^{\Sigma,o}} = \phi_{f_i^{\Sigma,o}}^{\mathrm{num}} \frac{c_{f_i^{\Sigma,o}}^{\mathrm{SGS}}}{c_{f_i^{\Sigma,o}}^{\mathrm{num}}}. \tag{3.44}$$

Also for the advective term, to simplify the notation, $\phi_{f_i^{\Sigma,o}}$ will be address as ϕ^{SGS}, where ϕ^{SGS} contains the modified local values from the SGS model in the required faces. For the other faces, the original numerical fluxes are kept. Note that $\phi^{\mathrm{SGS}} = \phi^{\mathrm{num}}_{f_i^{\Sigma,o}}\, c^{\mathrm{SGS}}_{f_i^{\Sigma,o}} / c^{\mathrm{num}}_{f_i^{\Sigma,o}}$. Thus, if $c^{\mathrm{num}}_{f_i^{\Sigma,o}}$ and $c_{f_i^{\Sigma,o}}$ are interpolated with the same scheme, the modification of the advective term at the interested faces translates into enforcing $c^{\mathrm{SGS}}_{f_i^{\Sigma,o}}$; in fact $\phi^{\mathrm{num}}_{f_i^{\Sigma,o}} \left(c^{\mathrm{SGS}}_{f_i^{\Sigma,o}} / c^{\mathrm{num}}_{f_i^{\Sigma,o}} \right) c_{f_i^{\Sigma,o}} = \phi^{\mathrm{num}}_{f_i^{\Sigma,o}} c^{\mathrm{SGS}}_{f_i^{\Sigma,o}}$. This also assures that the method remains conservative.
The advection correction via the SGS model is applied only if the concentration profile in the first three cell layers close to the interface is monotonic, see section 3.3.3 for more details on exception handling. This condition is fundamental to avoid non-physical (unbounded) concentrations; cf. [93].

Algorithm 1 Iterative computation of δ with a Newton-Bisection method.

Data:
$\eta_c = (\bar{c} - c|_\Sigma) \,/\, (c_0 - c|_\Sigma)$
$\delta_0 = l / \left[\sqrt{\pi} \left(\eta_c + (\pi/12)\eta_c^3 \right) \right]$
$\delta_n = \delta_0$
$\delta_{\min} = 1 \cdot 10^{-15}$
$\delta_{\max} = 10\delta_0$
$\mathrm{tol} = 1 \cdot 10^{-9}$
$\eta^{\mathrm{SGS}} = \mathrm{erf}(l/\delta) + (\delta/l) \left[e^{-(l/\delta)^2} - 1 \right] / \sqrt{\pi}$
$\mathrm{res}_{\min} = \eta^{\mathrm{SGS}}(\delta_{\min}) - \eta_c$
$\mathrm{res}_{\max} = \eta^{\mathrm{SGS}}(\delta_{\max}) - \eta_c$
repeat
  Compute $\eta^{\mathrm{SGS}}(\delta_n)$
  $\mathrm{res} = \eta^{\mathrm{SGS}}(\delta_n) - \eta_c$
  $\eta' = \left(e^{-(l/\delta)^2} - 1 \right) / (l\sqrt{\pi})$
  $\delta_{n+1} = \delta_n - \left(\bar{\eta}^{\mathrm{SGS}}(\delta_n) - \eta_c \right) / \eta'$
  if $(\delta_{n+1} < \delta_{\min})$ or $(\delta_{n+1} > \delta_{\max})$ **then**
    if $\mathrm{res} \cdot \mathrm{res}_{\max} > 0$ **then**
      $\delta_{n+1} = (\delta_{\min} + \delta_n)/2$
      $\delta_{\max} = \delta_n$
    else
      $\delta_{n+1} = (\delta_{\max} + \delta_n)/2$
      $\delta_{\min} = \delta_n$
    end if
  end if
  $\delta_n = \delta_{n+1}$
until $\left(\left| \frac{\eta^{\mathrm{SGS}}(\delta_n) - \eta_c}{\eta_c} \right| \leq \mathrm{tol} \right)$

Return: δ_n

3.3.2 Algorithm for the SGS model parameter calculation

In this section, the main steps to compute the SGS model parameter δ are explained. An iterative approach is adopted, as described in [95], to find the model parameter δ that fulfils

$$\bar{\eta}_{\mathrm{C}} = \frac{\bar{c} - c_{|\Sigma}}{c_\infty - c_{|\Sigma}} \overset{!}{=} \frac{1}{V} \int_V \eta(x/\delta) \mathrm{d}V = \eta_{\mathrm{SGS}}, \tag{3.45}$$

where $\bar{\eta}_C$ is the volume averaged cell-centred value coming from the finite volume discretization, which has to be equal to the volume average computed with the SGS model. Above, η is given as

$$\eta(x,y) = \frac{c(x,y) - c_{|\Sigma}}{c_\infty - c_{|\Sigma}} = \mathrm{erf}(x/\delta(y)) \tag{3.46}$$

according to equation (3.30). The quantity $\bar{c}$ is the average concentration in an interface cell (c_i in figure 3.5), $c_{|\Sigma}$ is the bulk concentration at the interface ($c_{f_i^\Sigma}$ in figure 3.5). The iterative solution based on equation (3.45) requires the evaluation of the volume integral. Here only the main steps from [95] are reported.
The iterative algorithm is based on the work of [1] and uses a combined Newton-Bisection method to search for δ, which converges very quickly, usually after three iterations. The maximum number of iterations is set to 10. As initial guess for δ_0 the first two terms of a series expansion for the inverse error function are taken, that is $\delta_0 = (l/2) \,/\, (0.5\pi\,(\eta_c + \pi/12\eta_c^3))$, with l being the first cell thickness. Bounding values for δ are taken equal to $\delta_{\min} = 1 \cdot 10^{-15}$ and $\delta_{\max} = 10\delta_0$. The convergence tolerance is set to $\mathrm{tol} = 10^{-9}$.
In each time step, there is an initialization step for the required parameters. The result of the iterative procedure will be a vector containing all the δ values (for all the interface cells). The procedure is displayed as pseudo-code in algorithm 1. Note that the formula to compute the residual has been corrected with respect to [95].

Exception handling Before the iterative procedure is started, a check that the values of η_c are between 0 and 1 is done. If the maximum number of iterations is reached without a converged value for δ or if the computed δ is larger than the first cell thickness by a factor of 1000, then δ is set to -1 and the SGS correction will not be applied at the corresponding face.

3.3.3 Correction of diffusive and advective fluxes within the SGS modelling

After the iterative computation of the model parameter δ, the SGS correction is applied to the diffusive and advective fluxes as explained at the beginning of section 3.3. A weighting factor w is introduced in the flux correction to reduce the influence of the SGS model when a linear interpolation is already sufficient. This means that the corrected flux $\phi^*_{i,\mathrm{SGS}}$ at the face i is computed as

$$\phi^*_{i,\mathrm{SGS}} = w_i \phi_i^{\mathrm{SGS}} + (1 - w_i)\phi_i^{\mathrm{num}}, \tag{3.47}$$

where ϕ_i^{SGS} is $(\partial_n c)^{\mathrm{SGS}}_{f_i^\Sigma}$, $(\partial_n c)^{\mathrm{SGS}}_{f_i^{\Sigma,o}}$ or $c^{\mathrm{SGS}}_{f_i^{\Sigma,o}}$. The weighting factor is different for the species transfer problem and the surfactant transport. The weighting (3.47) is applied to all three flux corrections, i.e. diffusive fluxes at the interface, and diffusive and advective (or better to the concentration) fluxes at the face next to the interface. The various steps for the flux correction are reported in algorithm 2.

3.3.3.1 Weighting for species transfer

For the species transfer problem, a quadratic weighting is adopted. The weighting factor is chosen as the square of the volume averaged cell-centred value $\bar{\eta}_C$:

$$w = \eta_C^2 = \left(\frac{\bar{c} - c_{|\Sigma}}{c_\infty - c_{|\Sigma}} \right)^2. \tag{3.48}$$

In case of steep gradients at the interface, that is when the difference $\bar{c} - c_{|\Sigma}$ is high, the SGS model is preferred. Instead, if the concentration in the cell centre is very close to the concentration on the interface, the linear interpolation has a bigger impact on the solution.

3.3.3.2 Weighting for surfactant transport

For the surfactant bulk transport problem, a linear weighting is employed. The weighting factor here is chosen as

$$w = \frac{|\bar{c} - c_{|\Sigma}|}{c_\infty}. \tag{3.49}$$

This means that when the absolute value of the bulk concentration on the interface is very close to the bulk concentration in the cell centre, a linear interpolation is preferred over the SGS model correction, and vice-versa. This weighting prevents the SGS model to over-correct the fluxes when the surfactant concentration on the interface reaches relatively high values.

Exception handling The diffusive and advective fluxes are corrected only if the iterative procedure to compute δ converged. Furthermore, a check that the gradient and the concentration close to the interface are non-zero is included, $\left|(\partial_n c)^{\text{num}}_{f_i^*}\right| > 10^{-15}$ and $\left|c^{\text{num}}_{f_i^{\Sigma,o}}\right| > 10^{-15}$. If these checks fail, the standard discretization is used.
An additional exception handling is implemented specifically for the correction of the diffusive fluxes at the second layer of faces $f_i^{\Sigma,o}$. The SGS correction is applied only if the ratio between the SGS gradient and the numerical one is smaller than unity, $\left|(\partial_n c)^{\text{SGS}}_{f_i^*} / (\partial_n c)^{\text{num}}_{f_i^*}\right| < 1$. If the correction factor is larger than one, the SGS model application is not necessary and the diffusivity will not be corrected at the respective face.
The last exception regards the correction of the advective fluxes. The SGS model correction is applied only if the concentration profile within the first three cells close to the interface is monotonic. If the cell centres from the interface outwards are numbered as $c_1,\ c_2,\ c_3$, then the SGS correction is applied only if $(c_1 - c_2)(c_2 - c_3) > 0$.

Algorithm 2 Correction of diffusive and advective fluxes within the SGS model.

for all (faces f_i^Σ) **do**
  if $(\delta > 0)$ **then**
    at f_i^Σ: $(\partial_n c)^{\text{SGS}}_{f_i^\Sigma} = w_i \left(\frac{2}{\sqrt{\pi}} \frac{c_0 - c_{f_i^\Sigma}}{\delta_i} \right) + (1 - w_i)(\partial_n c)^{\text{num}}_{f_i^\Sigma}$
    at $f_i^{\Sigma,o}$: $(\partial_n c)^{\text{SGS}}_{f_i^{\Sigma,o}} = w_i \left(\frac{2}{\sqrt{\pi}} \frac{c_0 - c_{f_i^\Sigma}}{\delta} e^{-(l_i/\delta_i)^2} \right) + (1 - w_i)(\partial_n c)^{\text{num}}_{f_i^{\Sigma,o}}$
    $c^{\text{SGS}}_{f_i^{\Sigma,o}} = w_i \left[c_{f_i^{\Sigma,o}} + \left(c_0 - c_{f_i^{\Sigma,o}} \right) \text{erf}\,(l_i/\delta_i) \right] + (1 - w_i) c^{\text{num}}_{f_i^{\Sigma,o}}$
    Diffusion correction: $D_{f_i^*} = D^{\text{mol}} \frac{(\partial_n c)^{\text{SGS}}_{f_i^*}}{(\partial_n c)^{\text{num}}_{f_i^*}}$
    Advection correction: $\phi_{f_i^{\Sigma,o}} = \phi^{\text{num}}_{f_i^{\Sigma,o}} \frac{c^{\text{SGS}}_{f_i^{\Sigma,o}}}{c^{\text{num}}_{f_i^{\Sigma,o}}}$
  end if
end for

3.3.3.3 SGS model and fast sorption

The inverse expression of the adsorption isotherm (3.18) serves as a Dirichlet boundary condition for the bulk transport. The bulk transport is coupled to the surface balance via the source term (3.19). To compute the source term, the locally corrected SGS diffusion coefficients are applied, i.e.

$$s_{f_i^\Sigma}^\Sigma = -D_{f_i^\Sigma}^{\mathrm{SGS}} \left(\partial_n c\right)_{f_i^\Sigma}^{\mathrm{num}} . \tag{3.50}$$

3.3.4 SGS model for reactive mass transfer

The reactive SGS model outlined here for a decay reaction has been described and employed in [97], where the complete derivation is reported. The substitute setting sketched in figure 3.4 holds also for the case with a decay reaction. The initial boundary value problem describing the reactive boundary layer now consists of the partial differential equation below,

$$v\frac{\partial c}{\partial y} = D\frac{\partial^2 c}{\partial x^2} - kc \quad \text{for } x \geq 0 \text{ and } y \geq 0 \tag{3.51}$$

with the initial and boundary conditions

$$c(x, y=0) = 0, \quad c(x \to \infty, y > 0) = 0, \quad c(x=0, y > 0) = c|_\Sigma. \tag{3.52}$$

An analytical solution can be computed using Laplace transformation and reads

$$\bar{c}(x, \widetilde{y}) = \frac{c}{c_{|\Sigma}} = \frac{e^{Ax}}{2}\mathrm{erfc}\left(\frac{Cx}{\widetilde{y}} + B\widetilde{y}\right) + \frac{e^{-Ax}}{2}\mathrm{erfc}\left(\frac{Cx}{\widetilde{y}} - B\widetilde{y}\right), \tag{3.53}$$

with $\widetilde{y} = \sqrt{y}$, $A = \sqrt{\frac{k}{D}}$, $B = \sqrt{\frac{k}{v}}$, $C = \sqrt{\frac{v}{4D}}$. In the reactive case, the aim is to find the model parameter $\widetilde{y}$ that fulfils

$$\bar{c}_{num} - \frac{1}{L}\int_{x=0}^{L} \bar{c}(x, \widetilde{y})\mathrm{d}x = 0 \ , \tag{3.54}$$

i.e. the analytical solution (cell-centred concentration) in each interface cell is adjusted to the numerical one $\bar{c}_{num} = c_{num}/c_{|\Sigma}$. In equation (3.54), L is the thickness of the interface cell. As for the non-reactive case, an iterative Newton-Bisection algorithm is employed to find $\widetilde{y}$.
After $\widetilde{y}$ has been computed, advective and diffusive fluxes in the interface cells can be corrected. The diffusive fluxes at $x = 0$ and $x = L$ are given by the relations

$$\left.\frac{\partial \bar{c}}{\partial x}\right|_{x=0} = -A\left[\frac{e^{-(B\widetilde{y})^2}}{\sqrt{\pi}B\widetilde{y}} + \mathrm{erf}\left(B\widetilde{y}\right)\right], \tag{3.55}$$

$$\left.\frac{\partial \bar{c}}{\partial x}\right|_{x=L} = \frac{A}{2}\left[e^{LA}\mathrm{erfc}\left(\frac{LC}{\widetilde{y}} + B\widetilde{y}\right) - e^{-LA}\mathrm{erfc}\left(\frac{LC}{\widetilde{y}} - B\widetilde{y}\right)\right] - \frac{2Ce^{-(LC/\widetilde{y})^2 - (B\widetilde{y})^2}}{\sqrt{\pi}\widetilde{y}}. \tag{3.56}$$

A more accurate approximation of the concentration value at $x = L$ comes directly from equation (3.53).
The chemical reaction introduces another difficulty compared to the non-reactive model. As $\widetilde{y}$

becomes larger, the boundary layer and its thickness approach a steady state. In the limit as $\widetilde{y} \to \infty$, the solution of the simpler film-theory is obtained, i.e.

$$\lim_{\widetilde{y}\to\infty} \bar{c}(x, \widetilde{y}) = e^{-Ax}. \tag{3.57}$$

Consequently, also the average model concentration value in relation (3.54) is limited by

$$\bar{c}_{max} = \lim_{\widetilde{y}\to\infty} \frac{1}{L} \int_{x=0}^{L} \bar{c}(x, \widetilde{y}) \mathrm{d}x = \frac{1 - e^{-LA}}{LA}. \tag{3.58}$$

If the cell-centered concentration value $\bar{c}_{\mathrm{num}}$ is larger than $\bar{c}_{\mathrm{max}}$, it becomes impossible to find a suitable $\widetilde{y}$. Such values typically appear in the rear part of a rising bubble. The normal velocity component close to the interface causes an additional convective transport of the chemical species and, hence, the boundary layer becomes thicker. Because normal velocity contributions are not included in the substitute problem, the model function cannot be used without modification. A heuristic solution which works excellently consists of the following two steps:

1. When the maximum average concentration $\bar{c}_{\mathrm{max}}$ is smaller than $\bar{c}_{\mathrm{num}}$, the film theory solution is fitted by adjusting the parameter A. Decreasing A corresponds to increasing the ratio of diffusive flux into the boundary layer to reactive decay. This adjustment emulates the additional convective flux normal to the interface in the numerical simulation.

2. The full SGS model fluxes are not applied, but rather a combination between numerical and SGS model fluxes. A simple blending of the form $\phi^{*}_{\mathrm{SGS}} = (1 - w)\phi^{\mathrm{SGS}} + w\phi^{\mathrm{num}}$ works well with ϕ representing either the concentration value or its gradient. A sensible weight is $w = \bar{c}_{\mathrm{num}}$. As c_{num} approaches the interface value $c_{|\Sigma}$, the boundary layer is typically well resolved and no model correction is required. On the other hand, when c_{num} is very small, a simple linear approximation will overestimate fluxes leaving the interface cell, while the SGS model fluxes yield much better results.

3.4 Surfactant effects on species transfer

As mentioned in the mathematical modelling section 2.3, the study of the surfactant effects on mass transfer is an open topic. It seems that a sophisticated model including hindrance effects is necessary, but the question on how to model it numerically in terms of boundary conditions at the interface is still open.
In this work the effects of surfactant on the mass transfer problem are taken into account in two ways, increasing progressively the difficulty of the problem. First, the species transfer problem and the surfactant transport are solved as two independent scalar transports. Note that the SGS model is applied independently to the species transfer and the surfactant transport. The second step is to include the hindrance effect of the surfactant on the species transfer, as described in section 2.3. The numerical solution of this problem is outlined below, where also the standard solution procedure for the species transfer problem is reported for completeness.

3.4.1 Standard algorithm to solve the mass transfer problem

The solution procedure of the standard species transfer problem (2.16)-(2.17) applying Henry's law follows an iterative algorithm [94], solving the species transport problem from both sides

of the interface until the transmission condition (2.61) is fulfilled, see algorithm 3.
In algorithm 3 the two phases are coupled via the so-called Dirichlet-Naumann coupling. As mass transfer is not the main topic of this work, a simplified version of this coupling is implemented. In detail, the species concentration in the gas phase is considered uniform. This assumption is supported by the fact that the species diffusivity in the gas phase is some orders of magnitude higher than in the liquid phase, thus being well mixed. Under this hypothesis the gas phase can be discarded and a uniform species concentration on the gas side of the interface is considered, i.e. $c^-|_\Sigma = c_0^-|_\Sigma = \text{constant}$. Thus, only the liquid side transport equation with a Dirichlet boundary condition is solved.

Algorithm 3 Solution algorithm for the standard mass transfer problem.

repeat
- Update the liquid side Dirichlet boundary condition: $c_i^+|_\Sigma = c_i^-|_\Sigma / H_i$
- Solve the liquid side species transport equation
- Update the species gradient at the liquid side: $\partial_n c^+|_\Sigma$
- Update the gas side Neumann boundary condition: $\partial_n c^-|_\Sigma = D^+/D^-\ \partial_n c^+|_\Sigma$
- Solve the gas side species transport equation

until $D^- \partial_n c^-|_\Sigma = D^+ \partial_n c^+|_\Sigma$

3.4.2 Generalized algorithm to solve the mass transfer problem with hindrance effect

Again the solution procedure follows an iterative algorithm, solving the species transport problem from both sides of the interface until the transmission condition (2.61) is fulfilled, although in this case the interface boundary conditions are different to take into account the presence of surfactant, see equation (2.62). For brevity, in algorithm 4 the species mass fluxes at the interface are denoted as $\dot{n}^\pm$, thus (2.61) reduces to $\dot{n}^- = \dot{n}^+$. Using (2.61) and (2.62), an expression for the liquid side species concentration can be derived and it reads

$$c^+|_\Sigma = \frac{\dot{n}^-}{k_{\text{red}}} + \frac{c^-|_\Sigma}{H}. \tag{3.59}$$

Algorithm 4 Solution algorithm for the mass transfer problem in presence of surfactants.

repeat
- Consider the gas side species concentration: $c^-|_\Sigma$
- Consider the gas side species concentration gradient: $\dot{n}^- = D^- \partial_n c^-|_\Sigma$
- Update the liquid side Dirichlet boundary condition: $c^+|_\Sigma = \dot{n}^-/k_{\text{red}} + c^-|_\Sigma / H$
- Solve the liquid side species transport equation
- Update the species gradient at the liquid side: $\partial_n c^+|_\Sigma$
- Update the gas side Neumann boundary condition: $\partial_n c^-|_\Sigma = D^+/D^-\ \partial_n c^+|_\Sigma$
- Solve the gas side species transport equation

until $\dot{n}^- = \dot{n}^+$

Also in this case, as in section 3.4.2, the species concentration in the gas phase is considered uniform, thus the solution of the gas side species transport is not necessary any more. Equations (2.61) and (2.62) are still used to derive the Dirichlet boundary condition for the liquid side species transport problem. Algorithm 4 is reduced to the steps reported in algorithm 5.
For the moment no physical values for $\overline{k}$ are available, thus a parameter study will be necessary,

see section 6.2. Nevertheless, the choice of $\overline{k}$ cannot be arbitrary, but it has to be chosen such that $c^+|_\Sigma$ does not become negative, since $c^+|_\Sigma < 0$ would not be physical.

Algorithm 5 Simplified solution algorithm for the mass transfer problem in presence of surfactants.

for all (faces f_i^Σ) **do**
- Compute the liquid side species concentration gradient: $\dot{n}^+ = D^+ \partial_n c^+|_\Sigma$
- Compute the mass transfer reduction coefficient: $k_{\text{red}} = \overline{k} \exp\left(-\frac{\sigma_0 - \sigma}{RT c_\infty^\Sigma}\right)$
- Update the liquid side Dirichlet boundary condition: $c^+|_\Sigma = \dot{n}^-/k_{\text{red}} + c^-|_\Sigma/H = \dot{n}^+/k_{\text{red}} + c^-|_\Sigma/H$
- Solve the liquid side species transport equation

end for

3.5 Solution algorithm overview

In figure 3.6, a schematic overview of the numerical solution procedure is depicted.

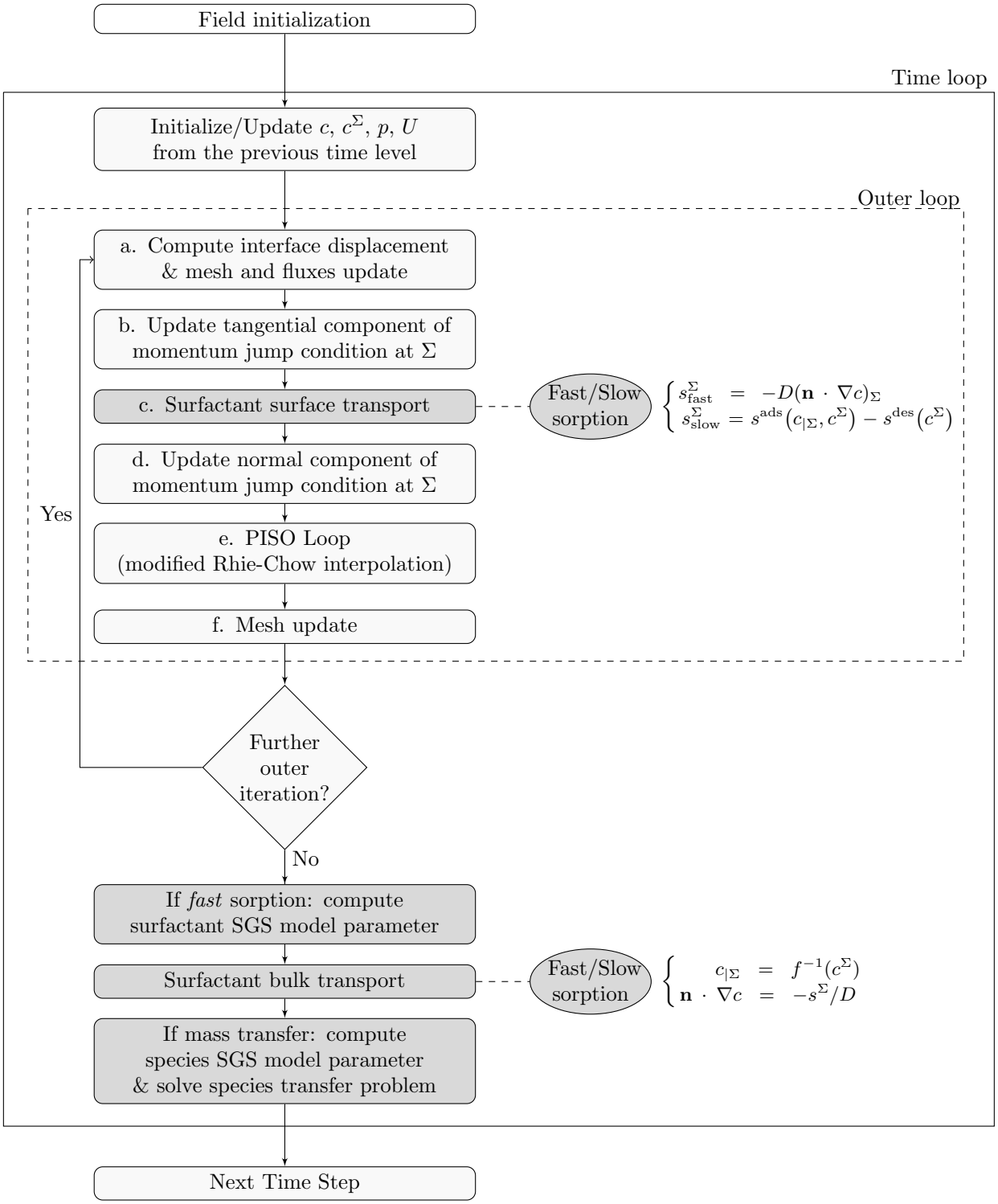

Figure 3.6: Overview of the algorithm to solve the full problem: hydrodynamics with mesh motion, species transfer, surfactant transport and sorption.

Chapter 4

Validation and verification

Validation is necessary to check the accuracy of the model's representation of the real system. Since the modelling and simulation of multiphase flows is a challenging problem, a validation of the full problem is not possible. If one looks at the problem as a compound of smaller, easier problems, the validation and verification for these reduced problems can be performed. In this chapter, the verification of the interpolation scheme for the surface operators is first presented. Then the validation of the hydrodynamics of two-phase flows is shown. It follows the validation of the surfactant sorption processes at the interface, in particular of the source term. The validation of the non-reactive and reactive (decay reaction) SGS models is also given, based on different test cases with an increasing level of difficulty. Finally, a comparison of the bubble rise velocity in contaminated water with experimental data and with numerically resolved results is presented.

4.1 Surface operators

In this section, the discretization of the surface operators to approximate the surface gradient and divergence are tested and the newly introduced edge interpolation scheme (see section 3.2.2) is verified against an analytical solution.

4.1.1 Test case set-up

Consider a sphere of dimensionless radius r = 1. The surface of the sphere is denoted by Σ such that $\Sigma = \mathbf{x} : ||\mathbf{x}|| = 1$. A function $\mathbf{f}(\mathbf{x}) = \begin{bmatrix} x_2 \\ -x_1 \\ 0 \end{bmatrix} x_3$ is defined. The surface gradient is defined as the projection of the gradient on the surface, i.e. $P_\Sigma \nabla \mathbf{f}(x) := \nabla_\Sigma \mathbf{f}(\mathbf{x})$. In general, the projection P_Σ of a vector $\mathbf{v}$ is defined as $P_\Sigma \mathbf{v} = \mathbf{v} - \langle \mathbf{v}, \mathbf{n} \rangle \mathbf{n}$ with $\mathbf{n} = \frac{\mathbf{x}}{||\mathbf{x}||}$. To compute the surface gradient, one has to first compute the gradient of the function $\mathbf{f}(\mathbf{x})$ and then subtract the normal component of the gradient from it, i.e.

$$\nabla_\Sigma \mathbf{f}(\mathbf{x}) = \nabla \mathbf{f}(\mathbf{x}) - \langle \nabla \mathbf{f}(\mathbf{x}), \mathbf{n} \rangle \mathbf{n}. \tag{4.1}$$

The analytical solution of $\nabla_\Sigma \mathbf{f}(x)$ can be computed as described above and the resulting tensor

reads as

$$\nabla_\Sigma \mathbf{f}(\mathbf{x}) = \begin{bmatrix} -2x_1x_2x_3 & 2x_1^2x_3 - x_3 & 0 \\ x3 - 2x_2^2x_3 & 2x_1x_2x_3 & 0 \\ x_2 - 2x_2x_3^2 & 2x_1x_3^2 - x_1 & 0 \end{bmatrix}. \tag{4.2}$$

The surface divergence is defined as the trace of the surface gradient, i.e. $\nabla_\Sigma \cdot \mathbf{f}(\mathbf{x}) = tr(\nabla_\Sigma \mathbf{f}(\mathbf{x}))$. Thus, an analytical solution for the surface divergence can be derived, too, and it reads

$$\nabla_\Sigma \cdot \mathbf{f}(\mathbf{x}) = 0. \tag{4.3}$$

4.1.2 Test case set-up in OpenFOAM

The surface of a sphere of radius r = 1 is spatially discretized with different mesh types. The surface mesh, *faMesh* object, is the boundary of a volume mesh, which, in this test case, is not considered. Four different mesh types are considered: triangular, polygonal, rectangular from *blockMesh* and quadrilateral/polygonal from *snappyHexMesh*.

- The triangular mesh is created with Salome[1] using the *Netgen 1D-2D* algorithm and imported in OpenFOAM with the utility *ideasUnvToFoam*
- The polygonal mesh is created first as a triangular mesh as above, imported in OpenFOAM with the utility *ideasUnvToFoam* and then the dual (polygonal) mesh is generated from the triangles via the *polyDualMesh* utility
- The quadrilateral mesh is created with the OpenFOAM *blockMesh* utility
- The quadrilateral/polygonal mesh is created with the OpenFOAM *snappyHexMesh* utility

An example for each mesh type is shown in figure 4.1.

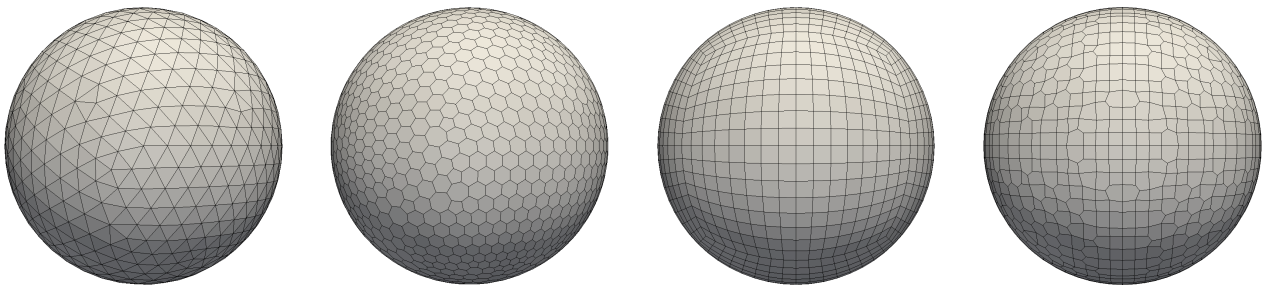

(a) *Netgen mesh.* (b) *Polydual mesh.* (c) *blockMesh.* (d) *snappyHexMesh.*

Figure 4.1: Examples of surface mesh topologies.

The surface operators tested are reported in section 3.2.2. A first preliminary test for the gradient schemes *Gauss linear* and *leastSquares*, and the divergence scheme *Gauss linear* highlighted that the linear interpolation (from the face centre to the edge centre) is introducing high errors. Another important information was that the *Gauss linear* discretization scheme provided the best results for the polygonal faces. In the following section the results of a parameter study involving also the new edge interpolation scheme are reported and discussed.

[1] http://www.salome-platform.org

4.1.3 Parameter study

The parameter study involves the variations on mesh size and discretization scheme reported below.

- Mesh dependency: six different surface mesh resolutions are considered, $N_f \approx 380$, 1520, 6080, 9600, 13500, 24320. These mesh resolutions correspond to six average edge length sizes computed from the average face areas A_f. The inverse of the average edge length $\ell = 1/\sqrt{A_f}$ is used to plot the error norms.
- For the gradient discretization, three different schemes are tested:
  - Gauss linear,
  - Gauss leastSquares,
  - leastSquares.
- For the divergence discretization, two different schemes are tested:
  - Gauss linear,
  - Gauss leastSquares.

This parameter variation results in 18 cases per mesh.

4.1.4 Discussion of the results

The results of the parameter study are investigated and compared in terms of error norms. The errors are computed with respect to the analytical solution provided in section 4.1.1. L_1, L_2 and L_∞ error norms are considered and computed according to the definition given in [56, section 10.2]:

$$L_1 = \frac{1}{N_f} \sum_{i=1}^{N_f} |x_{i,\text{num}} - x_{i,\text{an}}|, \tag{4.4}$$

$$L_2 = \sqrt{\frac{1}{N_f} \sum_{i=1}^{N_f} |x_{i,\text{num}} - x_{i,\text{an}}|^2}, \tag{4.5}$$

$$L_\infty = \max|x_{i,\text{num}} - x_{i,\text{an}}|, \tag{4.6}$$

where $x_{i,\text{num}}$ and $x_{i,\text{an}}$ are the numerical and analytical solutions, respectively.
In figure 4.2, the various error norms for the tested discretization schemes are reported. Here the trace of the surface gradient, i.e. the surface divergence, is considered. The errors on the gradient are not reported here because they are very similar to the one for the divergence. For each norm and each discretization scheme, the errors for the different mesh topologies are depicted. As a reference, the lines corresponding to order of convergence 1 and 2 are plotted in black and red. As can be seen from figure 4.2, the *blockMesh* (*blockM* in the legend) and the polygonal (*poly* in the legend) surface meshes show the best convergence rates and smaller errors in comparison to the *snappyHexMesh* (*snappy* in the legend) and the triangular (*tets* in the legend) meshes. In case Gauss discretization method with linear edge interpolation is used, the errors are higher (one order of magnitude comparing the same mesh to the other two schemes) and the mesh convergence rate is very poor from zero up to one. For Gauss leastSquares and leastSquares the convergence rates for blockMesh and polygonal meshes vary between 1.81 and 2, while the other two mesh topology have at least order of convergence 1.

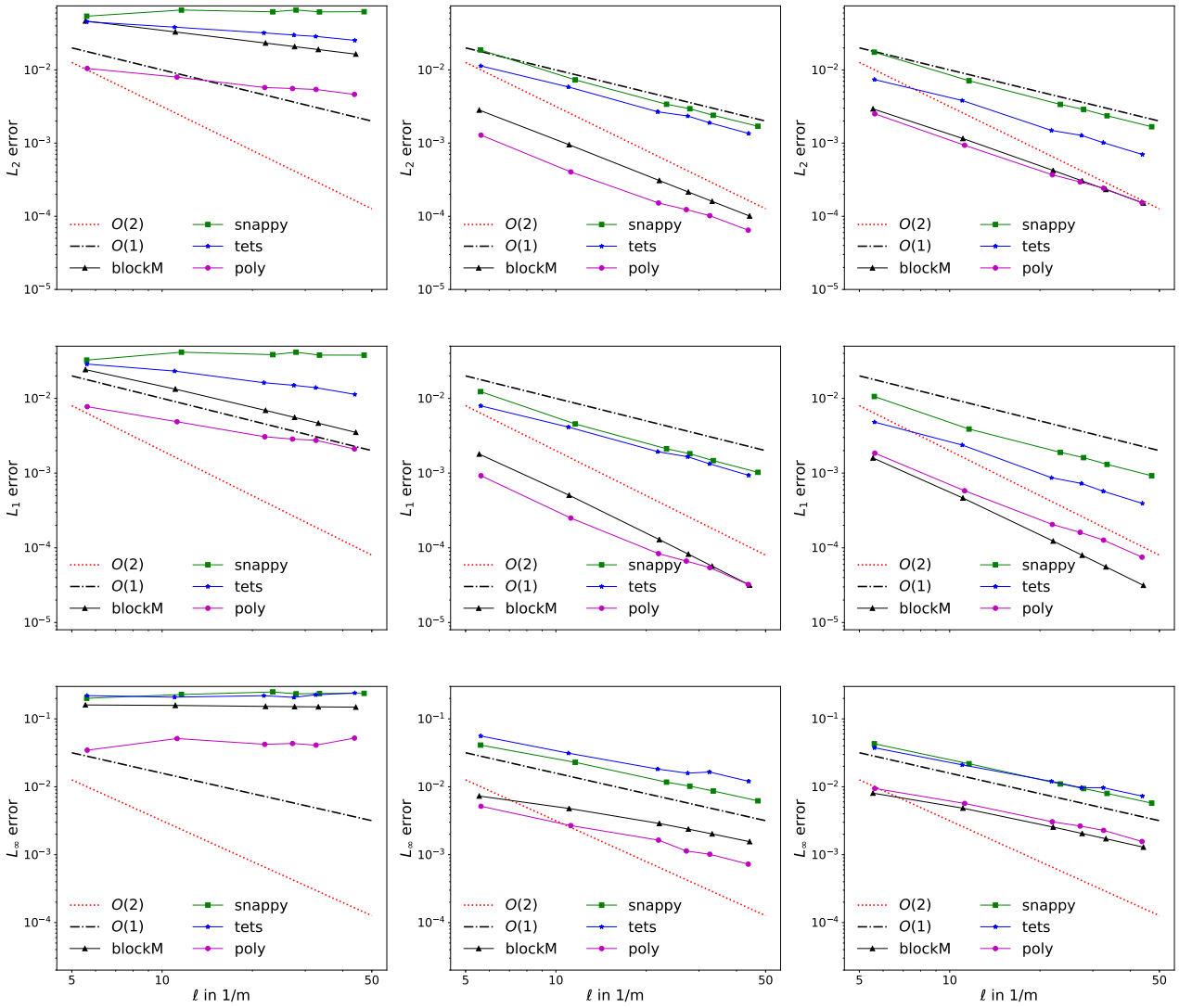

(a) *Gauss linear.* (b) *leastSquares.* (c) *Gauss leastSquares.*

Figure 4.2: Error norms computed according to equations (4.4)-(4.6) for the trace of the surface gradient for the different discretization schemes and various mesh topologies plotted against the inverse of the average edge length $\ell = 1/\sqrt{A_f}$, mesh convergence study.

These errors may derive from different sources among which the curvature computation, the surface mesh qualities, and the mesh creation process. The surface mesh qualities are computed for each mesh type according to the utility *checkFaMesh* implemented within this work and described in appendix C. An example of the outcome of the surface mesh check in relation to the errors on the surface operators is reported in figure 4.3. For this figure the quadrilateral mesh (*blockMesh*) is considered, with Gauss leastSquares gradient scheme and $N_f = 6140$. On the left in figure 4.3a, the local errors on the trace of the surface gradient are depicted. The errors are the highest in isolated locations on the grid. These locations correspond to the edges where non-orthogonality (see figure 4.3b) and skewness error (see figure 4.3c) are the highest. For this test case, the analytical curvature is known, as well. Thus, also the error norms on the curvature computation can be computed and visualized as above. The curvature errors are

depicted in figure 4.4. From this figure, it can be seen that the polygonal mesh gives the worst curvature approximation with errors of order of magnitude $L \approx 10^{-2}$ against at least $L \approx 10^{-5}$ for the other mesh topologies. It is also interesting to note that for the other mesh topologies, the error is increasing with an increasing number of faces; nevertheless, it stays very small, up to $L \approx 10^{-5}$. The reason for this behaviuor is not known yet. The higher error in the curvature computation for polygonal grids can be explained considering how the mesh is created. The curvature computation (see [91]) relies on the position of the points of the surface mesh. If the points are on the theoretical surface, here the sphere, then the curvature computation will be more precise. By default, the triangular faces have all their points lying on the sphere; see figure 4.5. Then, loosely speaking, the polygonal faces are created connecting the centres of these triangles. Thus the mesh points of the polygonal mesh will have a small offset from the theoretical sphere. This offset is decreasing with increasing number of faces; see figure 4.5.

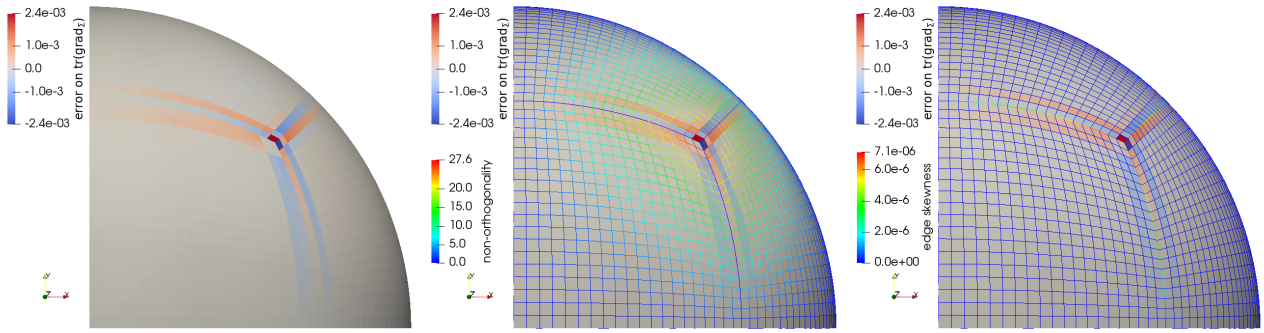

(a) *Error for tr(grad).* (b) *Face non-orthogonality and error for tr(grad).* (c) *Skewness and error for tr(grad).*

Figure 4.3: Local errors for the computation of the trace of the surface gradient (faces) and face non-orthogonality (grid).

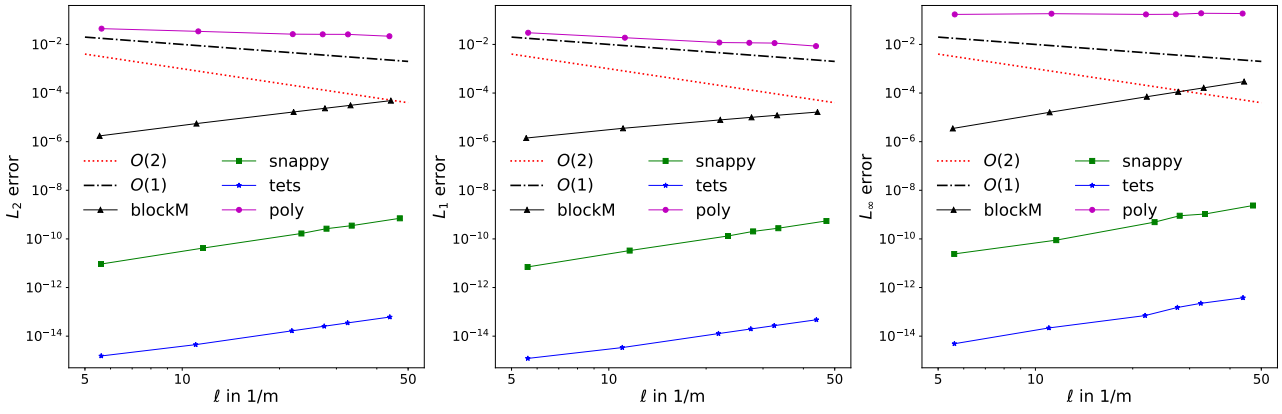

Figure 4.4: Error norms on the curvature computation computed according to equations (4.4)-(4.6) for the various mesh topologies plotted against the inverse of the average edge length $\ell = 1/\sqrt{A_f}$.

To summarize the results of this test case, quadrilateral meshes created with *blockMesh* and polygonal meshes created from a triangular mesh provide results with the lowest error norms for each discretization scheme tested. On the other hand, the triangular meshes from *Salome* and the quadrilateral/polyhedral meshes created with *snappyHexMesh* have the smallest errors

for the curvature computation. The choice of one mesh topology with respect to the others should be then based on the characteristics of the case one has to simulate, taking into account the following aspects:

- complexity of the geometry (*Salome, snappyHexMesh*)
- required accuracy for the solution of transport processes on the surface (*blockMesh, Salome - polygonal mesh*)
- necessity of highly accurate curvature computation (*Salome - triangular mesh, snappyHexMesh*).

Furthermore, the outcome of this study suggests to employ either *leastSquares* or *Gauss leastSquares* as discretization schemes for the surface gradient computation. For the surface divergence computation, the *Gauss leastSquares* scheme should be used, since the error norms for the *Gauss linear* scheme are much higher.

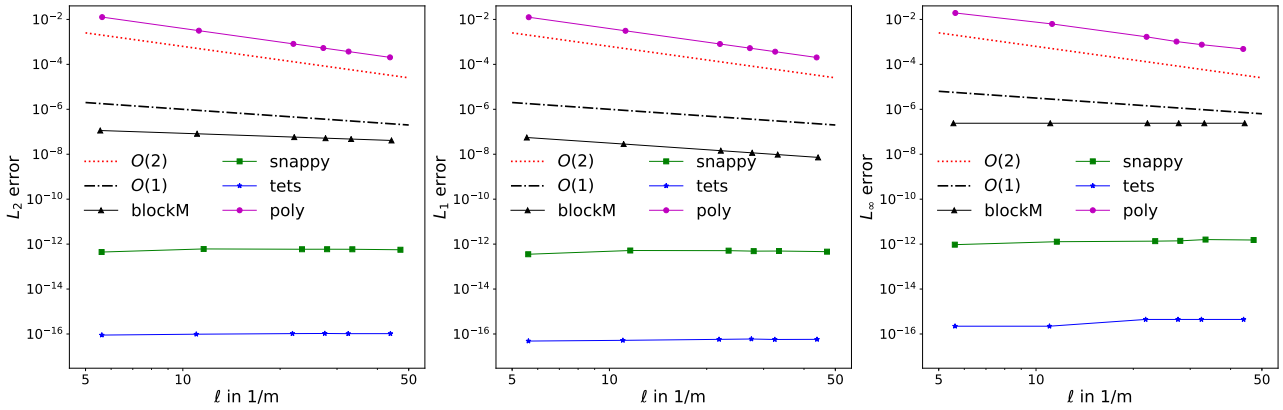

Figure 4.5: Error norms on the point positions with respect to the theoretical sphere computed according to equations (4.4)-(4.6) for the various mesh topologies plotted against the inverse of the average edge length $\ell = 1/\sqrt{A_f}$.

4.2 Hydrodynamics

Due to necessary changes listed below and refactoring in the Interface Tracking library, the validation of the hydrodynamics of two-phase flows is necessary, in particular for rising bubbles. These changes include a revision of the boundary conditions at the interface in case of two-phase flows, necessary corrections in the Finite Area methodology, i.e. correction for the surface gradient computation (*GaussFaGrad* and addition of the new edge interpolation scheme) within the Finite Area method, and the corrected Rhie-Chow interpolation from Tuković et al. [91].

4.2.1 Test case set-up

A single air bubble rising in purified water is considered. The computational domain is divided into two sub-domains, one representing the gas phase and the other one representing the liquid phase. The two sub-domains are coupled at the interface. The meshes used for the simulations consist of polyhedral cells in the gas phase and prismatic cells with polyhedral base in the

liquid phase, as can be seen in figure 4.6. The mesh resolution close to the interface should be such that at least the first three to four cells lie inside the hydrodynamic boundary layer. The boundary layer thickness has been estimated via equation (3.24). This equation gives an average boundary layer thickness of 45 μm, thus the thickness of the cells close to the interface is set to approximately 12 μm. The interface consists of polyhedral faces with an edge length of around 40 μm. The total number of cells varies between approximately 190000 to 500000, according to the bubble radius r_{B} and with outer domain radius equal to $20r_{\mathrm{B}}$. This mesh resolution is a compromise between computation time requirements and accuracy of the results. Nevertheless, it has to be underlined that such resolution is enough to get a correct value of the terminal rise velocity, but it may not render an accurate path, as reported also in [91]. The bubble path is determined by the wake. If the flow in the wake of the bubble is not fully resolved then the simulated path can disagree with the experimental one. Unfortunately, this is the price to pay for using the prismatic layered mesh and limit the computational costs.

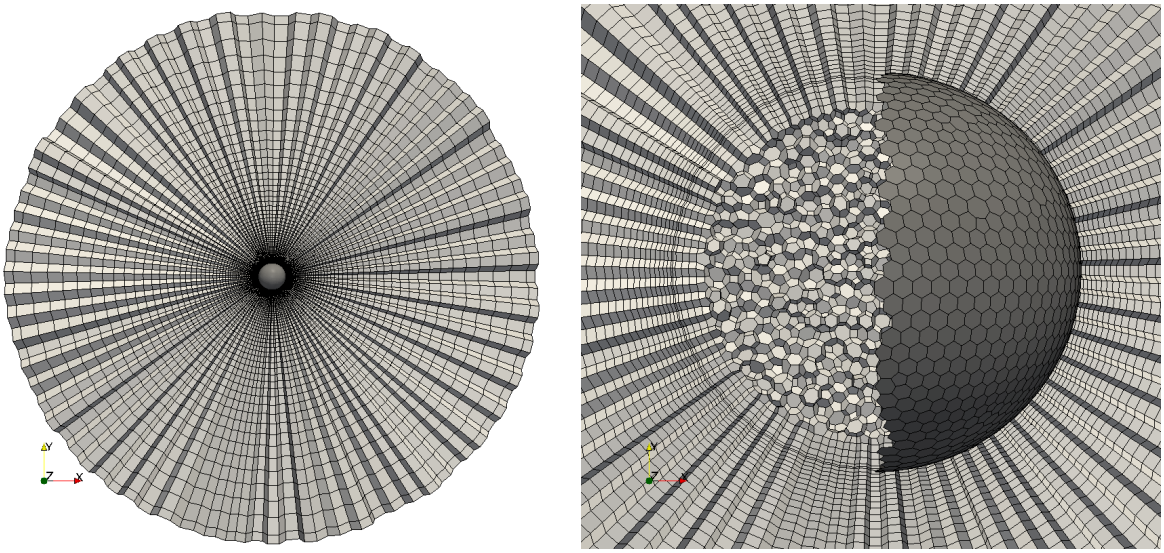

(a) *Full domain.* (b) *Enlarged view of the bubble region.*

Figure 4.6: Example of the 3D computational domain for a rising bubble. Inner, outer and surface (dark grey on the right) meshes.

The bubble is positioned in the centre of a spherical domain. The calculation is performed in a moving reference frame (MRF) that follows the bubble centre during its rise, while the interface is deformable. Thus, the bubble is always kept in the centre of the domain. The presence of a non-inertial reference frame located in the center of the bubble is taken into account via a correction in the momentum equation ($\rho\mathbf{a}_{\mathrm{MRF}}$ added to the momentum equation) and the velocity boundary condition at the outer domain boundary, $\mathbf{v}_{\mathrm{out}} = -\mathbf{v}_{\mathrm{MRF}}$[2].

4.2.2 Single bubble rising in purified water

A careful literature survey, looking for the most reliable data in case of super purified water, suggested comparing the simulation results to the experimental ones provided by Duineveld

[2]The boundary condition *inletOutlet* available in OpenFOAM is used. The inlet velocity is set to $-\mathbf{v}_{\mathrm{MRF}}$, at the outlet a *zeroGradient* condition is set.

in [20]. The parameters needed to set up the simulations are the fluid properties of the liquid and the gas phases at a given temperature. In the experiment, the working temperature is $T = 293$ K; the liquid phase is pure water with $\rho_A = 998.3$ kg/m^3, $\mu_A = 1 \cdot 10^{-3}$ kg/(ms); the gas phase is air with $\rho_B = 1.205$ kg/m^3, $\mu_B = 1.82 \cdot 10^{-5}$ kg/(ms). The surface tension between pure water and air at the given temperature is $\sigma_0 = 0.0727$ N/m.
The comparison with respect to the rise velocities (squares), and the aspect ratios (circles), for different bubble sizes, is given in figure 4.7. As can be seen from figure 4.7, there is a very good agreement between experimental and simulation results. The small deviation from the experimental results in terms of aspect ratio for the bigger bubbles can be addressed to the relatively coarse mesh resolution.

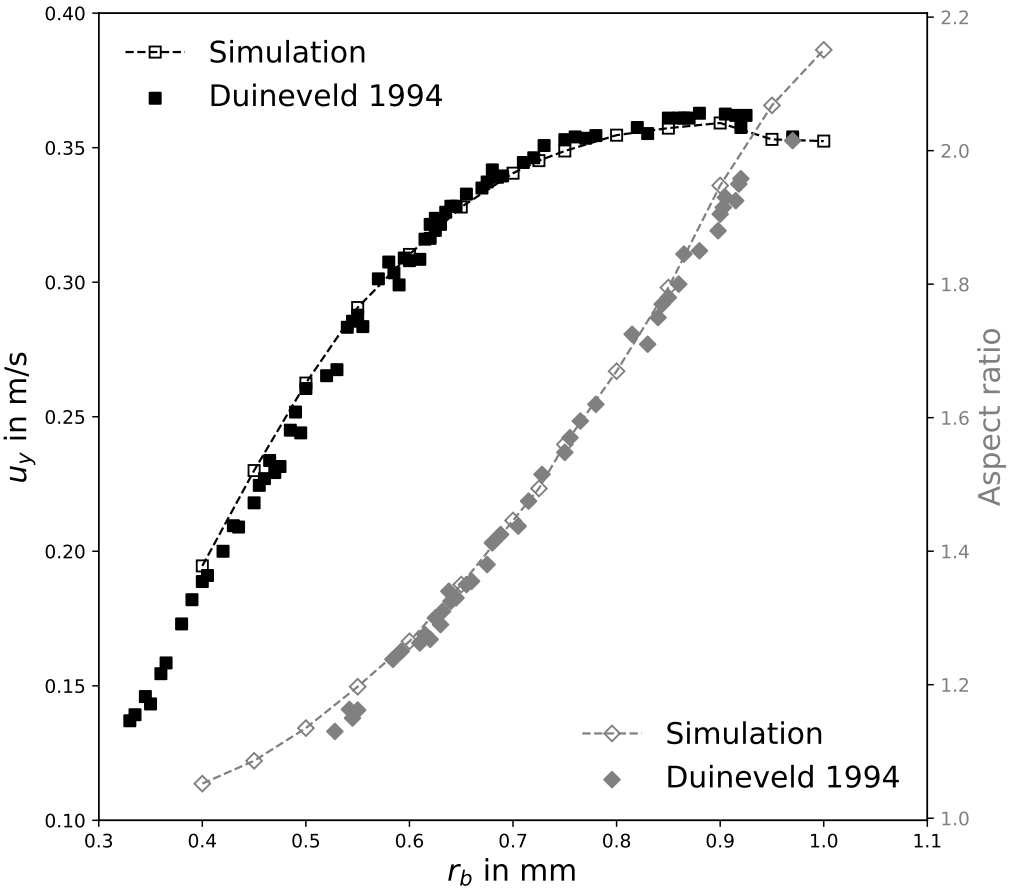

Figure 4.7: Simulation results compared to experimental ones from Duineveld [20], terminal rise velocity and aspect ratio.

4.3 Sorption processes

To validate the different treatment of the so-called fast and slow sorption processes, a simplified test case is considered, as done in [66]. Here, not only the slow sorption case is considered, but also the fast one and the exact analytical solution is derived.
The test case, in analogy to a typical transient heat conduction problem [12], consists of a spherical domain of radius r_0, where the surfactant is only transported by diffusion in the bulk.

At the initial time, the surface of the sphere is clean. The surfactant can be adsorbed either via a *fast* or a *slow* mechanism. For both cases, an analytical solution for $c(t,r)$ and $c^{\Sigma}(t)$ can be derived. Figure 4.8 shows a sketch of the domain.

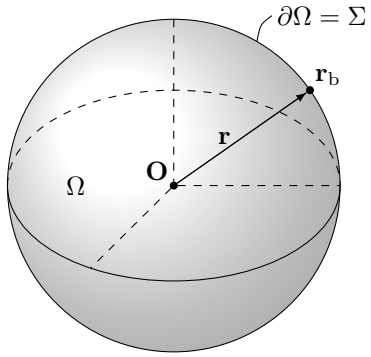

Figure 4.8: Domain for the diffusion/sorption model problem.

In spherical coordinates, the rotationally symmetric problem for the transport of the surfactant in the bulk phase, $\Omega \setminus \Sigma$, is governed by

$$\partial_t c - \mathrm{D}\frac{1}{r^2}\partial_r\left(r^2\partial_r c\right) = 0, \quad t > 0,\ 0 < r < r_\mathrm{b}. \tag{4.7}$$

On the interface, a simplified surface transport equation is considered, namely

$$\partial_t c^{\Sigma} = s^{\Sigma}, \quad t > 0,\ r = r_\mathrm{b}, \tag{4.8}$$

with $c^{\Sigma}(0) = 0$, and s^{Σ} is specified below.
To describe the two different processes of fast and slow sorption, different initial and boundary conditions as well as source terms will be considered, as already described in section 2.2.2.

4.3.1 Slow sorption problem closure

In case of kinetically controlled sorption, the initial and boundary conditions for the bulk equation read as

$$c(r,0) = c_0, \tag{4.9}$$
$$(\partial_r c)\,|_{r=0} = 0, \tag{4.10}$$
$$(\partial_r c)\,|_{r=r_\mathrm{b}} = -\frac{s^{\Sigma}}{\mathrm{D}}, \tag{4.11}$$

while the source term, only considering the adsorption mechanism within the Henry model, is

$$s^{\Sigma} = k^{\mathrm{ad}} c(r_\mathrm{b}, t). \tag{4.12}$$

4.3.2 Fast sorption problem closure

In case of diffusion-controlled sorption, the initial and boundary conditions for the bulk equation read as (with $0 \le \alpha \le c_0/r_\mathrm{b}$ and α arbitrarily chosen)

$$c(r,0) = c_0 - \alpha r, \tag{4.13}$$
$$(\partial_r c)\,|_{r=0} = 0, \tag{4.14}$$
$$c(r_\mathrm{b}, t) = c^{\Sigma}/\mathrm{H}, \tag{4.15}$$

while the source term is directly derived from the transmission condition at the interface (equation (2.20)):

$$s^{\Sigma} = -\mathrm{D}\left(\partial_r c\right)|_{r=r_\mathrm{b}}. \tag{4.16}$$

4.3.3 Analytical solution

The governing equations are then transformed into dimensionless form. The space and time variables become $\hat{r} = r/r_\mathrm{b}$ and $\hat{t} = t\mathrm{D}/r_\mathrm{b}^2$, such that $0 \leq \hat{r} \leq 1$ and $\hat{t} \geq 0$. The dimensionless bulk concentration is defined in two different ways: for slow sorption $\hat{c}(\hat{r},\hat{t}) = c(r,t)/c_0$, while $\hat{c}(\hat{r},\hat{t}) = \left(c(r,t) - c_\infty\right)/\left(c_0 - c_\infty\right)$ for fast sorption, such that in both cases $0 \leq \hat{c}(\hat{r},\hat{t}) \leq 1$. The non-dimensional surface concentration becomes $\hat{c}^{\Sigma}(\hat{t}) = c^{\Sigma}(t)/c_\infty^{\Sigma}$, where $0 \leq \hat{c}^{\Sigma}(\hat{t}) \leq 1$. A dimensionless number, comparable to the Biot number usually defined for heat transfer problems, is defined here for the surfactant (only for slow sorption) as

$$\mathrm{Bi} = k^{\mathrm{ad}} r_\mathrm{b}/\mathrm{D}. \tag{4.17}$$

It can be demonstrated that an analytical solution exists for short times or for infinite domains, thus the bulk and the surface concentrations $\hat{c}(\hat{r},\hat{t})$, $\hat{c}^{\Sigma}(\hat{t})$ can be obtained. In the following, only the final results are reported. The solution for the concentration in the bulk is

$$\hat{c}\left(\hat{r},\hat{t}\right) = \sum_{k=1}^{\infty} C_k \frac{\sin\left(\omega_k \hat{r}\right)}{\hat{r}} e^{-\omega_k^2 \hat{t}}. \tag{4.18}$$

where ω_k is solution of the eigenvalue problem derived from (4.10) or (4.14), that is

$$\omega_k \cot \omega_k = 1 - \mathrm{Bi}, \tag{4.19}$$

for slow sorption, and

$$\omega_k \cot \omega_k = 1 + (\mathrm{H}/r_\mathrm{b})\omega_k^2, \tag{4.20}$$

for fast sorption. The coefficients C_k are computed from the initial conditions (4.9) and (4.13) for slow and fast sorption, respectively. Once the solution in the bulk is known, the final form of the solution on the free surface can be derived. For kinetically controlled sorption, it reads

$$\hat{c}^{\Sigma}(\hat{t}) = \frac{r_\mathrm{b} c_0 \mathrm{Bi}}{c_\infty^{\Sigma}} \sum_{k=1}^{\infty} \frac{C_k}{\omega_k^2}\left(1 - e^{-\omega_k^2 \hat{t}}\right). \tag{4.21}$$

For diffusion controlled sorption, the analytical solution on the interface is

$$\hat{c}^{\Sigma}(\hat{t}) = \frac{r_\mathrm{b}(c_0 - c_\infty)}{c_\infty^{\Sigma}} \sum_{k=1}^{\infty} C_k \frac{\sin\omega_k - \omega_k \cos\omega_k}{\omega_k^2}\left(1 - e^{-\omega_k^2 \hat{t}}\right). \tag{4.22}$$

4.3.4 Sorption processes results

4.3.4.1 Slow sorption

The system of equations (4.9)-(4.12) is solved analytically and numerically with the following parameters: $r_\mathrm{B} = 1$ m, $c_0 = 1$ mol/m^3, $D = 1$ m^2/s and $k^{\mathrm{ad}} = 1$ m/s. Three mesh resolutions are considered (coarse, medium, fine) with approximately 11000, 30000 and 60500 cells in the bulk phase and 4400, 8800 and 17500 faces on the interface, respectively. Figure 4.9 shows the

comparison between the analytical solution (solid lines) and the simulation results (markers) at different times for the slow sorption case. As can be seen from this figure, the concentration in the bulk is progressively decreasing with time; the surfactant leaving the bulk phase is then adsorbed on the interface. This transfer of surfactant is described by the adsorption model above. There is a very good agreement between the analytical solution and the simulation results.

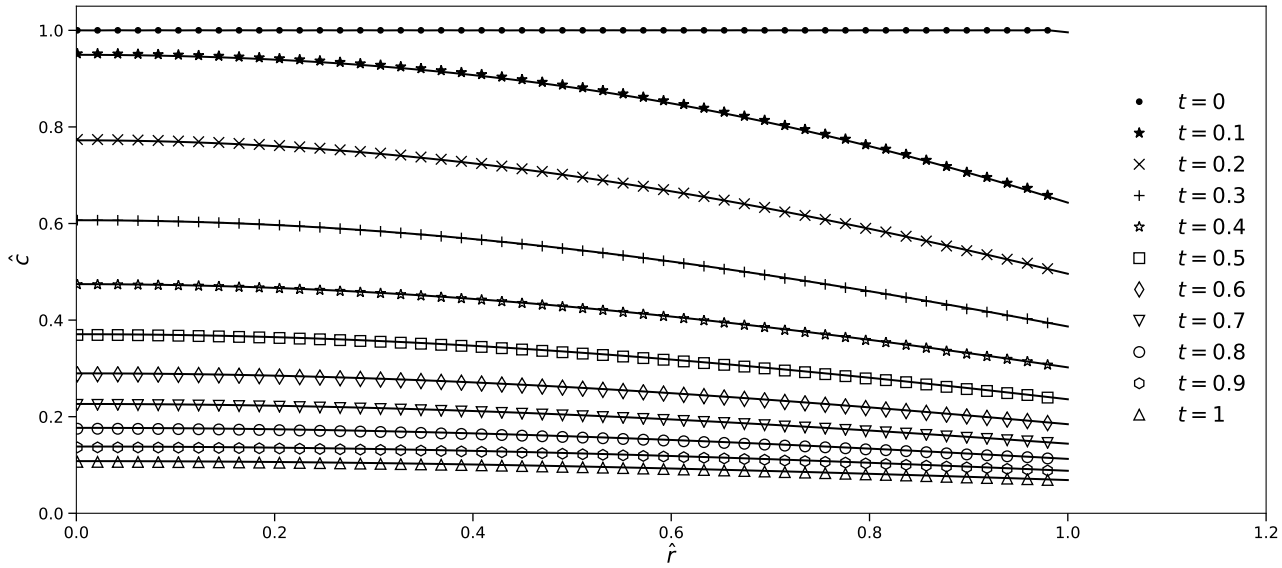

Figure 4.9: Profiles of $\hat{c}(\hat{r}, \hat{t})$ in case of slow sorption, the continuous lines represent the analytical solution.

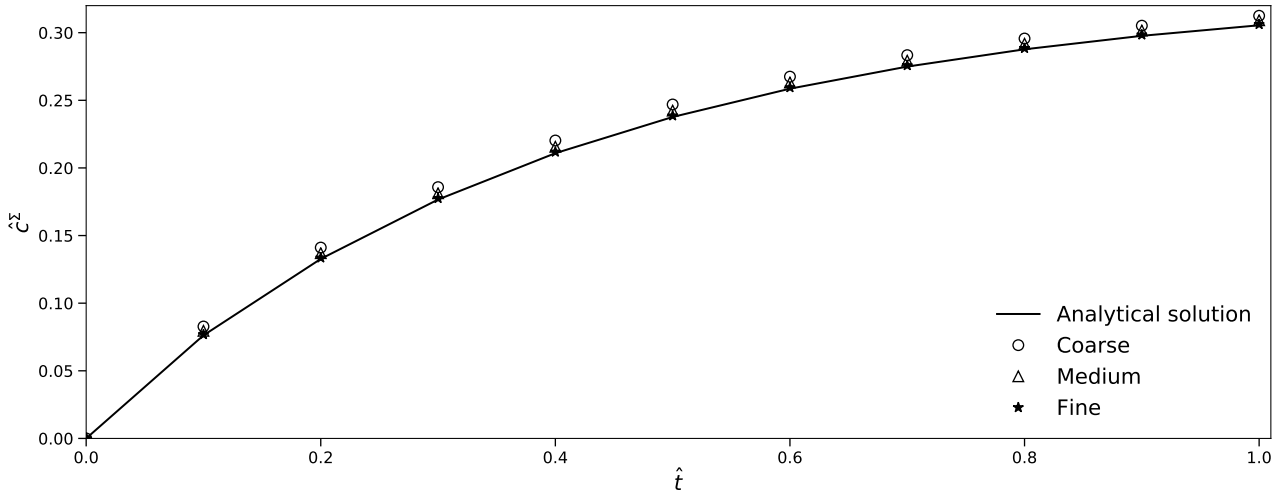

Figure 4.10: Surfactant concentration on the free surface with slow sorption, mesh convergence study.

For the same case, also the analytical solution on the interface is compared with the average concentration on the interface resulting from the simulations; see figure 4.10. In this figure, the mesh convergence study is shown. Further mesh refinement will not improve the numerical results.

4.3.4.2 Fast sorption

The system of equations (4.13)-(4.16) is solved analytically and numerically with the following parameters: $r_B = 1$ m, $c_0 = 1$ mol/m^3, $\alpha = 0.8$ mol/m^4, $D = 1$ m^2/s and $H = 1$ m.

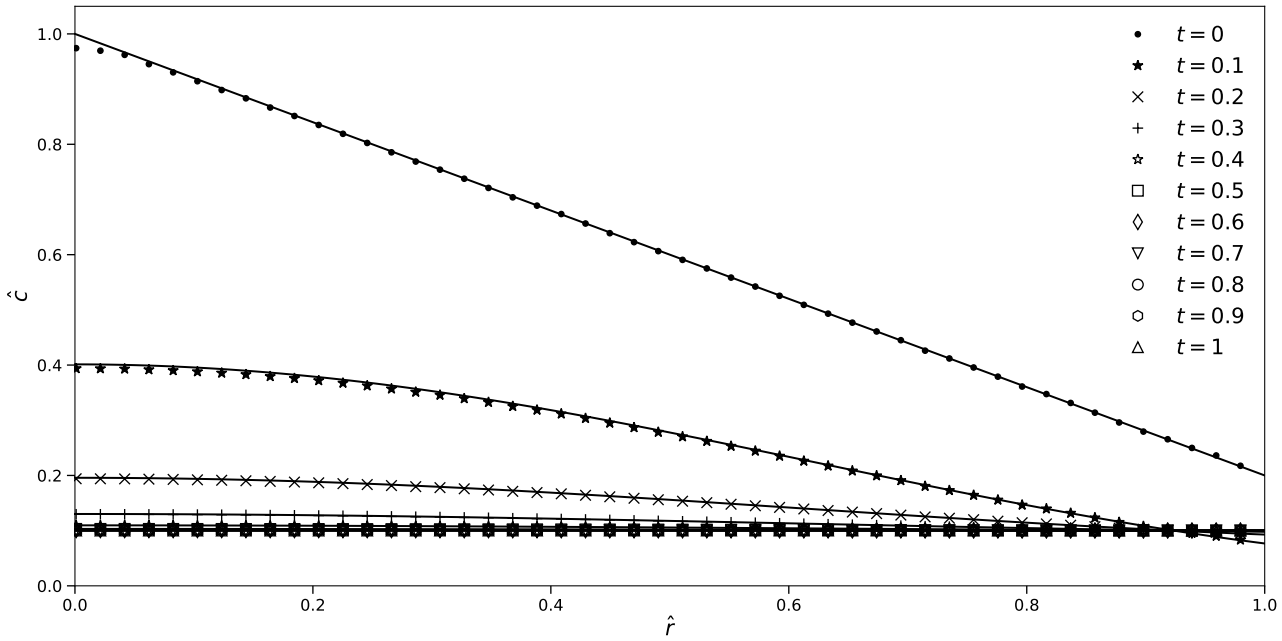

Figure 4.11: Surfactant concentration in the bulk at different time instances with fast sorption (simulation results from the finest mesh), the continuous lines represent the analytical solution.

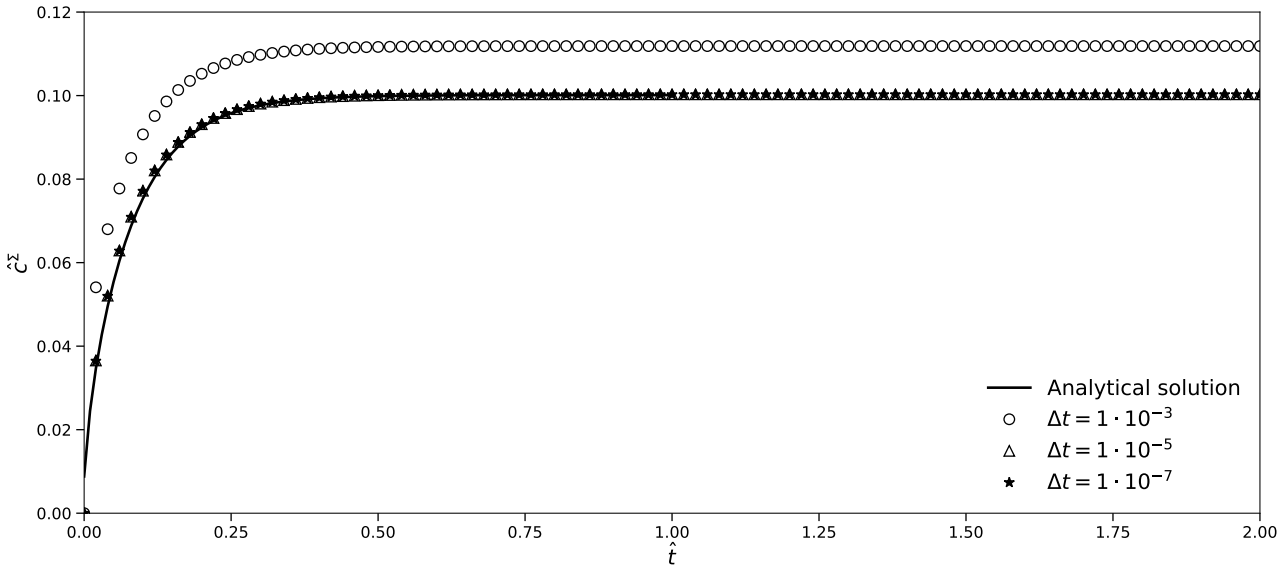

Figure 4.12: Surfactant concentration on the free surface with fast sorption: time step convergence study.

The results for the fast sorption validation case are reported in figure 4.11. The simulations have been run for the three mesh resolutions, as in section 4.3.4.1, giving almost the same results.

The initial distribution of the surfactant in the bulk phase here is linear. The surfactant is then adsorbed on the interface, and the bulk concentration decreases accordingly until it reaches an equilibrium value. As can be seen from the figure, also for the fast sorption case there is a very good agreement between the analytical solution and the simulation results.
In figure 4.12, the simulation results in terms of mean surfactant concentration on the free surface are displayed against the analytical solution. Here the coarsest mesh have been used and three different sets of simulation results are shown, this time studying the sensitivity to the time step size. Figure 4.12 shows that for decreasing time steps, the simulation results are approaching the analytical solutions and below a certain threshold the results are independent with respect to the time step size.

4.4 SGS model for non-reactive species transfer

To validate the solution of the species transfer problem with SGS modelling, test cases with increasing complexity are presented. The local Sherwood number $\mathrm{Sh}_{\mathrm{loc}}$ is used for comparison with the reference solution.

4.4.1 2D model problem

This test case refers directly to the simplified problem formulation on which the SGS model is based. The implementation of the SGS model has been validated against the analytical solution taken from [95] and reported in section 3.3. The problem set-up under investigation is sketched in figure 4.13. All the simplifying assumptions of the model problem are fulfilled if the computational domain size is large enough. The distance between the interface and the boundaries in x-direction is approximately 50 times the maximum species boundary layer thickness, to ensure that the difference to the reference solution can be negligible. The presence of the gas phase is modelled via the boundary condition for the species concentration at Σ. The boundary and initial conditions can be found in figure 4.13.

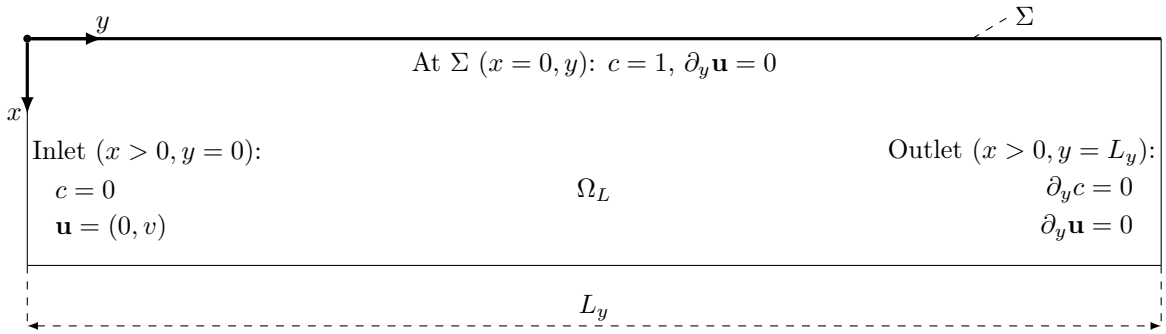

Figure 4.13: SGS 2D model problem set-up.

Four different mesh resolutions are considered from 5 to 40 μm. Since the interest is mainly on advection-dominated problems, a high Péclet number of $\mathrm{Pe} = 10^5$ is chosen. The local Sherwood number is computed as

$$\mathrm{Sh}_{\mathrm{loc}}(y_i) = (\partial_n c)_{f_i^{\Sigma}} \; \frac{L_y}{c_{i|\Sigma} - c_{\infty}} \tag{4.23}$$

with the normal derivative at the interface $(\partial_n c)_{f_i^\Sigma}$ [3], the concentration in the boundary cell center $c_{i|\Sigma}$ and the species concentration far away from the interface c_∞.
Figure 4.14 depicts the comparison between the analytical solution and the numerical results obtained with and without the SGS model. When the problem is solved with linear interpolation, the relatively coarse meshes are not able to predict the solution precisely. The finest mesh (5 μm) provides a good approximation of the local Sherwood number except for the region close to the inlet. All the cases where the SGS model is applied are in very good agreement with the reference solution. The enlarged view in figure 4.14 shows also mesh convergence for the SGS model results.

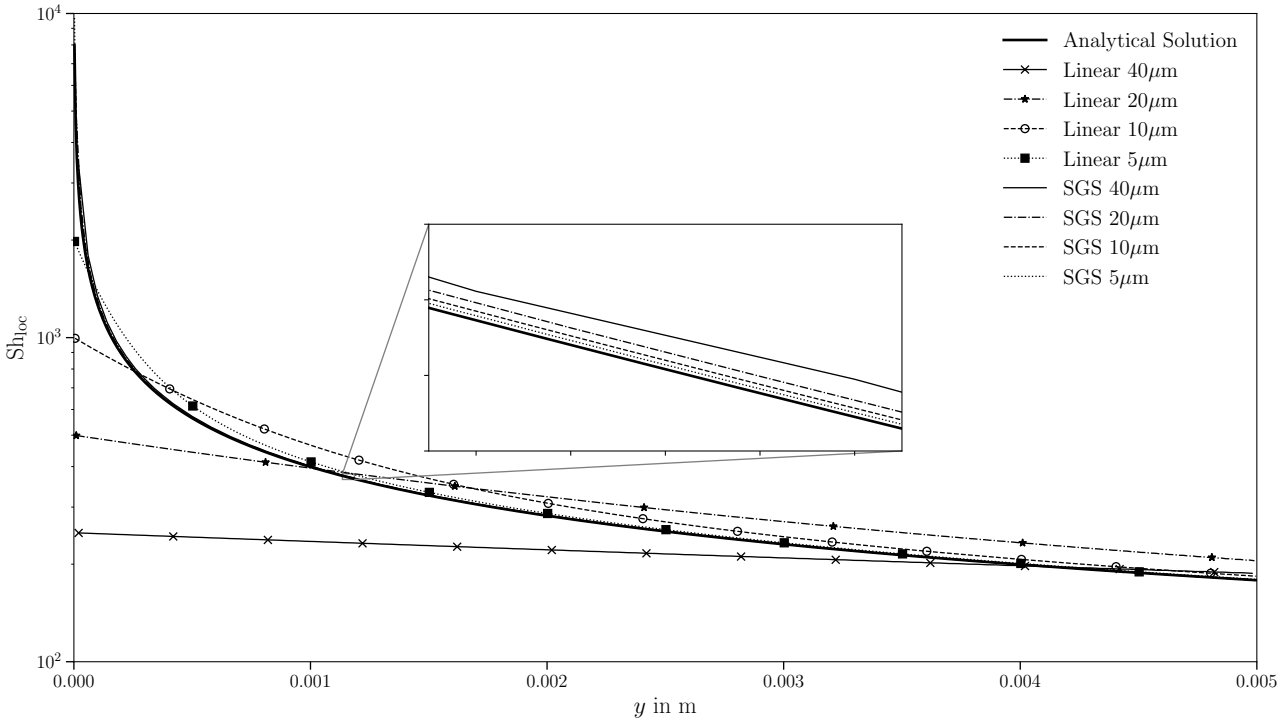

Figure 4.14: Local Sherwood number for the 2D model problem.

4.4.2 Spherical bubbles at small Reynolds number

A spherical bubble at small Reynolds number is considered. For this case, a semi-analytical solution of the species transport equation is possible. The solution is termed semi-analytical here, because the species transport equation is solved numerically using an analytical expression for the velocity field to compute convective fluxes. The velocity field is based on the solution of Satapathy and Smith [79] (spherical particle of radius r_b rising in a larger sphere R). On top of this velocity field, the species transport equation can be solved numerically using a very high grid resolution (cell thickness $l \approx 0.06$ μm close to the interface). Four different molecular diffusivities are considered corresponding to Schmidt numbers[4] of Sc $= 10^4,\ 10^5,\ 10^6,\ 10^7$. The

[3]Without the SGS model the gradient is computed as $(\partial_n c)_{f_i^\Sigma} = \left(c_{i|\Sigma} - c_{f_i^\Sigma}\right)/d_i$, where d_i is the distance between the boundary face center and the boundary cell center, and $c_{f_i^\Sigma}$ is the concentration at the interface face; otherwise $(\partial_n c)_{f_i^\Sigma}^{\mathrm{SGS}}$ is used.

[4]Recall that Sc $= \nu/D$, where ν is the liquid's kinematic viscosity and D the diffusion coefficient of the transported species.

bubble radius is $r_\mathrm{b} = 1$ mm and the Reynolds number is set to $\mathrm{Re} = 0.56$. The local Sherwood number $\mathrm{Sh}_\mathrm{loc}(\theta_i)$ is computed as in equation (4.23), where θ_i is the polar angle, i.e. the angle following a streamline on the bubble surface from the top ($\theta = 0$) to the bottom ($\theta = \pi$). The bubble equivalent diameter d_{eq} is taken as reference length.

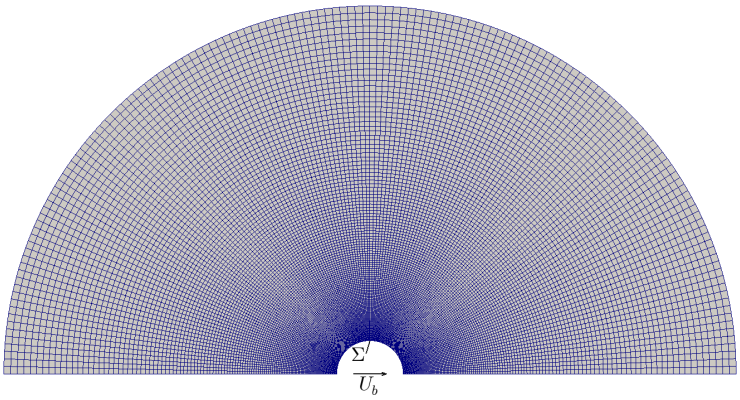

Figure 4.15: Domain used to solve the species transport with the given analytical velocity field.

4.4.2.1 Axisymmetric species transfer with given velocity field

The species transport is solved on top of the velocity field provided by the solution of Satapathy and Smith for the different Schmidt numbers. The results obtained with the SGS model are compared to the mesh independent direct numerical solution. The set-up for this simulations is depicted in figure 4.15.

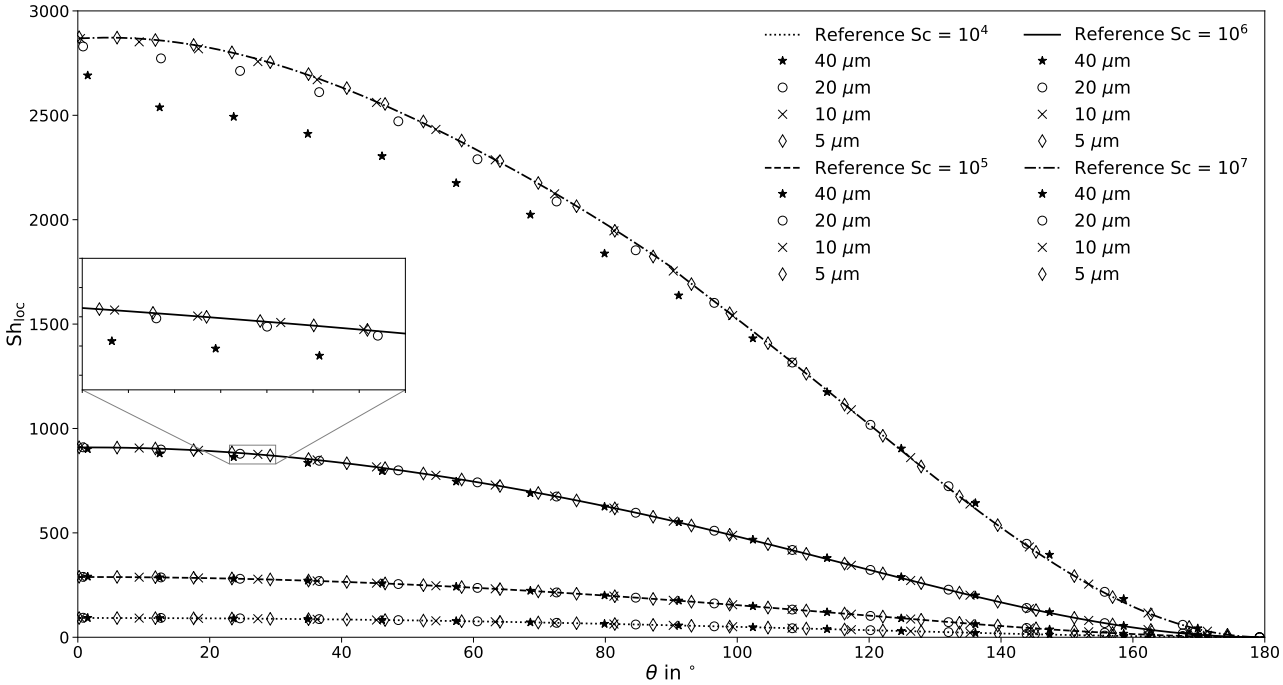

Figure 4.16: Local Sherwood number for the species transfer problem with given Satapathy-Smith velocity profile.

The fluid properties for the liquid side (identified with a $^+$) can be found in table 4.1. Four different mesh resolutions are considered with a cell thickness l close to the interface ranging from 5 to 40 μm. The four different diffusion coefficients are 10^{-8}, 10^{-9}, 10^{-10} and 10^{-11} m^2/s. The species concentration at the interface Σ is set to $c|_\Sigma = 1$ mol/m^3, while the initial bulk concentration in Ω^+ is set to $c_0 = c_\infty = 0$.
In figure 4.16, an overview of the results obtained applying the SGS model compared to the reference solutions is depicted. Figure 4.16 shows a very good agreement between the numerical results using the SGS model and the respective references for each tested Schmidt number. This test case shows also that the two coarsest meshes ($l = 40,\ 20$ μm) are not fully capable to properly resolve the species transport for the highest Schmidt number, under-predicting the Sherwood number in the upper part of the bubble. Such behaviour has to be considered in the application case set-up with surfactant transport and sorption, mainly in the choice of the mesh resolution.

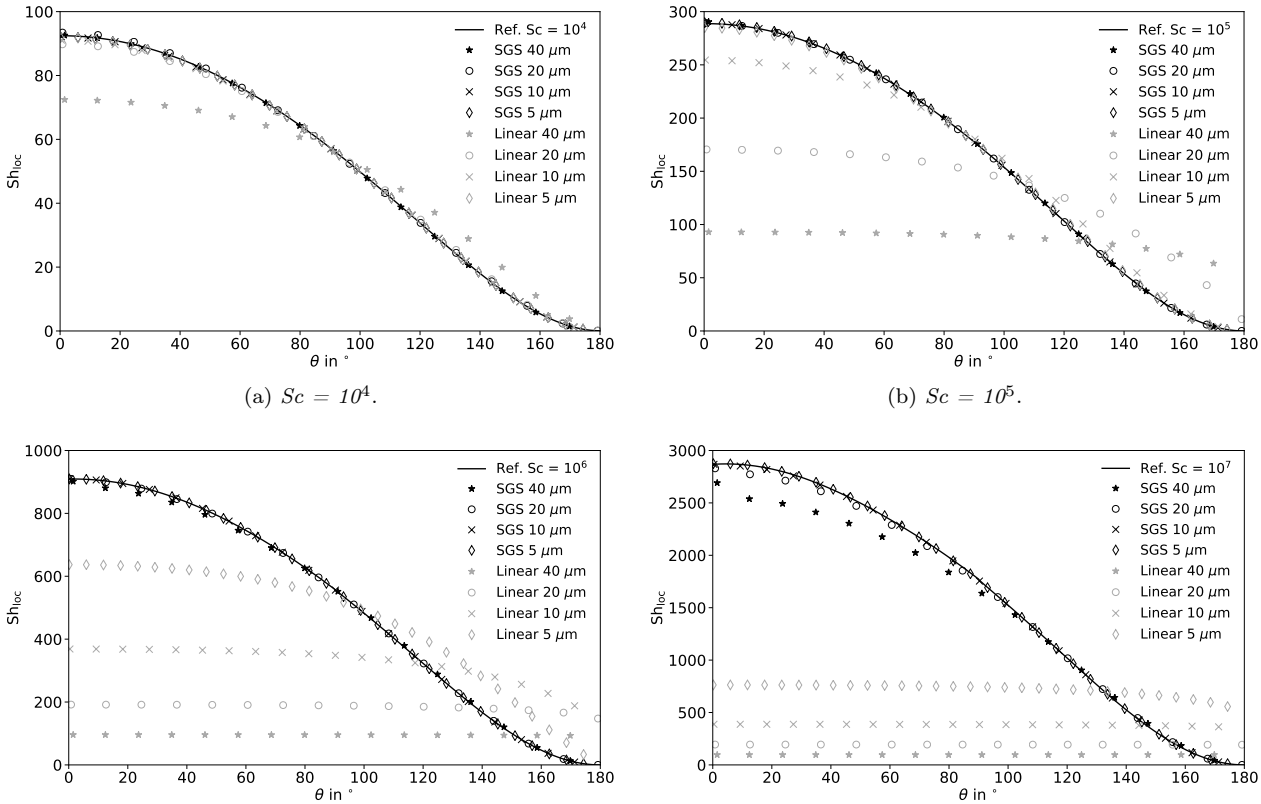

(a) $Sc = 10^4$.

(b) $Sc = 10^5$.

(c) $Sc = 10^6$.

(d) $Sc = 10^7$.

Figure 4.17: Local Sherwood number for the species transfer problem with given Satapathy-Smith velocity profile. Black symbols: with SGS modeling, grey symbols: linear interpolation.

For completeness, in figure 4.17, the comparison between the cases with and without SGS modelling is shown. The results obtained applying the SGS model are coloured in black, while the ones obtained with a linear interpolation method are grey. Already for Sc $= 10^5$ the standard discretization is inadequate to correctly describe the species transfer close to the interface for the given mesh resolutions. This comparison confirms again that with the SGS model one can save several mesh refinement levels.

4.4.2.2 Species transfer with computed velocity field

The species transport problem from a rising bubble is considered. The full 3D problem, hydrodynamics, and species transfer are solved within the Interface-Tracking framework, see the algorithm in figure 3.6. The case set-up follows the one described in sections 4.2.1 and 6.1.1. The interface consists of polyhedral faces with an edge length of approximately 50 μm and a first cell layer thickness of $l = 12$ μm or $l = 25$ μm. The initial shape of the bubble is a sphere of radius $r_b = 1$ mm. The bubble is positioned in the center of a spherical domain of radius $10r_b$. The fact that the interface is deformable is not relevant for the Satapathy-Smith case because, due to the choice of the fluid properties, the bubble does not deform significantly.
The initial and boundary conditions for the transferred species are the same as for the semi-analytical solution. The fluids properties are given in table 4.1. For this test case the smallest and the highest Schmidt numbers are considered, i.e. $\mathrm{Sc} = 10^4,\ 10^7$. As a reference, the semi-analytical solution presented in the former paragraph is used. The calculated velocity profile in the interface-tracking framework slightly differs from the Satapathy-Smith solution (less than 1.2%; see [94, section 4.1.2]), because the latter is based on a Stokes flow. This small difference can have some impact on the concentration profile close to the interface.

Table 4.1: Fluid properties for the Satapathy-Smith case.

ρ^+ kg/m^3	ρ^- kg/m^3	μ^+ kg/(ms)	μ^- kg/(ms)	σ_0 N/m
1000	1.1965	0.1	$1.8 \cdot 10^{-5}$	0.0724

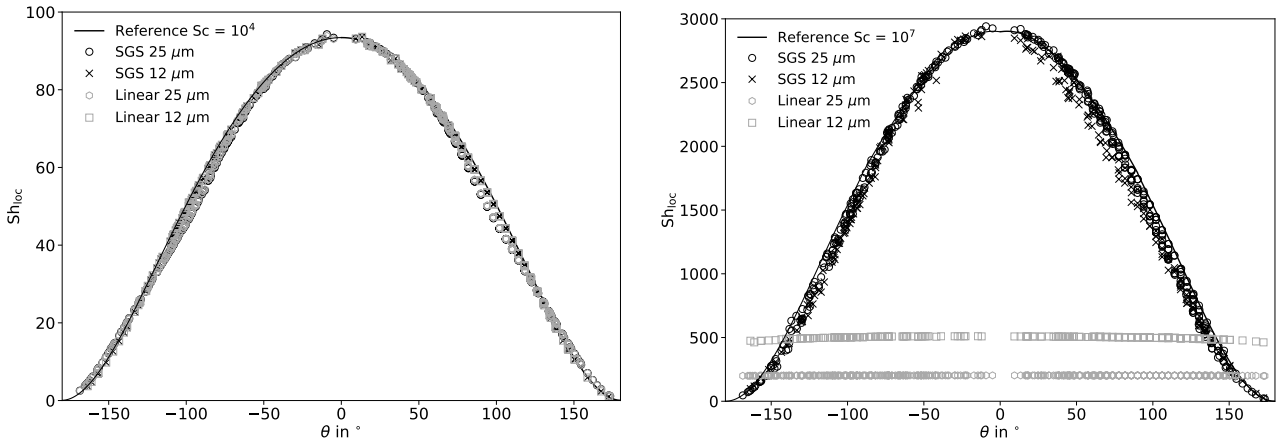

(a) $Sc = 10^4$.

(b) $Sc = 10^7$.

Figure 4.18: Local Sherwood numbers for the species transfer problem with Satapathy-Smith set-up. Black symbols: with SGS modelling, grey symbols: linear interpolation.

In figure 4.18, the results in terms of Sherwood number for the 3D case are reported. As can be seen from the two graphs, there is a good agreement between the reference solution and the numerical one employing the SGS model. As anticipated, the reference solution is computed based on the Satapathy-Smith velocity profile, thus, since we are dealing with highly non-linear functions (species concentration close to Σ), small deviations in the velocity field could be enough to produce the observed discrepancies in the results close to the bubble equator. In figure 4.18, also the results without the SGS model are plotted. For small Schmidt

numbers, figure 4.18a, the standard discretization and the SGS model provide results in very good agreement with the reference solution. On the other hand, for high Schmidt numbers and the given mesh resolution, figure 4.18b, the standard discretization provides underestimated Sherwood numbers, while the ones obtained with the SGS model are in good agreement with the reference.

4.5 Validation of the SGS model for reactive species transfer

In analogy to the validation of the SGS model for non-reactive mass transfer, two test cases are considered. Also here, the main quality indicator is the local Sherwood number. The selection of a meaningful reaction system is not trivial.

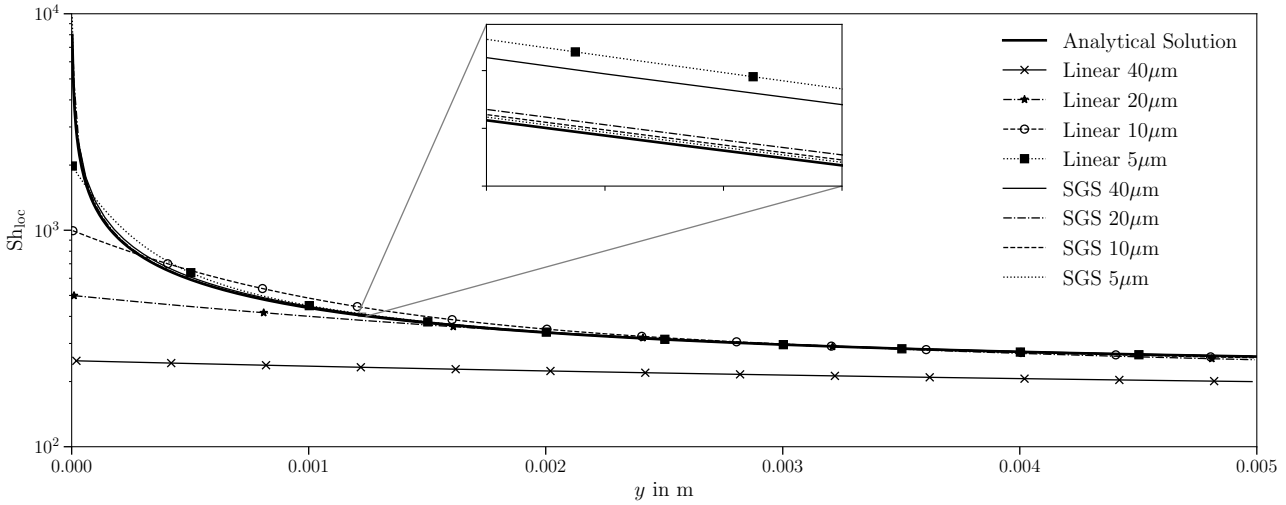

(a) Da = 0.5.

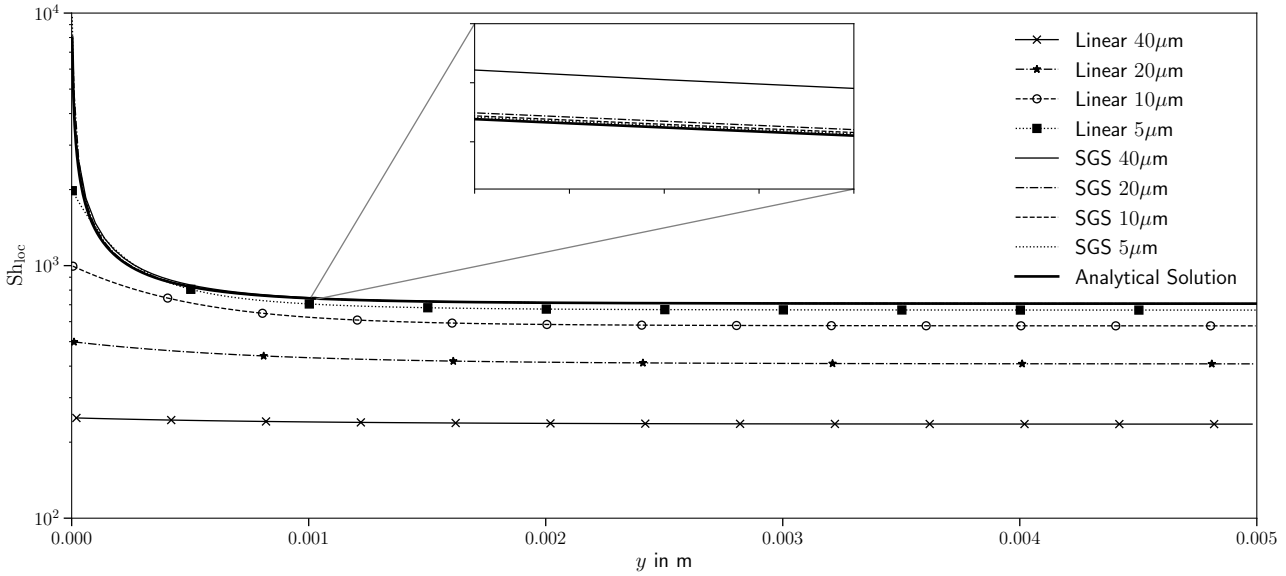

(b) Da = 5.

Figure 4.19: Local Sherwood number for the reactive 2D model problem.

For a gas-liquid interface, as described in [97], a characteristic time-scale describing the contact time may be defined as $\tau_{\text{conv}} = L_y/U$. The time-scale of a first-order reaction is simply the inverse of the reaction rate constant $\tau_{\text{r}} = 1/k$. An important dimensionless group defined as the ratio of both time-scales is the Damköhler number

$$\text{Da} = \tau_{\text{conv}}/\tau_{\text{r}} = kL_y/U. \tag{4.24}$$

The Damköhler number will be used in the following sections to distinguish between the test cases presented.

4.5.1 2D model problem

The first test case mirrors the set-up described in section 4.4.1, solving the simplified problem (3.51) and comparing it to the analytical solution (3.53). The local Sherwood number is computed according to equation (4.23). For this test case, two Damköhler numbers are considered, $\text{Da} = 0.5$ and $\text{Da} = 5$. All the other parameters remain fixed with respect to 4.4.1.
As can be seen from figure 4.19, for all the cases where the reactive SGS model is applied, the simulation results are in very good agreement with the analytical solution. Instead, when the problem is solved with linear interpolation, for $\text{Da} = 0.5$, the relatively coarse meshes are not able to predict the solution precisely; see figure 4.19b. The finest mesh (5 μm) provides a good approximation of the local Sherwood number except for the region close to the inlet. For $\text{Da} = 5$, only the finest mesh (5 μm) is close to the analytical solution, even though the error is much higher than that for all the cases where the SGS model is employed; see figure 4.19b.

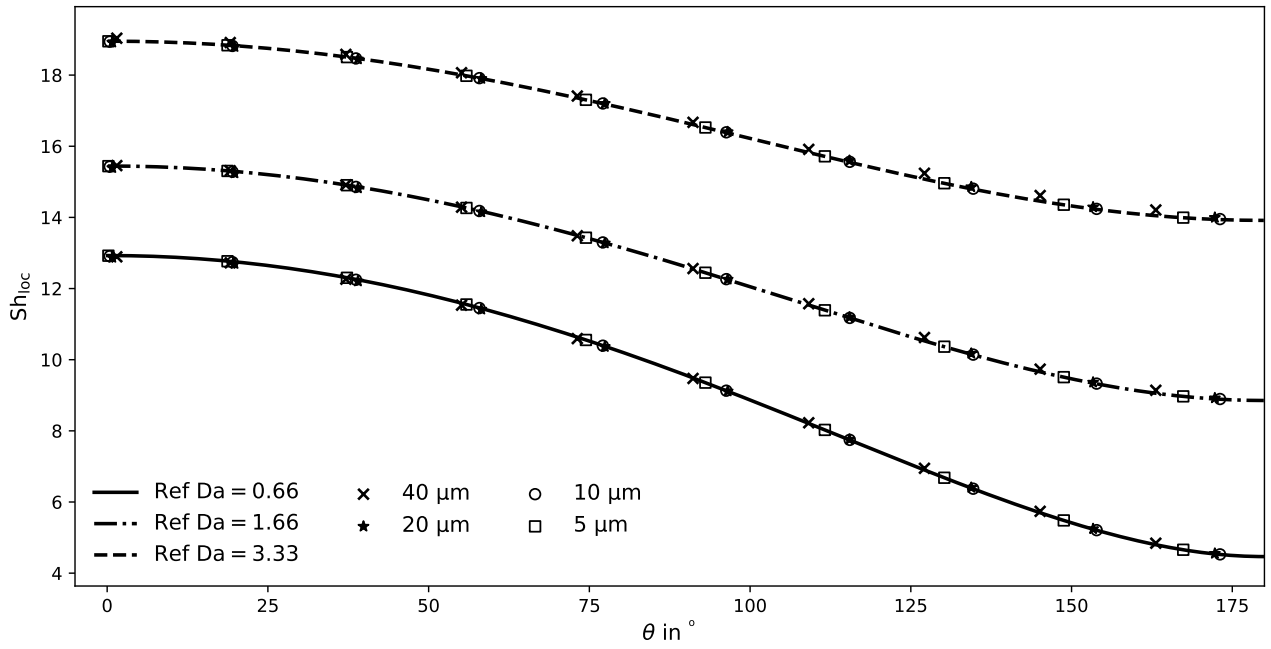

Figure 4.20: Local Sherwood numbers for different reactive time scales and mesh resolutions; Pe = 280; figure based on [97].

4.5.2 Spherical bubbles at small Reynolds number: Axisymmetric reactive species transfer with given velocity field

The second test case for the reactive SGS model validation involves the comparison with the semi-analytical solution of the species transfer from a spherical bubble rising at a very low Reynolds number, in analogy to section 4.4.2.
The reference solution is computed on a mesh where the first cell layer thickness was approximately 0.1 μm. From figure 4.20, two observations can be made: i) The species transfer enhancement due to the chemical reaction in the boundary layer is captured well, and ii) the solution shows very little dependence on the computational mesh. Even the global Sherwood numbers computed on the coarsest mesh employing the reactive SGS model deviate much less than 1% from the reference.

4.6 Rising bubble in contaminated solution

In literature, there are several experimental works about rising bubbles in aqueous solutions contaminated by surfactants. Nevertheless, either not all the set-up parameters are available, the bubble sizes are outside the range that can be simulated, or they use complex chemical compounds for which the hypothesis of the mathematical model not always holds, e.g. no phase change, no electrical effect due to ionic surfactants, dilute surfactant concentrations.
After a careful selection, the experimental work by Fdhila & Duineveld [29] has been considered for comparison.

4.6.1 Comparison with published experimental results

From the various experimental results in [29], the ones for Triton X-100 are considered. Triton X-100 is a non-ionic surfactant known to follow a fast sorption mechanism. The numerical model accounts for the deformable bubble interface employs the Langmuir fast sorption model to describe the sorption mechanism and the SGS model is used to predict the surfactant bulk transport close to the interface. This comparison should then allow to validate the results obtained employing the SGS model for the surfactant transport in the liquid phase. Two bubble radii are considered, $r_B = 0.4,\ 0.7$ mm, and a set of different initial surfactant bulk concentrations, $c_0 = 1 \cdot 10^{-7},\ 1 \cdot 10^{-5},\ 1 \cdot 10^{-4},\ 2 \cdot 10^{-4},\ 3 \cdot 10^{-4},\ 4 \cdot 10^{-4},\ 5 \cdot 10^{-4},\ 1 \cdot 10^{-3},\ 2 \cdot 10^{-3}$ mol/m^3. Experiments were conducted at room temperature ($T = 293$ K). The fluid properties are given in table 4.2, while the Triton-X100 sorption parameters can be found in table 4.3.

Table 4.2: Fluid properties at the given temperature of $T = 293$ K from [29].

ρ^+ kg/m^3	μ^+ kg/(ms)	ρ^- kg/m^3	μ^- kg/(ms)	σ_0 N/m
997.6	$9.538 \cdot 10^{-4}$	1.2	$1.8253 \cdot 10^{-5}$	0.07278

The surface diffusivity D^Σ is only an estimate since it is not possible to accurately measure it. Nevertheless, a parameter study with D^Σ varying in the range of $[10^{-6} \ldots 10^{-10}]$ m^2/s confirmed that its variation has only a minor effect on the sorption dynamics and rise velocity because the transport is advection dominated. The initial surface concentration is set to $c_0^\Sigma = 0$ mol/m^2

because no information is given in the publication about the bubble formation and release time. A fundamental information from [29] is the position, where velocity measurements were taken. In the work it is reported that the bubble velocity was measured at $y = 0.035$ m, i.e. 3.5 cm from the bubble release point.

Table 4.3: Surfactant (Triton X-100) properties, fast Langmuir adsorption model parameters.

c_∞^Σ mol/m^2	a_L mol/m^3	D m^2/s	D^Σ m^2/s	T K
$2.9 \cdot 10^{-6}$	$6.6 \cdot 10^{-4}$	$2.6 \cdot 10^{-10}$	$7.8 \cdot 10^{-7}$	293

The experimental and numerical terminal velocities for different initial surfactant concentration are reported in figure 4.21. The straight lines with square markers correspond to the experimental results, while the dashed lines correspond to the simulation data. The simulation results do not agree well with the experiments and the differences can be explained as follows.

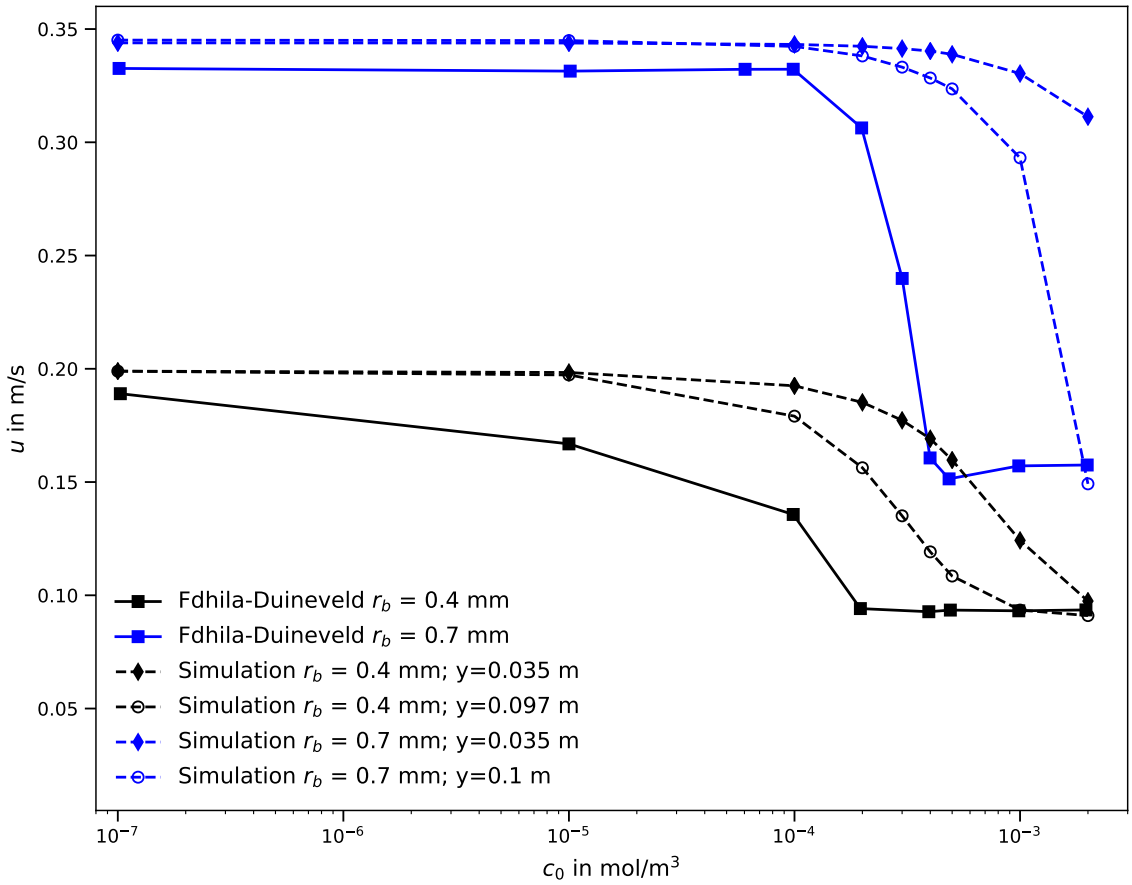

Figure 4.21: Experimental and numerical terminal rise velocities for $r_B = 0.4,\ 0.7$ mm with different initial surfactant bulk concentrations.

Consider, for instance, the bubble with radius 0.4 mm. In the experiment, the bubbles rising in a solution with $c_0 \geq 2 \cdot 10^{-4}$ mol/m^3 reach similar terminal velocities. The resulting velocities for initial surfactant concentrations up to $c_0 \leq 1 \cdot 10^{-4}$ mol/m^3 are questionable because these

intermediate velocities are not to be expected. In fact, as known from other experimental works, e.g. [54, 55, 61, 72], bubbles rising in a solution contaminated with a highly surface active agent[5] reach similar terminal velocities independently from the initial surfactant bulk concentration if let rise for a sufficient amount of time/distance. Thus, a reasonable explanation for this behaviour is that the measuring position was too close to the capillary.
In figure 4.21, also the velocities from the simulation at a higher position in the column are marked with empty circles. As can be seen, at this position the rise velocities are smaller and tend towards the final steady state velocity, i.e. the one for $c_0 = 2 \cdot 10^{-3}$ mol/m^3. To further support this hypothesis, the transient rise velocities for the two bubble radii are reported in figure 4.22. The measuring point from the experiments is depicted as vertical dashed line. Except from the three smallest initial bulk concentrations ($c_0 = 1{\cdot}10^{-7}$, $1{\cdot}10^{-5}$, $1{\cdot}10^{-4}$ mol/m^3), the rise velocities all tend to a similar steady state, as expected. This hypothesis is also supported by later experimental observations from Zhang and Finch in [99] and Palaparthi et al. in [69].

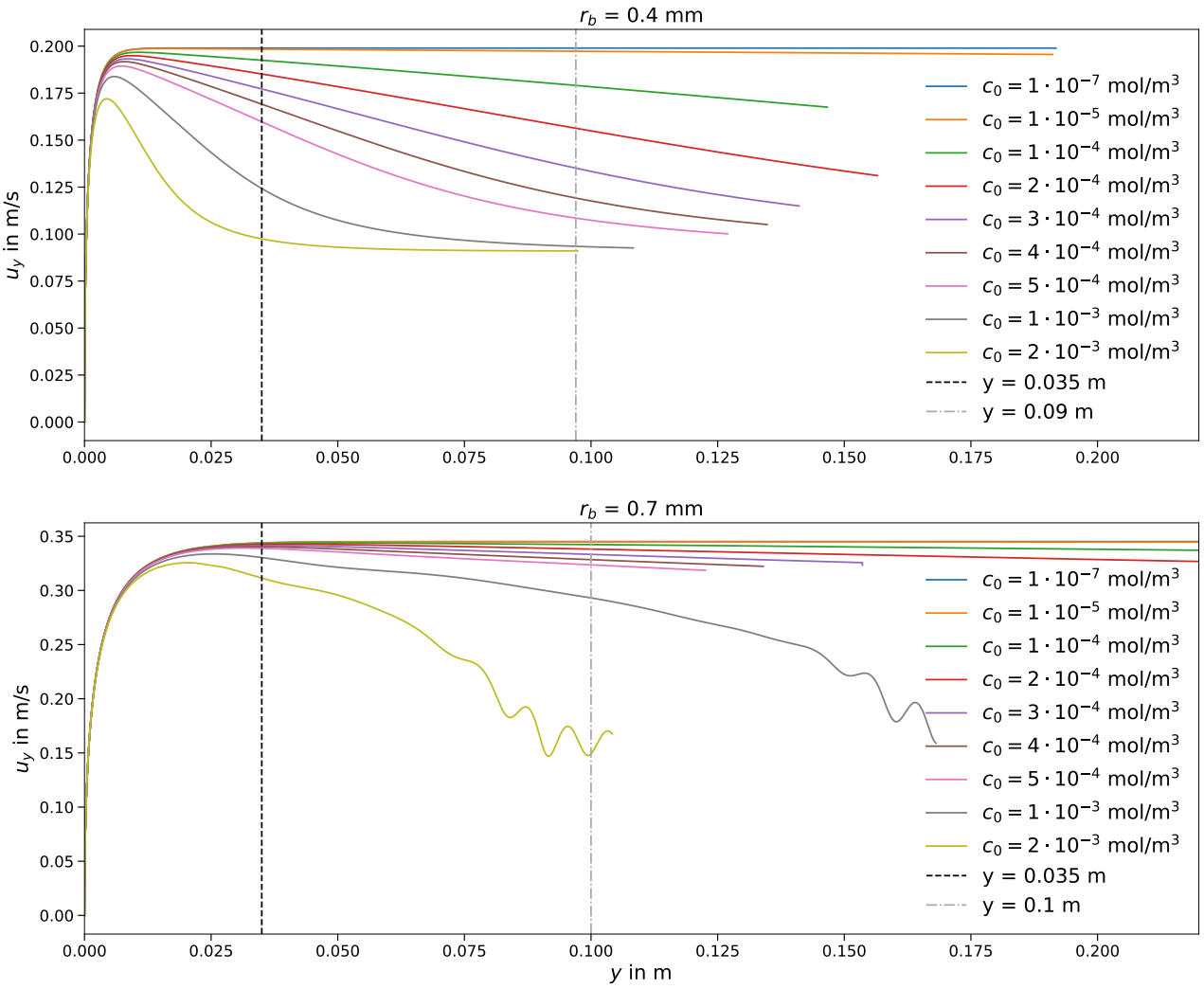

Figure 4.22: Transient rise velocities for $r_B = 0.4,\ 0.7$ mm with different initial surfactant concentrations.

[5] Triton X-100 is known to be highly surface active.

Moreover, it is very likely that, due to a finite bubble formation/release time, a certain pre-contamination on the bubble interface at release is present that unfortunately is unknown. If the bubble surface is already contaminated at release, then at the measuring position its velocity will be smaller than for the one with a clean interface. This argument would explain why the bubbles in the simulations need more time to reach the terminal velocity reported from the experiments.
Because of these consideration, the decision not to compare and then not to validate the simulation results against these experimental data was made. As a transient rise velocity is present, there is the need for transient experimental measurement as well. The difficulty to find accurate experimental data with an exhaustive description of the set-up still holds.

4.6.2 Highly resolved 2D simulations

To still validate the simulation results for rising bubbles under the influence of surfactant, a different strategy has been followed. Simulations of a 2D bubble rising in contaminated water are performed with and without SGS modelling for the surfactant transport. The simulation set-up follows the one described in section 4.2.1, but in 2D. This setting aims to demonstrate that the SGS model predicts the surfactant transfer well under dynamic conditions, e.g. when the bubble deforms, accelerates or decelerates, or when the flow detaches and vortices form; see figure 4.23. As can be seen from figures 4.24, 4.25 and 4.26, the results where the SGS model has been employed are matching the mesh independent results obtained with standard interpolation.

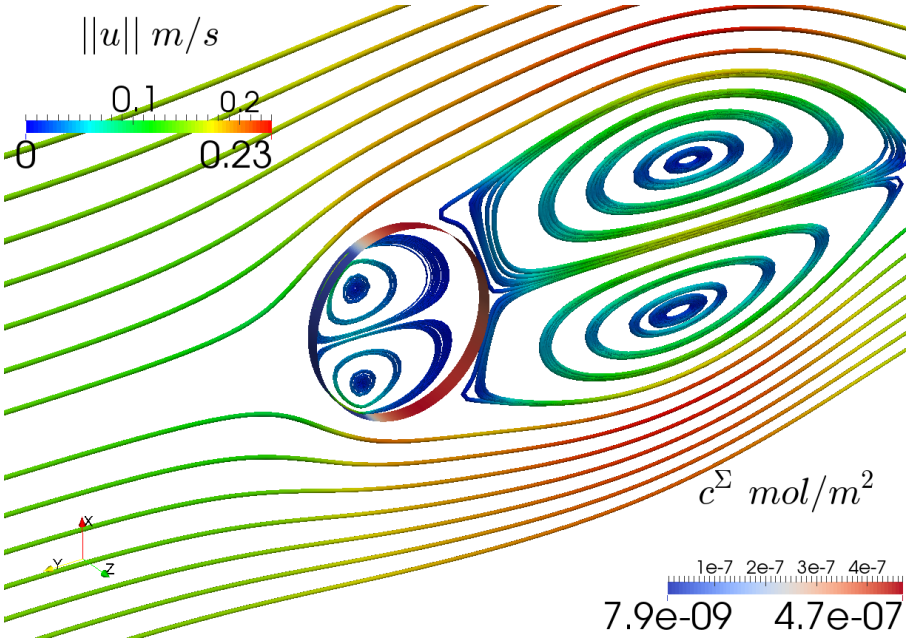

Figure 4.23: Flow field around and inside the rising bubble. The bubble surface is coloured by the surfactant concentration; $t = 0.2$ s.

For these tests, the same set-up parameters used in section 6.1.1 are applied. An intermediate initial concentration of C_{12}DMPO is used, i.e. $c_0 = 0.008$ mol/m^3, with $c_0^{\Sigma} = 0$ mol/m^2. Different bulk diffusivities, $D = 5 \cdot 10^{-7},\ 5 \cdot 10^{-8},\ 5 \cdot 10^{-9}, 5 \cdot 10^{-10}$ m^2/s, and mesh resolutions, first cell thickness $\ell = 16,\ 12,\ 8,\ 3,\ 1.7,\ 1.2$ μm, are considered. The changes between

$\ell = 1.7$ μm and $\ell = 1.2$ μm in rise velocity and surfactant transport are always less than 1.15%. Therefore one can consider the results on the finest mesh employing standard discretization as mesh independent and use them as reference solution (solid lines in the plots). The results for mesh resolutions with a first cell thickness equal to 16, 8, 3 and 1.2 μm are selected for the plots below.
Figure 4.24 shows that the rise velocities obtained applying the SGS modelling are all in agreement with the reference. On the other hand, the results obtained with standard interpolation follow a very different trend. Only the 3 μm mesh gets close to the reference for the physical value of the diffusivity.

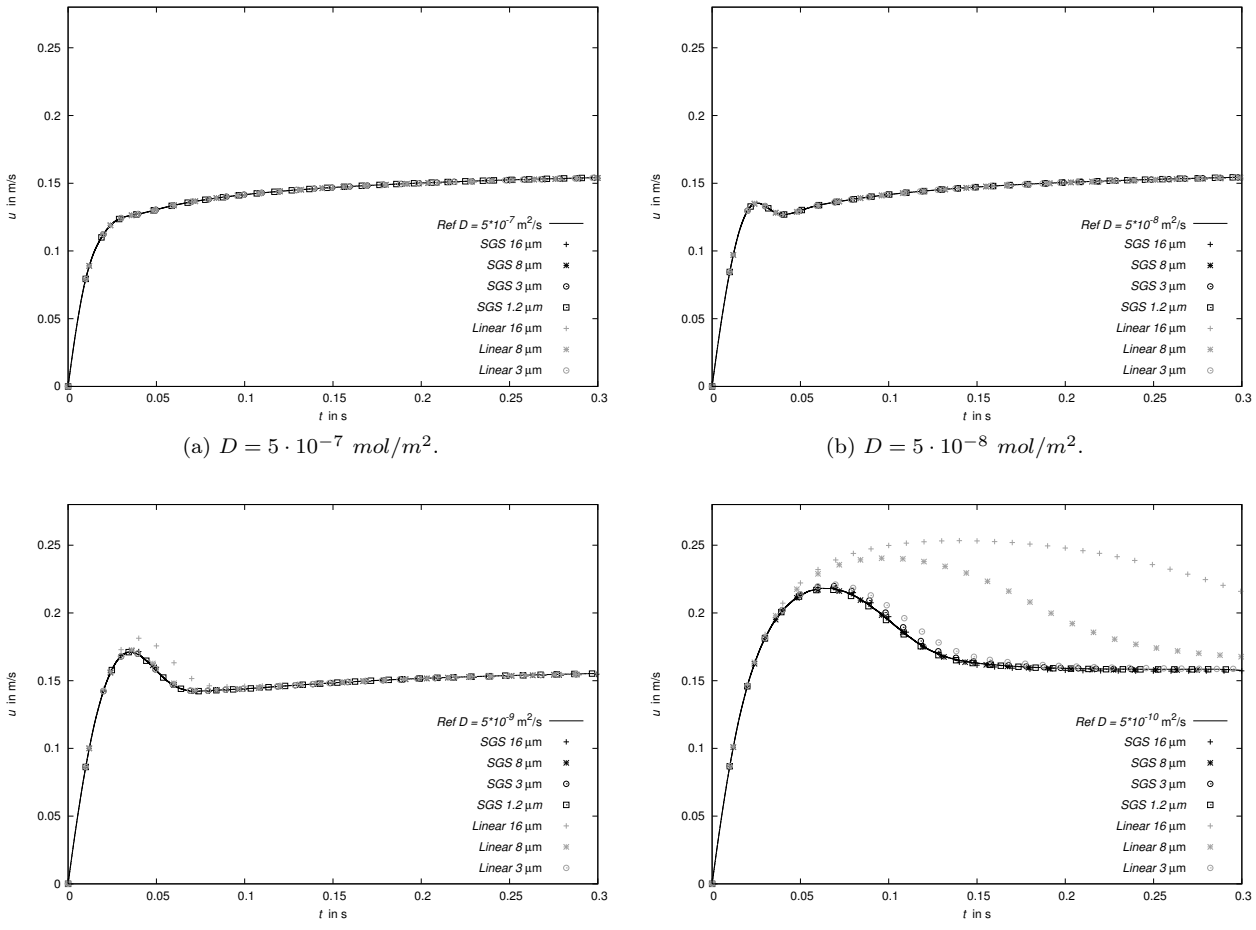

(a) $D = 5 \cdot 10^{-7}$ mol/m^2.

(b) $D = 5 \cdot 10^{-8}$ mol/m^2.

(c) $D = 5 \cdot 10^{-9}$ mol/m^2.

(d) $D = 5 \cdot 10^{-10}$ mol/m^2.

Figure 4.24: Rise velocities of a 2D bubble rising in contaminated water; comparison between cases with and without SGS modelling. Black symbols: with SGS modelling, grey symbols: linear interpolation.

Not only the rise velocities are in good agreement with the reference, but also the total amount of surfactant on the interface, as shown in figure 4.25 for different diffusion coefficients. As can be seen from the graphs, the results obtained with the SGS modelling are all lying on the reference curves, while for $D = 5 \cdot 10^{-9}$ m^2/s and $D = 5 \cdot 10^{-10}$ m^2/s, only the finer meshes with standard interpolation tend to the correct result.
So far, only global quantities were considered for comparison. Further confirmation that the SGS model is performing well and corresponding to the standard interpolation results is given

by the local Sherwood numbers for the different diffusivities at $t = 0.2$ s; see figure 4.26. Here it can be seen that all the cases where the SGS model has been used deliver a very good approximation of the local Sherwood number. Moreover, the shape of the local Sherwood number profile reflects the flow field around the bubble; cf. figure 4.23.

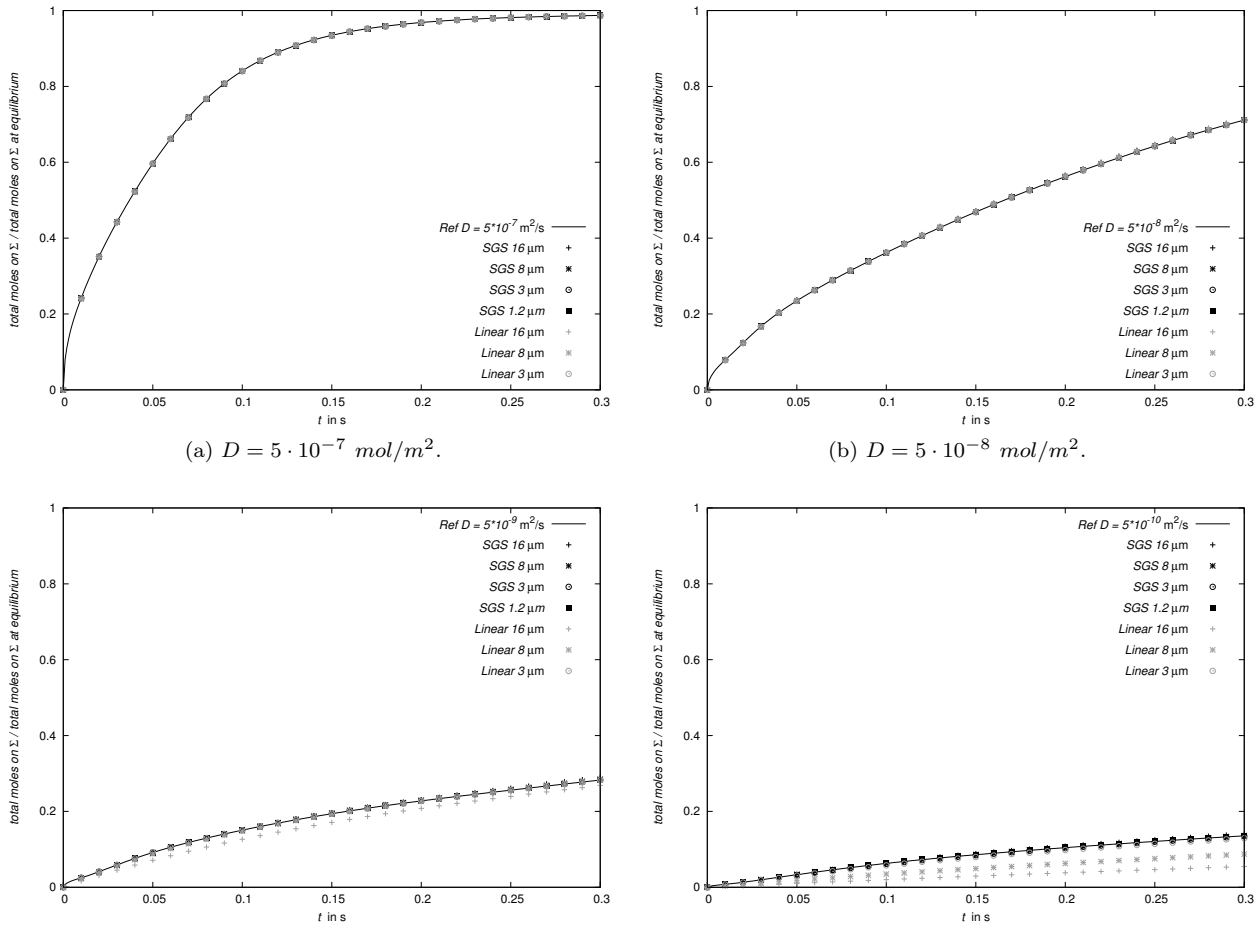

(a) $D = 5 \cdot 10^{-7}\ mol/m^2$.

(b) $D = 5 \cdot 10^{-8}\ mol/m^2$.

(c) $D = 5 \cdot 10^{-9}\ mol/m^2$.

(d) $D = 5 \cdot 10^{-10}\ mol/m^2$.

Figure 4.25: Relative number of moles of surfactant on the interface of a 2D bubble rising in contaminated water; comparison between cases with and without SGS modelling. Black symbols: with SGS modelling, grey symbols: linear interpolation.

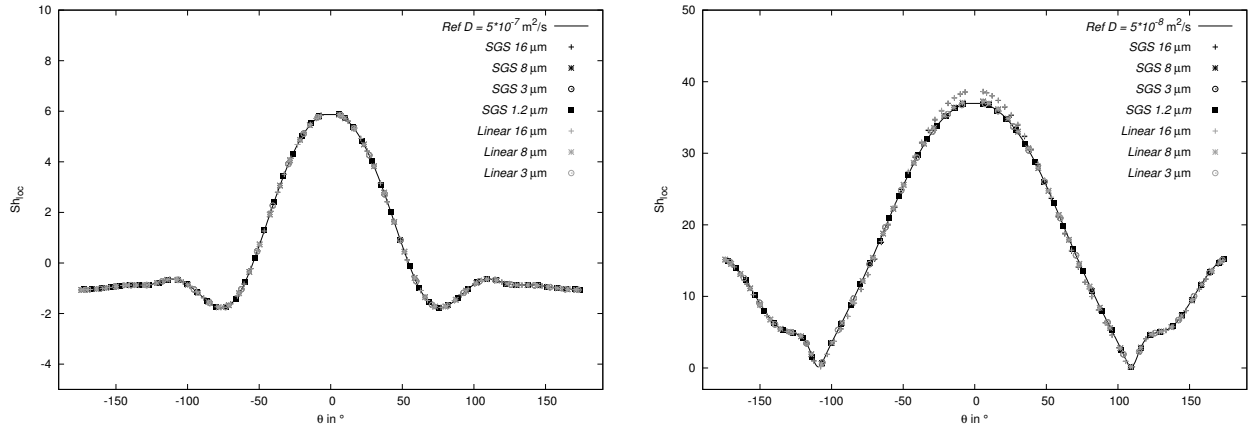

(a) $D = 5 \cdot 10^{-7}\ mol/m^2$.

(b) $D = 5 \cdot 10^{-8}\ mol/m^2$.

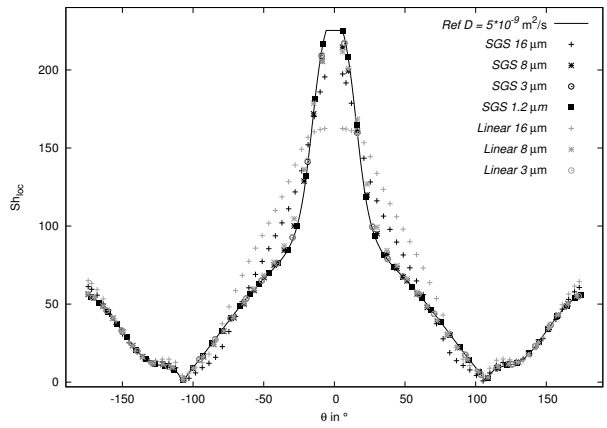

(c) $D = 5 \cdot 10^{-9}\ mol/m^2$.

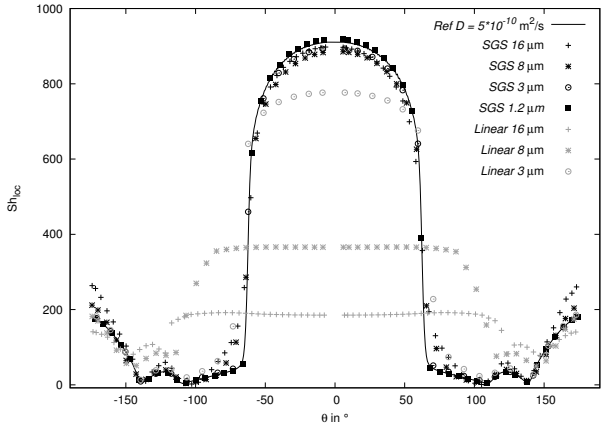

(d) $D = 5 \cdot 10^{-10}\ mol/m^2$.

Figure 4.26: Local Sherwood numbers for the surfactant transport problem at a 2D bubble rising in contaminated water; comparison between cases with and without SGS modelling. Black symbols: with SGS modelling, grey symbols: linear interpolation.

Chapter 5

A qualitative analysis of fast and slow sorption models

In the context of numerical simulations, verification of a model means confirming that it is correctly implemented with respect to the mathematical model from which it was derived. One of the techniques that can be used to verify a model is to examine the model outputs for plausibility under a variety of settings of the input parameters. Within the sorption library, a variety of models is implemented. To verify the correctness of the implementation, a 2D bubble rising in contaminated water is considered. From the literature, the surfactant parameters for different sorption models are known. These data are used in this test case to confirm that the various models are delivering reasonable results. In addition, from these test cases, one can also discuss the differences in the outcomes of different sorption models and mechanisms.

5.1 Test case set-up

Simulations of a 2D bubble rising in contaminated water are performed with[1] and without SGS modelling for the surfactant bulk transport. This setting aims to demonstrate that the implementation of the various sorption models is correct and provides reasonable results. A bubble diameter of $d_B = 1.45$ mm is considered. The fluid properties are the same as the ones reported in sections 4.6.2 and 6. The bubbles rise for a physical time of 0.4 s. Beyond this threshold, the two-dimensional simulation results are not reliable any longer. The results for the aggregation model are not reported here because they do not look physical. The reason is related to the presence of the critical surfactant concentration in the surface tension equation of state, but further testing and possibly a more complex implementation of the model is required to get reliable results with this model, too. For the slow sorption cases without SGS modelling, two mesh resolutions are employed with a cell thickness of 1 μm (M1) and 2 μm (M2), respectively, at the interface. In case of fast sorption, the finest grid is used and compared to the results with SGS modelling on a coarser grid of 8 μm cell thickness close to the interface, indicated as SGS in the legends of the graphs.
Among the various surfactant known to follow a fast sorption mechanism [13], C_{12}DMPO and Triton X-100 are considered. For both surfactants, Henry, Langmuir, Frumkin and Reorientation models are tested. The model parameters are listed in table 5.1. The respective initial

[1] The SGS model is available only for fast sorption cases for the moment. For slow sorption, a different approximating function has to be derived and implemented.

surfactant concentrations, saturated surface concentrations and bulk diffusivities are reported in table 5.2. The initial concentrations have been chosen such that they are much smaller than the respective CMC concentration.

Table 5.1: Surfactant properties for fast sorption models.

Surfactant	**Model**	**Parameters**				**Source**
C_{12}DMPO	Henry	$K = 8.598 \cdot 10^{-4}$ m				[26]
	Langmuir	$a_L = 4.8 \cdot 10^{-3}$ mol/m^3				[26]
	Frumkin	$\omega = 2.44 \cdot 10^5$ m^2/mol		$a = 0.35$	$b = 1.5 \cdot 10^2$ m^3/mol	[26]
	Reorientation	$\omega_1 = 12.7 \cdot 10^5$ m^2/mol	$\omega_2 = 2.38 \cdot 10^5$ m^2/mol	$\alpha = 0.0$	$b = 1.95 \cdot 10^2$ m^3/mol	[26]
Triton X-100	Henry	$K = 4.39 \cdot 10^{-3}$ m				[26]
	Langmuir	$a_L = 6.6 \cdot 10^{-4}$ mol/m^3				[26]
	Frumkin	$\omega = 3.0 \cdot 10^5$ m^2/mol		$a = -4.5$	$b = 4.52 \cdot 10^4$ m^3/mol	[25]
	Reorientation	$\omega_1 = 4.0 \cdot 10^5$ m^2/mol	$\omega_2 = 9.6 \cdot 10^5$ m^2/mol	$\alpha = 4.5$ $a = 0.2$	$b = 8.43 \cdot 10^2$ m^3/mol	[25]
	Frumkin B	$\omega = 3.87 \cdot 10^5$ m^2/mol		$a = -0.48$	$b = 3.74 \cdot 10^3$ m^3/mol	[26]
	Reorientation B	$\omega_1 = 11.8 \cdot 10^5$ m^2/mol	$\omega_2 = 3.96 \cdot 10^5$ m^2/mol	$\alpha = 0.2$	$b = 2.39 \cdot 10^3$ m^3/mol	[26]

Table 5.2: Initial surfactant concentrations and properties for fast sorption models.

Surfactant	D in m^2/s	c_∞^Σ in mol/m^2	c_0 in mol/m^3
C_{12}DMPO	$5 \cdot 10^{-10}$	$4.17 \cdot 10^{-6}$	$c_0 = 8.0 \cdot 10^{-3}$
Triton X-100	$2.9 \cdot 10^{-10}$	$2.9 \cdot 10^{-6}$	$c_0^1 = 4.4 \cdot 10^{-4}$ $c_0^2 = 2.0 \cdot 10^{-3}$

To test the slow sorption model library, 1-Penthanol and n-Hexanol are selected. Note that 1-Penthanol is known to have a high desorption coefficient in comparison to the adsorption coefficient and to the desorption coefficient of other surface active agents. For both surfactants, Henry and Langmuir slow sorption models are considered. The model parameters are listed in table 5.3.

Table 5.3: Surfactant properties for slow sorption models.

Surfactant	**Model**	**Parameters**		**Source**
1-Penthanol	Henry	$K_H = 4.8 \cdot 10^{-7}$ m		[13, 48]
	Langmuir	$k_{\text{ads}} = 5.5 \cdot 10^{-5}$ m/s	$k_{\text{de}} = 6.9 \cdot 10^{-4}$ mol/(m^2/s)	
n-Hexanol	Henry	$K_H = 1.62 \cdot 10^{-6}$ m		[13, 48]
	Langmuir	$k_{\text{ads}} = 1.6 \cdot 10^{-4}$ m/s	$k_{\text{de}} = 5.9 \cdot 10^{-4}$ mol/(m^2/s)	

The respective initial surfactant concentrations, saturated surface concentrations and bulk diffusivities are reported in table 5.4. The initial concentrations have been chosen according to

the ones used in the experimental works for rising bubbles by Tagawa et al. [83] for 1-Penthanol and by Krzan et al. [54] for n-Hexanol.

Table 5.4: Initial surfactant concentrations and properties for slow sorption models.

Surfactant	D in m^2/s	c_∞^Σ in mol/m^2	c_0 in mol/m^3
1-Penthanol	$5.2 \cdot 10^{-10}$	$6.0 \cdot 10^{-6}$	$c_0^1 = 0.28$ $c_0^2 = 1.8$ $c_0^3 = 11.0$ $c_0^4 = 22.0$
n-Hexanol	$5.2 \cdot 10^{-10}$	$6.0 \cdot 10^{-6}$	$c_0^1 = 0.2$ $c_0^2 = 0.4$ $c_0^3 = 0.7$ $c_0^4 = 2.0$

5.2 Verification test results

In this section, the results of the verification test case are reported in terms of bubble rise velocities.

5.2.1 Verification of fast sorption models

5.2.1.1 C_{12}DMPO

First of all, the results in figure 5.1 show that all the sorption models are providing reasonable rise velocity profiles (three-stage process, see section 6.1.1). Moreover, the simulation results for the cases with and without SGS modelling are in very good agreement. For the case depicted in figure 5.1, Henry and Frumkin models provides very similar results. The rise velocities resulting from the application of the Langmuir model are very close to the ones from Henry and Frumkin, a difference can be seen only in the deceleration phase (up to 1.8 % smaller than the rise velocity with Frumkin model). The results obtained with the reorientation model show a similar profile to the others, but with a smaller rise velocity (up to 7 % smaller) during almost all the transient, i.e. 0.03 s $\leq t \leq$ 0.2 s. Whether the surfactant behaviour is better described by one model rather than the other must be validated against experiments. As it is known from the literature, C_{12}DMPO is well described both by Langmuir and Frumkin isotherms.

5.2.1.2 Triton X-100

For Triton X-100 two different initial concentrations are considered. For clarity, in figure 5.2 only the results without the SGS model and the two initial concentrations are reported. For Frumkin and reorientation models two sets of model parameters found in literature have been tested. For the smallest initial concentration, c_0^1, the rise velocity profiles coincide, apart from the velocity obtained with the Frumkin model (black dotted line). More differences among the various models are visible for the higher initial concentration, c_0^2. For c_0^2 the results for *Frumkin B* (blue dotted line) are much closer to the results for the other models than the results with Frumkin parameters (red dotted line.) Also for this case, experiments must suggest which model describes the surfactant effects the best.

For completeness, the same cases have been run employing the SGS model and the results have been compared to the linear case. In all the cases, the SGS model provides results being in agreement with the finest grid results, thus those plots are not shown here.

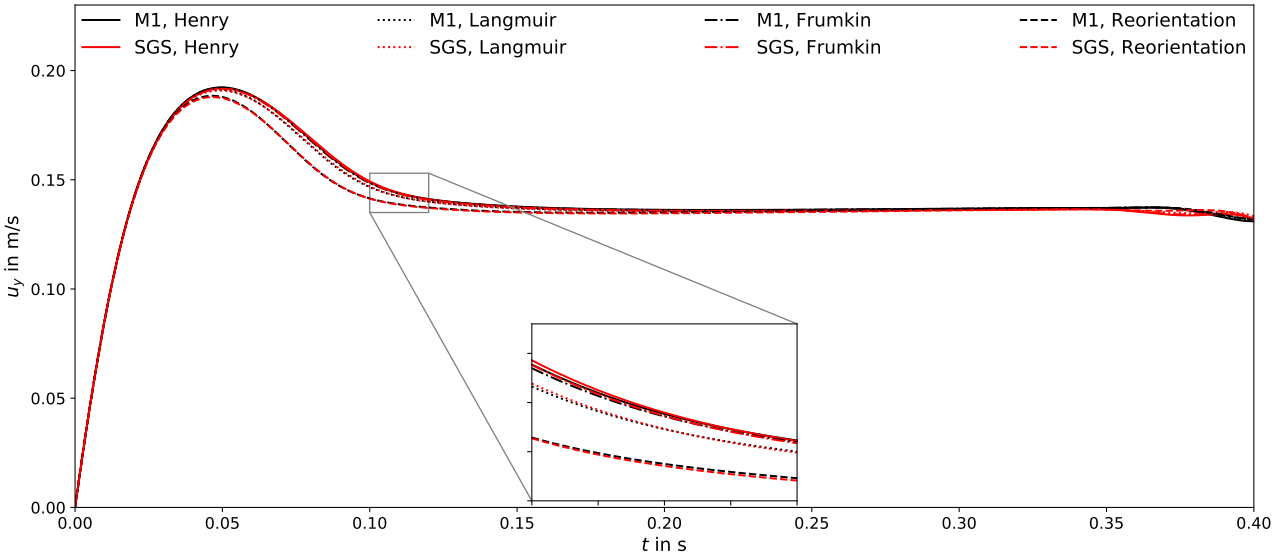

Figure 5.1: Bubble rise velocities for different fast sorption models; surfactant: C_{12}DMPO.

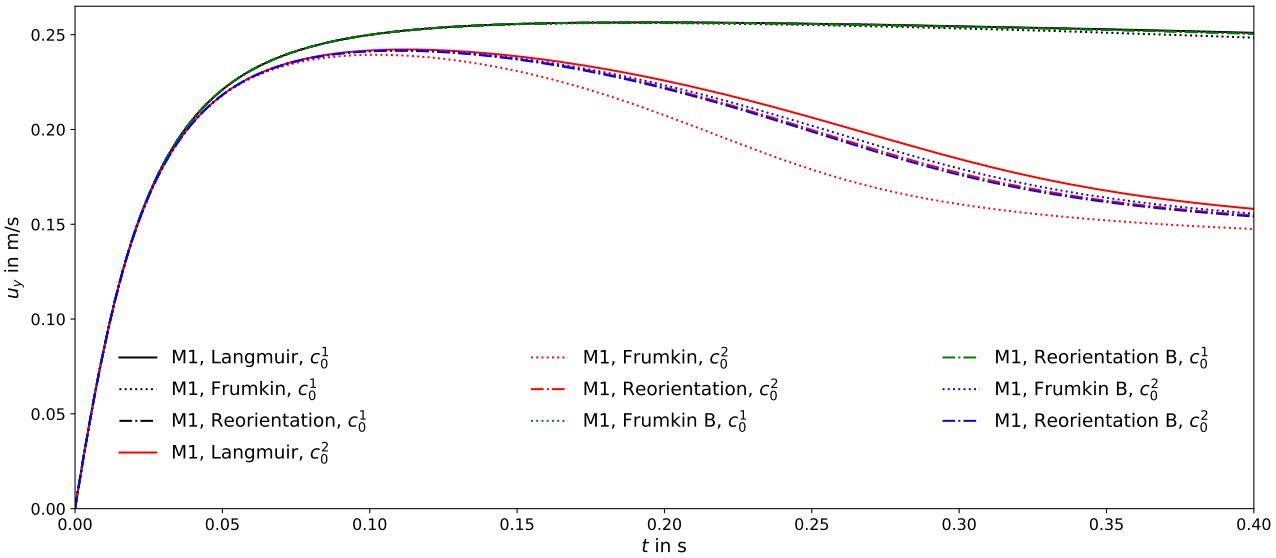

Figure 5.2: Bubble rise velocities for different fast sorption models and initial surfactant concentrations (without SGS modelling); surfactant: Triton X-100.

5.2.2 Verification of slow sorption models

For the slow sorption models, an SGS model is not available yet, thus the grid resolution has to be high enough to fully resolve the surfactant transport close to the interface. To be sure that the results are mesh independent, the simulations are run for two mesh resolutions and

the results are compared in figures 5.3 and 5.4. As can be seen from the plots, considering the same case but computed on different meshes (M1 with $\ell = 1\mu$m and M2 with $\ell = 2\mu$m in the legends), the results are almost the same. Thus, all the cases can be considered mesh convergent.

5.2.2.1 1-Penthanol

Consider the results for 1-Penthanol in figure 5.3. For all the initial surfactant concentrations, Henry and Langmuir models provide very similar results; the maximum deviation has been computed and it does not exceed 0.6%. Possibly, major differences between the two models may be seen in later time steps, but this is out of the scope of this verification test case.

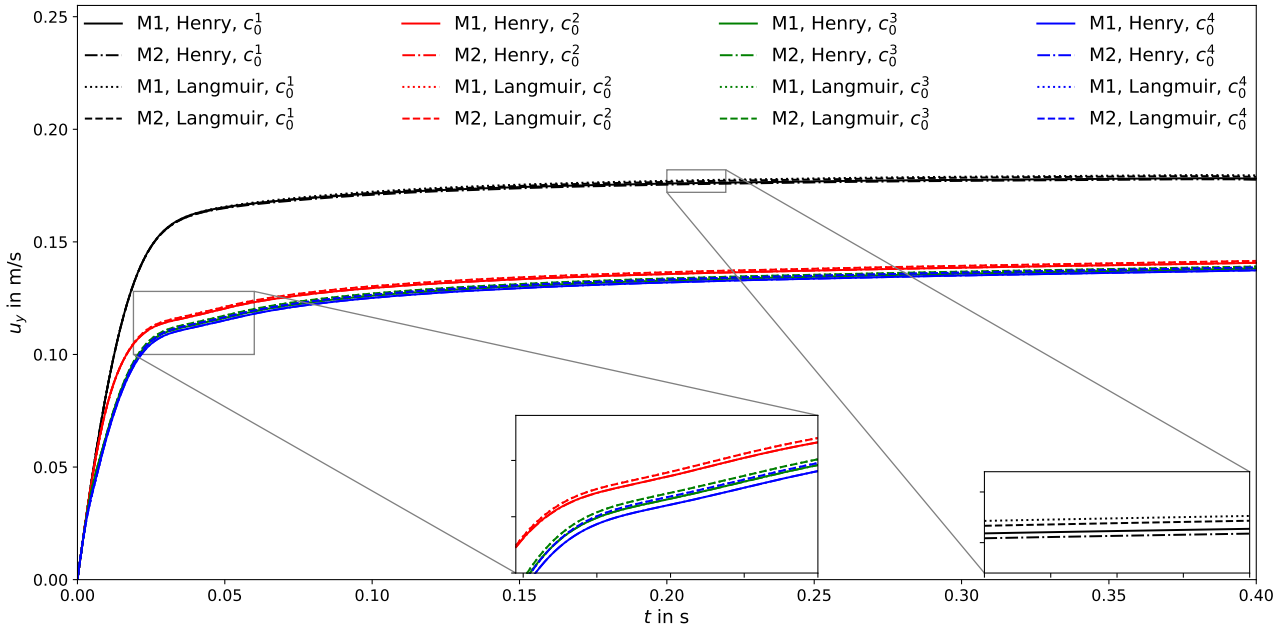

Figure 5.3: Bubble rise velocities for different slow sorption models and initial surfactant concentrations; surfactant: 1-Penthanol.

5.2.2.2 n-Hexanol

Also for n-Hexanol, Henry and Langmuir slow sorption models give almost the same results; see figure 5.4. In this case, the maximum deviation is approximately 0.8%. Thus, it can be concluded that both model are valid, at least for the time range (during which only adsorption occurred) and the concentrations considered.
In addition, the simulation for c_0^1 of n-Hexanol is performed also with the fast Langmuir model. The Langmuir constant has been taken equal to $a_L = k_{\text{de}}/k_{\text{ads}} = 3.7$ mol/m^3. The comparison in terms of rise velocity shows that there is only a relatively small difference in the velocity peak (6.25 %), but the terminal rise velocity is the same. This result should advice to perform a careful testing and comparison with available experimental results to choose the best fitting adsorption model.

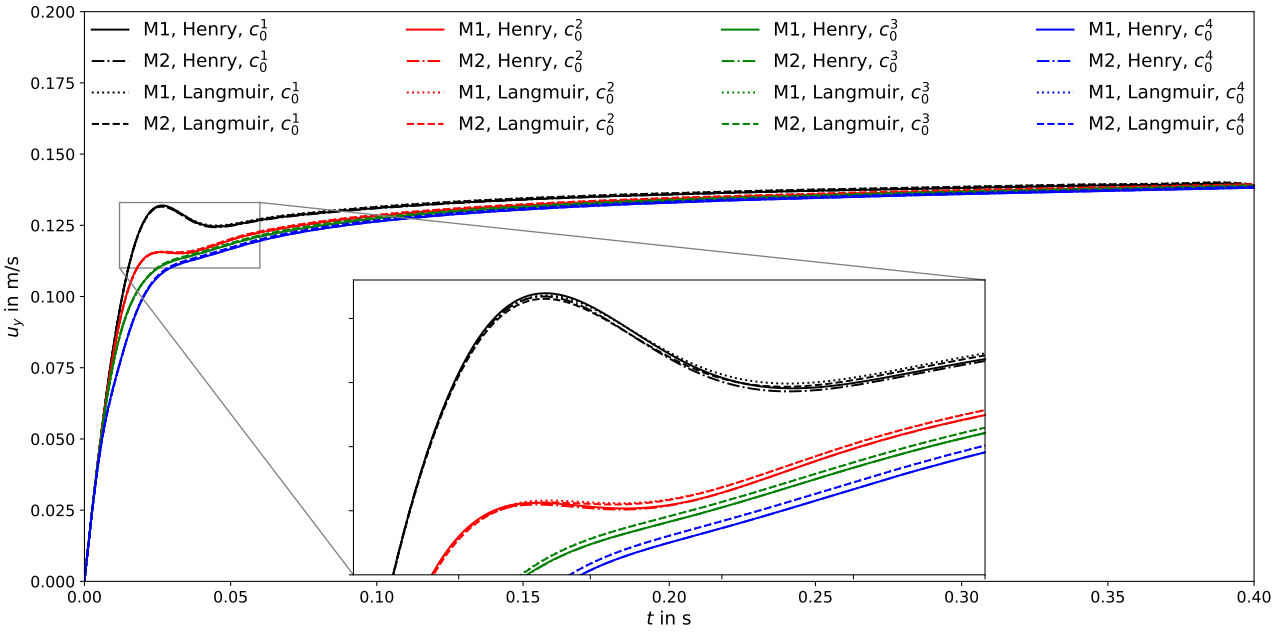

Figure 5.4: Bubble rise velocities for different slow sorption models and initial surfactant concentrations; surfactant: n-Hexanol.

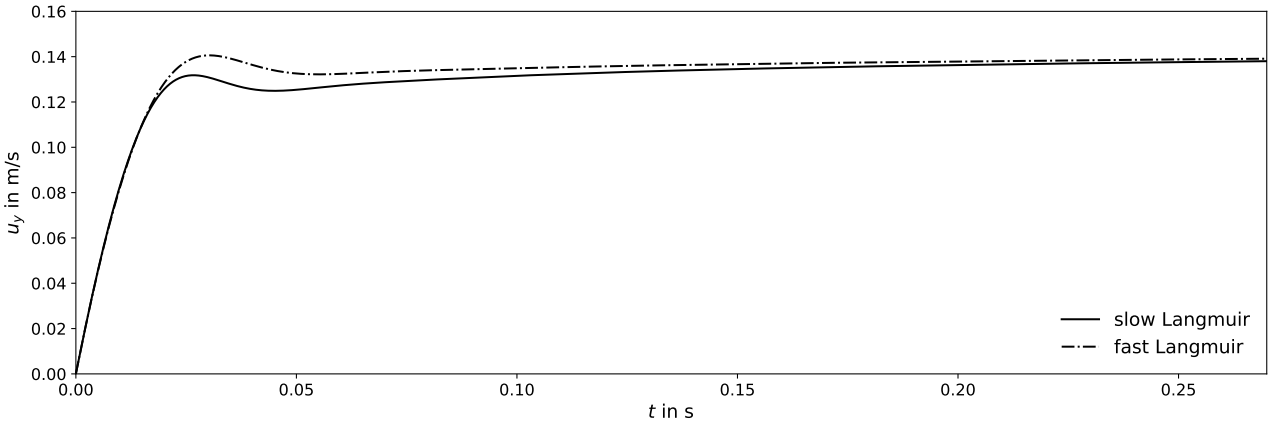

Figure 5.5: Bubble rise velocities with slow and fast sorption models. Surfactant: n-Hexanol, initial surfactant concentrations c_0^1. Test performed on mesh 2.

To conclude, this study has shown that all the implemented models in the sorption library provide reasonable and, most of the time, similar results. Nevertheless, a thorough quantitative study comparing to experimental results is necessary to choose the best model for the surfactant species under investigation.
Another issue that this study highlights is the necessity to understand better when a surfactant follows a slow or a fast sorption mechanism.

Chapter 6

Results and discussion

6.1 Rising bubble under the effects of surfactants

A single air bubble rising in aqueous solution contaminated by surfactant is considered. For this prototypical problem, a direct comparison with experimental results is possible. The experimental data and a short description of the corresponding set-up can be found in [72]. More details on the experimental set-up are presented in [54, 55]. Briefly, a digital camera was used to record the bubble motion at various distances from the orifice. Four to eight images of the bubble were obtained for each camera position, illuminating the region of interest with a strobe frequency from 100 to 200 Hz. The highest frequency was used for the initial acceleration stage. From the distances between the subsequent positions of the bubble and knowing the strobe frequency, the local bubble velocity was computed. The measurement at each camera position was performed at least three times from which mean local velocity values were calculated.

6.1.1 Simulations set-up

The simulation set-up corresponds to the one described in section 4.2.1. The material properties used in the simulations are reported in the tables 6.1 and 6.2. The bubble diameter is $d_B = 1.45$ mm. The initial shape of the bubble is a sphere positioned in the center of a spherical domain with a radius of twenty times the bubble radius. The initial velocity of the bubble is set to zero.
A constant time step $\Delta t \approx 10^{-6}$ s is chosen to fulfil the criterion for the interface numerical stability reported in section 3.2.4, equation (3.23) from [91]. The surfactant used in the experiments is the non-ionic C_{12}DMPO, whose molecular structure is depicted in figure 1.1. Its sorption process is modelled via the fast Langmuir sorption model. To model the surfactant transport in the bulk phase in the vicinity of the interface, the SGS model described in section 3.3 is used. The experimental data for the clean case and contaminated cases with different initial surfactant concentrations are considered as a reference.

Table 6.1: Fluid properties.

ρ^+ kg/m^3	μ^+ kg/(ms)	ρ^- kg/m^3	μ^- kg/(ms)	σ_0 N/m
997.3	$9.3 \cdot 10^{-4}$	1.1965	$1.83 \cdot 10^{-5}$	0.0724

Table 6.2: Surfactant (C_{12}DMPO) properties, fast Langmuir adsorption model parameters.

c_∞^Σ mol/m^2	a_L mol/m^3	D m^2/s	D^Σ m^2/s	T K
$4.17 \cdot 10^{-6}$	$4.85 \cdot 10^{-3}$	$5 \cdot 10^{-10}$	$5 \cdot 10^{-7}$	296

As for the case set-up in section 4.6.1, the surface diffusivity D^Σ is only an estimate since it is currently not possible to accurately measure it.
The experimental results from [72] are given in figure 6.1, and they will be the base for the discussion of the simulation results. According to [72], the average accuracy of the experimental data (rise velocity) is ±5%. Eight different initial concentrations in the liquid phase[1] are considered, covering a range that spans from $c_0^1 = 5 \cdot 10^{-4}$ mol/m^3 to $c_0^8 = 5 \cdot 10^{-2}$ mol/m^3. To these initial surfactant concentrations correspond the Marangoni numbers Ma reported in table 6.3, which express the ratio between surface tension and viscous forces. The Marangoni number here is defined as

$$\mathrm{Ma} = \frac{RTc_\infty^\Sigma}{\mu^+ u_y^{\max}}, \tag{6.1}$$

where $u_y^{\max}$ is the peak rise velocity reached by the bubble. Moreover, the respective surface equilibrium concentrations computed from the Langmuir isotherm (2.41) can be found in table 6.4.

Table 6.3: Marangoni number for the various initial surfactant concentrations.

Case	c_0 mol/m^3	$u_y^{\max}$ m/s	Ma
1	$5 \cdot 10^{-4}$	0.344	32
2	$1 \cdot 10^{-3}$	0.348	32
3	$2 \cdot 10^{-3}$	0.330	34
4	$5 \cdot 10^{-3}$	0.262	42
5	$8 \cdot 10^{-3}$	0.208	53
6	$1 \cdot 10^{-2}$	0.174	63
7	$2 \cdot 10^{-2}$	0.165	67
8	$5 \cdot 10^{-2}$	0.177	62

In figure 6.1, the well-known velocity profile of rising bubbles under the effects of surfactants can be observed. The bubble rising in clean water (black crosses), thus with a fully mobile surface, after an initial acceleration reaches a constant velocity that is the terminal velocity. The same can be observed for bubbles rising in highly contaminated solutions (yellow diamonds, azure stars and orange triangles). After an initial acceleration, the bubble velocity reaches a constant value, although it is much lower than the velocity for a mobile interface. At intermediate concentrations (between $5 \cdot 10^{-4}$ and $8 \cdot 10^{-3}$ mol/m^3) there is still an acceleration phase, but after reaching the peak velocity the bubble decelerates. The bubbles keep decelerating until they reach a quasi-steady terminal velocity which is similar to the case with very high contamination. In applications involving bubbly flows, it is fundamental to correctly reproduce the initial transient stage of the bubble rise, because it determines the overall contact time, the position and the velocity of the bubble and perhaps also how it will interact with other

[1] The surfactant concentration in the gas phase is set to zero.

bubbles. Moreover, these quantities affects the mass transfer from the bubble into the liquid phase. Thus in sections 6.1.2, 6.1.3 and 6.1.4 the attention is focused on whether the transient velocity profiles are correctly reproduced.
The simulation results for the clean case have already been compared to the experimental ones in [72] showing a very good agreement. These results are reproduced in section 6.1.5.2 with additional information about the bubble path.

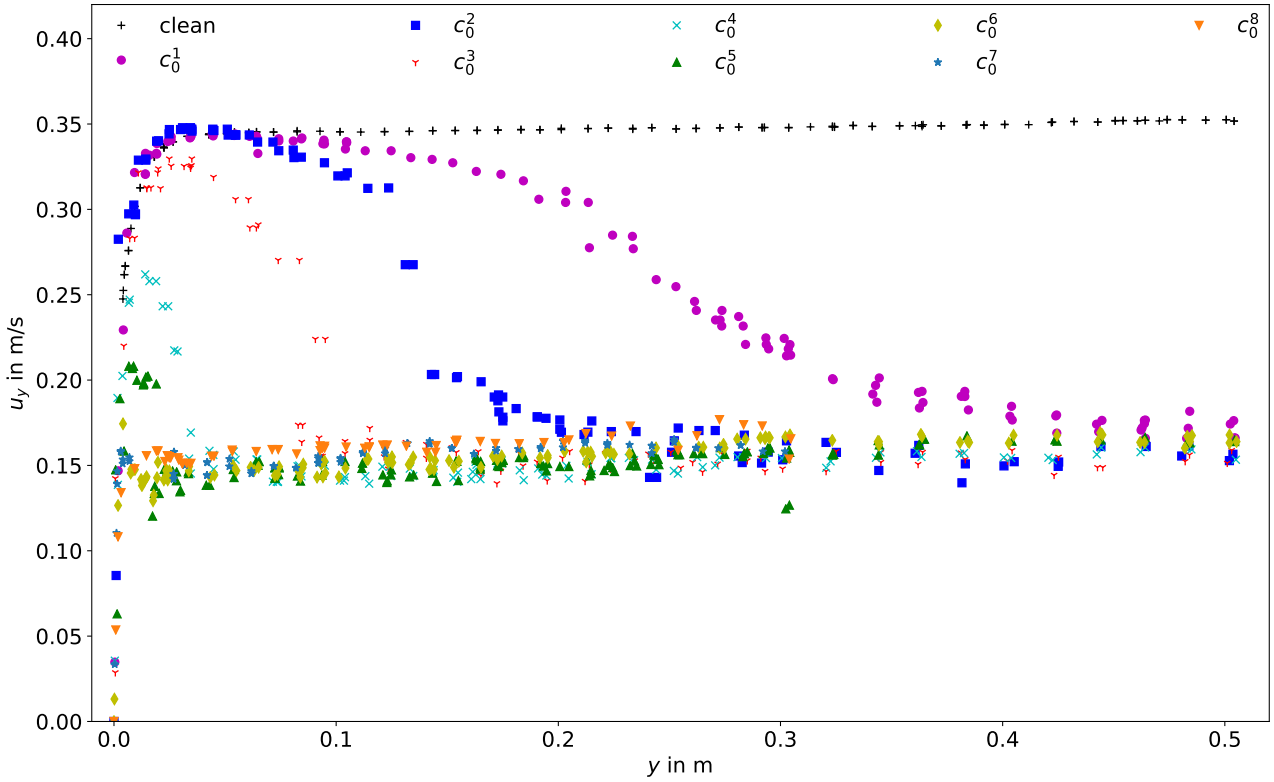

Figure 6.1: Experimental bubble center velocities in rise direction y. Data from [72].

6.1.2 Effect of under-resolved species boundary layers

The surfactant transport problem is a typical case with highly non-linear concentration profiles at the interface in a very thin boundary layer. Thus a standard linear interpolation from the cell centres to the face centres leads to over- or underestimated diffusive and convective fluxes normal to the interface, resulting in an unphysically thick boundary layer. Only thanks to the application of the SGS model described in section 3.3 it becomes possible to study cases with real diffusion coefficients for the surfactant in the liquid phase. The usage of physical diffusivities is imperative to get the correct transient velocity since it is not only affecting the surfactant bulk transport but also the sorption mechanism itself, as described in section 3.2.3 and in [72]. A comparison between the standard interpolation and the flux correction by the SGS model is given in figure 6.2. The results there refer to an intermediate surfactant bulk concentration $c_0^5 = 8 \cdot 10^{-3}$ mol/m^3. The first set of simulations is run without SGS modelling to test the sensitivity to different diffusivities with a fixed mesh resolution (first cell thickness $l \approx 16$ μm). For a realistic diffusivity, the rise velocity is overpredicted; see figure 6.2. On

the other hand, increased diffusion coefficients result in thicker species boundary layers that can be resolved by this mesh, but at the same time they speed up the adsorption process and, consequently, the rise velocity approaches the steady state value too quickly.

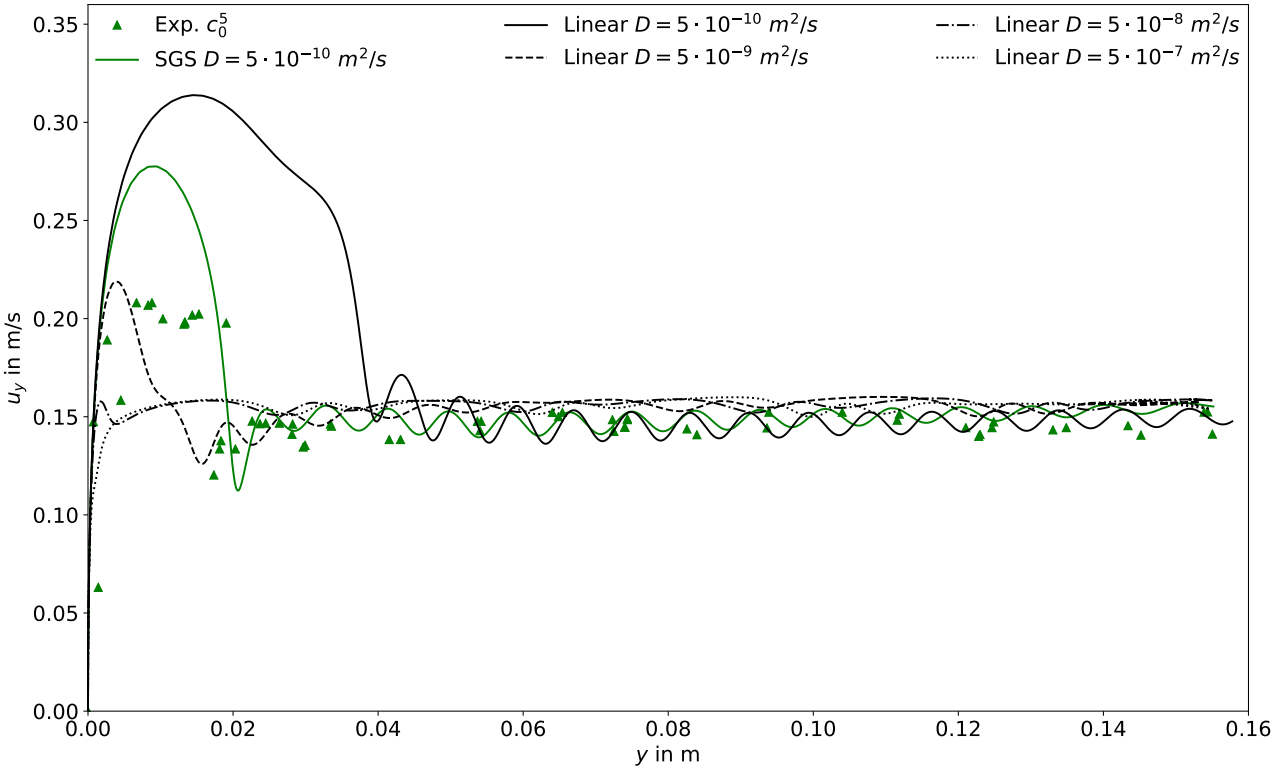

Figure 6.2: Comparison between simulations without (black lines) and with SGS model (coloured line) for $c_0 = 8 \cdot 10^{-3}$ mol/m^3; simulated time $t = 1$ s.

Figure 6.2 depicts also the velocity profile obtained with the SGS approach and the physical diffusivity. The initial transient velocity is reproduced much better, but the velocity peak is still overestimated. This difference can be explained considering the bubble formation and detachment time in the experiments. As it is known from experimental works, e.g. [55, 61, 92, 51], the initial transient velocity depends strongly on the time of bubble formation and release. During the bubble formation process, the newly generated bubble surface is exposed to the contaminated solution. Thus, when the bubble detaches from the capillary, its interface holds already a certain amount of surfactant. This relatively small (not above 10% of c_{eq}^{Σ}) initial surface contamination significantly influences the peak rise velocity. From the experiments, the adsorption time for a detaching bubble is known to be about 1.6 s. Hence, during this time there is a diffusion of surfactant towards the growing bubble surface. The surface coverage at release is a function of time and bulk surfactant concentration, and it can be estimated as

$$c_0^{\Sigma}(t) = \frac{1}{3}\left(2c_0\sqrt{\frac{3Dt}{7\pi}}\right), \tag{6.2}$$

a formula taken from [22, pp. 118-119]. A summary of the estimated surface coverages at detachment is reported in table 6.4. Within the used simulation set-up, different detachment times can be investigated varying the initial surfactant surface concentration.

Table 6.4: Initial surface coverage estimates at release time $t_{rel} = 1.6$ s with $D = 5 \cdot 10^{-10}$ m^2/s.

Case	c_0 mol/m^3	c^{Σ}_{eq} mol/m^2	$c^{\Sigma}_0(t_{rel})$ mol/m^2	% $c^{\Sigma}_{\mathrm{eq},i}$
1	$5 \cdot 10^{-4}$	$3.90 \cdot 10^{-7}$	$3.48 \cdot 10^{-9}$	0.89
2	$1 \cdot 10^{-3}$	$7.13 \cdot 10^{-7}$	$6.97 \cdot 10^{-9}$	0.98
3	$2 \cdot 10^{-3}$	$1.22 \cdot 10^{-6}$	$1.39 \cdot 10^{-8}$	1.14
4	$5 \cdot 10^{-3}$	$2.12 \cdot 10^{-6}$	$3.48 \cdot 10^{-8}$	1.65
5	$8 \cdot 10^{-3}$	$2.60 \cdot 10^{-6}$	$5.57 \cdot 10^{-8}$	2.15
6	$1 \cdot 10^{-2}$	$2.81 \cdot 10^{-6}$	$6.97 \cdot 10^{-8}$	2.48
7	$2 \cdot 10^{-2}$	$3.36 \cdot 10^{-6}$	$1.39 \cdot 10^{-7}$	4.25
8	$5 \cdot 10^{-2}$	$3.80 \cdot 10^{-6}$	$3.48 \cdot 10^{-7}$	9.16

Before presenting the parameter study on the initial surface coverage, a mesh sensitivity study of the full problem with SGS modelling is necessary. Note that for the simulations corresponding to figures 6.2 and 6.3 the initial surface concentration was set to zero, $c^{\Sigma}(t = 0) = 0$ mol/m^2.

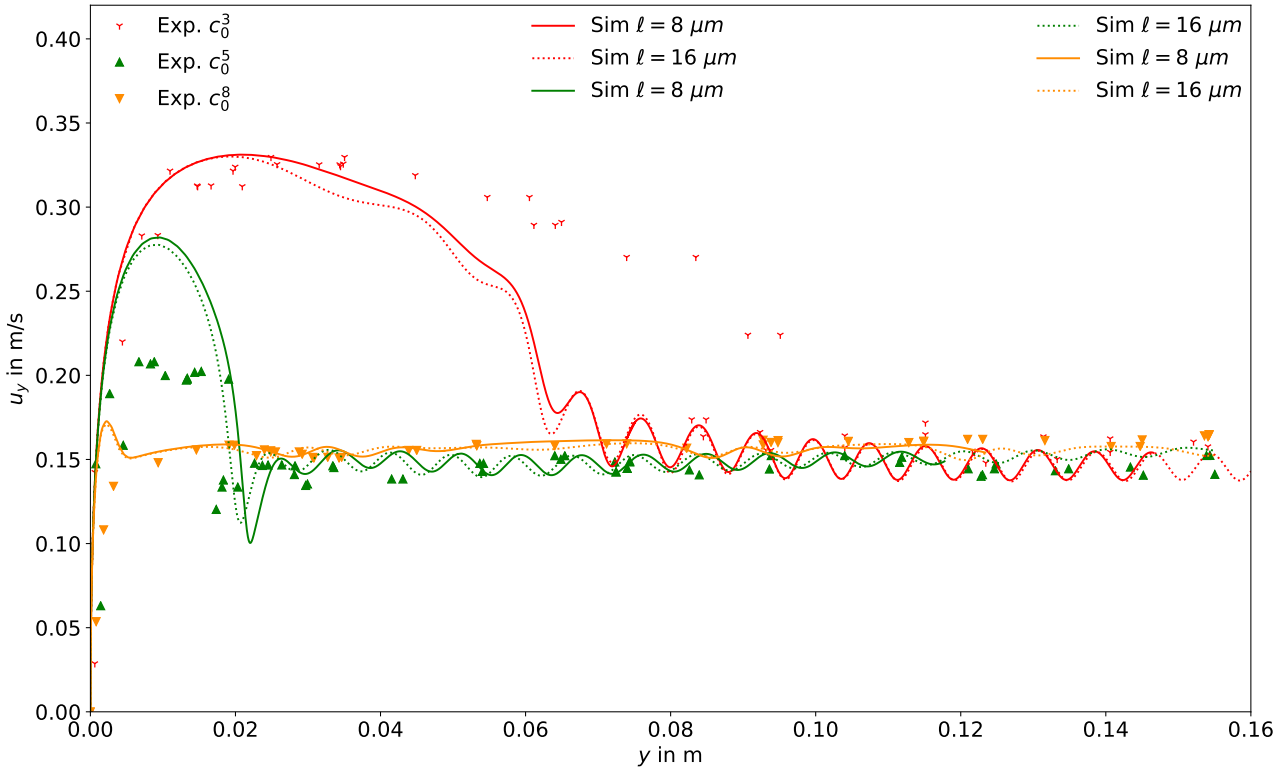

Figure 6.3: Rise velocity for three initial surfactant bulk concentrations. Results for two mesh resolutions (continuous lines - fine mesh; dotted lines - coarse mesh); simulated time up to $t = 0.6$ s.

6.1.3 Mesh sensitivity study

To study the dependence of the numerical results with respect to the mesh resolution, simulations with different initial bulk concentrations and zero initial surface coverage are performed

on two different meshes, a fine one ($\approx$ 320000 cells) with a first layer thickness of $\ell \approx 8$ μm and 3700 faces on the interface, and a coarser one ($\approx$ 160000 cells) with a first layer thickness of $\ell \approx 16$ μm and 2400 faces on the interface.
As can be noticed from figure 6.3, the biggest difference between fine and coarse mesh is encountered in the decelerating phase for the smallest initial bulk concentration. For higher c_0, the bubble rises slower, thus the Reynolds number is smaller and, consequently, the hydrodynamic boundary layer thicker. A thicker hydrodynamic boundary layer is then well resolved by a coarser mesh, too. Even though there is a small difference between the coarse and the fine mesh results, for the simulations that are reported below it has been decided to use where possible (e.g. higher contamination) the coarser mesh because of the required computational time. For the least contaminated bubbles, the finest mesh is chosen to get a higher accuracy for the deceleration phase and path approximations. The fine and coarse cases ran in parallel (MPI) on three and eight cores, respectively, with the interface (liquid side) and its counterpart (gas side) on the same processor. A study on the mesh decomposition and its performances has been conducted within the master thesis by M. Steinhausen [81, chapter 4], where two domain decomposition techniques have been compared: manual and scotch decomposition, showing the pros and contra of the two methods for the rising bubble cases. The runtime comparison with respect to the number of cells per processor has been performed, too, suggesting important guidelines for the domain decomposition. The computations took between thirty and forty days to reach at least 1 s of simulated physical time.

6.1.4 Initial surface coverage

6.1.4.1 Parameter study on the initial surface coverage

The detachment time is varied via pre-contaminating the bubble surface, while the initial shape deformation at detachment is neglected. Since equation (6.2) provides only an estimate of the initial surface coverage at release, it was found appropriate to conduct a parameter study varying c_0^Σ for the different bulk concentrations to obtain a more precise value of the initial surface contamination. In figure 6.4, the results of this parameter study for three selected initial concentrations ($c_0^3,\ c_0^5,\ c_0^8$) are presented.
Figure 6.4a shows that for a small initial bulk surfactant concentration, the surface coverage at detachment must have been almost zero (estimated value $\approx 1\%\ c_{\mathrm{eq},3}^\Sigma$), since the simulation results for $c_0^\Sigma = 0$ mol/m^2 are the closest to the experimental ones. After reaching the peak velocity, the bubble starts to decelerate until the rise velocity oscillates around its steady-state value. The most noticeable difference between the experimental and the numerical results for the case in figure 6.4a is that in the simulation, the bubble decelerates sooner than in the experiments. This discrepancy can result from small perturbations occurring at different times for simulations and experiments. In fact, the case studied is strongly sensitive to the onset of path instability. Perturbations triggering path instabilities are caused by different mechanisms in experiments and simulations. In experiments, perturbations could result for instance from initial shape deformations. In numerical simulations, such perturbations can be numerical errors which are highly dependent on the mesh topology. Moreover, the discrepancy between experiments and simulations is only more pronounced for the least contaminated case which is also the case with the highest oscillations in the experimental data; see figure 6.14a and table 6.7. For intermediate and high initial surfactant bulk concentrations, the presence of initial surface contamination is evident; see figures 6.4b and 6.4c. The higher the initial bulk

concentration, the more contaminated the bubble surface at release and the lower the velocity peaks. Figure 6.4b shows that the best agreement between numerical and experimental results is obtained with an initial contamination of approximately 2% $c^{\Sigma}_{eq,5}$ which is in agreement with the estimated value in table 6.4. For the highest initial bulk concentration, see figure 6.4c, the velocity peak disappears for $c^{\Sigma}_0 > 4\%\ c^{\Sigma}_{eq,8}$. A very good agreement with the experimental results is found for $c^{\Sigma}_0 \approx 10\%\ c^{\Sigma}_{eq,8}$, that is approximately the value predicted by equation (6.2). With a further increase of the initial surface contamination, the rise velocity profile does almost not change any longer.
It is also interesting to note from figure 6.4 that after the initial transition period, all the bubble rise velocity values present small amplitude oscillations around a similar mean velocity value.

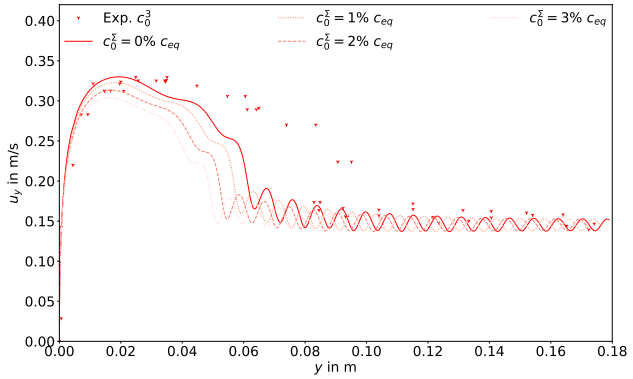

(a) $c_0 = 2 \cdot 10^{-3}$ mol/m^3.

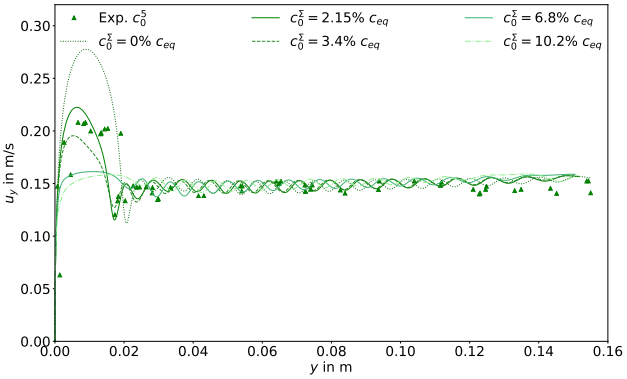

(b) $c_0 = 8 \cdot 10^{-3}$ mol/m^3.

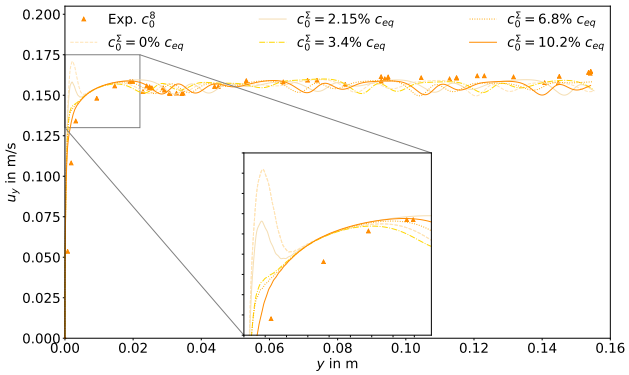

(c) $c_0 = 5 \cdot 10^{-2}$ mol/m^3.

Figure 6.4: Study on the effects of the initial surface coverage on the rise velocity; simulated time $t = 1$ s.

6.1.4.2 Effects of the initial surface coverage on bubble shape and path

In this section, the effects of the detachment time, or better the initial surface coverage for the simulations, are investigated in terms of bubble shapes and paths. Consider an intermediate initial bulk concentration, $c^5_0 = 8 \cdot 10^{-3}$ mol/m^3, that is the case shown in figure 6.4b. The velocity profiles for the different initial surface coverages are plotted again in figure 6.5 but over time. In figure 6.5, five time instances are marked where the bubble shape and the surface coverage are then compared and studied in figure 6.6. In figure 6.6, from the bottom to the top, the five bubbles are shown in their rise at the selected time instances (every column shows

one of the bubbles rising), while from left to right the initial surface concentration increases (see the surface coverage at $t = 0$ s). The bubble surfaces are coloured by the local surfactant surface concentration.

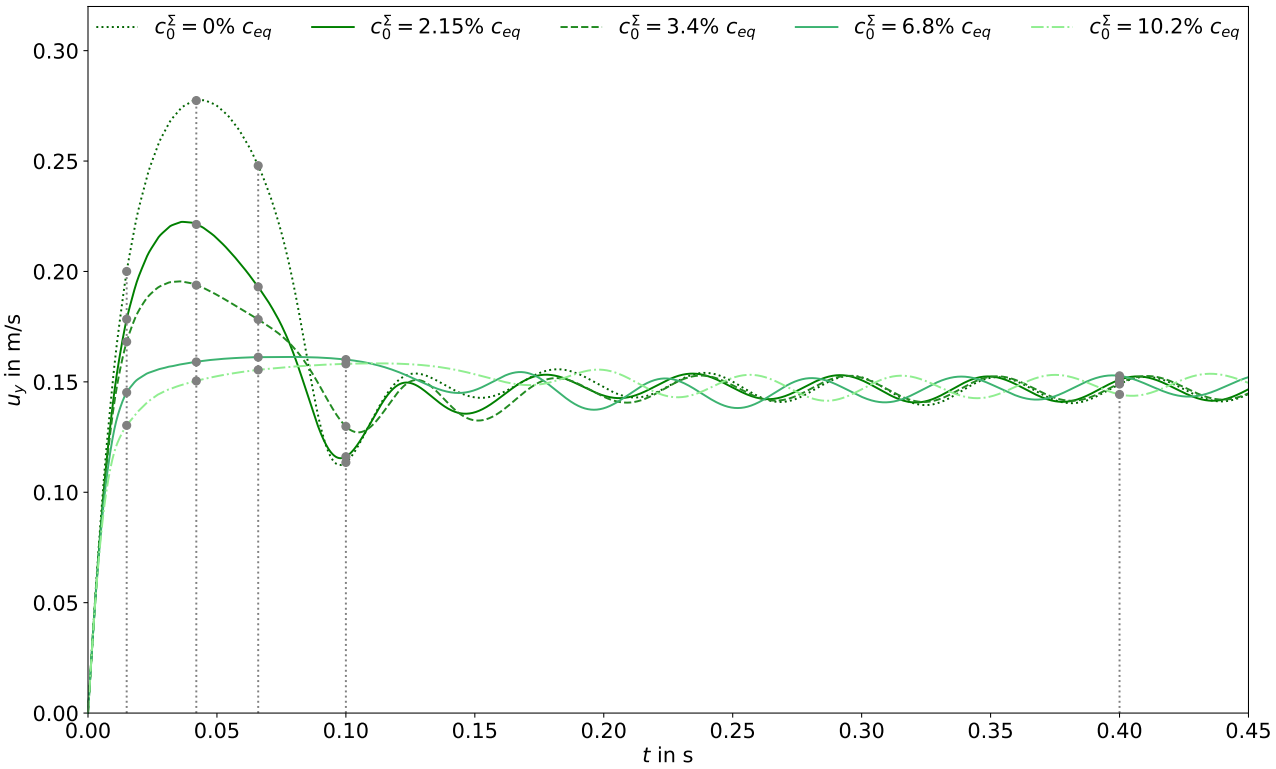

Figure 6.5: Influence of the detachment time for the initial bulk concentration $c_0 = 8 \cdot 10^{-3}$ mol/m^3.

From figure 6.5 and 6.6 it is clearly visible that increasing c_0^Σ results in a less deformed interface and a slower bubble. In fact, for $c_0^\Sigma = 0\% c_{eq}^\Sigma$, $2.15\% c_{eq}^\Sigma$ and $3.6\% c_{eq}^\Sigma$, respectively, the bubble surface is still deforming and reaches its maximum aspect ratio ($AR = 1.27,\ 1.1,\ 1.06$, respectively) with the peak velocity. During the deceleration phase the bubbles are going back to a more spherical shape; see $t = 0.066$ s. For the two cases on the right of figure 6.6 with the highest initial surface coverage, the amount of surfactant on the interface is high enough to result in an almost not deformed interface ($AR = 1.04$). These bubbles accelerate until reaching the quasi-steady state velocity and their shape remains spherical.
Consider the latest time ($t = 0.4$ s) in figure 6.6. The bubbles have a similar velocity, though, they do not have the same surface coverage. Moreover, with different c_0^Σ (and/or different initial bulk concentrations c_0, see figure 6.3) similar terminal velocities are obtained, but with a different final surface coverage that is not yet the equilibrium value, c_{eq}^Σ, and not even close to it. To confirm this, figure 6.7 shows the total amount of surfactant on the interface with respect to time. Here it can be seen that even at $t = 1$ s the total amount of surfactant on the interface is less than 30% of the equilibrium value. For the smallest initial surface concentration, the total amount of surfactant on the interface grows more rapidly than in the other cases. This behaviour can be explained by the fact that Péclet and Reynolds numbers are higher for smaller c_0^Σ. Also, the concentration difference between bulk and interface is larger (for a given bulk concentration and varying the initial surface concentration). This results in stronger advec-

tive transport, thus thinner concentration boundary layers. Instead, from $t \approx 0.6$ s, when the bubbles have approximately the same terminal velocity, the total amount of surfactant on the interface grows similarly for each bubble.

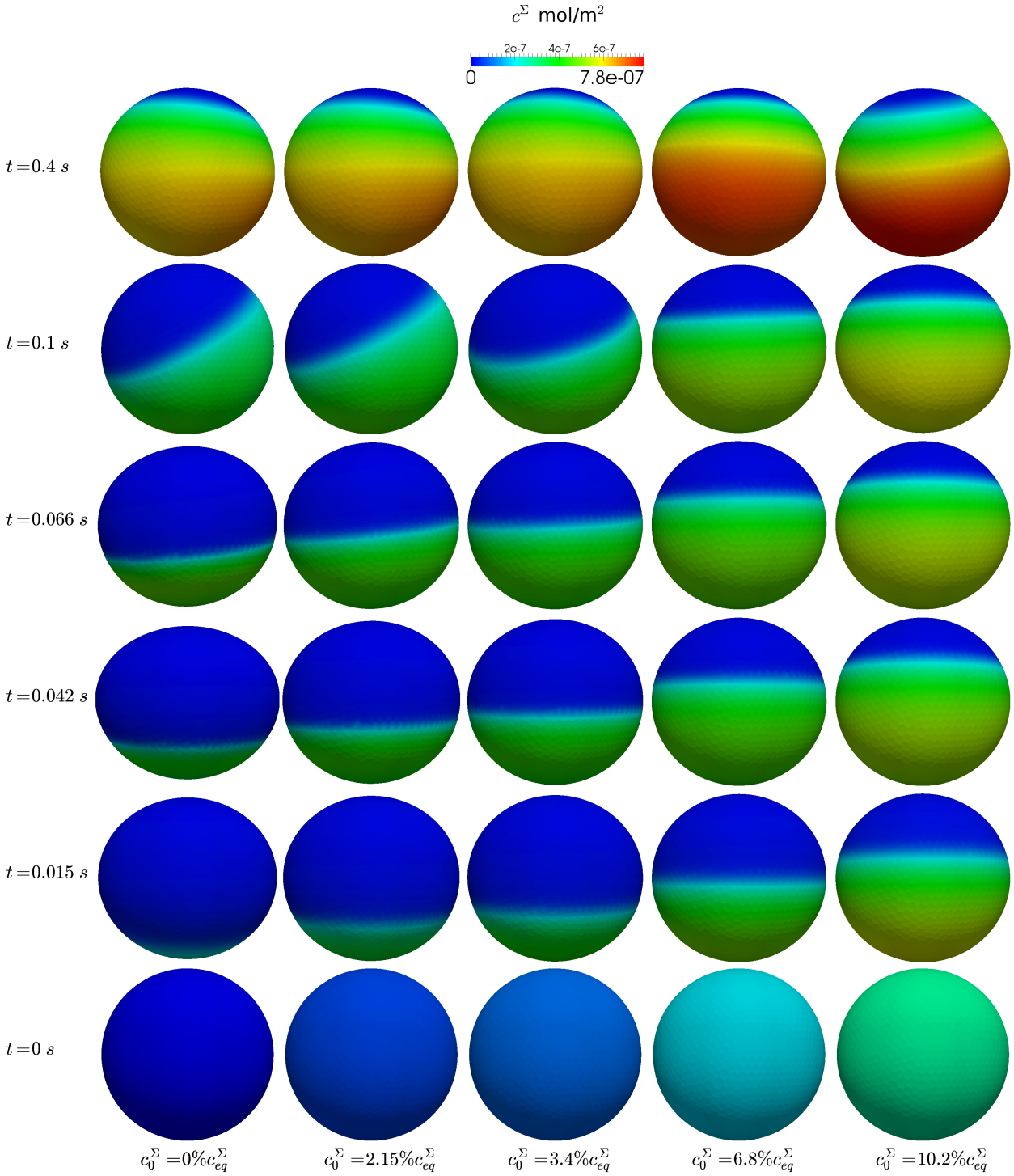

Figure 6.6: Influence of the detachment time on the bubble shape and local surface coverage for the initial bulk concentration $c_0 = 8 \cdot 10^{-3}$ mol/m^3. Figure reproduced from [73, figure 8] with permission of the copyright owner.

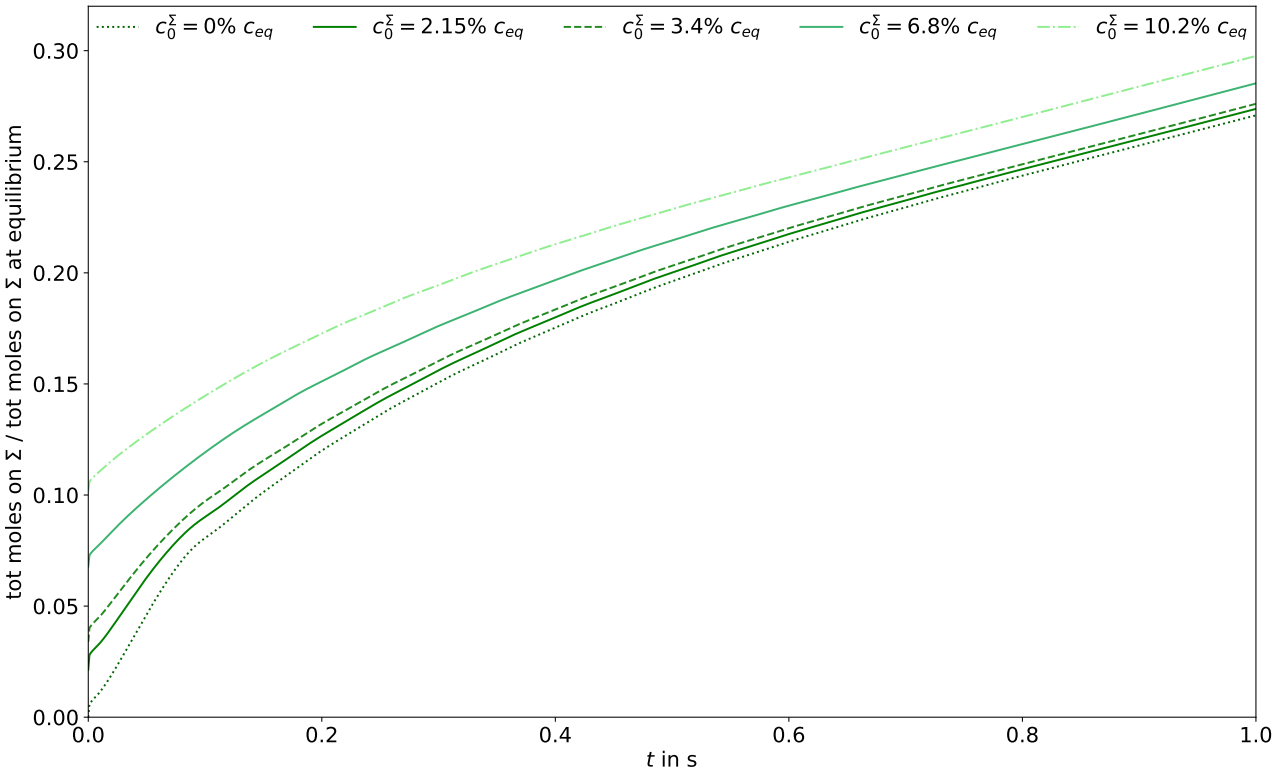

Figure 6.7: Influence of the detachment time on the total amount of surfactant on the interface divided by the respective equilibrium value for the initial bulk concentration $c_0 = 8 \cdot 10^{-3}$ mol/m^3.

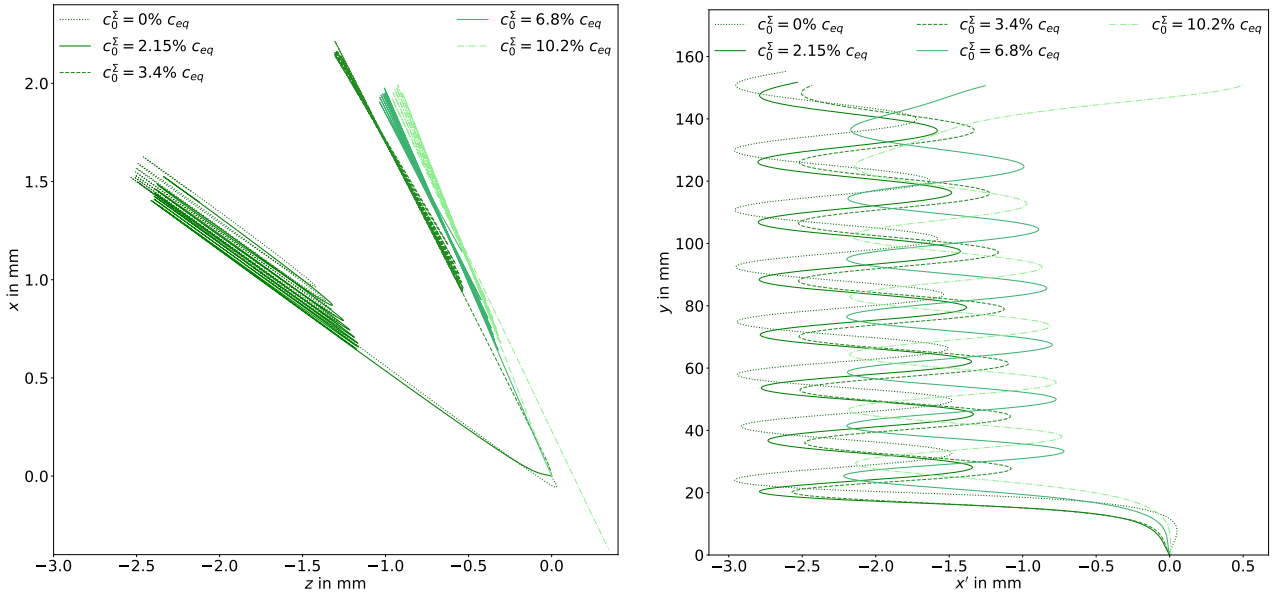

(a) *Top view of the bubble path.*

(b) *Lateral view of the bubble path.*

Figure 6.8: Effects of the initial surface coverage on the bubble path for the initial bulk concentration $c_0 = 8 \cdot 10^{-3}$ mol/m^3.

The respective bubble paths are depicted in figure 6.8. From the top view in figure 6.8a it can be observed that all the bubbles follow a zig-zag path, but the onset of path instability occurs later for less contaminated surfaces, as shown by the path front view, figure 6.8b.

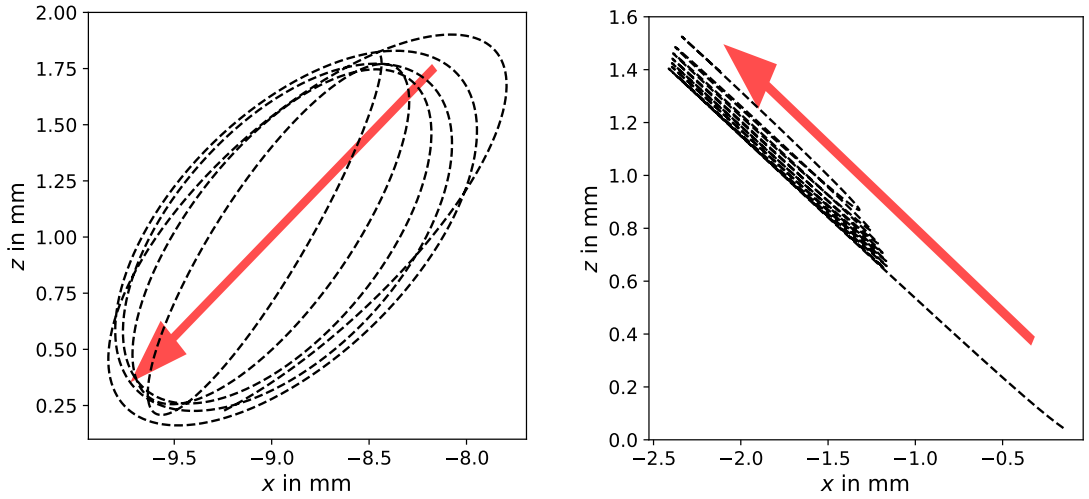

(a) *Spiral motion.*

(b) *Zigzag motion.*

Figure 6.9: Path top view and first principal component of the motion direction x' indicated by the red arrow.

In figure 6.8b, the path is reported with respect to the direction x' along which the motion occurs. This direction is computed with the aid of the principal component analysis (PCA) tool available in the Python library *scikit learn* [70]. The reader is refered to the documentation page of the PCA function [80] for more information. Loosely speaking, the bubble positions in the horizontal plane $x - z$ are given as inputs to the function. The PCA then uses the so-called *Singular Value Decomposition* to project the input data to a lower dimensional space. In the case of the bubble path, this lower dimensional space is the direction in which most of the motion occurs. For a better understanding, the figures in 6.9 show the bubble path from the top view and the orientation of the first principal component of the motion for two types of paths, spiral and zigzag.

Table 6.5: Initial surface coverage imposed at the beginning of the simulations based on the values given in table 6.4 and the parameter study reported in figure 6.4.

Case	c_0 mol/m^3	$c_0^{\Sigma}(t_{rel})$ mol/m^2	% $c_{\mathrm{eq},i}^{\Sigma}$
1	$5 \cdot 10^{-4}$	0.0	0.0
2	$1 \cdot 10^{-3}$	0.0	0.0
3	$2 \cdot 10^{-3}$	0.0	0.0
4	$5 \cdot 10^{-3}$	$4.15 \cdot 10^{-8}$	1.96
5	$8 \cdot 10^{-3}$	$5.57 \cdot 10^{-8}$	2.15
6	$1 \cdot 10^{-2}$	$8.63 \cdot 10^{-8}$	3.06
7	$2 \cdot 10^{-2}$	$1.22 \cdot 10^{-7}$	3.65
8	$5 \cdot 10^{-2}$	$3.48 \cdot 10^{-7}$	9.16

6.1.5 Initial bulk concentration

The simulation results with a certain initial contamination (see table 6.5) which agree best with the experimental ones are selected for the rest of the discussion and reported in figure 6.10. All the simulations run until reaching at least $t = 1$ s of physical time, thus the curves in figure 6.10 end at various vertical positions since they have different rise velocities.
In figure 6.10, also the estimated velocity from the correlation for fully contaminated systems proposed by Tomiyama in [88, equation (33)] is plotted. All the simulation results, including the least contaminated case, are in very good agreement with this estimated velocity at quasi-steady state.

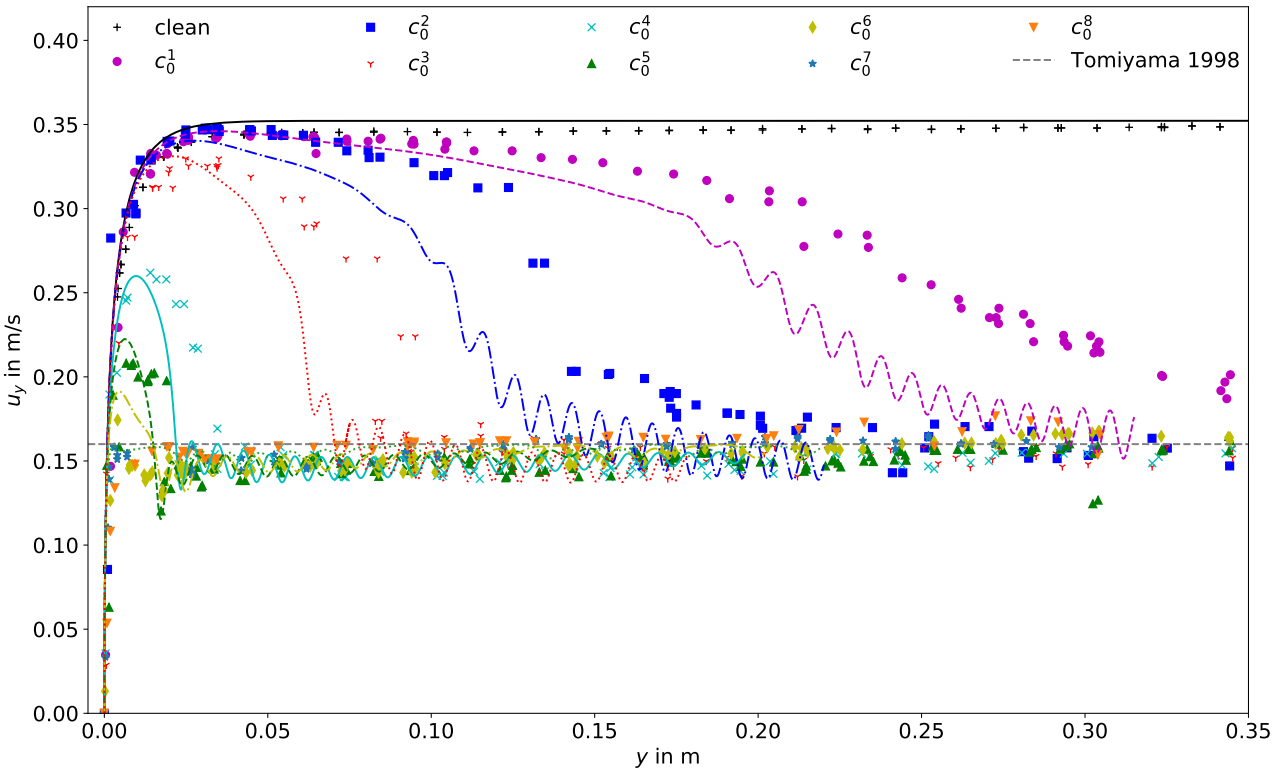

Figure 6.10: Bubble rise velocity, influence of the initial bulk concentration with pre-contaminated surface.

A further indicator of agreement between experimental and numerical results at quasi-steady state is the comparison of the standard deviation of the rise velocities within the range[2] $0.1 \text{ m} < y < 0.16 \text{ m}$. In fact, the numerical results show pronounced oscillations that are not clearly visible in the experiments. The values for the standard deviation reported in table 6.6 show a similar trend, i.e. oscillations decrease with increasing bulk concentration. The magnitude is in agreement between simulations and experiments, too. Note that the standard deviations for the first case are reported in gray because in the range considered the bubble has not fully reached the quasi-steady state, thus there could be some uncertainty in the data.

[2]For the initial concentrations c_0^1 and c_0^2 the considered ranges have been shifted to $0.29 \text{ m} < y < 0.32 \text{ m}$ and $0.15 \text{ m} < y < 0.2 \text{ m}$, respectively, when the bubbles are in the quasi-steady state.

Table 6.6: Standard deviation from the mean velocity value σ_v at quasi-steady state, 0.1 m $< y <$ 0.16 m.

Case	σ_v^{exp}	σ_v^{sim}
1	0.0131	0.0097
2	0.0105	0.0105
3	0.0068	0.0067
4	0.0032	0.0037
5	0.0045	0.0031
6	0.0031	0.0028
7	0.0037	0.0023
8	0.0022	0.0025

For completeness, also the frequency of the horizontal velocity and the vortex shedding from the rear part of a rigid sphere are computed as reported in [83] from [89] and [49], respectively, and compared to the simulation results; see table 6.7.

Table 6.7: Oscillation frequencies of the velocity components compared to the frequencies f and f_v reported in [83] from [89] and [49], respectively.

		Simulations				Correlations	
Case	$\overline{u}_b$ in m/s $0.1 \leq y \leq 0.16$	c_D	Re	f_{u_x,u_z}	f_{u_y}	f	f_v
1	0.168	0.296	393	8.91	20.09	7.145	16.662
2	0.151	0.790	241	9.97	19.34	8.988	10.205
3	0.146	0.885	228	9.30	18.83	9.230	9.639
4	0.148	0.861	230	8.87	17.23	9.171	9.774
5	0.152	0.815	237	8.69	17.42	9.054	10.046
6	0.156	0.780	242	8.28	17.17	8.962	10.266
7	0.157	0.773	244	8.16	15.06	8.942	10.316
8	0.155	0.789	241	7.24	10.47	8.985	10.212

The frequency of the bubble horizontal velocity is computed according to [89] as $f = \frac{u_b}{d_e} 0.1 c_D^{0.734}$, where u_b is the averaged quasi-steady velocity and d_e is the bubble equivalent diameter. The frequency of the vortex shedding from the rear part of a rigid sphere is $f_v = \frac{\omega \nu_l \text{Re}}{\pi d_e^2}$ (from [49]), where ω is taken equal to 0.30 as in [83, 49] and Re is computed based on u_b. The drag coefficient c_D is computed equating the drag to the buoyancy force as in [83] (equation 2.7 in the reference), thus $c_D = \frac{4 d_e g}{3 u_b^2}$, where g is the gravitational acceleration. From table 6.7 it can be seen that the oscillation frequencies of the vertical velocity are approximately twice the horizontal ones, as expected from [83, 65, 17]. Moreover, the intermediately contaminated cases (from c_0^2 to c_0^6) show a good agreement between the numerical and literature results. The least and the most contaminated cases are not relevant for this comparison since the velocity has not reached the quasi-steady state (c_0^1) or the oscillations are not as regular as the other cases ($c_0^7,\ c_0^8$).

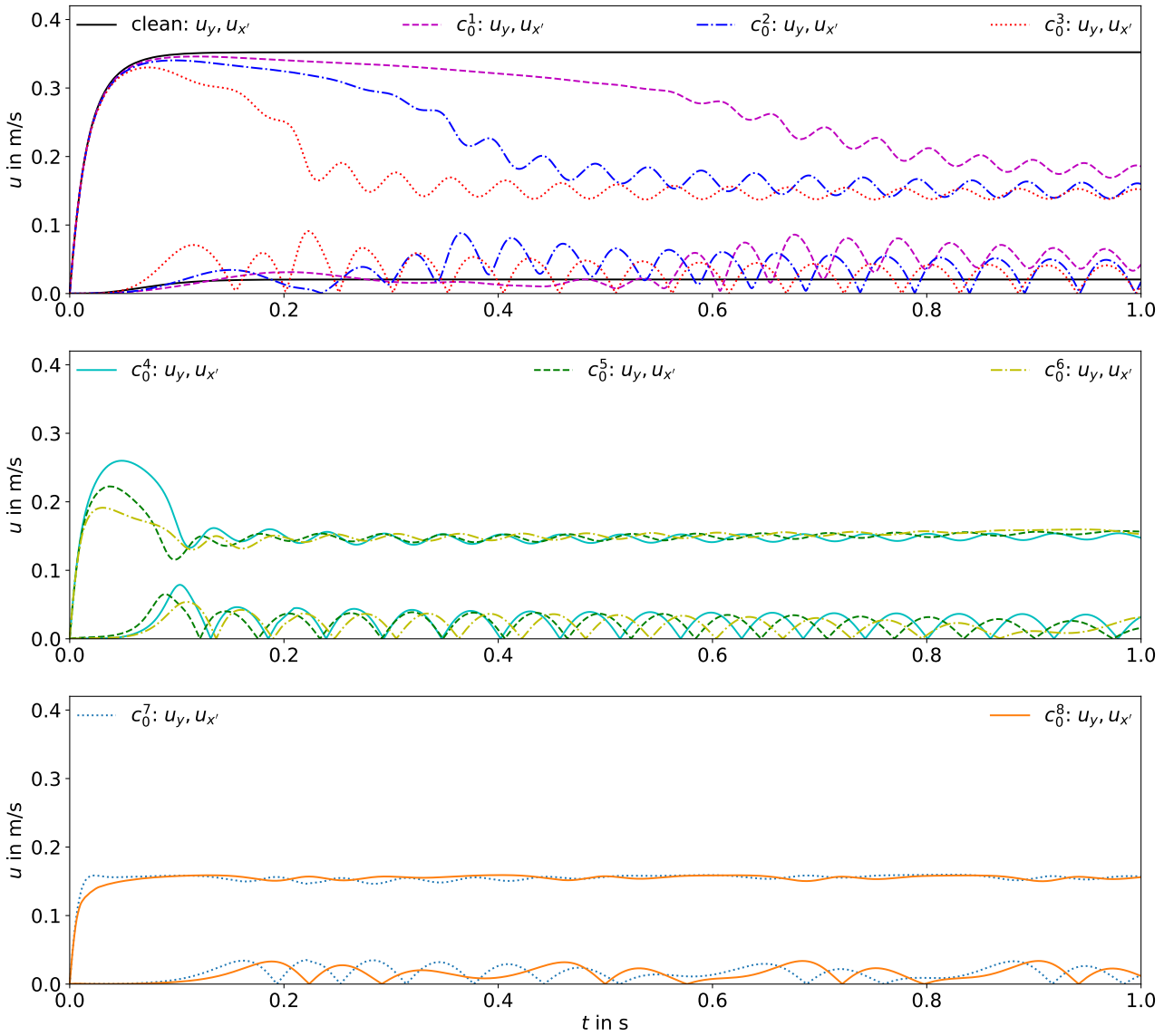

Figure 6.11: Bubble rise velocity, influence of the initial bulk concentration with $u_{x'} = \sqrt{u_x^2 + u_z^2}$.

6.1.5.1 Bubble shape and aspect ratio

Further information available from the experiments is the bubble shape, from which one can extract the aspect ratio. The shapes presented here are the results of the image post-processing step with the software *ImageJ* provided by Dr. M. Krzan, Polish Academy of Sciences. Unfortunately, this measurement can be done only in the plane where the picture of the bubble was taken and, since only one camera has been used, 3D data are not available. This point has to be kept in mind when comparing the aspect ratios obtained from the experiments to the ones from the simulations. Hence, the comparison between experimental and numerical results is reported only for one of the cases presented above. In figure 6.12 the aspect ratios for the case with initial bulk concentration c_0^2 are depicted, comparing experimental and numerical results. The simulation results follow the same trend as the experimental ones, but a quantitative com-

parison is not possible since the information on the orientation of the plane where the pictures were taken is not available.

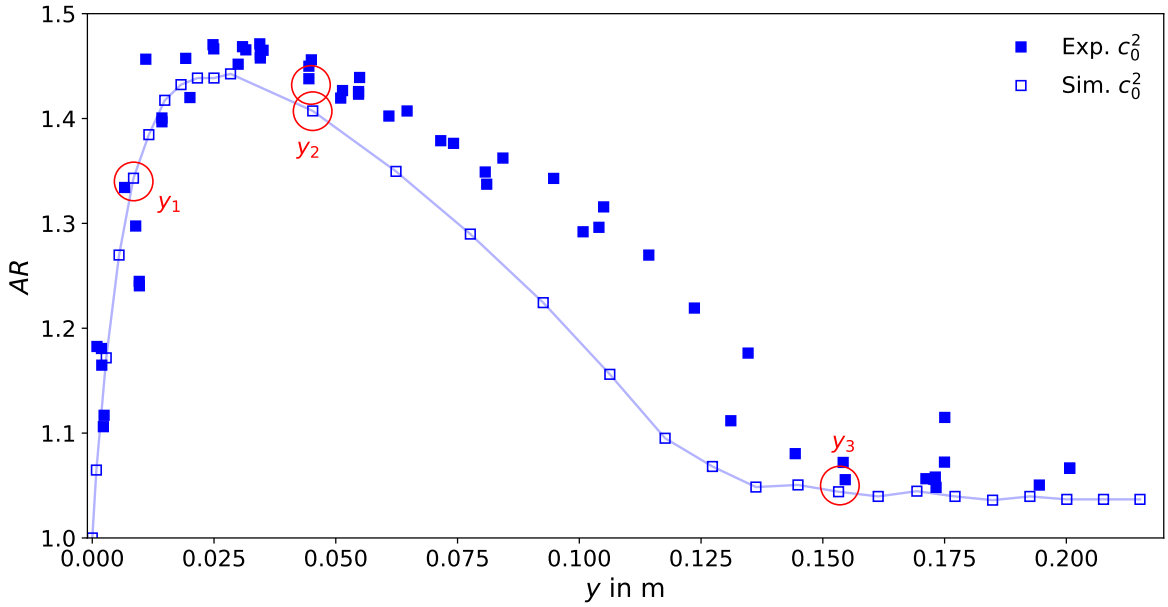

Figure 6.12: Bubble aspect ratio depicted over the vertical position, experimental (filled squares) and numerical (empty squares) results.

In figure 6.12, the points marked with the red circles corresponds to the instances where the bubble shapes from the experiment (solid line) and the simulation (grey area) are compared in figure 6.13. From figure 6.13 can be seen that at the beginning of the bubble rise, when the bubble is still rising straight, the shapes match almost perfectly; see figure 6.13a. On the other hand, when the bubble is path unstable, the match is not perfect. The differences may be caused by different factors: i) the compared bubbles are not exactly in the same vertical position in the experiment and in the simulation. ii) Possibly, if 3D data from the experiment would be available such that the bubble orientation would be known, one could select the correct bubble section to compare. iii) Another source of error can also be the fact that path instabilities occur at different instances in the simulation and in the experiments. Thus, the bubbles can have a different orientation.

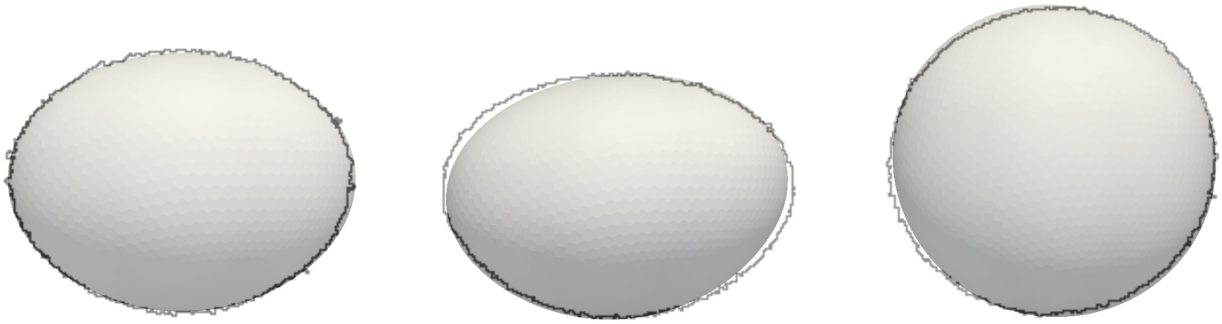

(a) y_1, $t = 0.04$ s. (b) y_2, $t = 0.15$ s. (c) y_3, $t = 0.6$ s.

Figure 6.13: Bubble shapes from the experiment (solid line) and the simulation (grey area).

6.1.5.2 Surfactant effects on the onset of path instability

The velocity components along the rise direction y and in the $x-z$ plane for the bubbles under investigation are reported in figure 6.11. The respective bubble paths are given in figures 6.14 (top view $x-z$ in 6.14a and lateral view $x'-y$ in 6.14b and 6.14c, where $x'=\sqrt{x^2+z^2}$). Even though the bubbles reach a similar terminal velocity, their lateral velocity components and paths show significant differences.

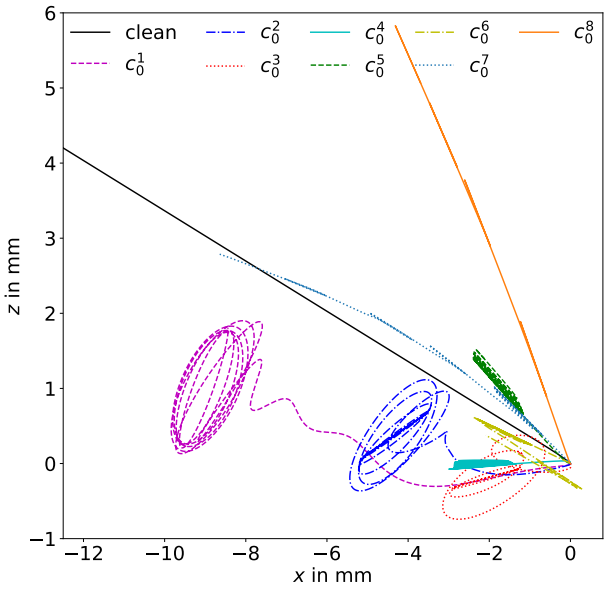

(a) *Top view of the bubble path.*

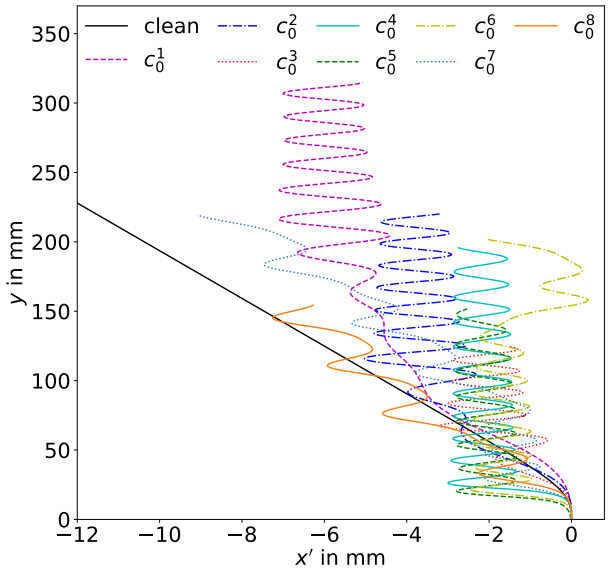

(b) *Lateral view of the bubble path.*

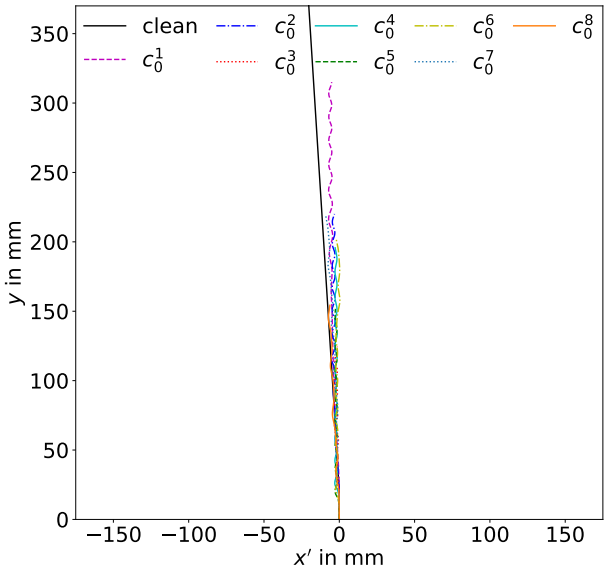

(c) *Lateral view of the bubble path, x-axis true scale.*

Figure 6.14: Study on the effects of the initial bulk concentration on the bubble path.

The least contaminated bubble (c_0^1), after a lateral drift, rises along a helical path of approximately 1.4 bubble diameters amplitude. The bubbles rising in the weakly contaminated aqueous

solutions ($c_0^2,\ c_0^3$) follow first a helical path until they start to oscillate around their terminal velocity (t $\approx$ 0.35 s and t $\approx$ 0.74 s, respectively) and then turn into a zig-zag path. The amplitude of this zig-zag path is around one bubble diameter. While the shift from zig-zag to a helical path was already observed for clean bubbles [11], the transition from helical to zig-zag trajectory occurs only in the presence of the surfactant and was first reported by [83]. The simulation results presented in this work can serve as a further confirmation of this phenomenon. For the intermediate surfactant bulk concentrations ($c_0^4,\ c_0^5,\ c_0^6$), after the initial transient stage when the bubbles accelerate and then decelerate towards their quasi-steady state, the bubbles follow zig-zag paths (starting from $t \approx 0.11$ s) with amplitudes around 0.7 bubble diameters. The bubbles rising in the most contaminated solutions ($c_0^7,\ c_0^8$), after the initial acceleration, start to follow a zig-zag path at $t \approx 0.22$ s, but with a pronounced drift towards one side.
For bubbles close to the path instability regime, lateral migration is a known effect both from experimental and numerical works [17, 2]. For small bubbles rising in clean systems, the lateral drift is almost zero, while for larger bubbles (but not yet path unstable) a significant migration can be observed. The lateral migration can be observed also for the bubble under investigation ($d = 1.45$ mm) rising in clean water, as reported in figure 6.15. In fact, looking at the lateral components of the rise velocity (figure 6.15a) it can be noticed that they are non-zero. This causes the drift visualized in the top view of the bubble path, see figure 6.15b. One can assume that in the current set-up, the instabilities are triggered by the unstructured nature of the computational mesh.

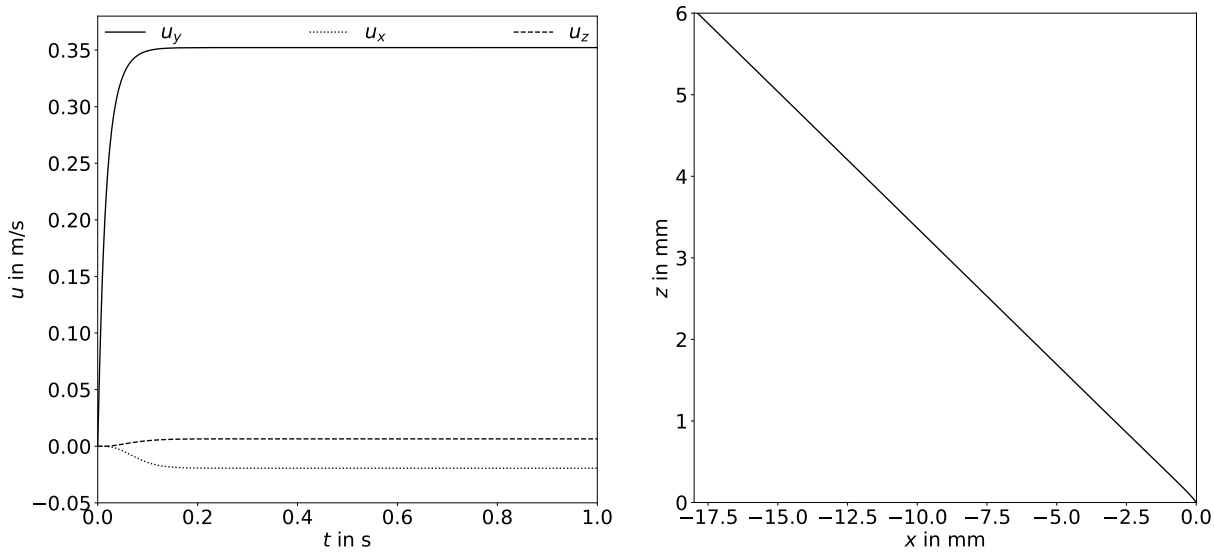

(a) *Rise velocity components.* (b) *Top view of the bubble path.*

Figure 6.15: Bubble rising in clean water, evidence of the later drift.

6.1.5.3 Amount of surfactant on the interface and in its vicinity

The temporal evolution of the total amount of surfactant on the interface is depicted in figure 6.16. It is remarkable that for all studied cases, the surface coverage is much smaller than the respective equilibrium concentration. Nonetheless, the quasi-steady state terminal velocity is reached. This finding is relevant because it shows that the steady-state velocity can be

reached without an equilibrium between ad- and desorption and without the bubble being "fully contaminated". This characteristic was also observed in a theoretical study by Matsumoto et al. in [62], where it is stated that a balance between drag and buoyancy forces is reached although adsorption is still occurring. Such a situation will also have a large impact on the mass transfer processes in contaminated systems. From the slopes of the depicted curves in figure 6.16, it becomes visible that the bubbles rising in the most contaminated liquid (c_0^7, c_0^8) are adsorbing the surfactant much quicker than in the other cases. The initial slope decreases with decreasing initial bulk concentration. For the initial concentrations from c_0^2 to c_0^6, the amount of surfactant on the interface increases with constant slope after the initial transient (approximately $t > 0.35$ s). The curve for the smallest initial bulk concentration, c_0^1, shows an approximately constant slope.
For all the initial contaminations, there are mainly three effects causing their behaviour: (i) With increasing surfactant bulk concentration the initial concentration difference between interface and bulk increases. Therefore, also the driving force for mass transfer is higher; (ii) the first effect is mitigated because at the same time the bubble accumulates surfactant quicker; (iii) since the surfactant distribution on the interface is coupled with the bubble hydrodynamics via the Marangoni forces, the shape of the surfactant boundary layer changes. In general, an increasing amount of surfactant will slow down the bubble, and therefore decrease the convective transport which in turn decreases the driving force for mass transfer. The last effect may be expressed as the dimensionless surfactant gradient at the sub-layer, i.e. the global Sherwood number computed as the sum of the local Sherwood numbers (equation (4.23)), $\mathrm{Sh}_{\mathrm{global}} = \sum(\mathrm{Sh}_{\mathrm{loc},i} A_{f_i})/A_\Sigma$; see figure 6.17.

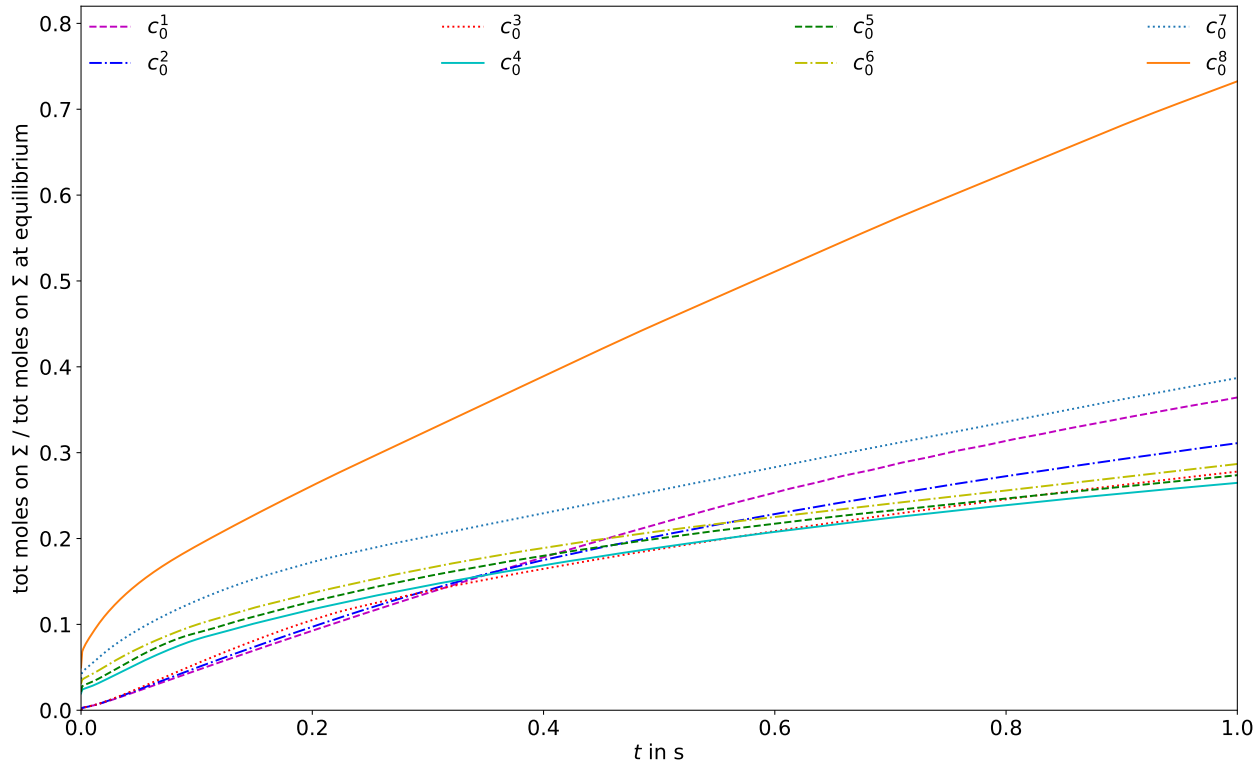

Figure 6.16: Temporal evolution of the total amount of surfactant on the interface divided by the respective equilibrium values for the various initial surface and bulk concentrations.

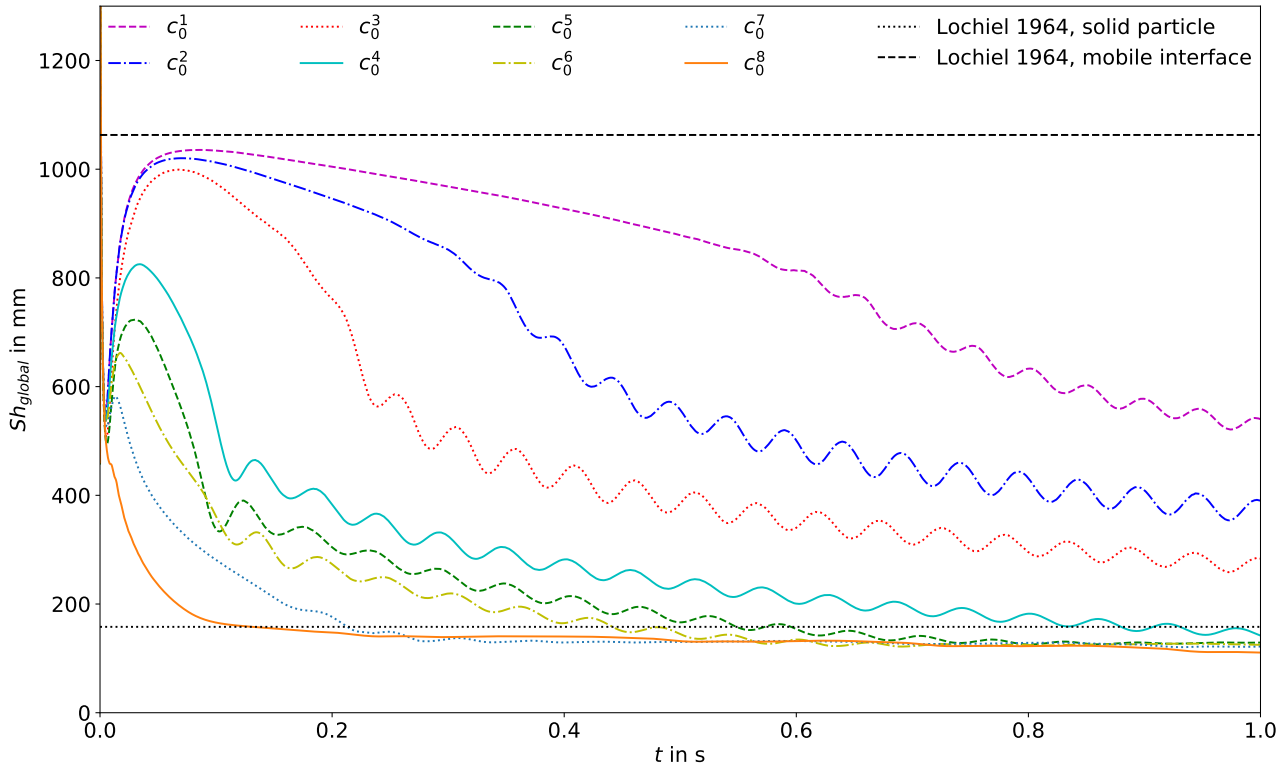

Figure 6.17: Global Sherwood number for the surfactant transport. The surface area change is less than 3%.

In the initial state, when the bubble is formed in the experiment, or at the very beginning of the numerical simulation, the bubble is stagnant and a surfactant boundary layer forms very quickly at the liquid-gas interface, driven by pure diffusion. This process is not depicted in figure 6.17, since the concentration difference is the highest and the boundary layer formation happens on a time scale much smaller than the course of the bubble rise from the initial release up to the quasi-steady state, i.e. $\mathcal{O}(1)$ s. When the bubble starts to rise, it accelerates and the initial boundary layer becomes thinner due to the strong convective transport. The cleaner the system, the higher the maximum rise velocity and, hence, the more pronounced this effect will be. After the initial increase in the acceleration phase, the Sherwood number decreases rapidly as the bubble decelerates. When the bubble velocity reaches a quasi-steady state, the Sherwood number for the cases with low and medium contamination keep decreasing, but at a much slower rate. This is because the Marangoni forces are constantly increasing with increasing surface contamination. The Marangoni forces, in turn, influence the shape of the hydrodynamic boundary layer and therefore also of the surfactant boundary layer. For the most contaminated bubble, a further increase of surfactant on the interface does not lead to an increase of the Marangoni forces. A more detailed view of all forces acting on the bubble will be given in the sections 6.1.5.5 and 6.1.6. In figure 6.17 the correlations for mass transfer problems based on the boundary layer theory from [59] are plotted, too. Two limiting situations are considered, that is fully mobile interface, [59, equation (58)], and solid particle, [59, equation (86)]. It is very interesting to notice that the global Sherwood number computed for the adsorbed surfactant tends to a value very close to the predicted one for solid particles. Moreover, for the least contaminated cases (c_0^1, c_0^2 and c_0^3), the global Sherwood number at the beginning of the rise is comparable with the one of a clean bubble. Note that there are only two reference lines

given, based on the Reynolds number of the clean case, Re = 544, and the average Reynolds number for the contaminated cases, Re = 235. Not much emphasis has been put on the mass transfer similarity to solid particles since the physical effects leading to a comparable quantitative outcome in both cases are actually very different.
So far, it has been described what one can observe from the simulation results in terms of rise velocity, surface coverage, and path. Nevertheless, to really disclose the bubble dynamics, a study of the local flow field in the proximity of the interface and the forces acting on the bubble surface, in particular, the local and global Marangoni forces generated by a non-uniform surface tension distribution and their interplay with deformable interfaces, viscous and pressure forces is performed below.

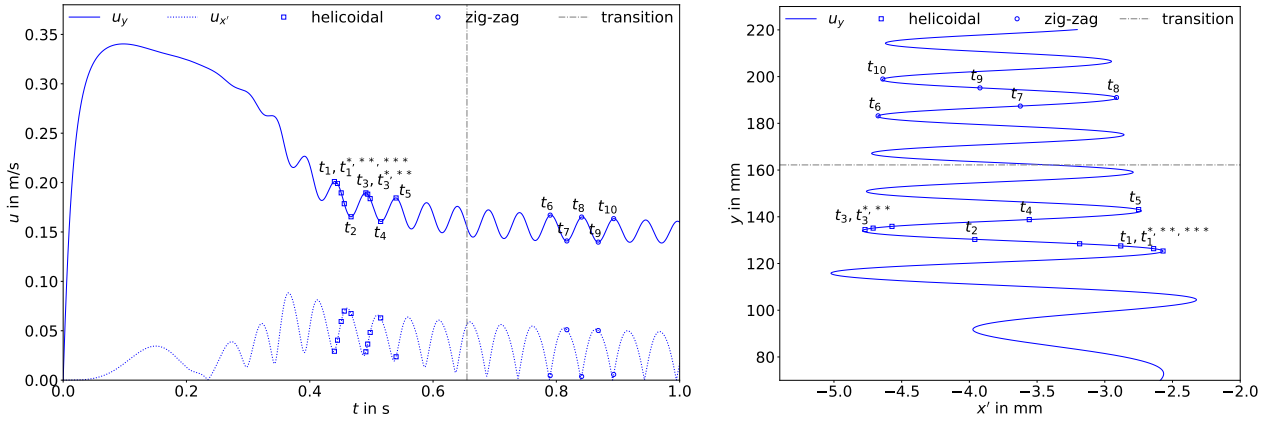

(a) *Rise velocity.* (b) *Lateral view of the bubble path.*

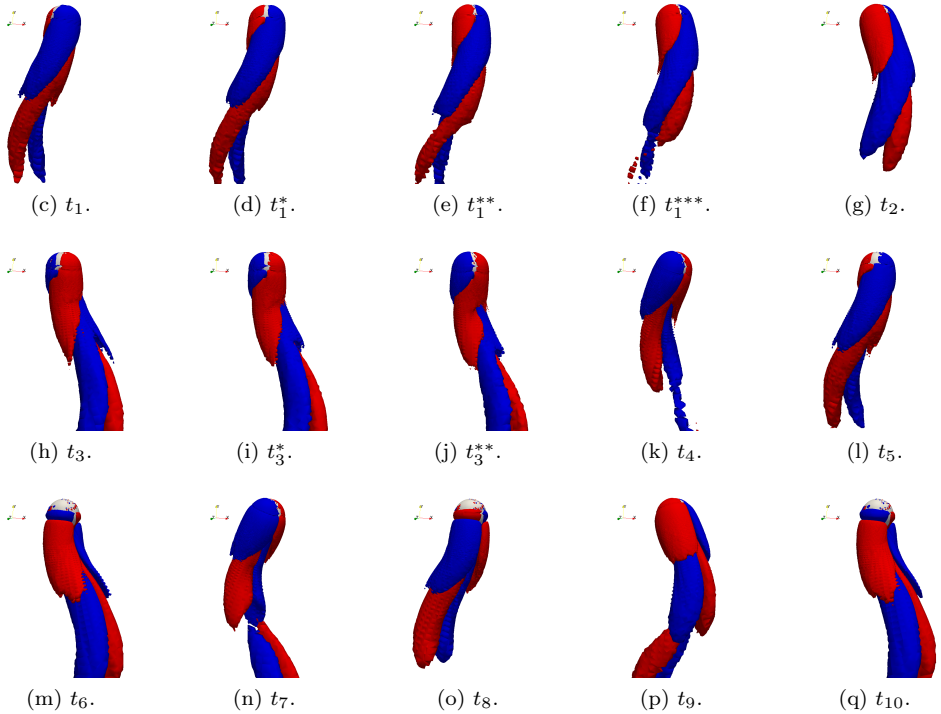

(c) t_1. (d) t_1^*. (e) t_1^{**}. (f) t_1^{***}. (g) t_2.

(h) t_3. (i) t_3^*. (j) t_3^{**}. (k) t_4. (l) t_5.

(m) t_6. (n) t_7. (o) t_8. (p) t_9. (q) t_{10}.

Figure 6.18: Vorticity contour plot ($\omega_y = \pm 20$ 1/s) at different time instances, $c_0 = 1 \cdot 10^{-3}$ mol/m^3, $c_0^{\Sigma} = 0$.

6.1.5.4 Flow field around the bubble

The flow around the bubble may be characterized by the vorticity ($\boldsymbol{\omega} = \nabla \times \boldsymbol{u}$) contour plots in rise direction reported here at various time instances for three of the different initial surfactant bulk concentrations; see figures 6.18, 6.19 and 6.20. Common to all the cases is the strong vorticity production already very close to the interface due to the presence of Marangoni forces. This behaviour related to the surfactant presence is not encountered for path unstable bubbles rising in clean water; see for instance the vorticity distribution in [65, figures 8 and 9]. Moreover, at the end of each period, that is when the bubble completes a full turn (from t_1 to t_5 in figure 6.18 for example), the streamwise vorticity does not vanish.

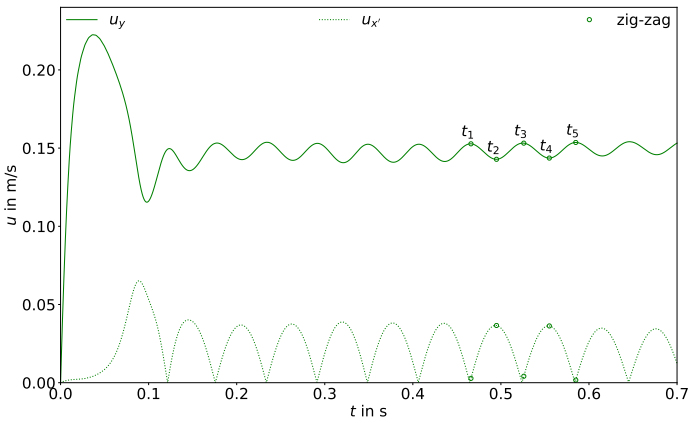

(a) *Rise velocity.*

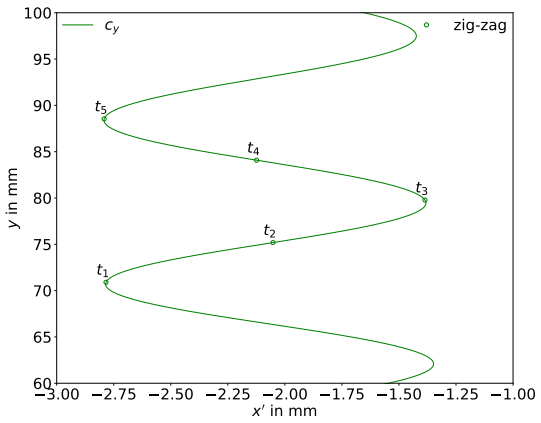

(b) *Lateral view of the bubble path.*

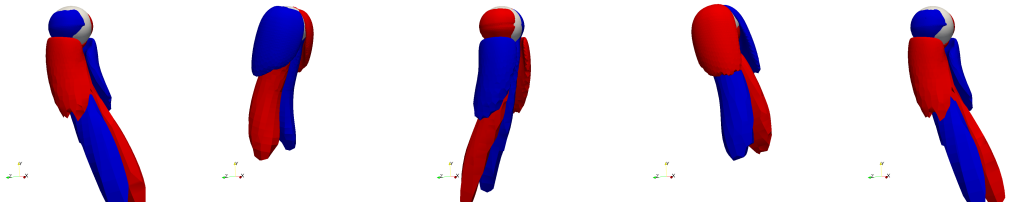

(c) t_1. (d) t_2. (e) t_3. (f) t_4. (g) t_5.

Figure 6.19: Vorticity contour plot ($\omega_y = \pm 40$ 1/s) at different time instances, $c_0 = 8 \cdot 10^{-3}$ mol/m^3, $c_0^{\Sigma} = 2\% c_{eq,2}^{\Sigma}$.

In the least contaminated case considered (c_0^2), the bubble follows first a helical and then a zig-zag path. This behaviour is confirmed by the vorticity contour plots in figure 6.18. The figures from 6.18c to 6.18l refer to time instances at which the bubble path is helical, while the figures from 6.18m to 6.18q refer to the zig-zag trajectory. As already observed by other authors [24, 65, 11], along with the helical trajectory, the vortical structure is formed by two counter-rotating vortices of opposite sign that produce a bubble inclination in both x and z directions. The two vorticity regions are wrapping around each other without any symmetry plane. On the other hand, when the bubble exhibits a zig-zag trajectory, the inclination changes only in one direction. In this case, the wake structure consists of two counter-rotating vortices with a symmetry plane. Common to both trajectories, at each cycle (from one velocity peak to another which corresponds from one side to the other of the path in the $x' - y$ view) the two vortices interchange their signs. Due to the high mobility of the interface in the initial stage, the bubble reaches a high terminal velocity and deforms. After the onset of the path instability,

the trajectory is helical. With increasing surface contamination, a symmetry between the wake vortices is established and the trajectory changes from helical to zig-zag. Interestingly this happens when the rise velocity is already very close to its quasi-steady value. One, therefore, can conclude that not only the pure deceleration but also the indirect influence of the Marangoni forces on the flow pattern around the bubble cause the observed transition. A similar zig-zag trajectory can be observed for the bubble in figure 6.19. Also in this case two counter-rotating vortices with a symmetry plane are present.

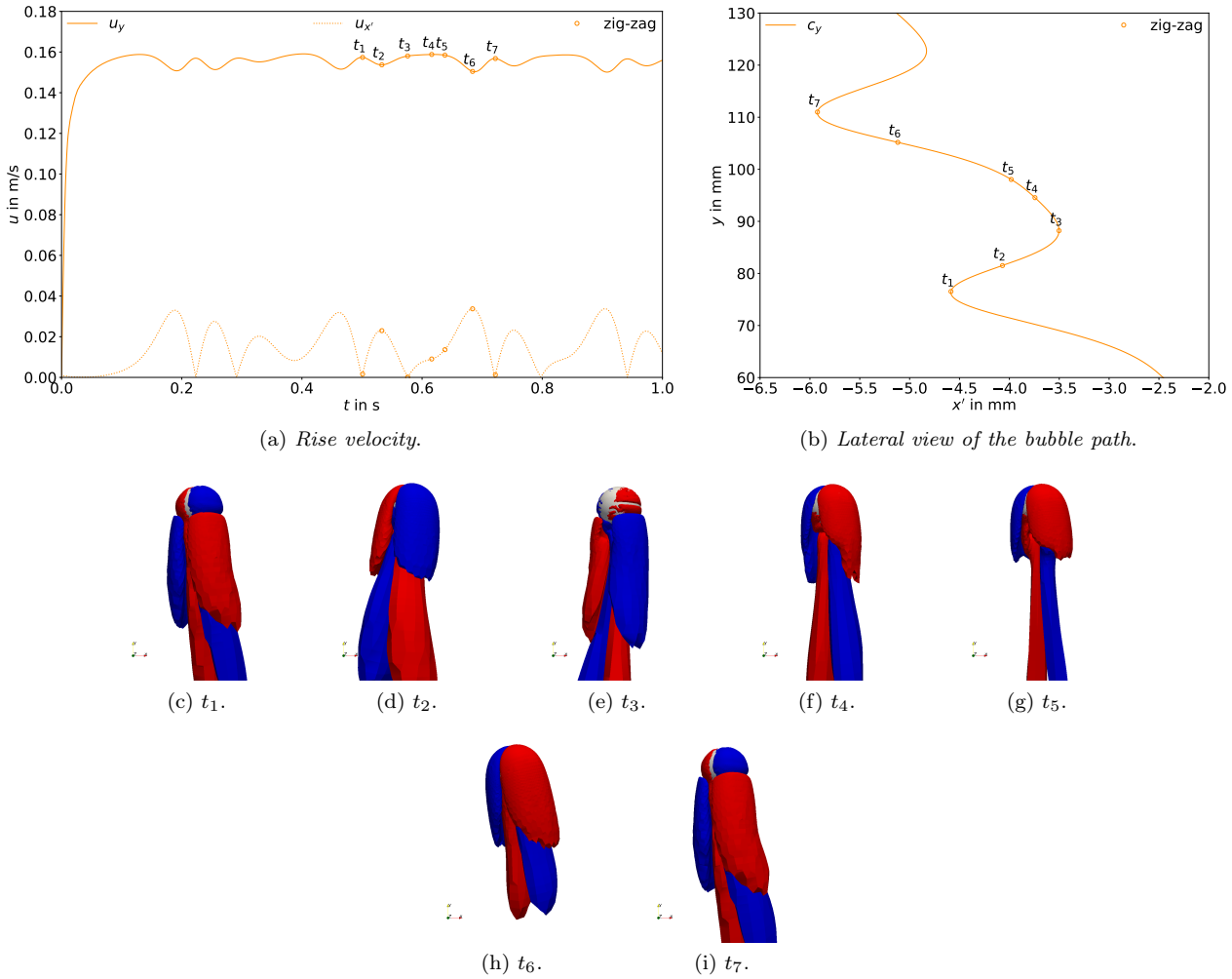

(a) *Rise velocity.*

(b) *Lateral view of the bubble path.*

(c) t_1.

(d) t_2.

(e) t_3.

(f) t_4.

(g) t_5.

(h) t_6.

(i) t_7.

Figure 6.20: Vorticity contour plot ($\omega_y = \pm 10$ 1/s) at different time instances, $c_0 = 5 \cdot 10^{-2}$ mol/m^3, $c_0^\Sigma = 5\% c_{eq,3}^\Sigma$.

A different behaviour is observed for the most contaminated case; see figure 6.20. The bubble follows a zig-zag trajectory, but the motion is accompanied by a lateral migration. The vortical structure is composed by two counter-rotating vortices with a symmetry plane, but the duration of each half-cycle is not constant any more, as it was for the cases in figures 6.18 and 6.19, due to the drift. Considering figure 6.20 from t_1 to t_3, the vorticity production is much higher than from t_4 to t_7. This means that a bigger portion of fluid around the interface is influenced by the bubble motion. Instead, at the sample times t_5 and t_6 the vorticity production is much less, thus the fluid around the bubble will be less perturbed and the drift towards the left side

lasts longer. At t_7 the same conditions as in t_1 are restored. It seems to be a superimposition of clean case migration and contaminated case oscillation. A possible explanation will be given in the next section.

6.1.5.5 Forces acting on the interface

Several experimental works derived correlations for global lift and drag coefficients of single rising bubbles, e.g. [88]. In this work, the focus is on the local forces acting on the interface and how they influence the integral lift and drag forces. The interfacial jump condition (2.10) is considered in order to evaluate the forces acting on the interface:

$$\left[\!\left[p_{\text{tot}}\, \boldsymbol{I} - \boldsymbol{S}^{\text{visc}} \right]\!\right] \cdot \boldsymbol{n}_\Sigma = \sigma\kappa\boldsymbol{n}_\Sigma + \nabla_\Sigma\sigma, \tag{6.3}$$

where p_{tot} is the total pressure, the sum of dynamic and hydrostatic contributions[3].
For clarity, we recall that $\boldsymbol{f}^{\text{ma}} = \nabla_\Sigma\sigma$ is the area specific Marangoni force, while $\boldsymbol{f}^{\text{ca}} = \sigma\kappa\boldsymbol{n}_\Sigma$ is the area specific capillary pressure force. Equation (6.3) at each interface element reads

$$\boldsymbol{f}_B^{p_{\text{tot}}} - \boldsymbol{f}_A^{p_{\text{tot}}} - \boldsymbol{f}_B^{\text{visc}} + \boldsymbol{f}_A^{\text{visc}} = \boldsymbol{f}^{\text{ca}} + \boldsymbol{f}^{\text{ma}}, \tag{6.5}$$

where $\boldsymbol{f}^*$ are the area specific forces $\boldsymbol{f}^* = \boldsymbol{f}^*(\boldsymbol{x}^\Sigma, t)$[4], A represents the liquid phase and B the gas phase. The symbols $\boldsymbol{f}^{p^{\text{tot}}}$ and $\boldsymbol{f}^{\text{visc}}$ indicate the total pressure and viscous forces, respectively. Comparing the magnitude of the forces between the sides A and B, it can be noticed that $|\boldsymbol{f}_B^*|$ is always at least one order of magnitude smaller than the respective force from the A-side, thus in the following analysis it will be neglected.
The local force balance at the interface (6.5) is projected in normal and tangential direction to the interface. For the liquid side (A, dropped from here onwards) the two balances read

$$-\boldsymbol{f}^{p_{\text{tot}}} + \boldsymbol{f}_\perp^{\text{visc}} = \boldsymbol{f}^{\text{ca}} \quad \text{normal to } \Sigma, \tag{6.6}$$

$$\boldsymbol{f}_\parallel^{\text{visc}} = \boldsymbol{f}^{\text{ma}} \quad \text{tangential to } \Sigma. \tag{6.7}$$

The total pressure force can be further decomposed into the hydrostatic and the dynamic contributions, i.e.

$$\boldsymbol{f}^{p_{\text{tot}}} = \boldsymbol{f}^{p_{\text{hydro}}} + \boldsymbol{f}^{p_{\text{dyn}}}. \tag{6.8}$$

Integrating the area specific forces $\boldsymbol{f}^*(\boldsymbol{x}^\Sigma, t)$ over the interface, one gets the force $\boldsymbol{F}^*(t)$ on Σ as

$$\boldsymbol{F}^*(t) = \int_\Sigma \boldsymbol{f}^*\left(\boldsymbol{x}^\Sigma, t\right) dA. \tag{6.9}$$

Thus, the following forces are acting on the bubble surface: the hydrostatic pressure force $\boldsymbol{F}^{p_{\text{hydro}}}$, the dynamic pressure force $\boldsymbol{F}^{p_{\text{dyn}}}$, normal and tangential viscous forces $\boldsymbol{F}_\perp^{\text{visc}}$, $\boldsymbol{F}_\parallel^{\text{visc}}$, the Marangoni force $\boldsymbol{F}^{\text{ma}}$, and the capillary pressure force $\boldsymbol{F}^{\text{ca}}$. The hydrostatic pressure force is approximately constant over time, so it is not analysed. As can be observed from equations (6.6) and (6.7), the tangential viscous force is balanced by the Marangoni force. Thus we can just

[3] Within the algorithm, equations (2.3) to (2.10) are solved for the modified pressure, or dynamic pressure p^{dyn} as we will refer to, that is the total pressure minus the hydrostatic contribution,

$$p^{\text{dyn}} = p^{\text{tot}} - p^{\text{hydro}} \tag{6.4}$$

with $p^{\text{hydro}} := \rho\mathbf{g}\cdot\mathbf{x}$. This means that in equation (2.5) the gravity term disappears and the transmission condition (2.10) has to be adapted according to relation (6.4), too.

[4] The superscript '*' stands for 'p_{tot}', 'visc', 'ca' or 'ma'.

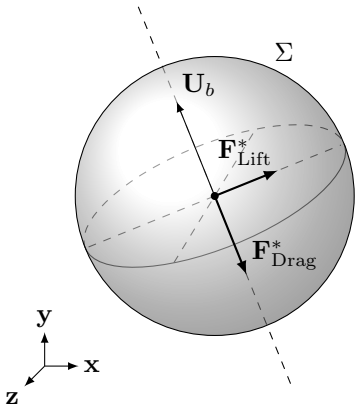

Figure 6.21: Schematic representation of the lift and drag directions.

consider one of them, say $\boldsymbol{F}_{\parallel}^{\text{visc}}$. For the same reason, we drop the capillary pressure force as it is equal in magnitude to the sum of total pressure force and normal viscous force. We are left with three integral forces, $\boldsymbol{F}_{\parallel}^{\text{visc}}$, $\boldsymbol{F}^{p_{\text{dyn}}}$ and $\boldsymbol{F}_{\perp}^{\text{visc}}$, that are decisive for understanding the bubble dynamics. Each force may be written as the sum of contributions parallel and perpendicular to the bubble velocity vector. The parallel component is referred to as drag and the remaining component as lift force:

$$\boldsymbol{F}^*(t) = \boldsymbol{F}^*_{\text{Lift}} + \boldsymbol{F}^*_{\text{Drag}}, \tag{6.10}$$

as depicted in figure 6.21. The drag force governs the bubble acceleration/deceleration and the lift force the bubble's change in direction. Figures 6.22 and 6.23 show the contributions from the three integral forces mentioned above to lift and drag for c_0^2, c_0^5 and c_0^8. The different line types correspond to the various initial bulk concentrations reported in the plots' legends. In order to have a common reference, the magnitude of the forces has been made non-dimensional with respect to the buoyancy force. For completeness, the full set of results is reported in the appendix D.

As can be noticed from figure 6.22 (and from figures D.1 to D.3 in appendix D.1), the major contribution to the lift force comes from the dynamic pressure force (up to 45% of the buoyancy force). The tangential viscous force contribution to the lift does not exceed 5%, while the normal viscous force contribution is below 1%. Considering the lift contribution of the dynamic pressure and the bubbles' paths in figure 6.14, one can see that a wider trajectory corresponds to a higher lift force (in terms of helical or zig-zag width); the lower the initial surfactant concentration, the higher the dynamic pressure force and the wider the path. The lateral motion is mainly driven by the dynamic pressure force. Whether or not the Marangoni forces/tangential viscous forces decrease the lateral motion directly will be clarified in section 6.1.6. From the plot of the force magnitude, one cannot draw any conclusion on the direction of the bubble motion. For instance, it is not possible to deduce from this plot when the least contaminated bubbles are changing their trajectory from helical to zig-zag. These aspects will be investigated later in this section; see figures 6.24 and 6.25.

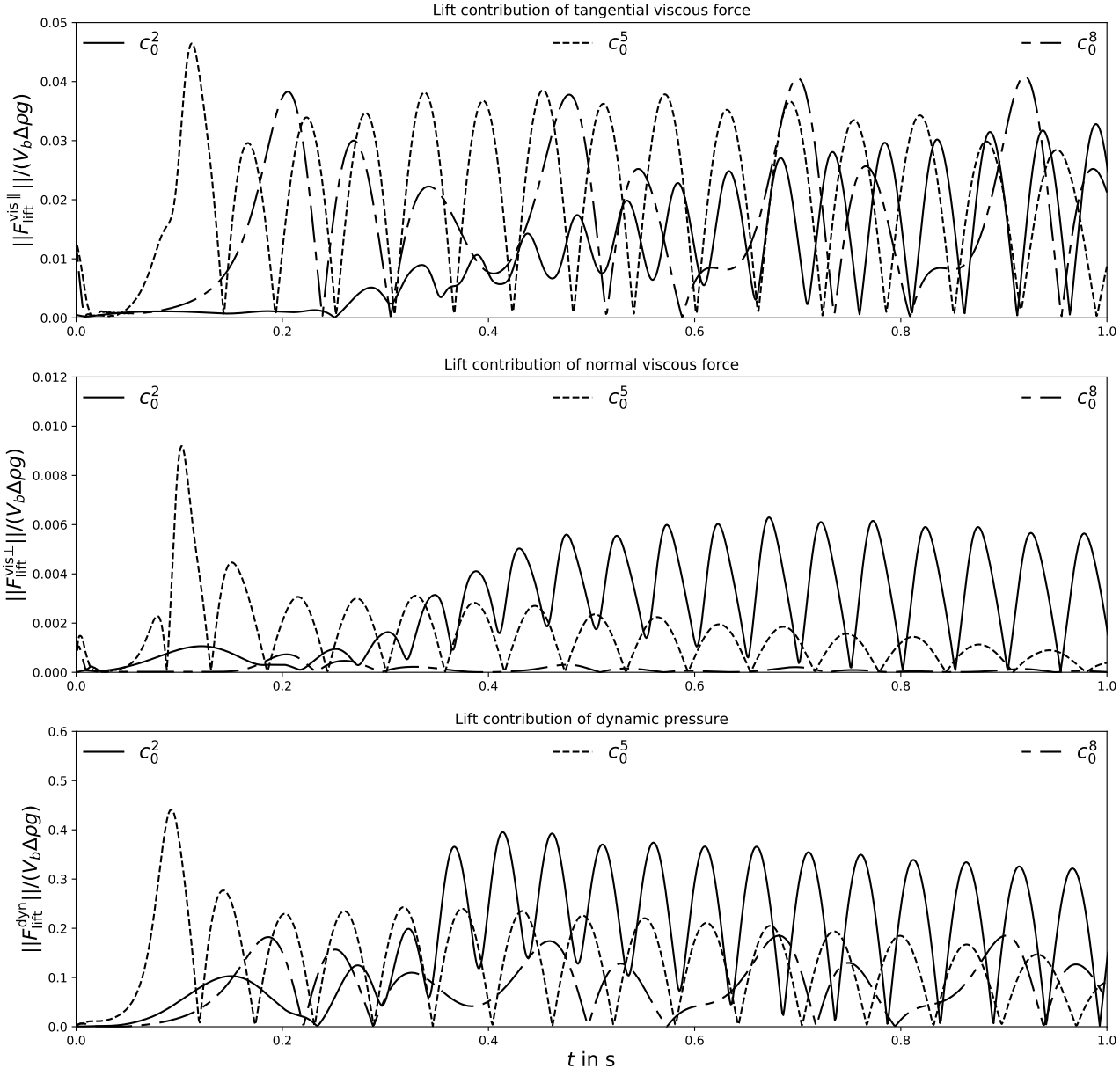

Figure 6.22: Integral lift force contributions, influence of the initial bulk concentration $c_0^2,\ c_0^5,\ c_0^8$.

Consider now the force contributions to the drag force, see figure 6.23 (and figures D.4 to D.6 in appendix D.2). As for the lift, the main contribution comes from the dynamic pressure force, although for the drag, tangential and normal viscous forces cannot be neglected. In the first graph of figure 6.23, the contribution of the tangential viscous force to the drag is reported. Increasing the initial surfactant concentration leads to a higher drag contribution of $\boldsymbol{F}_{\parallel}^{\text{visc}}$. When the bubble reaches the quasi-steady state, the tangential viscous force (as the Marangoni force) is still slowly increasing. This could be due to the fact that the equilibrium value of the interfacial concentration has not yet been reached and thus surfactant is still accumulating on the interface, changing its properties and consequently the Marangoni force. On the other hand, it can be seen from figure 6.23 that the drag contribution of the normal viscous force decreases with time. At the beginning of the bubble rise, there is a stronger change of the velocity normal to the interface, resulting in higher viscous stresses. The drag due to viscous forces is the highest for the lowest contaminations. For increasing initial surfactant concentration, this contribution becomes more and more negligible; see for instance the line corresponding to c_0^8. To conclude the analysis on the drag force, consider the dynamic pressure contribution to the drag in figure 6.23 (third graph). During the initial part of the acceleration phase at the beginning of the rise, the dynamic pressure force contributions reach values comparable to the gravitational force, being the highest for the least contaminated bubble, that is the one with highest rise velocity. After this initial phase, the contribution of the dynamic pressure force to the drag drops and oscillates at about 60% of the buoyancy force. As pointed out in the previous section, all studied surfactant bulk concentrations lead to a similar quasi-steady terminal velocity, even though ad- and desorption are not in equilibrium and the total surface coverage varies significantly. The steady state terminal velocity is a consequence of the overall drag force. For higher surfactant bulk concentrations, the viscous drag force increases due to higher surface tension gradients. At the same time, the dynamic pressure force decreases as a result of the decreasing mobility of the interface. These two counteracting effects lead to an approximately constant overall drag force. These considerations are summarized in a visual manner in the bottom plot of figure 6.23, where the force contributions to the drag are summed up for c_0^2, c_0^5 and c_0^8. Figure 6.23 confirms that a similar drag force acts on the bubble surfaces, hence the resulting rise velocities will be comparable, too.

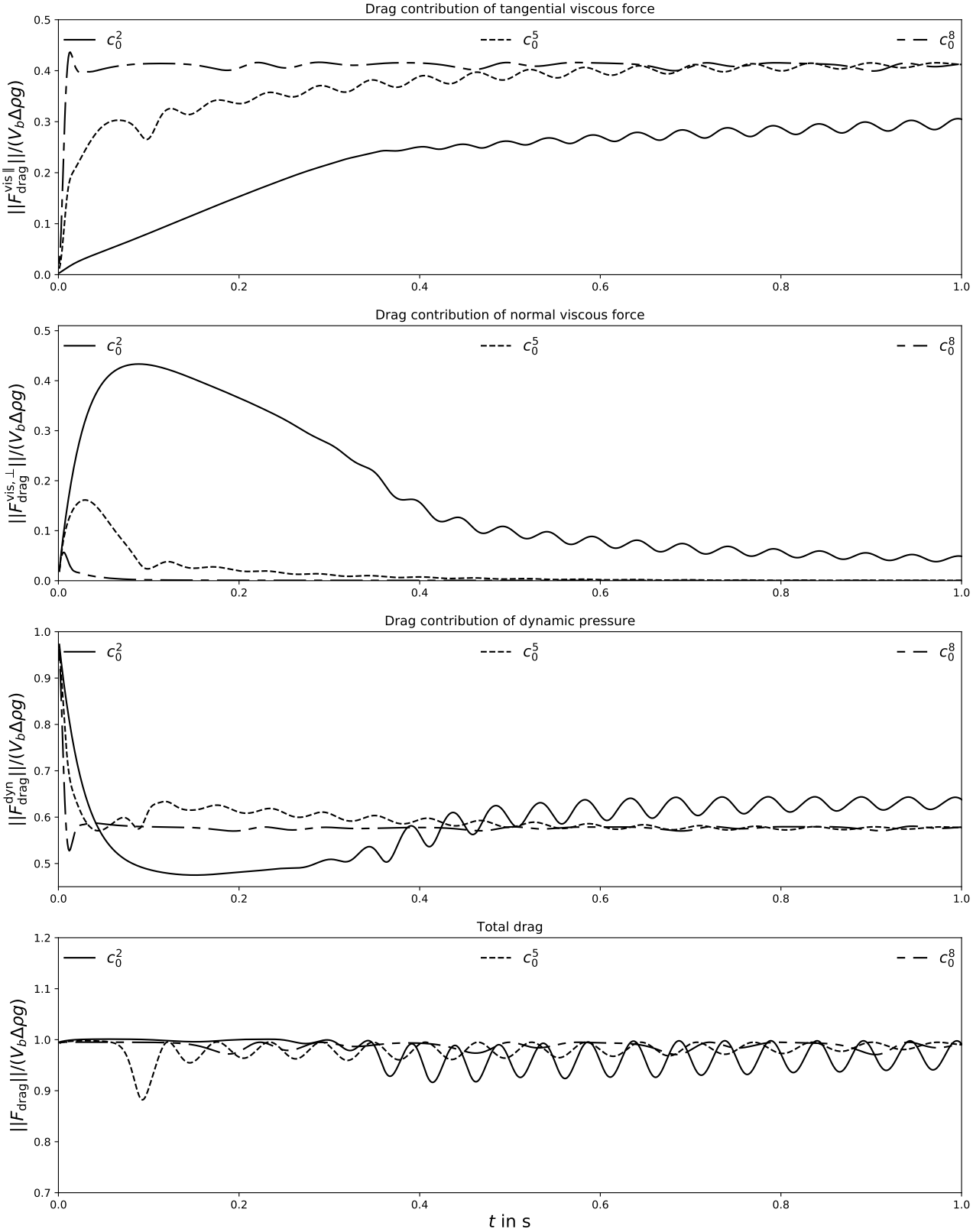

Figure 6.23: Integral drag force contributions, influence of the initial bulk concentration $c_0^2,\ c_0^5,\ c_0^8$.

In figures 6.24 and 6.25, the integral force contributions to the lift and drag from the tangential viscous force and the dynamic pressure force are depicted as vectors along the bubble path for c_0^5 and c_0^8. The same figure for c_0^2 is not reported here, because for a spiralling path, a 2D picture would be misleading since the vector orientation and magnitude would not be representative of the 3D motion. See [81, figures 5.17, 5.18] for the representation and explanation of the force components in case of spiralling path.

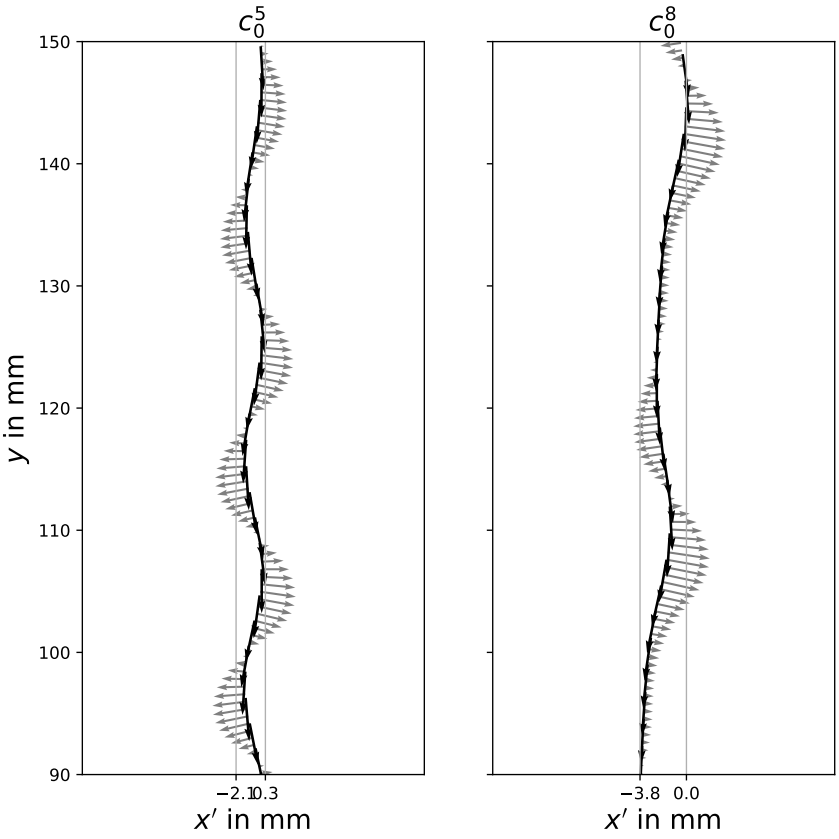

Figure 6.24: Lift (grey) and drag (black) due to tangential viscous forces along the path. The lift force is depicted ten times larger than the drag force and two times larger than the dynamic pressure contribution to the lift in figure 6.25.

From these plots one can clearly deduct how the forces are changing the bubble trajectory. The main contribution to the lift comes from the dynamic pressure; see figures 6.22. Thus, the deviation from a rectilinear path is mainly caused by the dynamic pressure force and not directly by the tangential viscous force (in response to the Marangoni force). Yet, with increasing contamination, the lateral motion of the bubble decreases and this effect may be caused by a non-axisymmetric (with respect to the rise velocity vector) distribution of the surfactant on the interface. As can be seen in figure 6.24, the Marangoni effect is actually adding to the lift. However, the reduction of the dynamic pressure is much stronger and, consequently, the overall lift is reduced. Regarding the drag component, the dynamic pressure force is still the dominating contribution, but the tangential viscous force contributes in comparable amounts to the drag. Even though the dynamic pressure force is the dominating component, locally the flow field is governed by the Marangoni stresses. A study of the local fields is performed in the following section 6.1.6.

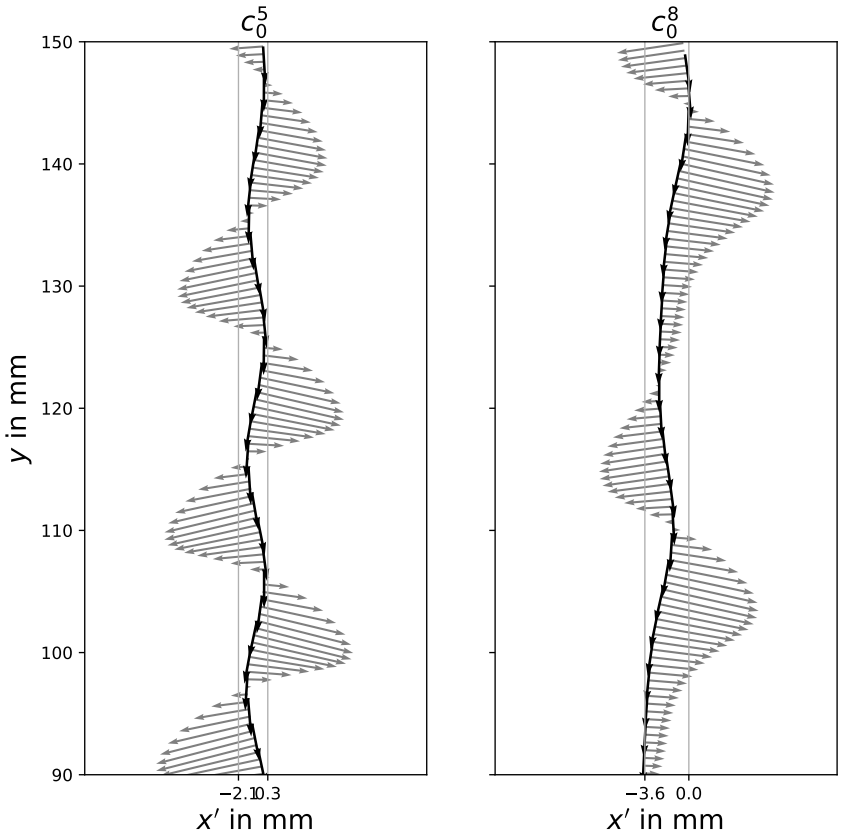

Figure 6.25: Lift (grey) and drag (black) due to dynamic pressure forces along the path. The lift force is depicted eight times larger than the drag force.

6.1.6 Local fields under the influence of surfactant

Figure 6.26 shows the velocity field in the liquid phase close to the bubble, while on the bubble surface the local Marangoni force vectors are depicted for three of the initial concentrations at different time instances, c_0^2, c_0^5 and c_0^8. At $t = 0.072$ s, the bubble rising in the most contaminated solution (right) has already reached a surfactant distribution characteristic of the steady state. In the lower hemisphere, where the surfactant concentration is the highest and uniformly distributed, the Marangoni forces are almost zero, while the surface coverage is not yet the equilibrium one. In fact, the surfactant species is still adsorbed; see figure 6.16. For the other two initial bulk concentrations, a longer initial transient stage is visible. The surface coverage is much smaller at the beginning of the rise, while much higher and more confined Marangoni stresses are visible. For the cases on the left and in the middle of figure 6.26, it is clearly visible that the line where the flow detaches corresponds to the region where the Marangoni forces are the highest. As the bubbles are rising, more and more surfactant is adsorbed and the region where the Marangoni stresses are present moves towards the upper hemisphere. At $t = 0.9$ s, the bubble in the middle has reached a similar state as the most contaminated bubble in terms of Marangoni stresses and terminal velocity, even though the surface coverage is approximately 60% smaller; see figure 6.16.

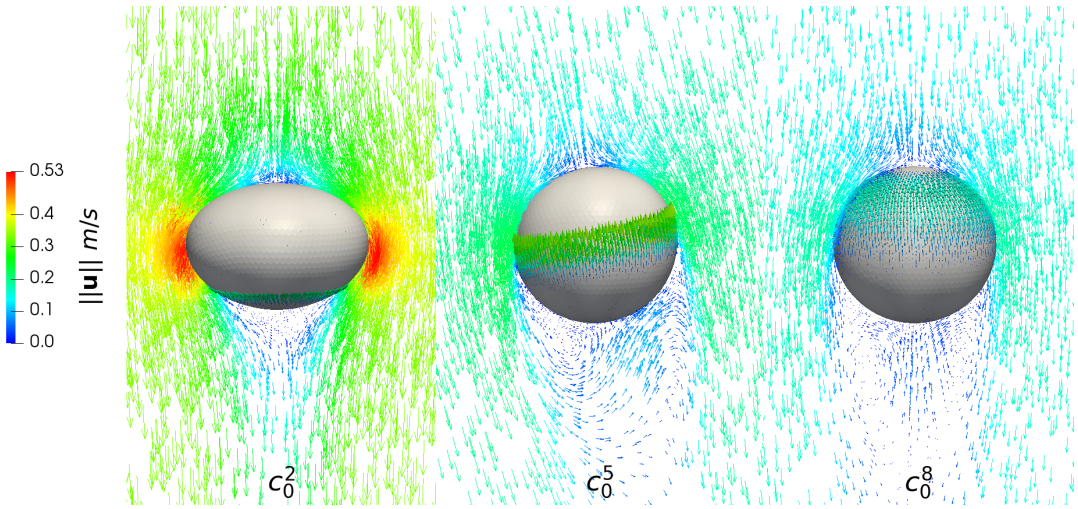

(a) $t = 0.072\ s.$

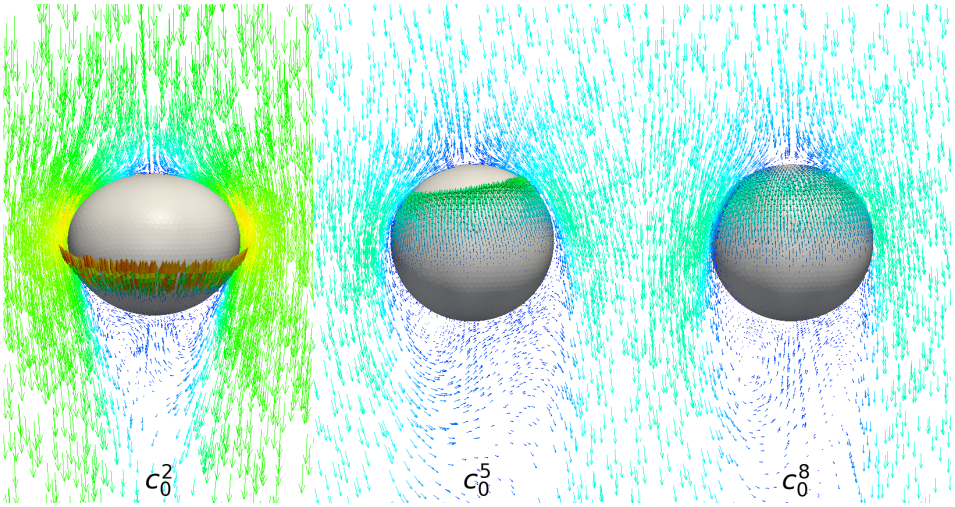

(b) $t = 0.3\ s.$

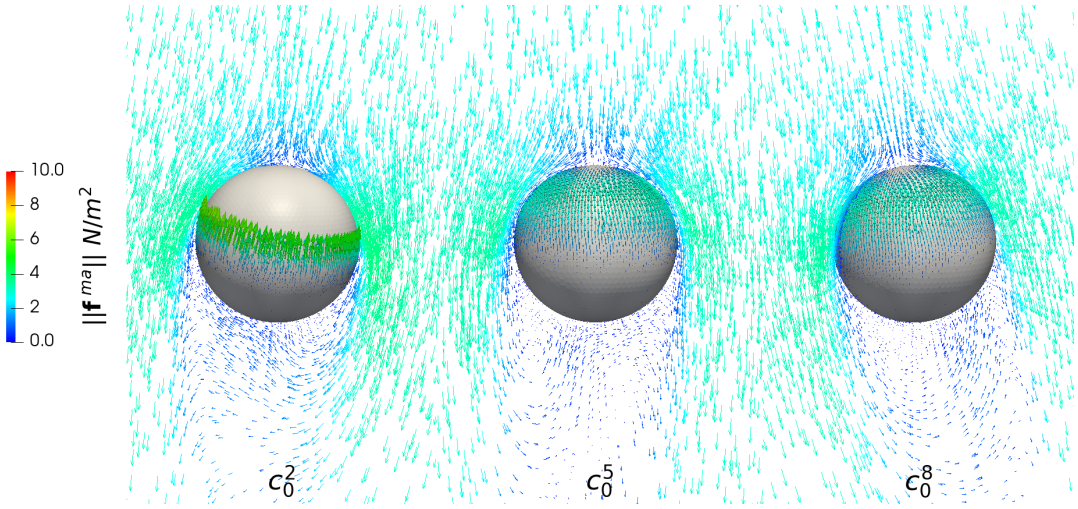

(c) $t = 0.9\ s.$

Figure 6.26: Velocity vectors (bulk) and Marangoni forces (interface) at different time instances for c_0^2, c_0^5, c_0^8.

It is reasonable to predict that the least contaminated bubble, if simulated for a longer time, would reach a similar state as the other two bubbles, but with an even lower surface coverage. To have a better understanding of the variation of the Marangoni forces and their local distribution, one can analyse the adsorption, advection and diffusion processes on the interface; see figures 6.26 and 6.27.
Three different stages during the bubble rise can be identified.

1. After being released, the bubble undergoes a strong acceleration due to the buoyancy force. The surface coverage is low and uniform and, therefore, the interface is fully mobile. A thin concentration boundary layer forms at the interface and the adsorption rates are the highest. The first stage may be very short, depending on the initial surface and bulk concentrations.

2. Due to the high mobility of the interface, the surfactant is quickly advected to the rear part of the bubble. As a consequence, the surface coverage becomes less uniform and surface tension gradients that are strong enough to locally reduce the tangential interface velocity in the rear part arise. The flow detaches, and vortices are shed. The interface below the detachment ring is almost stagnant, and the adsorption rates are small because the concentration difference with respect to the bulk decreases and no new surfactant is transported there by convection. The front of the bubble is still mobile and the adsorbed surfactant is quickly transported towards the cap. As a consequence, the transition from a very small to very high contamination happens in a small belt above the "stagnant cap" zone. Here the highest surface tension gradient and hence Marangoni forces are observed.

3. The transition from the second to the third stage happens on a larger time scale than between the first two stages. The convective surfactant transport at the bubble front slowly decreases. This happens, on the one hand, because the bubble decelerates (for small Marangoni numbers) and, on the other hand, due to the decreasing overall mobility of the interface. The narrow transition zone with high concentration gradients widens and the surfactant distribution in the front becomes approximately linear. Consequently, the resulting Marangoni forces have a smaller magnitude but act almost uniformly on the entire upper hemisphere. The total tangential viscous force due to the Marangoni stresses is, therefore, higher than in stage two.

To see a further transition to a fourth stage, a much longer physical time would have to be simulated since also the adsorption steadily decreases. Such an investigation shall be part of future studies.

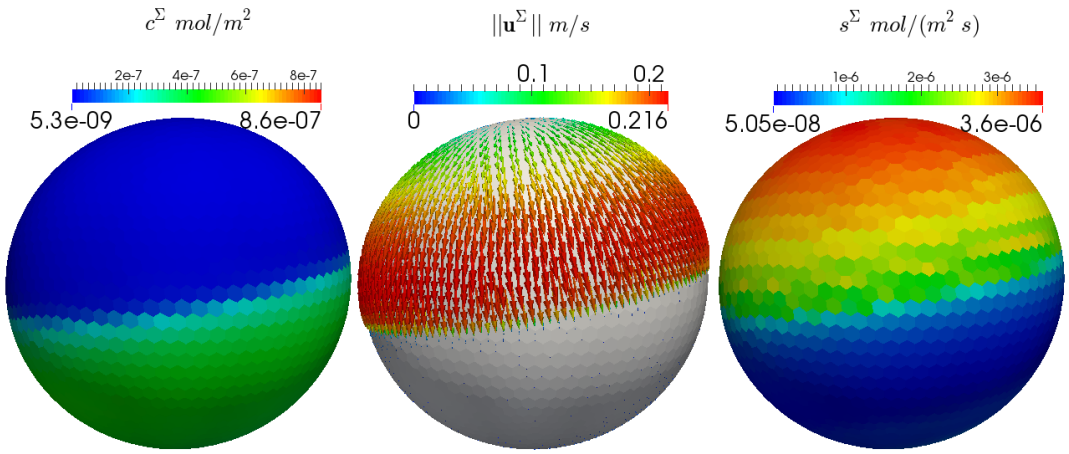

(a) $t = 0.072\ s.$

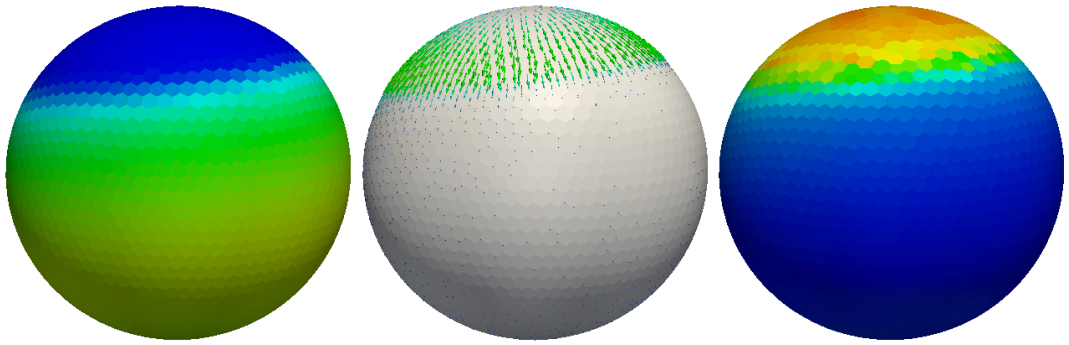

(b) $t = 0.3\ s.$

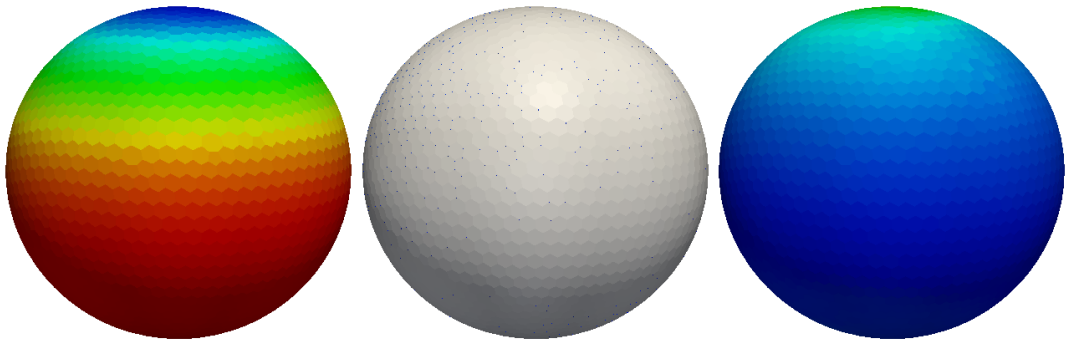

(c) $t = 0.9\ s.$

Figure 6.27: From left to right, surfactant distribution on Σ, interface velocity field and sorption source term at different time instances for the intermediate bulk concentration c_0^5. Figure reproduced from [73].

6.2 Influence of surfactant on mass transfer

The case of a bubble rising in a contaminated solution can be extended to investigate the effects of surfactant on the mass transfer. As mass transfer process, the dissolution of oxygen or carbon dioxide from the gas bubble into the liquid can be considered. As oxygen or carbon dioxide dissolve into the bulk phase, a volume change of the gas bubble occurs, cf. [33]. In the present simulations, any volume effect is neglected. The mass transfer problem requires the solution of the species transport equation (2.14) in the bulk phase. The presence of the gas phase is implicitly taken into account via the Dirichlet boundary condition at the interface (2.26). The species transport process is a typical high Péclet number problem, too. Thus, the SGS model described in section 3.3 is employed. The major and well known surfactant effect of drastically reducing the mass transfer derives from the presence of Marangoni stresses at the interface which cause a different flow field around the bubble. This effect is obtained in the simulations by simply treating the species transfer and surfactant transport processes as two independent scalar transport problems. The numerical procedure is outlined in section 3.4.1. The first set of results on mass transfer in the presence of surfactant presented in this section follows this solution strategy. First the results for the mass transfer (with a decay reaction) from a 3D oxygen bubble rising in clean and contaminated water solutions from [97] are presented; see section 6.2.1. Then, a 2D test case is set-up to investigate first the Marangoni effect on mass transfer (see sections 6.2.2.1 and 6.2.2.3) and, eventually, the hindrance effect.
The hindrance effect of surfactant on mass transfer can be taken into account, as described in section 2.3. In this case, the boundary condition at the interface for the species transfer problem is equation (2.62). To compute the boundary value it is necessary to set the value for the reduction factor $\overline{k}$. Its value is chosen such that the liquid-side concentration at the interface, $c_\ell|_\Sigma$, does not reach non-physical values, e.g. less than zero. Nevertheless, in the very first time steps, it is very likely that oscillations in the concentration values at the interface occur, thus, an exception handling should be implemented to allow for a wider range of reduction factors. The relative solution algorithm is described in section 3.4.2. The conceptual description and the understanding of the hindrance effect is much less mature than the Marangoni effect. Hence, only preliminary results, including the modelling of the hindrance effect, will be presented here; see sections 6.2.2.2 and 6.2.2.4.

The various simulation results are compared either in terms of local Sherwood number (see section 4.4 for its definition) or in terms of the mass transfer coefficient k_l, a global quantity that is computed as follows:

$$k_l = \frac{|\dot{n}_\Sigma|}{A_{\text{eq}} \Delta c_i} = \frac{D_\ell \sum_f \left(\partial_n c_\ell|_{\Sigma,f} A_f\right)}{A_{\text{eq}} \left(c_g|_\Sigma - c_{i,\infty}\right)}, \tag{6.11}$$

where $A_{\text{eq}} = \pi d_{\text{eq}}^2$ is the equivalent surface area and A_f the face area. For a 2D test case, the equivalent surface area corresponds to the surface of the cylinder, i.e. $A_{\text{eq}} = \pi d_{\text{eq}} h_{\text{cyl}}$, where h_{cyl} is the thickness of the 2D domain. Another global quantity is the global Sherwood number, which is computed from the mass transfer coefficient as

$$\text{Sh}_{\text{gl}} = \frac{k_l \; d_{\text{eq}}}{D_\ell}. \tag{6.12}$$

In the following discussion only the mass transfer coefficient is considered, because the global Sherwood number would show the same trend.

6.2.1 Reactive mass transfer from a 3D bubble rising in a contaminated solution

An oxygen bubble ($d_B = 0.7, 0.75, 0.8$ mm) rising in pure water and in a contaminated solution with C_{12}DMPO is considered. The case set-up, similar to the one in section 6.1.1, is described in details in [97], where also the comparison with experimental data is reported. The surfactant and species transfer equations are solved independently. For the mass transfer, a decay reaction is considered and the reactive SGS model outlined in section 3.3.4 is employed. Here, only a selection of the results is reported to show the main effect of surfactant on the mass transfer. In figure 6.28, the terminal rise velocities of the clean and contaminated bubbles are compared to correlations found in the literature to further confirm the validity of the simulation results and to underline the differences in terminal velocities for the clean and the contaminated cases.

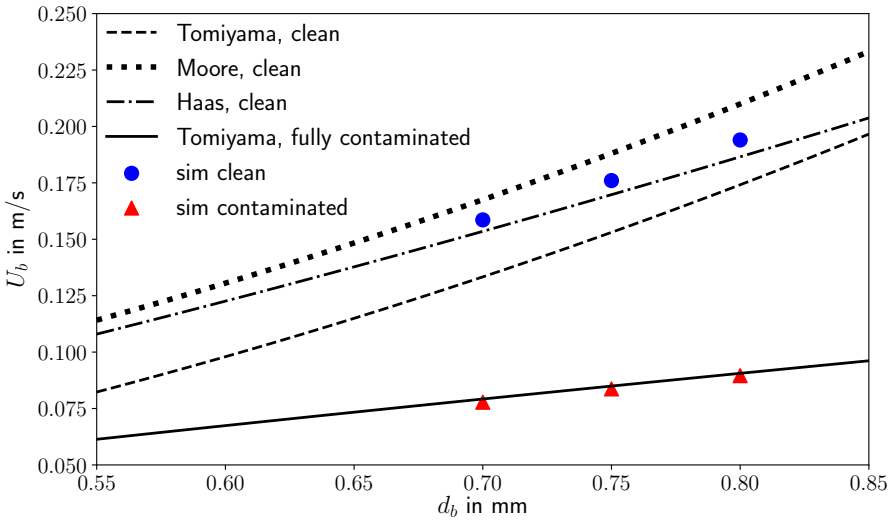

Figure 6.28: Bubble rise velocity according to simulations and correlations. The reference velocities (depicted as lines) were computed based on correlations for the drag coefficient c_D. See [97, table 7] for a summary of the correlations and their sources. Figure based on [97].

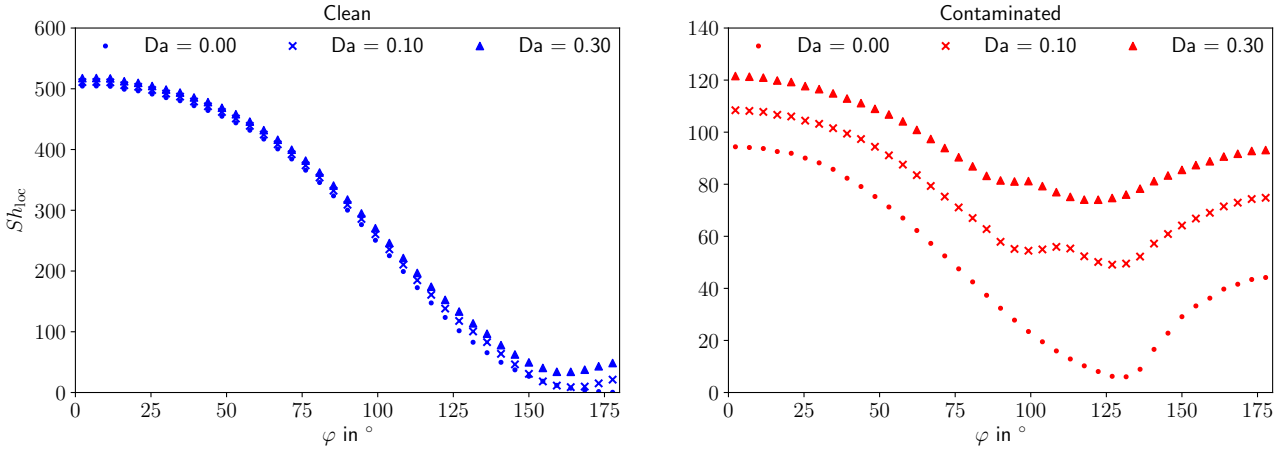

Figure 6.29: Local reactive Sherwood number over the polar angle for a clean (left) and contaminated (right) interface. Figure based on [97].

For the bubble with diameter $d_B = 0.75$ mm, the mass transfer problem is solved with different reaction rate constants, i.e. for different Da. The results in terms of local Sherwood numbers are depicted in figure 6.29 against the polar angle. As expected, the mass transfer is drastically reduced in the presence of surfactant. Regarding the reactive mass transfer, the enhancement of species transfer at the immobilized interface is much stronger. Additionally, a non-uniform local mass transfer enhancement in the presence of surfactant is visible, especially in the rear part of the bubble. The interested reader is referred to [97] for further discussions on the simulation results and the comparison with experimental data.

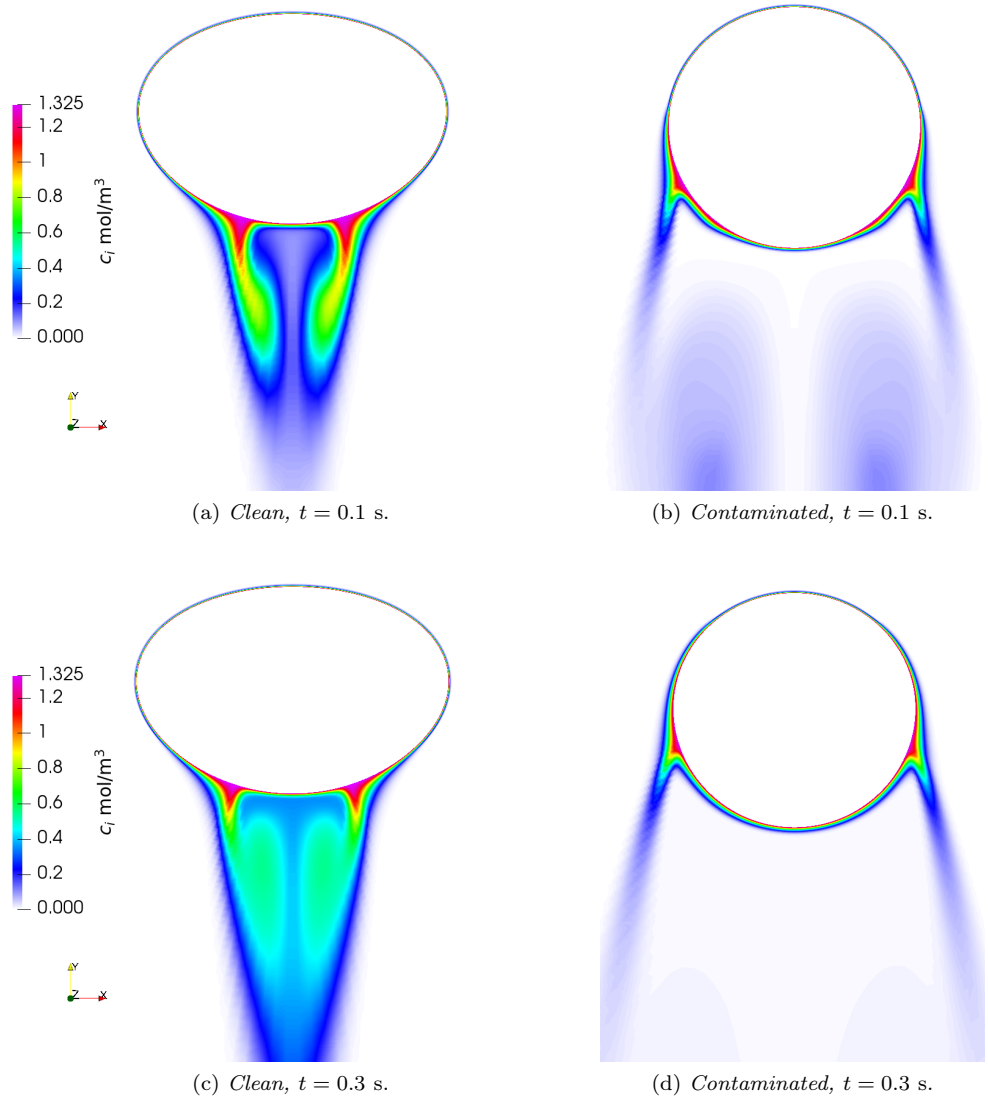

(a) *Clean*, $t = 0.1$ s. (b) *Contaminated*, $t = 0.1$ s.

(c) *Clean*, $t = 0.3$ s. (d) *Contaminated*, $t = 0.3$ s.

Figure 6.30: Concentration fields around a 2D bubble rising in contaminated solution, clean case and contaminated case with Henry model (no hindrance effect).

6.2.2 Mass transfer from a 2D bubble rising in a contaminated solution

A two-dimensional rising bubble test case is considered. The bubble radius is taken equal to $r_B = 0.6$ mm. The test case set-up is similar to the one described in sections 5.1 and 4.6.2. The dissolution of oxygen, O_2, and carbon dioxide, CO_2, in water is considered. In both cases the contaminant is C_{12}DMPO, whose properties can be found in table 6.2.

6.2.2.1 Surfactant effect on oxygen dissolving in water

The transfer of oxygen from the gas phase into the liquid is considered. The fluid properties for the liquid and the gas phase are reported in table 6.8.

Table 6.8: Fluid properties at $T = 295$ K.

ρ^+ kg/m^3	μ^+ kg/(ms)	ρ^- kg/m^3	μ^- kg/(ms)	σ_0 N/m
997.3	$9.3 \cdot 10^{-4}$	1.1965	$1.83 \cdot 10^{-5}$	0.0724

The oxygen concentration in the gas phase is $c_g = c_g|_\Sigma = 41.95$ mol/m^3 (pure O_2 bubble at standard conditions). The Henry coefficient for oxygen is $H_{O_2} = 31.0$, the diffusivity of oxygen in the water is $D_{O_2} = 2.0 \cdot 10^{-9}$ m^2/s. At $t = 0$, the oxygen concentration in water is set to zero. The mass transfer problem is solved with the Henry model, i.e. mass transfer and surfactant transport are solved independently.
The species concentration fields for the clean and a contaminated (Henry model) cases at different time steps are depicted in figure 6.30. The mass transfer reduction due to the presence of surfactant is remarkable. This difference can be better appreciated looking at the evolution of the mass transfer coefficient over time; see figure 6.31. Here it is shown that the mass transfer, just seeing a modified flow field, is reduced by more than 50%.

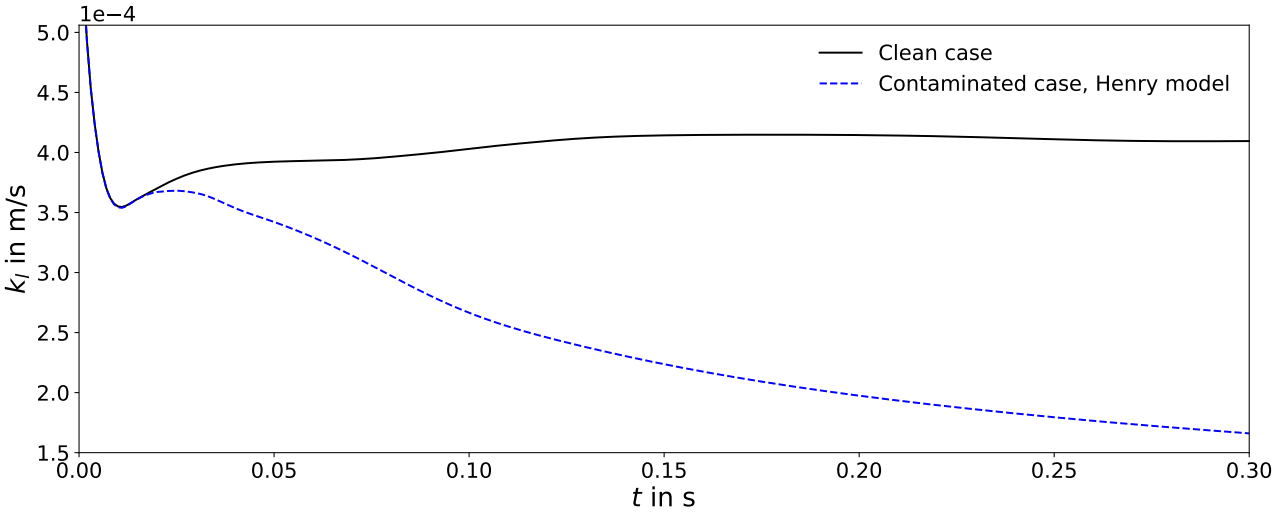

Figure 6.31: Mass transfer coefficient k_l over time for clean and contaminated cases.

6.2.2.2 Hindrance effect on oxygen dissolving in water

The mass transfer problem here is solved with the modified boundary condition to account for the surfactant presence. Different reduction factors $\overline{k}$ are considered. For the moment, as there are no inputs from the experimental side, the values of $\overline{k}$ are chosen arbitrarily, but with the limitation on the species concentration at the interface as described above. The evolution of the mass transfer coefficient over time is depicted in figure 6.32, where the results with the hindrance model are plotted together with the ones from figure 6.31. Only a very small reduction, up to 0.65% is referable to the hindrance effect; see figure 6.33. In fact, here, to have a precise measure of the hindrance effect for the contaminated cases, the quantity

$$\frac{|c_{i,\text{Henry}} - c_i|}{c_{i,\text{Henry}}} \cdot 100\% \tag{6.13}$$

is computed and plotted over time for the different reduction factors.

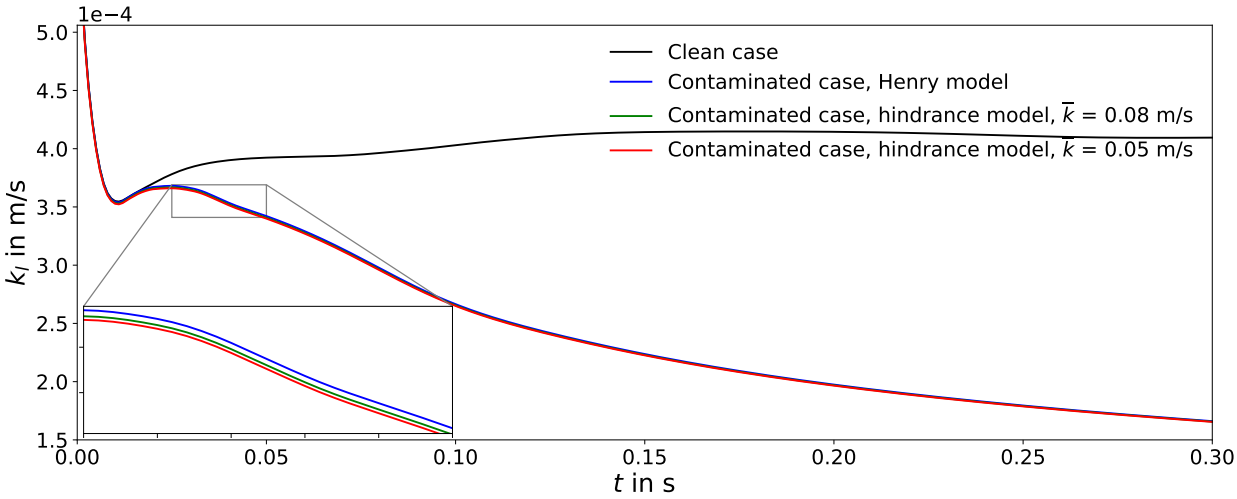

Figure 6.32: Mass transfer coefficient k_l over time for clean and contaminated cases.

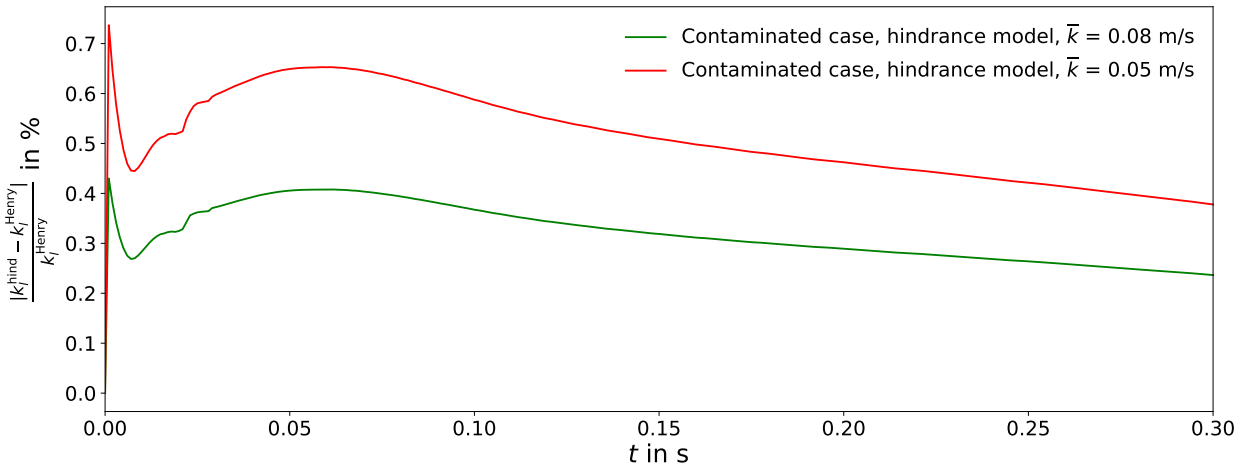

Figure 6.33: Mass transfer coefficient k_l difference (in %) between Henry and hindrance model for $\overline{k} = 0.08,\ 0.05$.

In figure 6.34, the local difference between the concentration fields obtained with Henry and with hindrance effect are reported. As can be seen from figure 6.34, the local mass transfer reduction referable to the hindrance effect is below 0.55%. For this test case, it can be concluded that the major reduction in the mass transfer with respect to the clean case is the consequence of the modified flow field around the bubble due to the presence of surfactants.

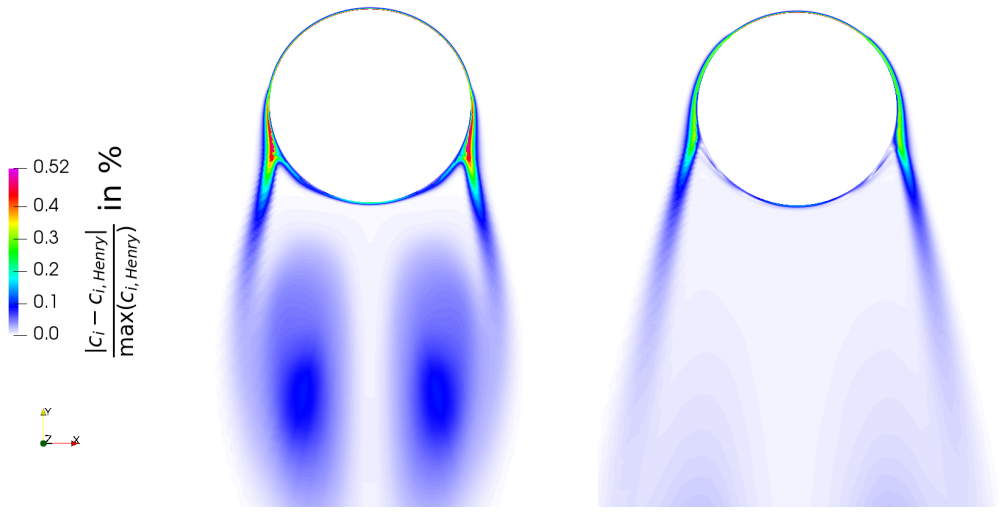

(a) $t = 0.1$ s. (b) $t = 0.3$ s.

Figure 6.34: Difference in % in the concentration fields around a 2D bubble rising in contaminated solution between mass transfer with Henry model and hindrance model, $\overline{k} = 0.05$.

6.2.2.3 Surfactant effect on carbon dioxide dissolving in water

A second set of test cases has been performed considering the dissolution of carbon dioxide from the bubble into the liquid phase. CO_2 has been chosen because stronger hindrance effects are expected, as the Henry coefficient of carbon dioxide is much smaller than the one of oxygen. The carbon dioxide concentration in the gas phase is $c_g = c_g|_\Sigma = 40.54$ mol/m^3. The Henry coefficient for CO_2 is $H_{CO_2} = 1.2$, the diffusivity of carbon dioxide in water is $D_{CO_2} = 1.9 \cdot 10^{-9}$ m^2/s. At $t = 0$, the carbon dioxide concentration in the water is set to zero. The fluid properties for the liquid and the gas phase are reported in table 6.9.

Table 6.9: Fluid properties at $T = 298$ K.

ρ^+ kg/m^3	μ^+ kg/(ms)	ρ^- kg/m^3	μ^- kg/(ms)	σ_0 N/m
997.13	$8.9 \cdot 10^{-4}$	1.784	$1.496 \cdot 10^{-5}$	0.0724

Table 6.10: Surfactant initial bulk concentrations and reduction factors for the parameter study.

$c(t=0)$ in mol/m^3	$5 \cdot 10^{-4}$	$1 \cdot 10^{-3}$	$2 \cdot 10^{-3}$	$5 \cdot 10^{-3}$	$8 \cdot 10^{-3}$	$1 \cdot 10^{-2}$	$2 \cdot 10^{-2}$	$5 \cdot 10^{-2}$
k_{red} in m/s	$6 \cdot 10^{-4}$	$8 \cdot 10^{-4}$	$1 \cdot 10^{-3}$	$2 \cdot 10^{-3}$	$4 \cdot 10^{-3}$	$6 \cdot 10^{-3}$	$1 \cdot 10^{-2}$	$1 \cdot 10^{-1}$

The parameter study covers different surfactant initial bulk concentrations, as reported in table 6.10. First, the mass transfer in clean and contaminated systems without hindrance effect (Henry's law) is investigated. The bubble rise velocities with different levels of contamination are reported in figure 6.35. The vertical dashed lines mark the times where local and global data are analysed in more details below. Note that the simulations were stopped at $t = 0.3$ s[5].

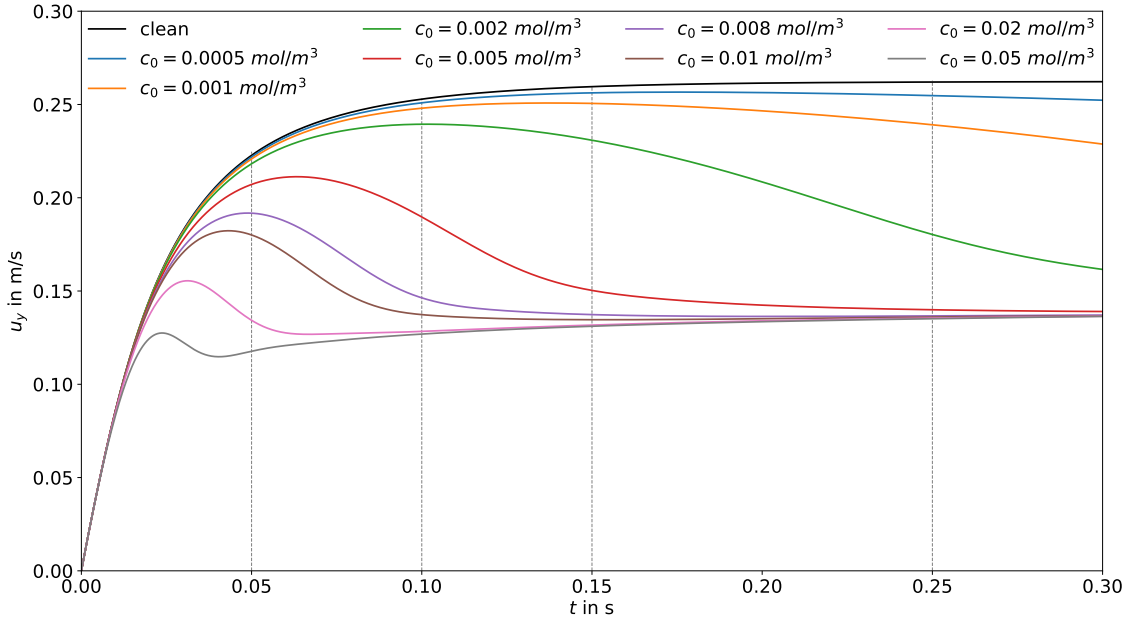

Figure 6.35: Bubble rise velocities under the effect of surfactant.

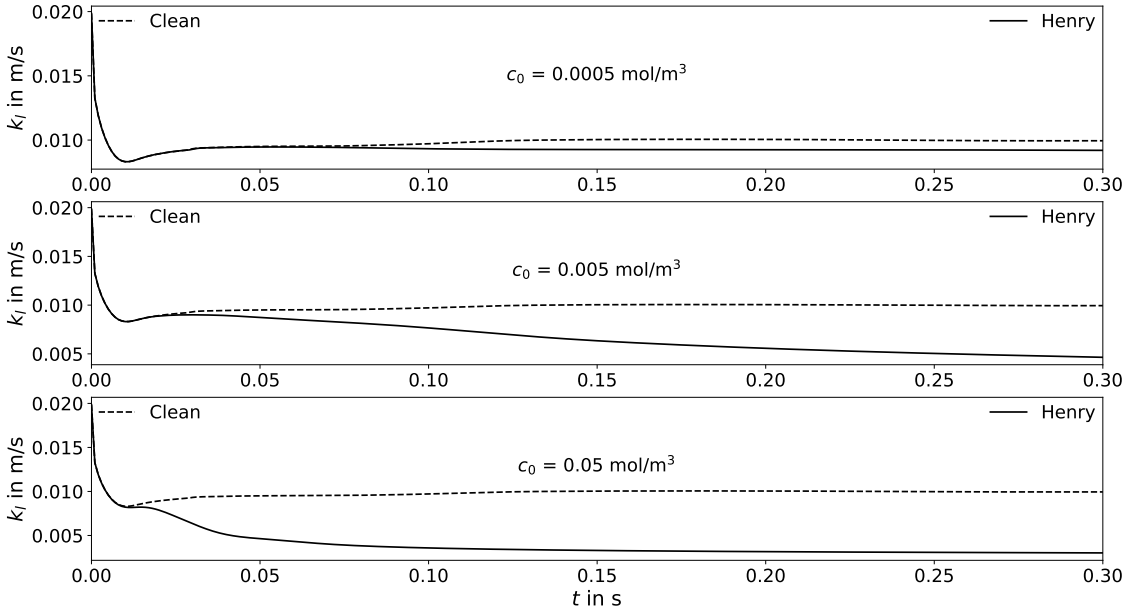

Figure 6.36: Mass transfer coefficient over time, clean and contaminated (Henry) cases.

[5]The bubble motion would be a three-dimensional non axisymmetric one and the lack of the third direction in the 2D test case results in non usable simulation data after the given time.

The mass transfer coefficients over time for a subset of the cases studied for the clean case and the cases without hindrance effects (the latter denoted by the label *Henry*) are depicted in figure 6.36. As can be seen from figure 6.36, an increase in the initial bulk surfactant concentration has a strong effect on the hydrodynamics and the mass transfer coefficients are reduced notably.

6.2.2.4 Hindrance effect on carbon dioxide dissolving in water

The mass transfer problem is then solved including the hindrance effect modelling with the various reduction factors listed in table 6.10. Figure 6.37 summarizes the mass transfer coefficients over time for the selected cases. Note that the cases with Henry's law, depicted in black, practically coincides with the cases with the highest reduction factor, i.e. gray lines.

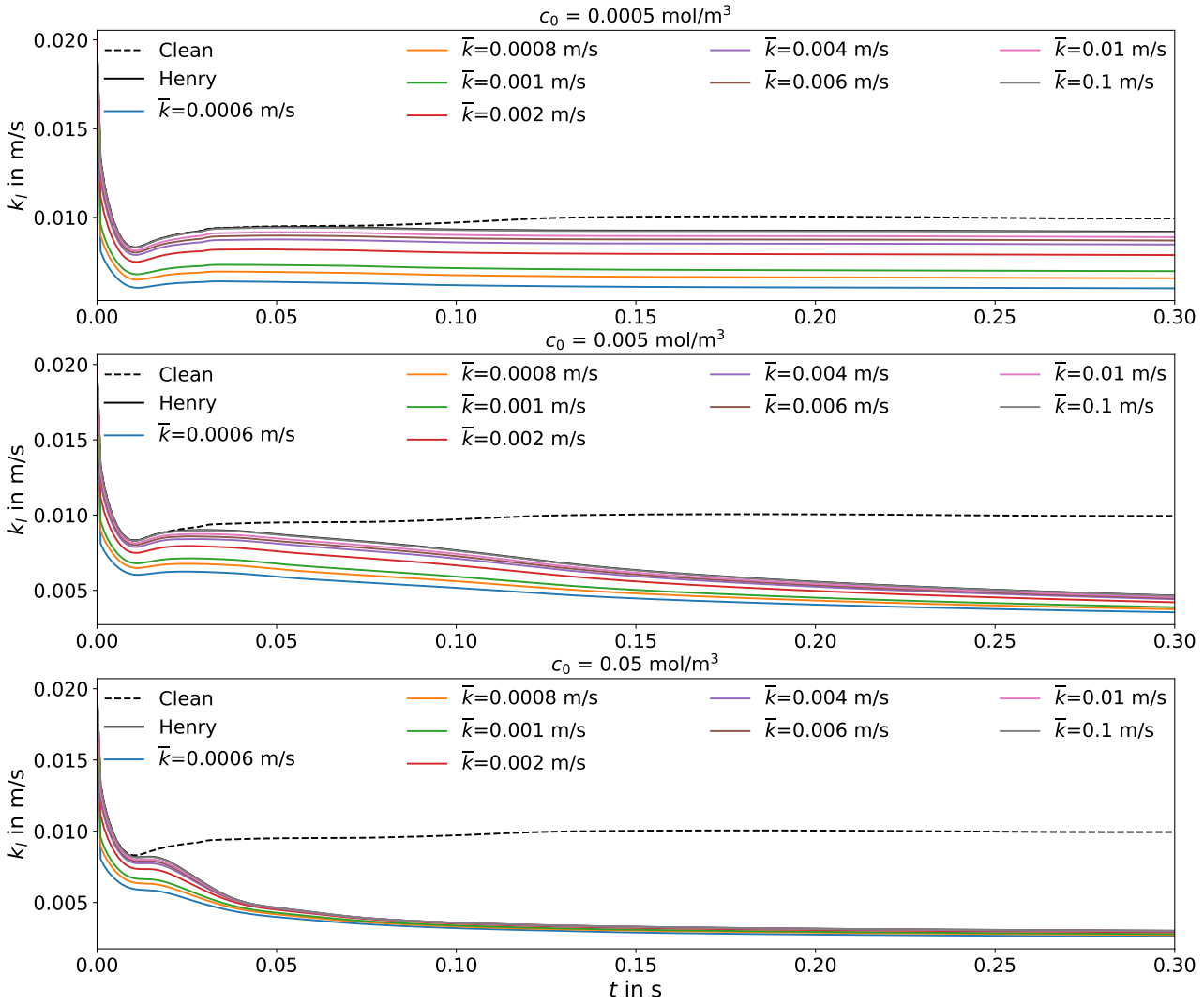

Figure 6.37: Mass transfer coefficient over time, clean and contaminated cases.

In this test case, the hindrance effect is much more pronounced than for the oxygen dissolving in water. The hindrance effect of the surfactant on the mass transfer is the strongest for the smallest contaminations and during the acceleration phase at the beginning of the bubble rise.

This behaviour is related to the molar flux; see equation (3.59). The hindrance effect is large when the molar flux $\dot{n}$ is large, i.e. during the acceleration phase or for low contaminations when the convective species transport at the interface is strong.
To have a precise measure of the hindrance effect for the contaminated cases, equation (6.13) is applied, and the difference between Henry and hindrance models is plotted over time for the different initial surfactant bulk concentrations in figure 6.38.

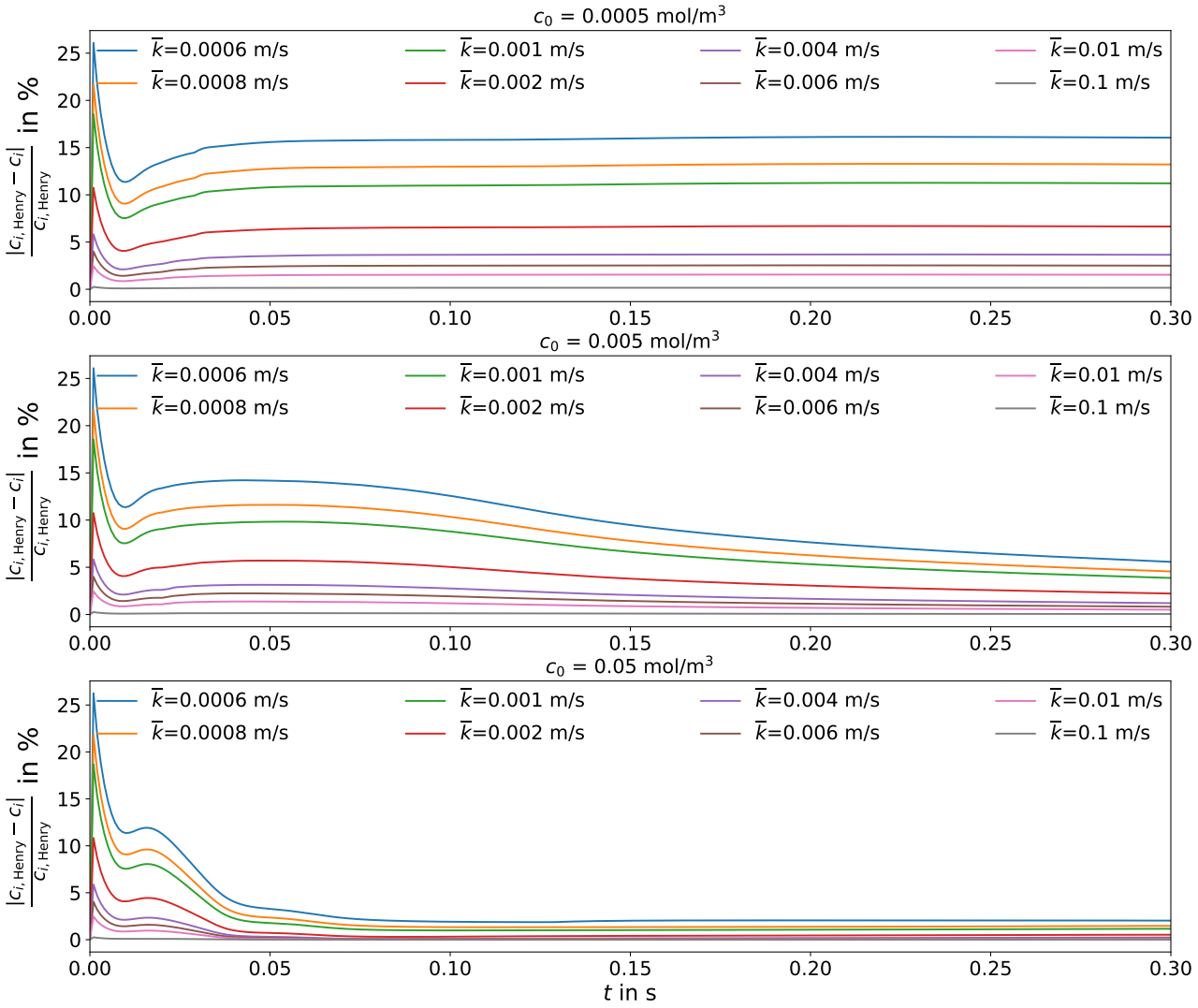

Figure 6.38: Mass transfer coefficient difference in % between Henry's law and hindrance effect for different initial surfactant bulk concentrations c_0.

As can be seen from figure 6.38, the presence of a very small amount of surfactant can have a hindrance effect on the mass transfer up to slightly above 15%. Nevertheless, as noticed before, increasing the initial surfactant concentration changes the flow field around the bubble dramatically and the mass transfer is reduced accordingly. In the most contaminated cases, apart from a pronounced hindrance effect (up to about 13%) of the surfactant on the mass transfer in the bubble acceleration phase, the hindrance effect reduces to less than 3% when the bubble reaches the steady state.

In figure 6.39, the dependence of the mass transfer coefficient on the reduction factor is depicted for the different initial surfactant concentrations at the marked time instances. As can be seen from this plot, the reduction of the mass transfer due to the presence of surfactant is less and less sensitive to the reduction factor for increasing surfactant concentrations.

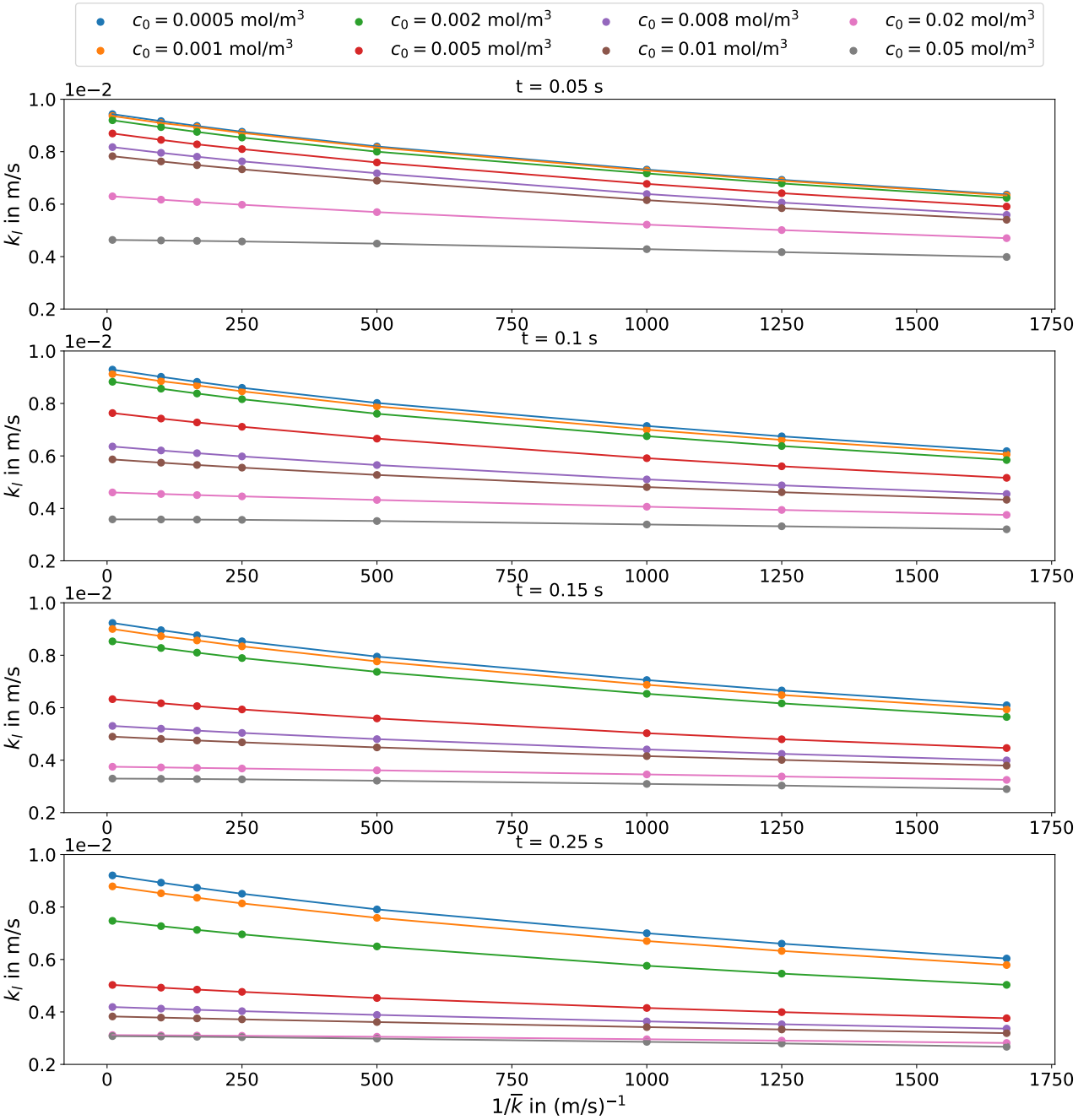

Figure 6.39: Mass transfer coefficient k_l with respect to the reduction factor $1/\overline{k}$.

Moreover, to highlight the dependence of the mass transfer coefficient on the initial surfactant bulk concentration, figure 6.40 is provided. Also for this plot, different time instances are considered. With increasing contamination levels, the mass transfer is more and more re-

duced, but the reduction due to the hindrance effects is marginal for the two highest surfactant concentrations.

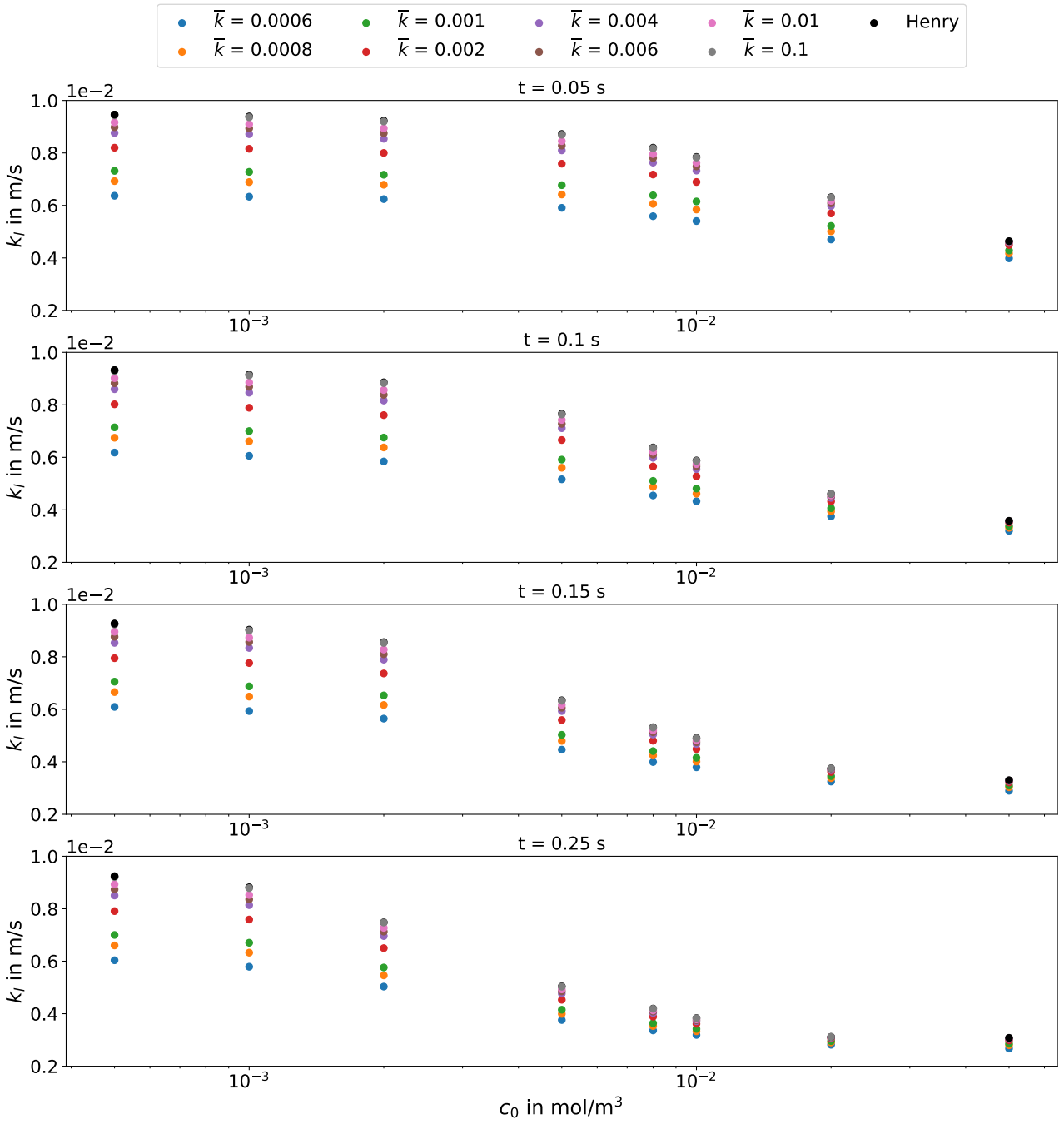

Figure 6.40: Mass transfer coefficient k_l with respect to the initial surfactant bulk concentration c_0.

Figures 6.41 to 6.43 show the flow field and the species bulk distribution at different time instances for the clean and the two contaminated cases (Henry and hindrance models). In all cases recirculation regions in the bubble wake appear. In the clean case, as expected and in agreement with the computed mass transfer coefficient, the species bulk concentration is the highest. In the contaminated cases, the mass transfer is reduced and small differences in the

amount of dissolved species in the liquid phase are visible from the comparison between Henry and hindrance model. Possibly, more remarkable differences could be visible if the bubble wake mesh was finer. In fact, the results in the wake look too diffusive and tests on finer meshes are necessary.
In conclusion, it is important to underline that the latter results are part of an initial study on the hindrance effect of surfactant on mass transfer and much more work has to be done in this field. First of all, the reduction factor has to be estimated from experiments, as described in the modelling section 2.3. Second, here only one surfactant species has been considered. The C_{12}DMPO is known to follow a *fast* sorption mechanism; it would be interesting to see the effects on mass transfer from a surfactant showing *slow* sorption dynamics. Moreover, since the hindrance effects depends not only on the reduction factor and surface tension distribution, but also on the reduction in surface tension $\sigma_0 - \sigma$, it would be interesting to study the effects of different surfactant species with varying surface activity. The maximum reduction in surface tension due to the presence of C_{12}DMPO is approximately 2.6% for the most contaminated case in the simulated physical time.

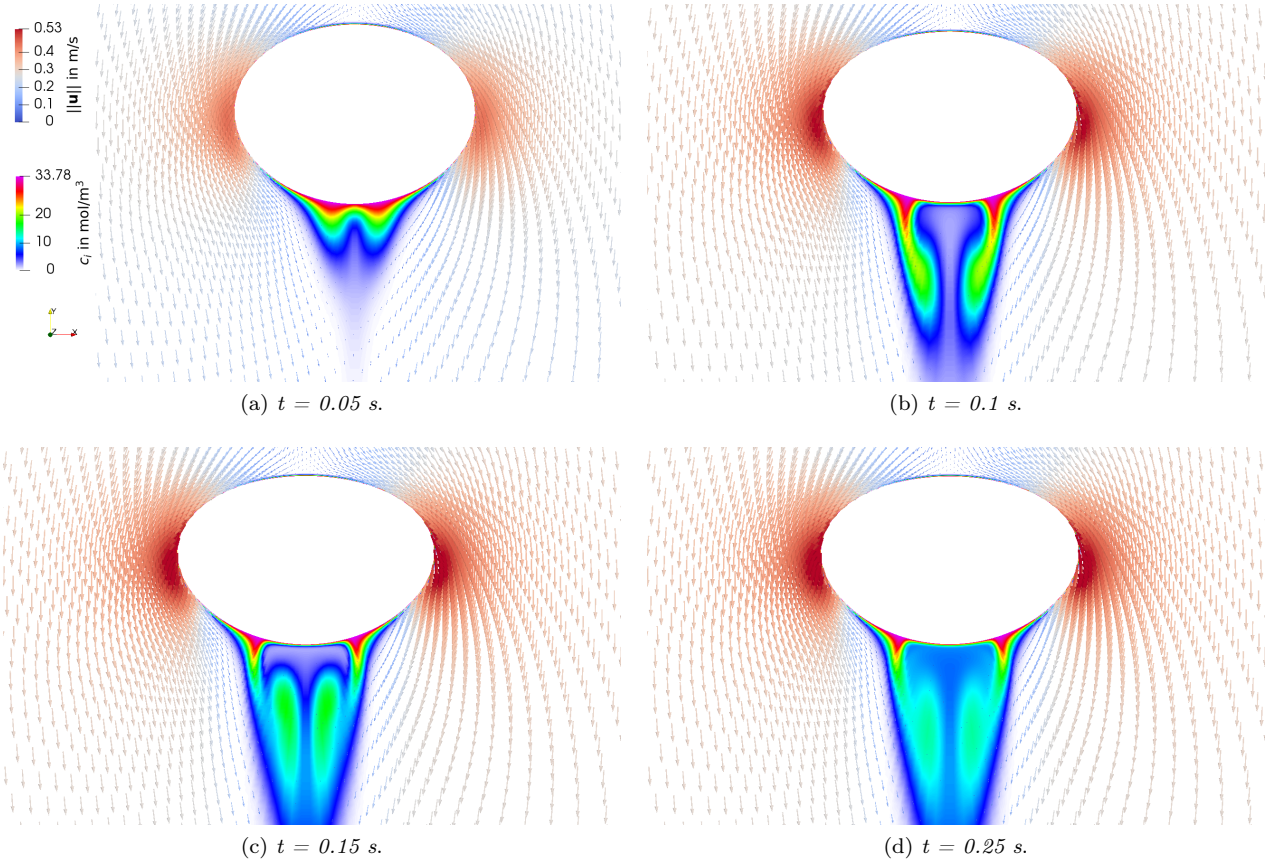

(a) *t = 0.05 s.*

(b) *t = 0.1 s.*

(c) *t = 0.15 s.*

(d) *t = 0.25 s.*

Figure 6.41: Flow field and species distribution in the bulk phase for the clean case.

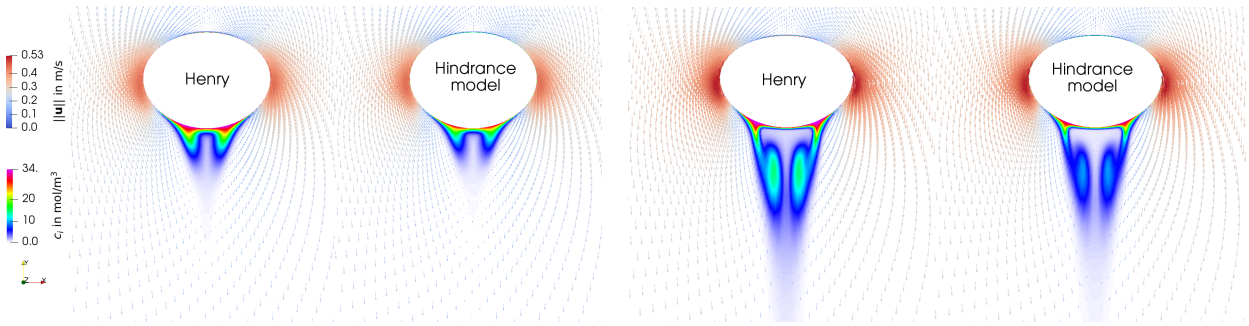

(a) $t = 0.05$ *s*. (b) $t = 0.1$ *s*.

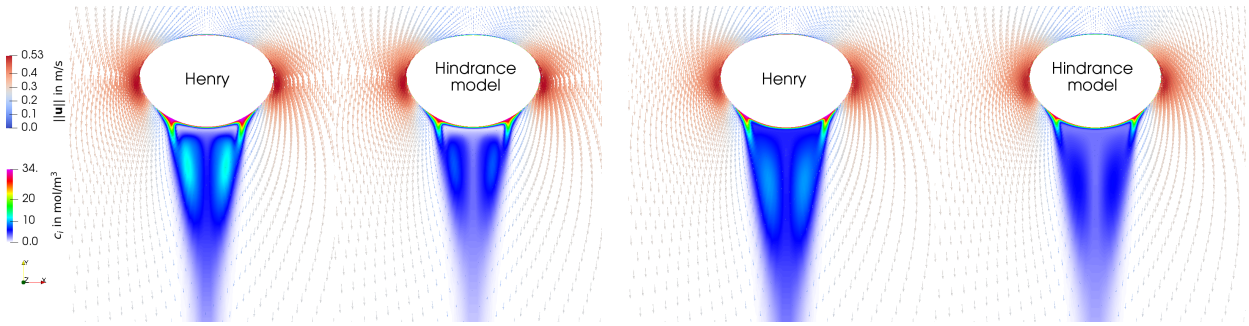

(c) $t = 0.15$ *s*. (d) $t = 0.25$ *s*.

Figure 6.42: Flow field and species distribution in the bulk phase for the least contaminated case; comparison between Henry's law mass transfer (left) and hindrance effect (right).

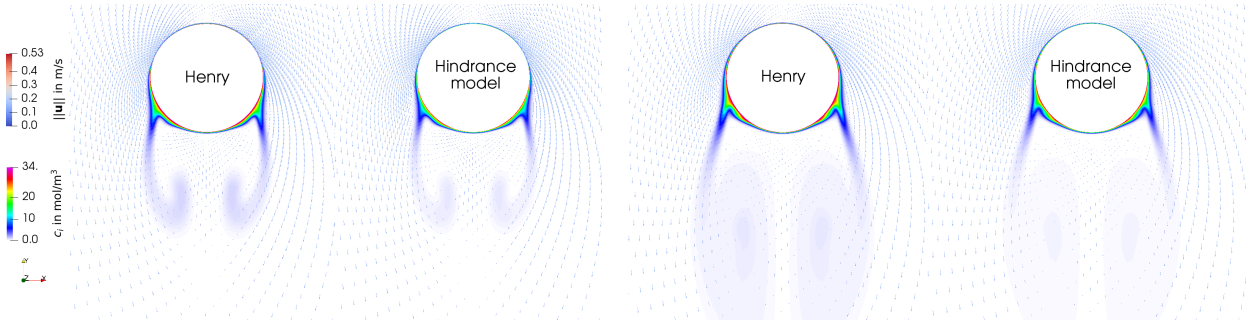

(a) $t = 0.05$ *s*. (b) $t = 0.1$ *s*.

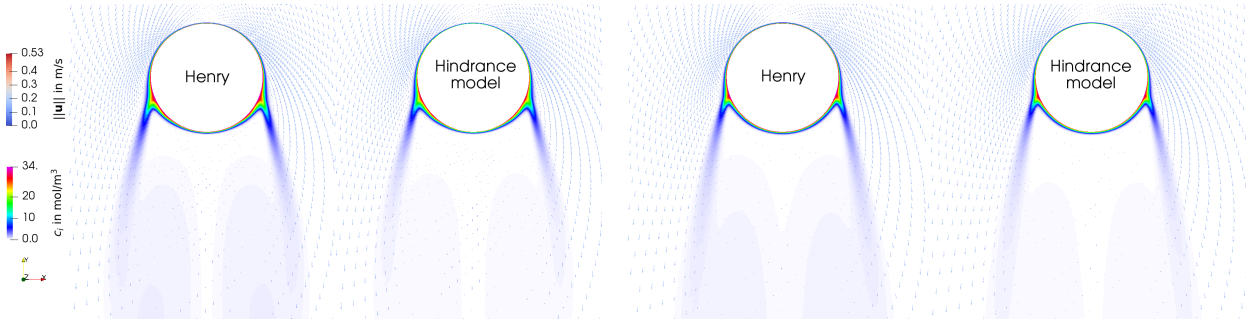

(c) $t = 0.15$ *s*. (d) $t = 0.25$ *s*.

Figure 6.43: Flow field and species distribution in the bulk phase for the most contaminated case; comparison between Henry's law mass transfer (left) and hindrance effect (right).

Chapter 7

Summary and outlook

7.1 Summary

The focus of the current work is on the dynamics of single bubbles rising in a solution contaminated with surfactant. Within this study, it has been possible to investigate realistic length and time scales thanks to a subgrid-scale model, and the available experimental results could be reproduced well. The necessity of a subgrid-scale model has been proven via specific test cases involving thin species boundary layers. The same methodology that allowed to simulate realistic surfactant systems has been applied to mass transfer problems to study the effect of surfactant on mass transfer.

First, a thorough validation and verification of the numerical methodology have been performed to assure high quality and reliable results. Then, a realistic application set-up has been investigated: a single bubble rising in contaminated solutions. For this topic, the influence of the initial surface coverage on the bubble rise velocity has been studied. In the experiments, there is a certain detachment time including the bubble formation till the release. During this phase, adsorption mechanisms are already occurring such that the bubble is pre-contaminated at release. The results show that the initial transient stage is very sensitive to the initial surface concentration. With a parameter study, varying the initial surface contamination, the initial surface coverage corresponding to the experiments could be found, a value that was not known a priori. For very high bulk concentrations, it has been demonstrated that a lower initial surface contamination than the one suggested by the theory (equation (6.2)) was already sufficient to obtain the correct bubble transient velocity. This information is fundamental in view of application cases because the initial stage determines, for instance, the position of the bubble in a channel or column, but also the mass transfer process is affected by the amount of surfactants on the interface and therefore the flow field around the bubble.

The focus then moved on to study the influence of the initial bulk concentration on the rise velocity and the flow field around the bubble. From the simulation results, global and local quantities can be evaluated. The bubble path depends both on the initial surface and bulk contaminations. For the least contaminated cases, a transition from helical to a zig-zag path is observed, as in the experimental work by [83]. It has also been found that the quasi-steady state velocity can be reached without ad- and desorption being in equilibrium. Moreover, the transfer of surfactant in the sub-layer in a steady-state regime of the bubble rise velocity is close to the mass transfer at a solid particle. The local vorticity fields have been used to characterize the flow in the vicinity of the bubble to understand the formation of vortices in the bubble

wake.
The forces acting on the bubble surface have been studied considering their contribution to lift and drag forces. The dynamic pressure force, being the major contributor to the lift force, is responsible for the deviation from a rectilinear path. The steady state terminal velocity is a consequence of the overall drag force. For higher surfactant bulk concentrations, the viscous drag force increases due to higher surface tension gradients. At the same time, the dynamic pressure force decreases due to the reduced mobility of the interface. These two counter-acting effects lead to an approximately constant overall drag force. In other Reynolds regimes, for example for very small bubbles as the one considered in [85] that rise along a straight path even if contaminated, these mechanisms could perhaps be different.
From the local distribution of the Marangoni forces it has been shown that the detachment of the flow from the bubble surface occurs where the Marangoni stresses are the highest. The quasi steady-state situation corresponds to a more uniform distribution of the Marangoni forces on the upper hemisphere of the bubble surface. These findings are relevant for deriving simplified models such as an improved stagnant-cap model. In fact, one should refer to the quasi steady-state not in terms of a "fully contaminated" surface, but regarding a certain Marangoni force distribution. The latter depends on the surfactant distribution on the interface and not, above a certain threshold, on the amount of surfactant on Σ. This implies that at quasi steady-state the surface concentration is not necessarily equal to the equilibrium concentration.
Considering the local sorption, advection and diffusion processes at the interface, three different stages during the bubble rise have been identified. A first stage where the adsorption rates are the highest, a second stage where the transport at the front of the bubble is advection-dominated while in the rear part it is diffusion-dominated, and a third stage with a uniform distribution of the Marangoni forces in the upper hemisphere of the bubble. A further transition to a fourth stage is foreseeable, but a much longer physical time would have to be simulated since also the adsorption steadily decreases. Such an investigation shall be part of future studies.

7.2 Outlook

First, to reduce the computational costs to simulate slow sorption processes of surfactants, a subgrid-scale model for this problem should be derived and implemented. Note that in this case, the boundary condition at the interface for the surfactant bulk transport is of Neumann type, i.e. the surfactant gradient at the interface is imposed.
With a subgrid-scale model available for both the sorption process, further applications could be studied. Also, simulations of bubbles in other flow regimes/larger bubbles rising in contaminated solutions should be performed and investigated. Bubbles up to 2 mm diameter have been simulated in the work of M. Steinhausen [81], but further investigations are necessary. Furthermore, more detailed experimental results to compare with are required. For instance, the experimental data should offer high-frequency measurements, mainly in the initial part of the bubble rise and should provide not only the rise velocity but also the information on the bubble lateral position/path. The latter could be obtained with the aid of two cameras recording the bubble rise from two different angles.
Also, the derivation of simplified models to account for the presence of surfactant in the bulk phase should be derived. A first tentative in this direction has been done in [81]. The next step would be to use the simplified model in other numerical frameworks, e.g. with Volume of Fluid (VoF) methods.

Regarding the mass transfer under the influence of surfactant, the results presented in this work (from [97] and the 2D test case) confirmed the occurance of a strong mass transfer reduction in the presence of surfactant. Moreover, the comparison with the experimental results reported in [97] confirmed the high accuracy and reliability of the results obtainable with the numerical procedure described in this work. However, only a draft derivation of the mathematical model of the hindrance effect and preliminary 2D results have been presented. Future works could focus on the modelling of this phenomenon continuing the work in [4, 7, 5]. In parallel, experimental studies could be performed, first to extract the mass transfer reduction coefficient necessary for the simulations, and, second, to provide test cases to validate and compare the numerical results for a deeper understanding of the phenomenon. In this context the numerical model has to be improved, too. In fact, the implementation and validation of the numerical model for the full mass transfer problem with Dirichlet-Neumann coupling at the interface and the hindrance effect taken into account should be done. Within the Interface Tracking framework, some studies regarding mass transfer have been performed (see [94, 28]), but they should be extended to account for the presence of surfactants.

Appendix A

Derivation of the balance equations for the ALE method

The derivation of the integral form of the balance equations for mass, momentum or, in general, of a quantity $\boldsymbol{\phi}$[1] starts from the Reynolds transport theorem (RTT). The RTT for a control volume $V(t)$, with boundary $\partial V(t)$ moving with velocity $\mathbf{w}$ and normal to the boundary $\mathbf{n}$, reads

$$\frac{d}{dt}\int_{V(t)} \boldsymbol{\phi}\, dV = \int_{V(t)} \partial_t \boldsymbol{\phi}\, dV + \int_{\partial V(t)} \boldsymbol{\phi} \otimes \mathbf{w} \cdot \mathbf{n}\, dS. \tag{A.1}$$

A.1 Integral balance equations for a single phase

To write the integral balance for a single phase, an arbitrary control volume $V(t)$ not crossing the interface is considered. The balance equations for mass, momentum, species molar mass are derived.

A.1.1 Integral mass balance

Applying the RTT with the transported quantity $\boldsymbol{\phi} = \rho$ yields

$$\frac{d}{dt}\int_{V(t)} \rho\, dV = \int_{V(t)} \partial_t \rho\, dV + \int_{\partial V(t)} \rho \mathbf{w} \cdot \mathbf{n}\, dS. \tag{A.2}$$

Locally, the mass balance reads

$$\partial_t \rho + \nabla\cdot(\rho \mathbf{v}) = 0, \tag{A.3}$$

where $\mathbf{v}$ is the fluid velocity[2]. From (A.3) an expression for $\partial_t \rho$ is derived and substituted in equation (A.2) gives

$$\frac{d}{dt}\int_{V(t)} \rho\, dV = -\int_{V(t)} \nabla\cdot(\rho \mathbf{v})\, dV + \int_{\partial V(t)} \rho \mathbf{w} \cdot \mathbf{n}\, dS. \tag{A.4}$$

[1] The quantity $\boldsymbol{\phi}$ can be a scalar, e.g. the density ρ or the molar concentration c, or a vector, e.g. the momentum $\rho\mathbf{v}$.
[2] The local form of the mass balance can be derived considering a co-moving control volume, i.e. $\mathbf{v} = \mathbf{w}$.

Applying the divergence theorem to the first term on the right-hand side[3], equation (A.4) results in the integral balance equation for the mass in the moving control volume $V(t)$ which reads

$$\frac{d}{dt}\int_{V(t)} \rho \, dV = -\int_{\partial V(t)} \rho(\mathbf{v}-\mathbf{w})\cdot\mathbf{n} \, dS. \tag{A.5}$$

A.1.2 Integral momentum balance

Applying the RTT with the transported quantity $\boldsymbol{\phi} = \rho\mathbf{v}$ yields

$$\frac{d}{dt}\int_{V(t)} (\rho\mathbf{v}) \, dV = \int_{V(t)} \partial_t(\rho\mathbf{v}) \, dV + \int_{\partial V(t)} (\rho\mathbf{v})\otimes\mathbf{w}\cdot\mathbf{n} \, dS. \tag{A.6}$$

Locally, the momentum balance reads

$$\partial_t(\rho\mathbf{v}) + \nabla\cdot(\rho\mathbf{v}\otimes\mathbf{v}) = \nabla\cdot\mathbf{S} + \rho\mathbf{b}, \tag{A.7}$$

where $\mathbf{S}$ is the stress tensor and $\mathbf{b}$ represents the body force density[4]. From (A.7) an expression for $\partial_t(\rho\mathbf{v})$ can be derived and substituted in equation (A.6), which becomes

$$\frac{d}{dt}\int_{V(t)} (\rho\mathbf{v}) \, dV = -\int_{V(t)} \nabla\cdot(\rho\mathbf{v}\otimes\mathbf{v}) \, dV + \int_{V(t)} \nabla\cdot\mathbf{S} \, dV + \int_{V(t)} \rho\mathbf{b} \, dV + \int_{\partial V(t)} \rho\mathbf{v}\otimes\mathbf{w}\cdot\mathbf{n} \, dS. \tag{A.8}$$

Applying the divergence theorem to the first and second term on the right-hand side, equation (A.8) results in the integral balance equation for the momentum in the moving control volume $V(t)$, namely

$$\frac{d}{dt}\int_{V(t)} (\rho\mathbf{v}) \, dV = -\int_{\partial V(t)} \rho\mathbf{v}\otimes(\mathbf{v}-\mathbf{w})\cdot\mathbf{n} \, dS + \int_{\partial V(t)} \mathbf{S}\cdot\mathbf{n} \, dS + \int_{V(t)} \rho\mathbf{b} \, dV. \tag{A.9}$$

A.1.3 Integral species transport equation

Applying the RTT with the transported species $\boldsymbol{\phi} = c_i$ yields

$$\frac{d}{dt}\int_{V(t)} c_i \, dV = \int_{V(t)} \partial_t c_i \, dV + \int_{\partial V(t)} c_i\mathbf{w}\cdot\mathbf{n} \, dS. \tag{A.10}$$

Locally, the species molar concentration balance reads

$$\partial_t c_i + \nabla\cdot(c_i\mathbf{v} + \mathbf{j}_i) = r_i, \tag{A.11}$$

where $\mathbf{j}_i$ is the diffusion flux and r_i is the source term (due to possible chemical reactions). From (A.11) an expression for $\partial_t c_i$ can be derived and substituted in equation (A.10), which becomes

$$\frac{d}{dt}\int_{V(t)} c_i \, dV = \int_{V(t)} r_i \, dV - \int_{V(t)} \nabla\cdot(c_i\mathbf{v} + \mathbf{j}_i) \, dV + \int_{\partial V(t)} c_i\mathbf{w}\cdot\mathbf{n} \, dS. \tag{A.12}$$

[3]The divergence theorem for the quantity $\mathbf{f}$ reads

$$\int_{\partial V(t)} \mathbf{f}\cdot\mathbf{n} \, dS = \int_{V(t)} \nabla\cdot\mathbf{f} \, dV.$$

[4]The local form of the momentum balance can be derived considering a co-moving control volume, i.e. $\mathbf{v} = \mathbf{w}$ (without exchange of mass), and applying Newton's second law to it, $\mathbf{F} = \frac{d}{dt}(m\mathbf{v}) = m\mathbf{a}$.

Applying the divergence theorem to the second term on the right-hand side, equation (A.12) results in the integral balance equation for the species molar concentration in the moving control volume $V(t)$

$$\frac{d}{dt}\int_{V(t)} c_i \, dV = -\int_{\partial V(t)} c_i(\mathbf{v}-\mathbf{w})\cdot\mathbf{n} \, dS - \int_{\partial V(t)} \mathbf{j}_i\cdot\mathbf{n} \, dS + \int_{V(t)} r_i \, dV. \tag{A.13}$$

A.2 Local balance equations for two-phase systems

Let now $V(t)$ be a control volume crossing the interface $\Sigma(t)$ between the two phases with $V(t)\cap\Sigma(t) = S(t)$, see figure 2.1.
In two-phase systems, another force contribution appears at Σ due to the forces inside the interface:

$$\mathbf{F}_\Sigma = \int_{\partial S(t)} \sigma\mathbf{N} \, d\ell, \tag{A.14}$$

that is the force with which the surrounding surface acts on $S(t)$. This line integral can be transformed in a surface integral, $\mathbf{F}_\Sigma = \int_{S(t)} \mathbf{f}^\Sigma \, dS$, with the local surface force $\mathbf{f}^\Sigma = \sigma\kappa\mathbf{n} + \nabla_\Sigma\sigma$. After including this term in the momentum balance, equation (A.9) becomes

$$\begin{aligned}\frac{d}{dt}\int_{V(t)} (\rho\mathbf{v}) \, dV = &-\int_{\partial V(t)} \rho\mathbf{v}\otimes(\mathbf{v}-\mathbf{w})\cdot\mathbf{n} \, dS \\ &+ \int_{\partial V(t)} \mathbf{S}\cdot\mathbf{n} \, dS + \int_{V(t)} \rho\mathbf{b} \, dV + \int_{S(t)} (\sigma\kappa\mathbf{n} + \nabla_\Sigma\sigma) \, dS.\end{aligned} \tag{A.15}$$

In addition, let the control volume be co-moving with the fluid. Thus, $\mathbf{v} = \mathbf{w}$ and the integral balance equations (A.5), (A.15) and (A.13) reduce to

$$\frac{d}{dt}\int_{V(t)} \rho \, dV = 0, \tag{A.16}$$

$$\frac{d}{dt}\int_{V(t)} (\rho\mathbf{v}) \, dV = \int_{\partial V(t)} \mathbf{S}\cdot\mathbf{n} \, dS + \int_{V(t)} \rho\mathbf{b} \, dV + \int_{S(t)} (\sigma\kappa\mathbf{n} + \nabla_\Sigma\sigma) \, dS. \tag{A.17}$$

$$\frac{d}{dt}\int_{V(t)} c_i \, dV = -\int_{\partial V(t)} \mathbf{j}_i\cdot\mathbf{n} \, dS + \int_{V(t)} r_i \, dV. \tag{A.18}$$

To obtain the integral form of the equations that is actually implemented in the numerical algorithm or to get the local form of the balance equations, the RTT has to be applied again to the left-hand side of equations (A.16), (A.17) and (A.18), but this time taking into account the presence of two phases and the interface in the control volume. Note that so far c_i indicated the molar concentration of whatever species, also the surfactant species, but in the following the distinction will be necessary. A *two-phase* version of the RTT and of the divergence theorem can be derived. Here only the theorems are reported from [6].
The two-phase divergence theorem and the two-phase Reynolds transport theorem for co-moving volumes reads as follow.

Theorem (Two-phase divergence theorem)**.** *Let $V \subset \mathbb{R}^3$ be open, bounded with ∂V piecewise C^1. Let $\Sigma \subset \mathbb{R}^3$ be a C^1 surface cutting V into $V^+ \cup V^- \cup S$ with $S := \Sigma \cap V$. Let $\mathbf{f} : V \to \mathbb{R}^3$*

be continuous on $V^+ \cup V^-$ such that $\mathbf{f}_{|V^+}$, $\mathbf{f}_{|V^-}$ admit continuous extensions to $\bar{V^+}$, $\bar{V^-}$. Fix an orientation of Σ, i.e. let $\mathbf{n}_\Sigma$ be a continuous normal field on Σ. Then

$$\int_{\partial V} \mathbf{f} \cdot \mathbf{n} \; dS = \int_{V \setminus S} \nabla \cdot \mathbf{f} \; dV + \int_S [\![\mathbf{f}]\!] \cdot \mathbf{n}_\Sigma \; dS. \tag{A.19}$$

To write the two-phase Reynolds transport theorem, a definition of co-moving volume and moving interface is needed. Given a flow map Φ^t, the co-moving volume starting with V_0 at $t = t_0$ is defined as $V(t) = \Phi^t(V_0)$.

Theorem (Two-phase Reynolds transport theorem for co-moving volumes)**.** *Let $V(t) = \Phi^t(V_0)$. Then*

$$\frac{d}{dt} \int_{V(t)} \boldsymbol{\phi} \; dV = \int_{V(t) \setminus S(t)} (\partial_t \boldsymbol{\phi} + \nabla \cdot (\boldsymbol{\phi} \otimes \mathbf{v})) \; dV + \int_{S(t)} [\![\boldsymbol{\phi} \otimes (\mathbf{v} - \mathbf{v}^\Sigma) \cdot \mathbf{n}_\Sigma]\!] \cdot \mathbf{n}_\Sigma \; dS. \tag{A.20}$$

A.2.1 Local mass balance

Applying the two-phase Reynolds transport theorem for co-moving control volumes (A.20) to the integral mass balance (A.16) yields

$$\int_{V(t) \setminus S(t)} (\partial_t \rho + \nabla \cdot (\rho \mathbf{v})) \; dV + \int_{S(t)} [\![\rho(\mathbf{v} - \mathbf{v}^\Sigma) \cdot \mathbf{n}_\Sigma]\!] \cdot \mathbf{n}_\Sigma \; dS = 0. \tag{A.21}$$

Localization yields

$$\partial_t(\rho) + \nabla \cdot (\rho \mathbf{v}) = 0 \quad \text{in } \Omega(t) \setminus \Sigma(t), \tag{A.22}$$

$$[\![\rho(\mathbf{v} - \mathbf{v}^\Sigma)]\!] \cdot \mathbf{n}_\Sigma = 0 \quad \text{on } \Sigma(t). \tag{A.23}$$

A.2.2 Local momentum balance

Applying the two-phase Reynolds transport theorem for co-moving control volumes (A.20) to the integral momentum balance (A.16) yields

$$\begin{aligned} \int_{V(t) \setminus S(t)} (\partial_t(\rho \mathbf{v}) + \nabla \cdot (\rho \mathbf{v} \otimes \mathbf{v})) \; dV + \int_{S(t)} [\![\rho \mathbf{v} \otimes (\mathbf{v} - \mathbf{v}^\Sigma) \cdot \mathbf{n}_\Sigma]\!] \cdot \mathbf{n}_\Sigma \; dS = \\ \int_{\partial V(t)} \mathbf{S} \cdot \mathbf{n} \; dS + \int_{V(t)} \rho \mathbf{b} \; dV + \int_{S(t)} (\sigma \kappa \mathbf{n} + \nabla_\Sigma \sigma) \; dS. \end{aligned} \tag{A.24}$$

The two-phase divergence theorem (A.19) is then applied to the contact forces term, i.e. $\int_{\partial V(t)} \mathbf{S} \cdot \mathbf{n} \; dS$, which results into

$$\int_{\partial V(t)} \mathbf{S} \cdot \mathbf{n} \; dS = \int_{V(t)} \nabla \cdot (S) \; dV + \int_{S(t)} [\![\mathbf{S}]\!] \cdot \mathbf{n}_\Sigma \; dS \tag{A.25}$$

For Newtonian fluids, the stress tensor $\mathbf{S}$ obeys the constitutive equation

$$\mathbf{S} = -p\mathbf{I} + \mathbf{S}^{\text{visc}}, \tag{A.26}$$

with $\mathbf{S}^{\text{visc}} = 2\mu \left(\nabla \mathbf{v} + (\nabla \mathbf{v})^T\right)$. After substituting the relation (A.25) in the balance (A.24), localization yields

$$\partial_t(\rho \mathbf{v}) + \nabla \cdot (\rho \mathbf{v} \otimes \mathbf{v}) = \nabla \cdot \mathbf{S} + \rho \mathbf{b} \quad \text{in } \Omega(t) \setminus \Sigma(t), \tag{A.27}$$

$$[\![\rho \mathbf{v} \otimes (\mathbf{v} - \mathbf{v}^\Sigma)]\!] \cdot \mathbf{n}_\Sigma + [\![p\mathbf{I} - \mathbf{S}^{\text{visc}}]\!] \cdot \mathbf{n}_\Sigma = \sigma \kappa \mathbf{n}_\Sigma + \nabla_\Sigma \sigma \quad \text{on } \Sigma(t). \tag{A.28}$$

A.2.3 Local balance for the species molar mass

Applying the two-phase Reynolds transport theorem for co-moving control volumes (A.20) to the temporal derivative and the two-phase divergence theorem (A.19) to the diffusive fluxes integral in the integral species molar mass balance (A.18) yields

$$\begin{aligned}\int_{V(t)\setminus S(t)} (\partial_t c_i + \nabla\cdot (c_i \mathbf{v}))\ dV + \int_{S(t)} \left[\!\left[c_i(\mathbf{v}-\mathbf{v}^\Sigma)\cdot \mathbf{n}_\Sigma \right]\!\right] \cdot \mathbf{n}_\Sigma\ dS = \\ -\int_{V(t)\setminus S(t)} \nabla\cdot \mathbf{j}_i\ dV - \int_{S(t)} [\![\mathbf{j}_i]\!]\cdot \mathbf{n}_\Sigma\ dS + \int_{V(t)\setminus S(t)} r_i\ dV.\end{aligned} \tag{A.29}$$

Localization yields

$$\partial_t(c_i) + \nabla\cdot(c_i\mathbf{v} + \mathbf{j}_i) = r_i \quad \text{in } \Omega(t)\setminus\Sigma(t), \tag{A.30}$$

$$\left[\!\left[c_i(\mathbf{v}-\mathbf{v}^\Sigma) + \mathbf{j}_i \right]\!\right]\cdot \mathbf{n}_\Sigma = 0 \quad \text{on } \Sigma(t). \tag{A.31}$$

A.2.4 Local balance for the surfactant molar mass

Starting point of the derivation is the integral balance equation written for an extensive quantity $\Phi(t,V(t)) = \int_{V(t)\setminus S(t)} c\ dV + \int_{S(t)} c^\Sigma\ dS$, where the additional terms with c^Σ account for the presence of surfactant on the interface. Hence, the balance equation for the surfactant molar concentration in integral form reads

$$\begin{aligned}\frac{d}{dt}\left(\int_{V(t)\setminus S(t)} c\ dV + \int_{S(t)} c^\Sigma\ dS\right) = \\ -\int_{\partial V(t)} \mathbf{j}\cdot\mathbf{n}\ dS - \int_{\partial S(t)} \mathbf{j}^\Sigma\cdot\mathbf{m}\ dl + \int_{V(t)} r\ dV + \int_{S(t)} r^\Sigma\ dS,\end{aligned} \tag{A.32}$$

where r and r^Σ are the source/sink terms due to chemical reactions in $V(t)$ and $S(t)$, respectively. In a system with a single surfactant species these two terms are zero. Then, equation (A.32) reduces to

$$\frac{d}{dt}\left(\int_{V(t)\setminus S(t)} c\ dV + \int_{S(t)} c^\Sigma\ dS\right) = -\int_{\partial V(t)} \mathbf{j}\cdot\mathbf{n}\ dS - \int_{\partial S(t)} \mathbf{j}^\Sigma\cdot\mathbf{m}\ dl. \tag{A.33}$$

Applying the two-phase Reynolds transport theorem for co-moving control volumes (A.20) to the temporal derivative $\frac{d}{dt}\int_{V(t)\setminus S(t)} c\ dV$ and the Reynolds transport theorem (A.1) to $\frac{d}{dt}\int_{S(t)} c^\Sigma\ dS$ in equation (A.33) yields

$$\begin{aligned}\int_{V(t)\setminus S(t)} (\partial_t c + \nabla\cdot(c\mathbf{v}))\ dV + \int_{S(t)} \left[\!\left[c(\mathbf{v}-\mathbf{v}^\Sigma)\right]\!\right]\cdot\mathbf{n}_\Sigma\ dS \\ + \int_{S(t)} (\partial_t c^\Sigma + \nabla_\Sigma\cdot(c^\Sigma\mathbf{v}^\Sigma))\ dS = \\ -\int_{\partial V(t)} \mathbf{j}\cdot\mathbf{n}\ dS - \int_{\partial S(t)} \mathbf{j}^\Sigma\cdot\mathbf{m}\ dl.\end{aligned} \tag{A.34}$$

The two-phase divergence theorem (A.19) is applied to the surface integral $\int_{\partial V(t)} \mathbf{j} \cdot \mathbf{n}\ dS$ and the divergence theorem to the line integral $\int_{\partial S(t)} \mathbf{j}^{\Sigma} \cdot \mathbf{m}\ dl$ giving

$$\begin{aligned} \int_{V(t)\setminus S(t)} (\partial_t c + \nabla\cdot (c\mathbf{v}))\ dV + \int_{S(t)} \left[\!\left[c(\mathbf{v}-\mathbf{v}^{\Sigma}) \right]\!\right] \cdot \mathbf{n}_{\Sigma}\ dS \\ + \int_{S(t)} (\partial_t c^{\Sigma} + \nabla_{\Sigma}\cdot (c^{\Sigma}\mathbf{v}^{\Sigma}))\ dS = \\ - \int_{V(t)\setminus S(t)} \nabla\cdot \mathbf{j}\ dV - \int_{S(t)} [\![\mathbf{j}]\!] \cdot \mathbf{n}_{\Sigma}\ dS - \int_{S(t)} \nabla\cdot \mathbf{j}^{\Sigma}\ dS. \end{aligned} \tag{A.35}$$

Rearranging the terms in equation (A.35), the final form of the integral balance for the surfactant molar concentration is obtained and it reads

$$\begin{aligned} \int_{V(t)\setminus S(t)} (\partial_t c + \nabla\cdot (c\mathbf{v}+\mathbf{j}))\ dV + \int_{S(t)} (\partial_t c^{\Sigma} + \nabla_{\Sigma}\cdot (c^{\Sigma}\mathbf{v}^{\Sigma}+\mathbf{j}^{\Sigma}))\ dS \\ + \int_{S(t)} \left[\!\left[c(\mathbf{v}-\mathbf{v}^{\Sigma}) + \mathbf{j} \right]\!\right] \cdot \mathbf{n}_{\Sigma}\ dS = 0. \end{aligned} \tag{A.36}$$

Localization yields

$$\partial_t c + \nabla\cdot (c\mathbf{v}+\mathbf{j}) = 0 \quad \text{in } \Omega(t)\setminus\Sigma(t), \tag{A.37}$$

$$\partial_t c^{\Sigma} + \nabla_{\Sigma}\cdot (c^{\Sigma}\mathbf{v}^{\Sigma}+\mathbf{j}^{\Sigma}) = -\left[\!\left[c(\mathbf{v}-\mathbf{v}^{\Sigma}) + \mathbf{j} \right]\!\right] \cdot \mathbf{n}_{\Sigma} \quad \text{on } \Sigma(t). \tag{A.38}$$

The term on the right-hand side of equation (A.38) expresses the amount of moles that are transferred from the bulk phases to the interface, i.e. a sorption mechanism. Hence, it is called sorption source term and is indicated as s^{Σ}.

Appendix B

Modelling of the hindrance effect of surfactant on mass transfer

As anticipated in section 2.3.1, the derivation of the reduction factor for the mass transfer in presence of surfactant comes from considerations on the thermodynamics of the system. This derivation has been obtained by Prof. Dieter Bothe based on his works in [4, 7, 5].
Consider the one-sided mass transfer as reported in section 2.3.1,

$$\dot{m}_i^{\pm,\Sigma} = s_{i,\pm}^{\mathrm{ad}} - s_{i,\pm}^{\mathrm{de}}; \tag{B.1}$$

recall figure 2.5 for a graphical interpretation. Under the hypothesis of *quasi-stationarity*, a reduced form of the surface mass balance can be written as

$$\dot{m}_i^{+,\Sigma} + \dot{m}_i^{-,\Sigma} = 0. \tag{B.2}$$

Furthermore, from the second law of thermodynamics, the entropy inequality has to be fulfilled. This means that the entropy production at the interface $\xi^{\Sigma}_{\mathrm{sorp}^{\pm}}$ due to the sorption mechanism [4] has to be equal to or grater than zero,

$$\begin{aligned}\xi^{\Sigma}_{\mathrm{sorp}^{\pm}} &= \sum_{i=1}^{N} \dot{m}_i^{\pm,\Sigma} \left(\frac{\mu_i^{\pm}}{T^{\pm}} - \frac{\mu_i^{\Sigma}}{T^{\Sigma}} + \frac{1}{T^{\Sigma}} \left(\frac{\left(\mathbf{v}^{\pm} - \mathbf{v}^{\Sigma}\right)^2}{2} - \mathbf{n}^{\pm} \cdot \frac{\mathbf{S}^{\pm,\mathrm{visc}}}{\rho^{\pm}} \cdot \mathbf{n}^{\pm} \right) \right) \\ &= \sum_{i=1}^{N} \left(s_{i,\pm}^{\mathrm{ad}} - s_{i,\pm}^{\mathrm{de}} \right) \left(\frac{\mu_i^{\pm}}{T^{\pm}} - \frac{\mu_i^{\Sigma}}{T^{\Sigma}} + \frac{1}{T^{\Sigma}} \delta_i^{\pm} \right) \geq 0, \end{aligned} \tag{B.3}$$

where $\delta_i^{\pm}$ represents the kinetic and viscous terms. In order to have $\xi^{\Sigma}_{\mathrm{sorp}^{\pm}} \geq 0$, each term of the sum has to be equal or grater than zero, i.e.

$$\left(s_{i,\pm}^{\mathrm{ad}} - s_{i,\pm}^{\mathrm{de}} \right) \left(\frac{\mu_i^{\pm}}{T^{\pm}} - \frac{\mu_i^{\Sigma}}{T^{\Sigma}} + \frac{1}{T^{\Sigma}} \delta_i^{\pm} \right) \geq 0 \quad \forall i. \tag{B.4}$$

In this inequality the term $\frac{1}{T^{\Sigma}} \delta_i^{\pm}$ can be neglected, the ad- and desorption terms need modelling, while the chemical potentials should be given by the thermodynamics, or better, by the equation of state of the free energy. To simplify this inequality the temperature is assumed continuous across the interface,

$$T^{+}_{|\Sigma} = T^{\Sigma} = T^{-}_{|\Sigma} =: T. \tag{B.5}$$

Additionally, a logarithmic closure for the ad- and desorption terms is employed, since the considered sorption processes can be far from thermodynamical equilibrium:

$$\left(s_{i,\pm}^{\mathrm{ad}} - s_{i,\pm}^{\mathrm{de}}\right) \approx \left(\ln s_{i,\pm}^{\mathrm{ad}} - \ln s_{i,\pm}^{\mathrm{de}}\right) = \ln\left(\frac{s_{i,\pm}^{\mathrm{ad}}}{s_{i,\pm}^{\mathrm{de}}}\right). \tag{B.6}$$

Thus, from equation (B.4):

$$\ln\left(\frac{s_{i,\pm}^{\mathrm{ad}}}{s_{i,\pm}^{\mathrm{de}}}\right) = \frac{\alpha_{\pm}}{RT}\left(\mu_i^{\pm} - \mu_i^{\Sigma}\right); \tag{B.7}$$

Note that we specialise to set the coefficient $\alpha_{\pm} = 1$, which turns out to be sufficient for our purpose.
If the species i is part of an ideal mixture, the chemical potentials in the bulk phase and on the interface depend on temperature, pressure and molar fraction according to

$$\mu_i^{\pm} = \mu_i^{\pm}\left(T, p, \chi_k\right) \tag{B.8}$$

in the bulk[1], and

$$\mu_i^{\Sigma} = \mu_i^{\Sigma}\left(T, p^{\Sigma}, \chi_k^{\Sigma}\right). \tag{B.9}$$

on the interface, where p^{Σ} and χ_k^{Σ} are the pressure and the molar fractions on the interface, respectively. Then, introducing the Gibbs free energy g_i as a function of temperature and pressure, the dependency on the molar fractions of the other mixture components χ_k can be dropped. This implies

$$\mu_i^{\pm}\left(T, p, \chi_k\right) = g_i^{\pm}\left(T, p\right) + RT \ln \chi_i^{\pm}, \tag{B.10}$$

and

$$\mu_i^{\Sigma}\left(T, p^{\Sigma}, \chi_k^{\Sigma}\right) = g_i^{\Sigma}\left(T, p^{\Sigma}\right) + RT \ln \chi_i^{\Sigma}. \tag{B.11}$$

Substituting the expressions for the chemical potentials (B.10) and (B.11) in equation (B.7) and writing it with respect to the adsorption term gives

$$s_{i,\pm}^{\mathrm{ad}} = s_{i,\pm}^{\mathrm{de}} \exp\left(\frac{g_i^{\pm} - g_i^{\Sigma}}{RT}\right) \frac{\chi_i^{\pm}}{\chi_i^{\Sigma}}. \tag{B.12}$$

It can be assumed that desorption $s_{i,\pm}^{\mathrm{de}}$ is proportional to the surface concentration, or better, molar fraction[2] according to

$$s_{i,\pm}^{\mathrm{de}} = k_{\pm}^{\mathrm{de}} \chi_i^{\Sigma}, \tag{B.13}$$

while nothing can be said about adsorption. Introducing (B.13) in the expression for the adsorption, (B.12) reads

$$s_{i,\pm}^{\mathrm{ad}} = k_{\pm}^{\mathrm{de}} \exp\left(\frac{g_i^{\pm} - g_i^{\Sigma}}{RT}\right) \chi_i^{\pm} =: k_{\pm}^{\mathrm{ad}} \chi_i^{\pm}, \tag{B.14}$$

where the abbreviation $k_{\pm}^{\mathrm{ad}} = k_{\pm}^{\mathrm{ad}}\left(T, p, p^{\Sigma}, \chi_k^{\Sigma}\right) = k_{\pm}^{\mathrm{de}} \exp\left(\frac{g_i^{\pm} - g_i^{\Sigma}}{RT}\right)$ has been introduced for simplicity. The expressions for ad- and desorption can now be plugged into the quasi-stationary mass balance (2.59), obtaining

$$k_{+}^{\mathrm{ad}} \chi_i^{+} + k_{-}^{\mathrm{ad}} \chi_i^{-} = \left(k_{+}^{\mathrm{de}} + k_{-}^{\mathrm{de}}\right) \chi_i^{\Sigma}. \tag{B.15}$$

[1] The already introduced equation (2.36) within the sorption modelling.
[2] Desorption is proportional to what is on the interface and could possibly want to desorb.

From the latter, an implicit relation for the surface molar mass is obtained, i.e.

$$\chi_i^\Sigma = \frac{k_+^{\mathrm{ad}}\chi_i^+ + k_-^{\mathrm{ad}}\chi_i^-}{k_+^{\mathrm{de}} + k_-^{\mathrm{de}}}, \tag{B.16}$$

and together with (B.13) and (B.14) used to write an expression for the one-sided mass flux $\dot{m}^{+,\Sigma}$:

$$\dot{m}^{+,\Sigma} = \frac{k_+^{\mathrm{ad}}k_-^{\mathrm{de}}}{k_+^{\mathrm{de}} + k_-^{\mathrm{de}}}\chi_i^+ - \frac{k_+^{\mathrm{de}}k_-^{\mathrm{ad}}}{k_+^{\mathrm{de}} + k_-^{\mathrm{de}}}\chi_i^-. \tag{B.17}$$

Including the full expression for k_+^{ad} in (B.17) results in

$$\dot{m}^{+,\Sigma} = \frac{k_+^{\mathrm{de}}k_-^{\mathrm{de}}}{k_+^{\mathrm{de}} + k_-^{\mathrm{de}}}\left(\exp\left(\frac{g_i^+ - g_i^\Sigma}{RT}\right)\chi_i^+ - \exp\left(\frac{g_i^- - g_i^\Sigma}{RT}\right)\chi_i^-\right). \tag{B.18}$$

The pre-factor $\frac{k_+^{\mathrm{de}}k_-^{\mathrm{de}}}{k_+^{\mathrm{de}}+k_-^{\mathrm{de}}}$ is indicated in the following as k^{des}.
Note that in equation (B.18) the surface Gibbs free energy g_i^Σ is unknown. To get an expression for it, recall the definition of the chemical potential as

$$\mu_i = \frac{\partial(\rho\psi)}{\partial\rho_i}, \tag{B.19}$$

where $\rho\psi$ is the *Helmoltz free energy*, i.e. the thermodynamic potential that measures the work obtainable from a closed thermodynamic system in absence of volume and temperature changes[3]. The interface chemical potential then reads $\mu_i^\Sigma = \frac{\partial(\rho^\Sigma\psi^\Sigma)}{\partial\rho_i^\Sigma}$.
According to Kralchevsky [53] (table 4.4, page 254 in the reference), using Langmuir adsorption model for all the mixture components, the surface free energy can be expressed as

$$\rho^\Sigma\psi^\Sigma = \sum_{k=1}^N c_k^\Sigma\mu_k^{\Sigma,\mathrm{ref}} + c_\infty^\Sigma RT\left[\sum_{k=1}^N \chi_k^\Sigma\left(\ln\chi_k^\Sigma - 1\right) + (1-\theta)\left(\ln(1-\theta) - 1\right)\right] + K^{\mathrm{ref}}, \tag{B.20}$$

where $\theta := \sum_{k=1}^N \chi_k^\Sigma$, $\chi_k^\Sigma := \frac{c_k^\Sigma}{c_\infty^\Sigma}$; $\mu_k^{\Sigma,\mathrm{ref}}$ does not depend on the mixture composition but it may depend on temperature and pressure and K^{ref} is a reference value, e.g. the reference pressure. Note that the first two terms would give Henry's model, and the third one comes from Langmuir. Now the derivative $\frac{\partial(\rho^\Sigma\psi^\Sigma)}{\partial\rho_k^\Sigma}$ is computed to obtain an expression for μ_k^Σ:

$$\begin{aligned}
\mu_k^{\Sigma,\mathrm{mol}} = M_k\frac{\partial}{\partial\rho_k^\Sigma}\left(\rho^\Sigma\psi^\Sigma\right)\left(T,\rho_1^\Sigma,\ldots,\rho_N^\Sigma\right) &= \frac{\partial}{\partial c_k^\Sigma}\left(\rho^\Sigma\psi^\Sigma\right) \\
= \mu_k^{\Sigma,\mathrm{ref}} + RT\left(\ln\chi_k^\Sigma - 1\right) + c_\infty^\Sigma RT\frac{\partial}{\partial c_k^\Sigma}\frac{c_k^\Sigma}{c_\infty^\Sigma} &+ RT(-1)\left(\ln(1-\theta) - 1\right) \\
&+ c_\infty^\Sigma RT\frac{1-\theta}{1-\theta}\left(-\frac{1}{c_\infty^\Sigma}\right) \\
&= \mu_k^{\Sigma,\mathrm{ref}} - RT\ln(1-\theta) + RT\ln\chi_k^\Sigma,
\end{aligned} \tag{B.21}$$

[3] $\rho\psi := \rho e - \rho sT$

where the species molar mass M_k has been introduced to exchange the derivative $\frac{\partial(\rho^\Sigma \psi^\Sigma)}{\partial \rho_k^\Sigma} = \frac{1}{M_k}\frac{\partial(\rho^\Sigma \psi^\Sigma)}{\partial c_k^\Sigma}$. From the Euler relation

$$\rho^\Sigma \psi^\Sigma + p^\Sigma = \sum_{k=1}^{N} \mu_k^{\Sigma,\mathrm{mol}} c_k^\Sigma, \tag{B.22}$$

an expression for the term $RT\ln(1-\theta)$ in (B.21) can be derived and it reads

$$RT\ln(1-\theta) = \frac{p^\Sigma + \gamma^{\mathrm{ref}}}{c_\infty^\Sigma}, \tag{B.23}$$

where the surface pressure p^Σ is computed according to

$$p^\Sigma = -c_\infty^\Sigma RT\ln(1-\theta) - \gamma^{\mathrm{ref}}. \tag{B.24}$$

Substituting relation (B.23) in equation (B.21) gives

$$\mu_k^{\Sigma,\mathrm{mol}} = \mu_k^{\Sigma,\mathrm{ref}} + \frac{p^\Sigma + \gamma^{\mathrm{ref}}}{c_\infty^\Sigma} + RT\ln\chi_k^\Sigma. \tag{B.25}$$

Then, the surface Gibbs free energy can be expressed with respect to the moles of the transferred species according to

$$g_k^{\Sigma,\mathrm{mol}} := \mu_k^{\Sigma,\mathrm{ref}} + \frac{p^\Sigma + \gamma^{\mathrm{ref}}}{c_\infty^\Sigma}. \tag{B.26}$$

Equation (B.26) can be substituted into (B.18) to get the one-sided mass flux as

$$\dot{m}^{+,\Sigma} = k^{\mathrm{trans}} \exp\left(-\frac{p^\Sigma + \gamma^{\mathrm{ref}}}{RTc_\infty^\Sigma}\right)\left[\chi_i^+ - \chi_i^- \exp\left(\frac{g_i^- - g_i^+}{RT}\right)\right], \tag{B.27}$$

where $k^{\mathrm{trans}} = k^{\mathrm{des}} \exp\left(\frac{g_i^+ - \mu_k^{\Sigma,\mathrm{ref}}}{RT}\right)$. In the absence of surfactants, hence no mass transfer resistance, the muss flux would read

$$\dot{m}^{+,\Sigma} = k^{\mathrm{trans}}\left(\chi_i^+ - \frac{\chi_i^-}{H_i}\right), \tag{B.28}$$

where the Henry coefficient has been defined as

$$H_i := \frac{1}{\exp\left(\frac{g_i^- - g_i^+}{RT}\right)}. \tag{B.29}$$

In the contaminated case, changing to the usual notation where $-p^\Sigma = \sigma$ and $\gamma^{\mathrm{ref}} = \sigma_0$, equation (B.27) becomes

$$\dot{m}^{+,\Sigma} = k^{\mathrm{trans}} \exp\left(-\frac{\sigma_0 - \sigma}{RTc_\infty^\Sigma}\right)\left(\chi_i^+ - \frac{\chi_i^-}{H_i}\right). \tag{B.30}$$

Appendix C

Surface mesh quality

As we are dealing with curved surfaces and surface operators, it is meaningful to check the quality of the surface mesh. As for the volume mesh, the main source of errors coming from the spatial discretization is non-orthogonality, skewness, and non-planarity of the faces. Additionally, for a curved surface, the accuracy of the curvature discretization is fundamental. A utility, *checkFaMesh*, has been written within the OpenFOAM framework to check the surface mesh quality. Very skewed or warped faces may not influence directly the simulation results, but they indicate poor mesh quality. The outcome of this check, in combination with the test case on the surface operators presented in section 4.1 and the parameter study performed in [81], should pose some guidelines for the mesh creation.

C.1 Non-orthogonality

The non-orthogonality expresses how far are two faces from the ideal condition of orthogonality, i.e. when the angle between the vector connecting the two face centres and the edge vector is zero (see the left side of figure C.1).

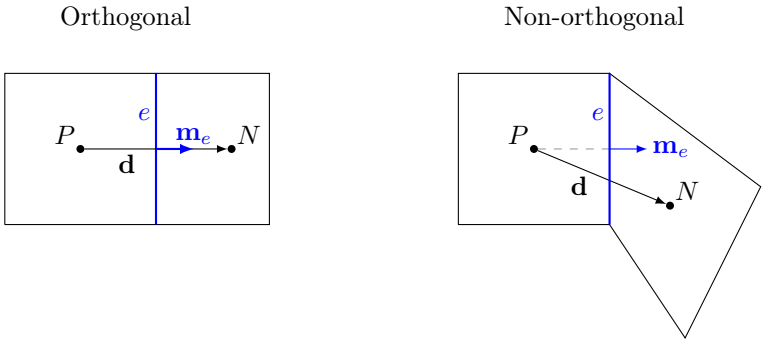

Figure C.1: Sketch to represent the surface mesh non-orthogonality.

The non-orthogonality between two faces of the surface mesh is an angle computed as

$$\text{nonOrtho} = \cos^{-1}\left(\frac{\mathbf{d}\cdot\mathbf{m}_e}{|\mathbf{d}||\mathbf{m}_e|}\right), \tag{C.1}$$

where the vector $\mathbf{d}$ is the distance vector between the two face centres, $\mathbf{d} = \mathbf{x}_P - \mathbf{x}_N$.
The threshold for the mesh check to fail is set to 70° for the maximum non-orthogonality, which is already a severe non-orthogonality.

C.2 Skewness

Face skewness is the critical metric to consider mainly for the advection term discretization. In fact skewness errors may arise when computing the advective fluxes from an interpolated value from face centre to edge centre. The skewness can be seen as the offset between the edge centre and the vector connecting the face centres sharing this edge. The computed flux may be underestimated due to the presence of this offset. Ideally, values of skewness should be as close as possible to zero; if not, this error will accumulate. See also [45] (pages 124, 125 in the reference) for a clear description of the skewness error in the Finite Volume calculus.

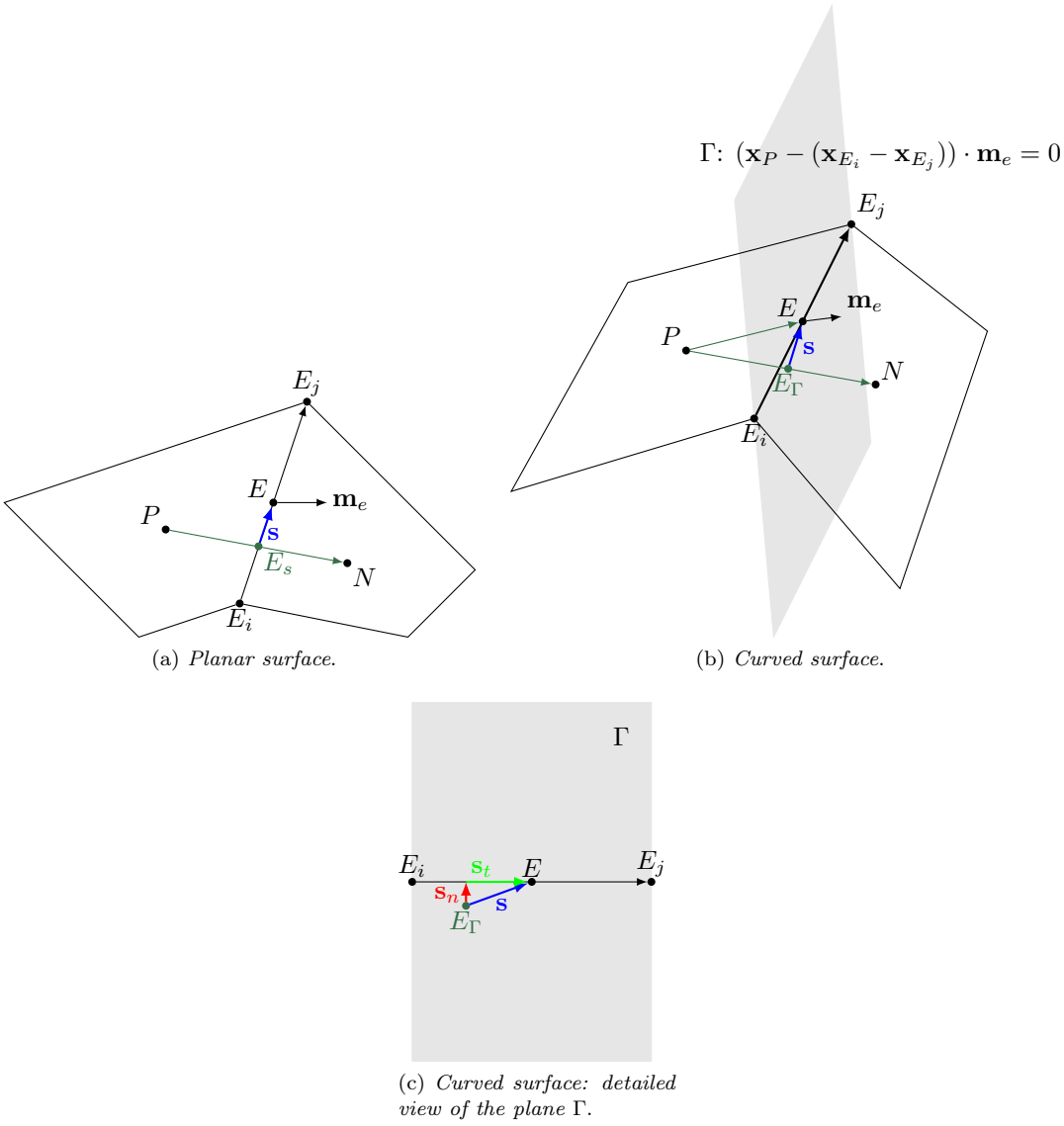

(a) *Planar surface.*

(b) *Curved surface.*

(c) *Curved surface: detailed view of the plane* Γ.

Figure C.2: Sketch to represent the surface mesh skewness.

Figure C.2 serves as an aid to visualize the face skewness for a planar and a curved surface. In case of a planar surface, see figure C.2a, the skewness vector is simply the distance vector between the edge centre E and the intersection E_s between the vector connecting the two area

centres $\mathbf{x}_P - \mathbf{x}_N$ and the edge that they share; see figure C.2, left. In case of curved surfaces, as in figure C.2b, the definition of skewness error is a bit more tricky. First a plane Γ passing through the edge $E_i - E_j$ and normal to the edge normal $\mathbf{m}_e$ has to be defined. The vector connecting the face centres $\mathbf{x}_P - \mathbf{x}_N$ now will not intersect the edge E, but the plane Γ in the point e_Γ. A skewness vector $\mathbf{s}$ can be defined as the distance vector between the point E_Γ and the edge centre E. Following the same procedure as in the finite volume mesh check of OpenFOAM, the skewness vector is computed as

$$\mathbf{s} = (\mathbf{x}_P - \mathbf{x}_E) - \lambda(\mathbf{x}_P - \mathbf{x}_N), \tag{C.2}$$

where $\lambda = \frac{(\mathbf{x}_P - \mathbf{x}_E)\cdot\mathbf{m}_e}{(\mathbf{x}_P - \mathbf{x}_N)\cdot\mathbf{m}_e}$. The skewness vector is first normalized, $\mathbf{s} = \mathbf{s}/|\mathbf{s}|$. The skewness indicator is then computed as the scaled magnitude of $\mathbf{s}$ with respect to the approximate distance between the two face centres d, i.e. $s_i = |\mathbf{s}|/d$. The vector $\mathbf{s}$ lies on the plane Γ, see figure C.2c, and it can be decomposed in tangential and normal component to the edge e. The tangential component $\mathbf{s}_t$ then corresponds to the "planar" skewness vector,

$$\mathbf{s}_t = \mathbf{s} \cdot (\mathbf{x}_{E_i} - \mathbf{x}_{E_j}), \tag{C.3}$$

while the normal component $\mathbf{s}_n$ is due to the surface curvature κ,

$$\mathbf{s}_n = \mathbf{s} - \mathbf{s}_t. \tag{C.4}$$

The maximum skewness threshold for the mesh check to fail is set to 4 for s_i. A skewness indicator above this value represents a poor mesh.

C.3 Non-planar faces

The non-planarity or flatness of a face is computed. In other words, it is checked how far is a face from being planar. If the faces are triangular, the check is skipped. The flatness is calculated as the ratio between the sum of the areas of the individual triangles forming the face $A_{f,i}^{\text{check}}$ and the overall area of the face $A_{f,i}$. Consider a polygonal face i with center C_i, as depicted in figure C.3, where P_j's are the N_{P_f} points constituting the face and $n_{A_{f,i}}$ is the face normal. The face can be decomposed in triangles with individual area normal vector $\mathbf{n}_j$ of magnitude $|\mathbf{n}_j| = A_j$.

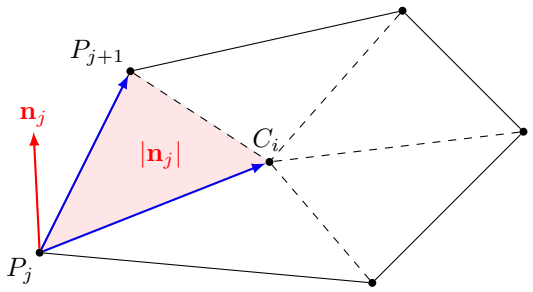

Figure C.3: Sketch to represent the face decomposition in triangles and computation of the respective areas.

The area normal vector of the individual triangles $\mathbf{n}_j$ is computed via the cross product between the vectors $(\mathbf{x}_{P_{j+1}} - \mathbf{x}_{P_j})$ and $(\mathbf{x}_{C_i} - \mathbf{x}_{P_j})$, more precisely

$$\mathbf{n}_j = \frac{1}{2}\left(P_{j+1} - P_j\right) \times \left(C_i - P_j\right). \tag{C.5}$$

The area of the individual triangle is simply the magnitude of $\mathbf{n}_j$, as reported above. The overall area of the face is computed as

$$A_{f,i} = \left| \sum_{j}^{N_{P_f}} \mathbf{n}_j \right|, \tag{C.6}$$

while the face area computed within the check procedure is

$$A_{f,i}^{\text{check}} = \sum_{j}^{N_{P_f}} |\mathbf{n}_j| = \sum_{j}^{N_{P_f}} A_j. \tag{C.7}$$

The flatness indicator or error $e_{fl,i}$ of a face i is computed as

$$e_{fl,i} = \frac{A_{f,i}^{\text{check}}}{A_{f,i}}, \tag{C.8}$$

where $e_{fl,i} = 1$ corresponds to a flat face and $e_{fl,i} < 1$ to a warped face. Faces with $e_{fl,i} < 0.8$ are reported as very warped faces.

C.4 Curvature

Regarding the curvature, an analytical value to compare with is available only for basic geometries, e.g. plane or sphere. Thus, in most of the cases, a curvature error cannot be computed. The utility *checkFaMesh* prints out minimum, maximum and average face curvature, such that the user has an indication of the correctness of the curvature computation. Within the finite area library, the curvature is computed as[1]

$$\kappa = \sum_{i} l_e \mathbf{m}_{e_i} \cdot \mathbf{n}_{A_{f_i}}, \tag{C.9}$$

where l_{e_i} is the edge length, $\mathbf{m}_{e_i}$ is the edge normal and $\mathbf{n}_{A_{f_i}}$ the face normal; see figure 3.1b.

[1] As reported originally in [91].

Appendix D

Forces acting on the bubble surface

Figures D.1 and D.6 show the contributions from tangential and normal viscous forces and from dynamic pressure force to the lift and drag for all the initial surfactant concentrations studied. The different line types correspond to the various initial bulk concentrations. For comparison purpose, the magnitude of the forces has been made non-dimensional with respect to the buoyancy force. For clarity, the results have been divided in three groups according to the surfactant initial concentration; low $c_0^1,\ c_0^2,\ c_0^3$ (figures D.1 and D.4), intermediate $c_0^4,\ c_0^5,\ c_0^6$ (figures D.2 and D.5), and high $c_0^8,\ c_0^8$ (figures D.3 and D.6) concentrations.

D.1 Lift forces

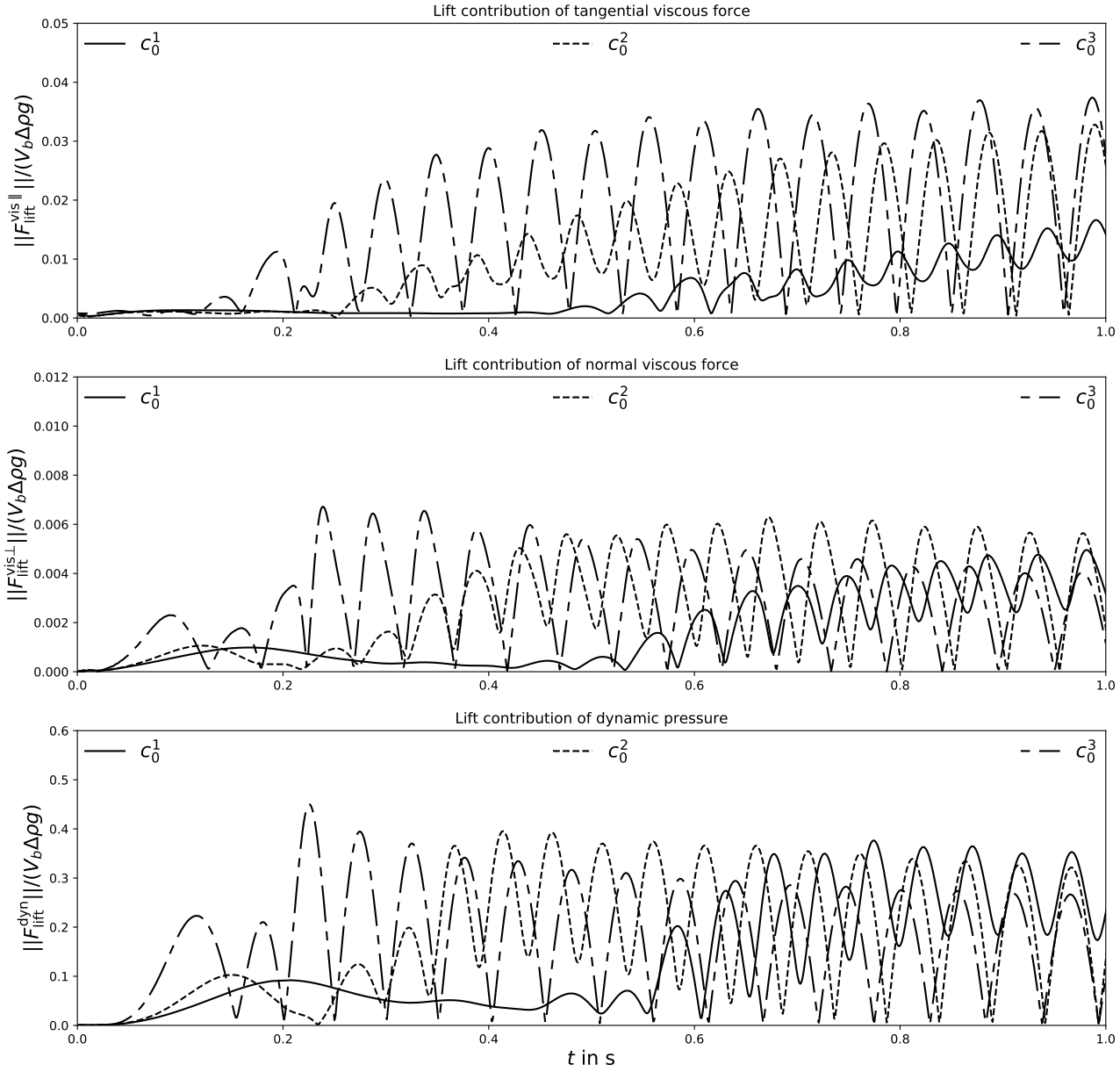

Figure D.1: Integral lift force contributions, influence of the initial bulk concentration $c_0^1,\ c_0^2,\ c_0^3$.

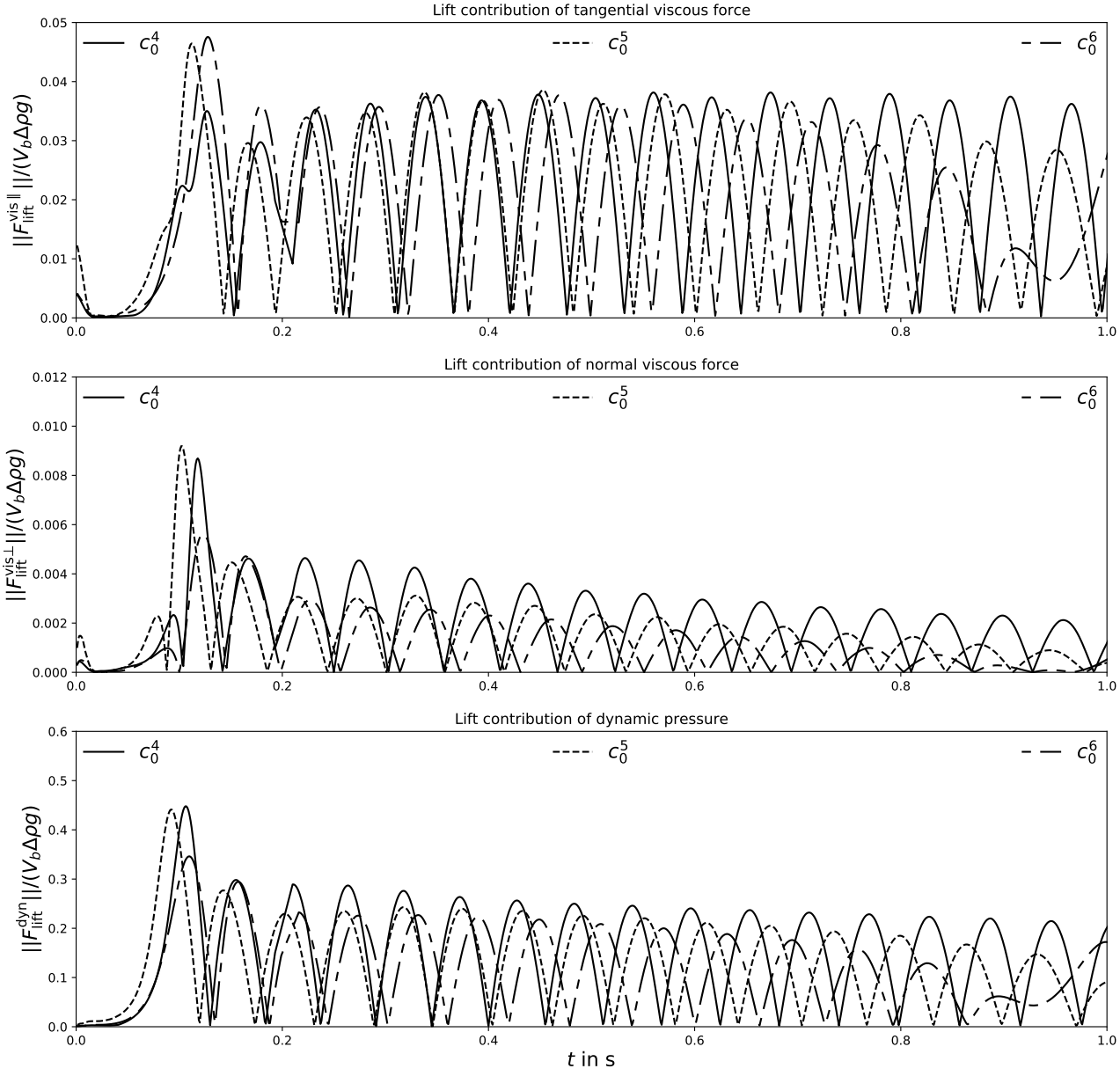

Figure D.2: Integral lift force contributions, influence of the initial bulk concentration $c_0^4,\ c_0^5,\ c_0^6$.

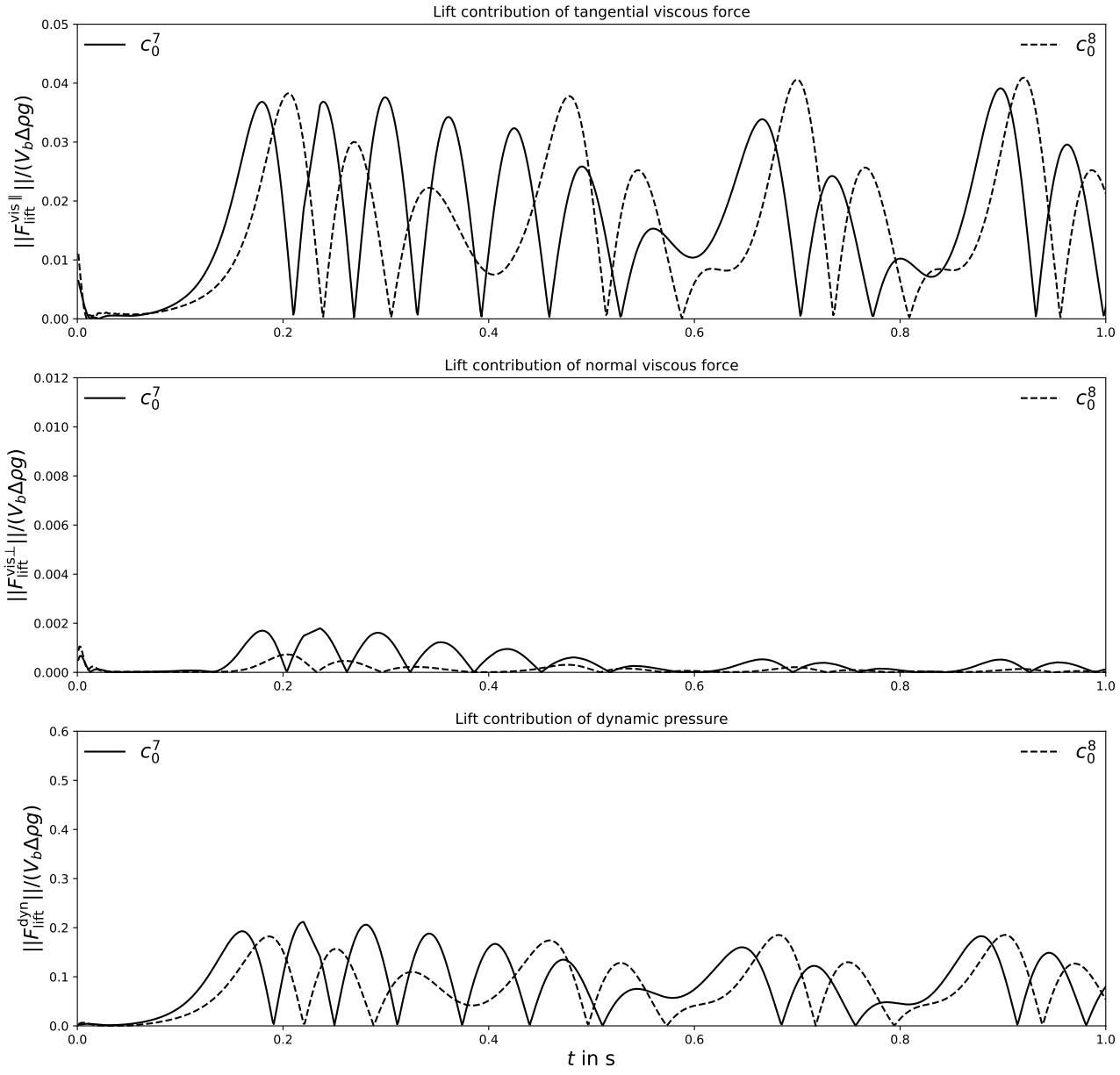

Figure D.3: Integral lift force contributions, influence of the initial bulk concentration $c_0^8,\ c_0^8$.

D.2 Drag forces

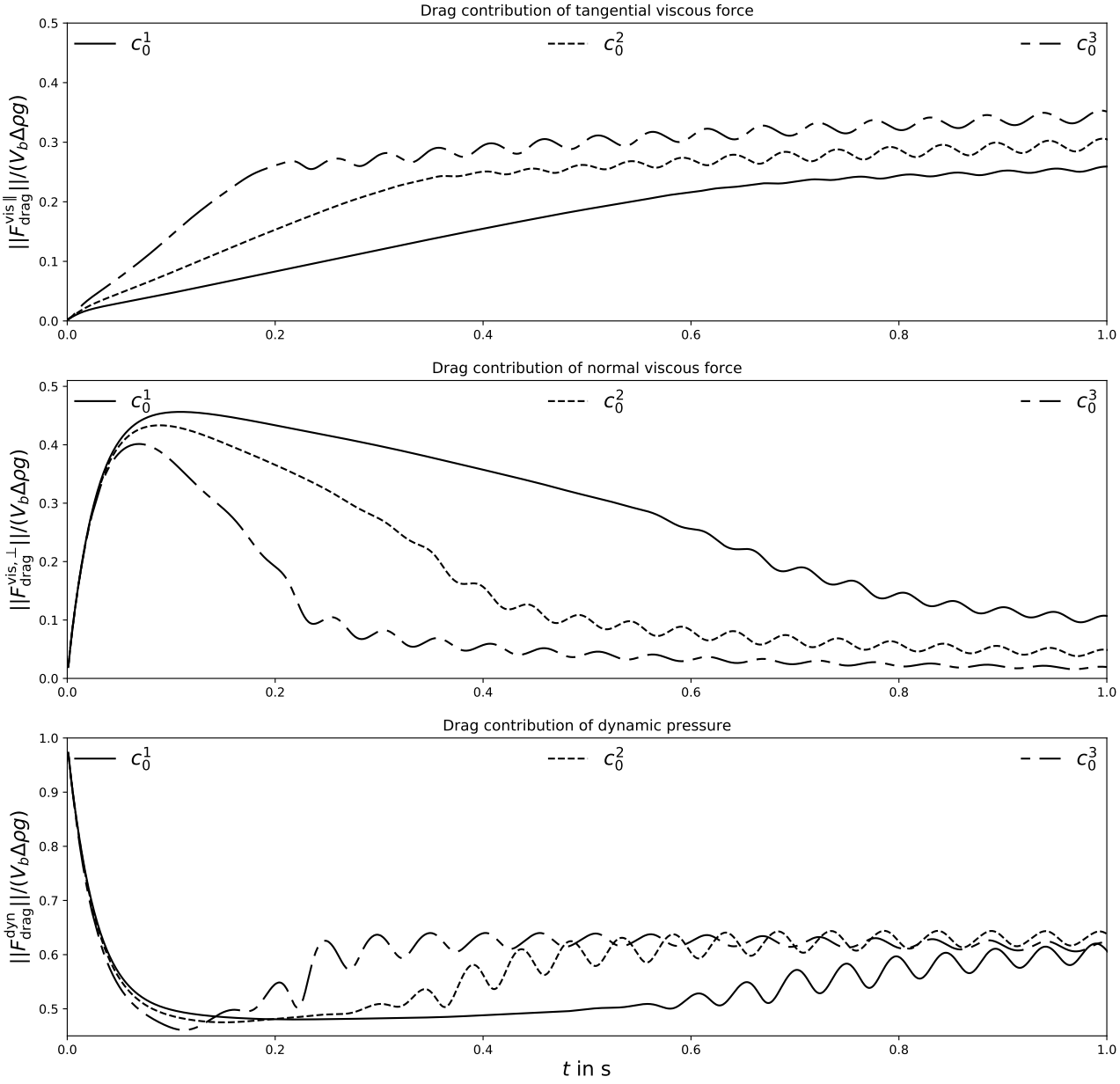

Figure D.4: Integral drag force contributions, influence of the initial bulk concentration $c_0^1,\ c_0^2,\ c_0^3$.

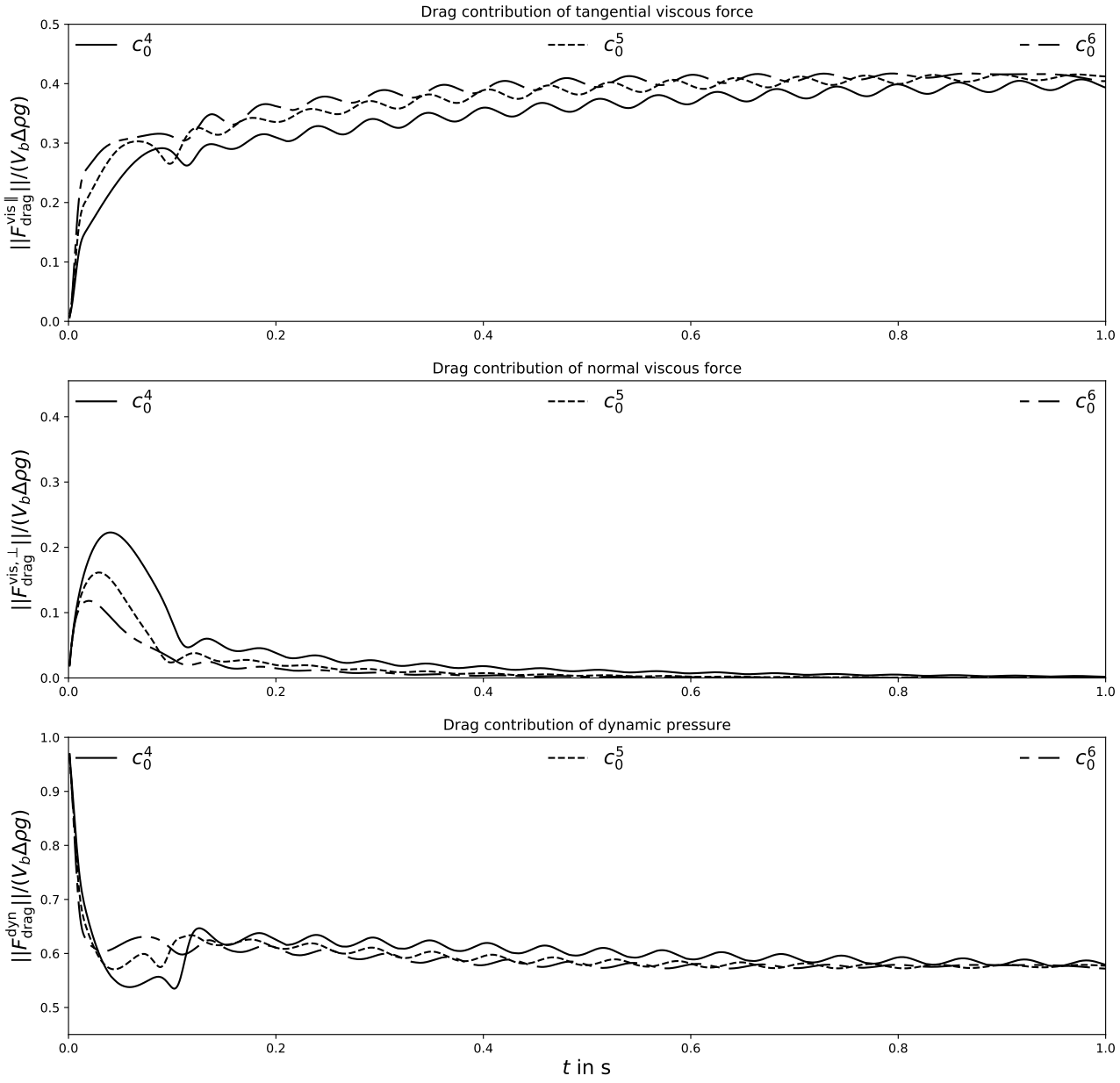

Figure D.5: Integral drag force contributions, influence of the initial bulk concentration $c_0^4,\ c_0^5,\ c_0^6$.

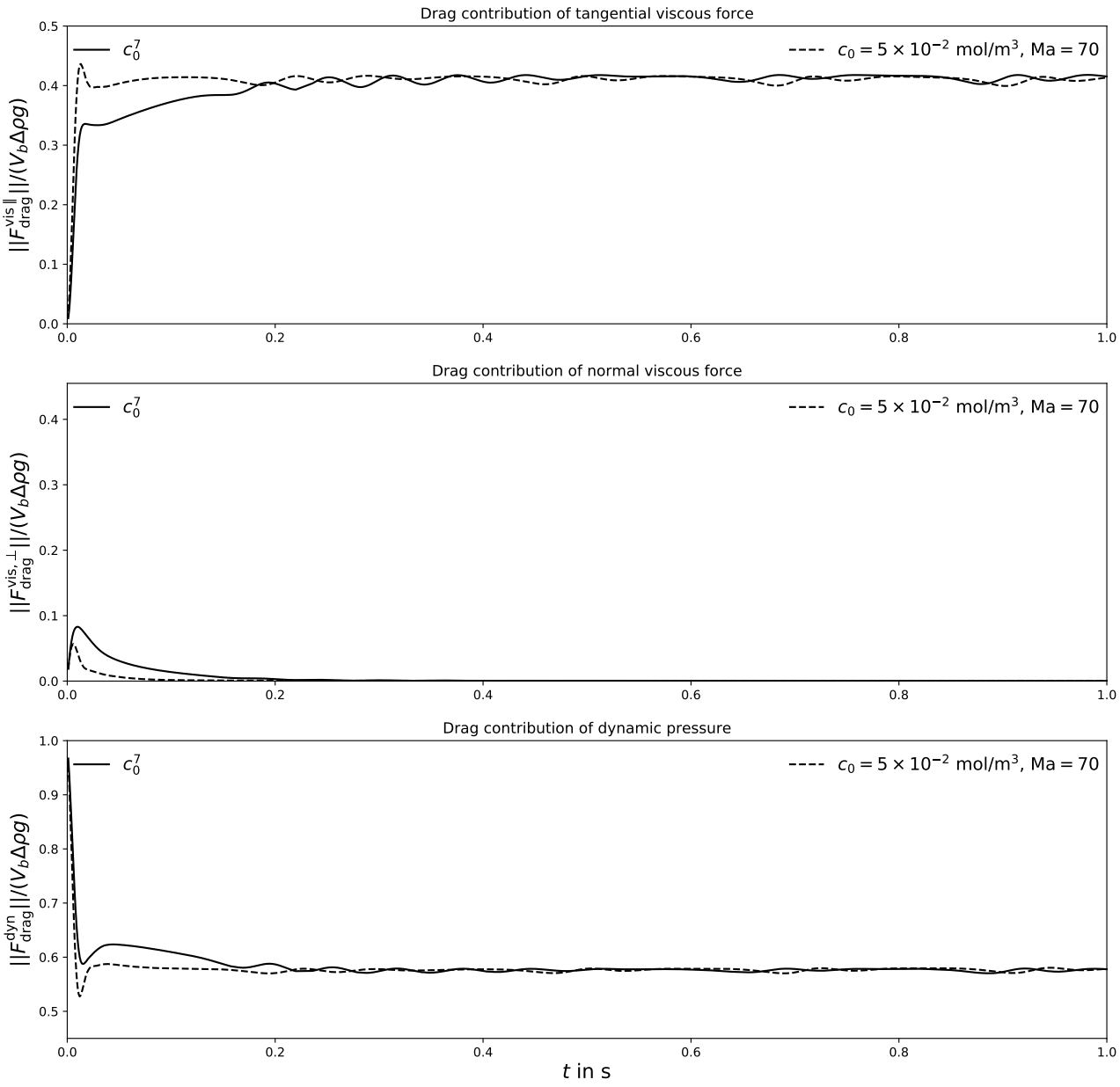

Figure D.6: Integral drag force contributions, influence of the initial bulk concentration $c_0^7,\ c_0^8$.

Bibliography

[1] H. T. Ahn and M. Shashkov. Geometric algorithms for 3d interface reconstruction. In M.L. Brewer and D. Marcum, editors, *Proceedings of the 16th International Meshing Roundtable*, pages 405–422. Springer, Berlin, 2008.

[2] C. Albert, J. Kromer, A. M. Robertson, and D. Bothe. Dynamic behaviour of buoyant high viscosity droplets rising in a quiescent liquid. *Journal of Fluid Mechanics*, 778:485–533, 2015.

[3] A. Alke and D. Bothe. 3D numerical modelling of soluble surfactant at fluid interfaces based on the Volume-of-Fluid method. *Fluid Dynamics & Materials Processing*, 5(4):345–372, 2009.

[4] D. Bothe. On the multi-physics of mass transfer across fluid interfaces. In F.-P. Schindler and M. Kraume, editors, *7th International Workshop - IBW7 on Transport Phenomena with Moving Boundaries and More*, volume Fortschr.-Ber. VDI Reihe 3, Nr. 947, pages 1–23. VDI-Verlag Düsseldorf, 2015.

[5] D. Bothe. Mass transfer across fluid interfaces - modeling the influence of adsorbed surfactant. In T. Hishida, editor, *RIMS Symposium on Mathematical Analysis of Viscous Incompressible Fluids*, pages 12–17. Kyoto University, 2016.

[6] D. Bothe. Lecture notes on Mathematical Modeling of Fluid Interfaces I, August 2018.

[7] D. Bothe and W. Dreyer. Continuum thermodynamics of chemically reacting fluid mixtures. *Acta Mechanica*, 226(6):1757–1805, 2015.

[8] D. Bothe and S. Fleckenstein. A Volume-of-Fluid-based method for mass transfer processes at fluid particles. *Chemical Engineering Science*, 101:283–302, 2013.

[9] D. Bothe, J. Prüss, and G. Simonett. Well-posedness of a two-phase flow with soluble surfactant. In J. Escher M. Chipot, editor, *Nonlinear Elliptic and Parabolic Problems*, pages 37–61. Birkhäuser, 2005.

[10] D. Bothe and A. Tomiyama. Modeling and experiments on the influence of non-ionic surfactant on mass transfer from CO_2 bubbles. In preparation.

[11] J. C. Cano-Lozano, C. Martínez-Bazán, J. Magnaudet, and J. Tchoufag. Paths and wakes of deformable nearly spheroidal rising bubbles close to the transition to path instability. *Physical Review Fluids*, 1(5):053604, 2016.

[12] Y. A. Cengel and M. A. Boles. *Thermodynamics: An Engineering Approach*. McGraw-Hill College, 2001.

[13] C. H. Chang and E. I. Franses. Adsorption dynamics of surfactants at the air/water interface: a critical review of mathematical models, data, and mechanisms. *Physicochemical Engineering Aspects*, 100:1–45, 1995.

[14] R. Clift, J. R. Grace, and M. E. Weber. *Bubbles, Drops, and Particles*. Dover Publications, Mineola, New York, 2 edition, 1978.

[15] B. Cuenot, J. Magnaudet, and B. Spennato. The effects of slightly soluble surfactants on the flow around a spherical bubble. *Journal of Fluid Mechanics*, 339:25–53, 1997.

[16] R. E. Davis and A. Acrivos. The influence of surfactants on the creeping motion of bubbles. *Chemical Engineering Science*, 21:681–585, 1966.

[17] A. W. G. de Vries, A. Biesheuvel, and L. van Wijngaarden. Notes on the path and wake of a gas bubble rising in pure water. *International Journal of Multiphase Flow*, 28:1823–1835, 2002.

[18] K. Dieter-Kissling, H. Marschall, and D. Bothe. Direct Numerical Simulation of droplet formation processes under the influence of soluble surfactant mixtures. *Computers & Fluids*, 113:93–105, 2015.

[19] K. Dieter-Kissling, H. Marschall, and D. Bothe. Numerical method for coupled interfacial surfactant transport on dynamic surface meshes of general topology. *Computers & Fluids*, 109:168–184, 2015.

[20] P. C. Duineveld. The rise velocity and shape of bubbles in pure water at high Reynolds number. *Journal of Fluid Mechanics*, 292:325–332, 1995.

[21] S. S. Dukhin, V. I. Kovalchuk, G. G. Gochev, M. Lotfi, M. Krzan, K. Malysa, and R. Miller. Dynamics of Rear Stagnant Cap formation at the surface of spherical bubbles rising in surfactant solutions at large Reynolds numbers under conditions of small Marangoni number and slow sorption kinetics. *Advances in Colloid and Interface Science*, 222:260–274, 2015.

[22] S. S. Dukhin, G. Kretzschmar, and R. Miller. *Dynamics of Adsorption at Liquid Interfaces*. Studies in Interface Science. Elsevier, 1995.

[23] S. S. Dukhin, M. Lotfi, V. I. Kovalchuck, D. Bastani, and R. Miller. Dynamics of rear stagnant cap formation at the surface of rising bubbles in surfactant solutions at large Reynolds and Marangoni numbers and for slow sorption kinetics. *Colloids and Surfaces A: Physicochemical Engineering Aspects*, 492:127–137, 2016.

[24] K. Ellingsen and F. Risso. On the rise of an ellipsoidal bubble in water: oscillatory paths and liquid-induced velocity. *Journal of Fluid Mechanics*, 440:235–268, 2001.

[25] V.B. Fainerman, S.V. Lylyk, E.V. Aksenenko, A.V. Makievski, J.T. Petkov, J. Yorke, and R. Miller. Adsorption layer characteristics of triton surfactants 1. surface tension and adsorption isotherms. *Colloids and Surfaces A: Physicochemical Engineering Aspects*, 334:1–7, 2009.

[26] V.B. Fainerman, R. Miller, E.V. Aksenenko, and A.V. Makievski. Equilibrium adsorption properties of single and mixed surfactant solutions. In V.B. Fainerman, D. Möbius, and

R. Miller, editors, *Surfactants Chemistry, Interfacial Properties, Applications*, volume 13 of *Studies in Interface Science*, pages 189–285. Elsevier, 2001.

[27] V.B. Fainerman, R. Miller, and H. Mohwald. General relationship of the adsorption behaviour of surfactants at the water/air interface. *Journal of Physical Chemistry B*, 106:809–819, 2002.

[28] M. Falcone, D. Bothe, and H. Marschall. 3d direct numerical simulations of reactive mass transfer from deformable single bubbles: An analysis of mass transfer coefficients and reaction selectivities. *Chemical Engineering Science*, 177:523–536, 2018.

[29] R. B. Fdhila and P. C. Duineveld. The effect of surfactant on the rise of a spherical bubble at high Reynolds and Péclet numbers. *Physics of Fluids*, 8:310–321, 1996.

[30] J. H. Ferziger and M. Perić. *Computational Methods for Fluid Dynamics*. Springer, 1996.

[31] James A. Finch, Jan E. Nesset, and Claudio Acuña. Role of frother on bubble production and behaviour in flotation. *Minerals Engineering*, 21(12):949–957, 2008.

[32] S. Fleckenstein and D. Bothe. Simplified modeling of the influence of surfactants on the rise of bubbles in VOF-simulations. *Chemical Engineering Science*, 102:514–523, 2013.

[33] S. Fleckenstein and D. Bothe. A volume-of-fluid-based numerical method for multi-component mass transfer with local volume changes. *Journal of Computational Physics*, 301:35–58, 2015.

[34] National Center for Biotechnology Information. PubChem Compound Database; CID=13380. `"https://pubchem.ncbi.nlm.nih.gov/compound/13380"`, accessed March 11, 2019.

[35] D. Gómez-Díaz, J.M. Navaza, and B. Sanjurjo. Mass-transfer enhancement or reduction by surfactant presence at a gas-liquid interface. *Industrial & Engineering Chemistry Research*, 48(5):2671 – 2677, 2009.

[36] J.F. Harper. Stagnant-cap bubbles with both diffusion and adsorption rate-determining. *Journal of Fluid Mechanics*, 521:115–123, 2004.

[37] M. Hartmann. Description of Marangoni-induced flow patterns through photo-switchable surfactants by means of Direct Numerical Simulation using OpenFOAM. Master's thesis, TU Darmstadt, 2016.

[38] Z. He, C. Maldarelli, and Z. Dagan. The size of stagnant caps of bulk soluble surfactant on the interface of translating fluid droplets. *Journal of Colloid and Interface Science*, 146:442–451, 1991.

[39] G. Hebrard, J. Zeng, and K. Loubiere. Effect of surfactants on liquid side mass transfer coefficients: A new insight. *Chemical Engineering Journal*, 148:132–138, 2009.

[40] C. W. Hirt, A. A. Amsden, and J. L. Cook. An Arbitrary Lagrangian-Eulerian computing method for all flow speeds. *Journal of Computational Physics*, 14:227–253, 1974.

[41] Y. Hori, Y. Hirota, K. Hayashi, S. Hosokawa, and A. Tomiyama. Combined effects of alcohol and electrolyte on mass transfer from single carbon-dioxide bubbles in vertical pipes. *International Journal of Heat and Mass Transfer*, 136:521 – 530, 2019.

[42] J. Huang and T. Saito. Discussion about the differences in mass transfer, bubble motion and surrounding liquid motion between a contaminated system and a clean system based on consideration of three-dimensional wake structure obtained from LIF visualization. *Chemical Engineering Science*, 170:105–115, 2017.

[43] J. Huang and T. Saito. Influence of gas-liquid interface contamination on bubble motions, bubble wakes, and instantaneous mass transfer. *Chemical Engineering Science*, 157:182–199, 2017.

[44] R. Issa. Solution of the implicitly discretised fluid flow equations by Operator-Splitting. *Journal of Computational Physics*, 62(1):40–65, 1986.

[45] H. Jasak. *Error analysis and estimation for the Finite Volume method with applications to fluid flows*. PhD thesis, Imperial College London, 1996.

[46] H. Jasak and Z. Tuković. Automatic mesh motion for the unstructured Finite Volume method. *Transactions of FAMENA*, 30(2):1–20, 2006.

[47] M. Jimenez, N. Dietrich, J.R. Grace, and G. Hébrard. Oxygen mass transfer and hydrodynamic behaviour in wastewater: Determination of local impact of surfactants by visualization techniques. *Water Research*, 58:111 – 121, 2014.

[48] P. Joos and G. Serrien. Adsorption kinetics of lower alkanols at the air/water interface: Effect of structure makers and structure breakers. *Journal of Colloid and lnterface Science*, 127(1):97–103, 1989.

[49] I. Kim and A. Pearlstein. Stability of the flow past a sphere. *Journal of Fluid Mechanics*, 211:73–93, 1990.

[50] J.A. Kleinkemper. A comparative study of different mesh types for transport processes near gas bubbles regarding accuracy, stability, and run time. Bachelor's thesis, TU Darmstadt, 2018.

[51] D. Kosior and J. Zawala. Initial degree of detaching bubble adsorption coverage and the kinetics of dynamic adsorption layer formation. *Physical Chemistry Chemical Physics*, 20(4):2403–2412, 2018.

[52] P. A. Kralchevsky, D. D. Krassimir, and N. D. Denkov. *Handbook of Surface and Colloid Chemistry*. CRC Press, New York, 2nd edition, 2002.

[53] P.A. Kralchevsky and K.D. Danov. *Handbook of Surface and Colloid Chemistry*, chapter Chemical Physics of Colloid Systems and Interfaces, pages 247–414. CRC Press, 4th edition, 2015.

[54] M. Krzan and K. Malysa. Profiles of local velocities of bubbles in n-butanol, n-hexanol and n-nonanol solutions. *Colloids and Surfaces A: Physicochemical Engineering Aspects*, 207:279–291, 2002.

[55] M. Krzan, J. Zawala, and K. Malysa. Development of steady state adsorption distribution over interface of a bubble rising in solutions of n-alkanols (C5, C8) and n-alkyl trimethyl ammonium bromides (C8, C12, C16). *Colloids and Surfaces A*, 298:42–51, 2007.

[56] R.J. LeVeque. *Numerical Methods for Conservation Laws*. Springer Basel AG, second edition, 2002.

[57] F.G. Levich. *Physicochemical Hydrodynamics*. Prentice-Hall, Englewood Cliffs, New York, first edition edition, 1962.

[58] Y. Liao and J. B. McLaughlin. Bubble Motion in Aqueous Surfactant Solutions. *Journal of Colloid and Interface Science*, 224:297–310, 2000.

[59] A. C. Lochiel and P. H. Calderbank. Mass Transfer in the continuous phase around axisymmetric bodies of revolution. *Chemical Engineering Science*, 19:471–484, 1964.

[60] R. H. Magarvey and Roy L. Bishop. Transition ranges for three-dimensional wakes. *Canadian Journal of Physics*, 39(10):1418–1422, 1961.

[61] K. Małysa, J. Zawala, M. Krzan, and M. Krasowska. Bubbles rising in solutions; local and terminal velocities, shape variations and collisions with free surface. In R. Miller and L. Liggieri, editors, *Bubble and Drop Interfaces*, volume 2 of *Progress in Colloid and Interface Science*. CRC Press, Taylor & Francis Group, 2011.

[62] Y. Matsumoto, T. Uda, and S. Takagi. The effect of surfactant on rising bubbles. In S. Balachandar and A. Prosperetti, editors, *Proceedings of the IUTAM Symposium on Computational Multiphase Flow*, pages 311–321. Springer, 2006.

[63] R. Miller and V. B. Fainerman et al. Surfactant adsorption layers at liquid interfaces. In L.S. Romsted, editor, *Surfactant science and technology. Retrospects and prospects*. CRC Press, 2014.

[64] G. Mougin and J. Magnaudet. Path instability of a rising bubble. *Physical Review Letters*, 88:14502, 2002.

[65] G. Mougin and J. Magnaudet. Wake-induced forces and torques on a zigzagging/spiralling bubble. *Journal of Fluid Mechanics*, 567:185–194, 2006.

[66] M. Muradoglu and G. Tryggvason. A front-tracking method for computation of interfacial flows with soluble surfactants. *Journal of Computational Physics*, 227(4):2238–2262, 2008.

[67] S. Muzaferija and M. Perić. Computation of free-surface flows using the Finite-Volume method and moving grids. *Numerical Heat Transfer, Part B: Fundamentals*, 32(4):369–384, 1997.

[68] L. Oellrich, H. Schmidt-Traub, and H. Brauer. Theoretische Berechnung des Stofftransports in der Umgebung einer Einzelblase. *Chemical Engineering Science*, 28(3):711–721, 1973.

[69] R. Palaparthi, D.T. Papageorgiou, and C. Maldarelli. Theory and experiments on the stagnant cap regime in the motion of spherical surfactant-laden bubbles. *Journal of Fluid Mechanics*, 559:1–44, 2006.

[70] F. Pedregosa, G. Varoquaux, A. Gramfort, V. Michel, B. Thirion, O. Grisel, M. Blondel, P. Prettenhofer, R. Weiss, V. Dubourg, J. Vanderplas, A. Passos, D. Cournapeau, M. Brucher, M. Perrot, and E. Duchesnay. Scikit-learn: Machine learning in Python. *Journal of Machine Learning Research*, 12:2825–2830, 2011.

[71] C. Pesci, K. Dieter-Kissling, H. Marschall, and D. Bothe. Finite Volume/Finite Area Interface Tracking method for two-phase flows with fluid interfaces influenced by surfactant. In M. T. Rahni, M. Karbaschi, and R. Miller, editors, *Progress in colloid and interface science*. CRC Press, Taylor & Francis Group, 2015.

[72] C. Pesci, H. Marschall, V. Ulaganathan, T. Kairaliyeva, R. Miller, and D. Bothe. Experimental and computational analysis of fluid interfaces influenced by soluble surfactant. In D. Bothe and A. Reusken, editors, *Transport Processes at Fluidic Interfaces*, Advances in Mathematical Fluid Mechanics, chapter 15. Springer International Publishing, AG Cham, 2017.

[73] C. Pesci, A. Weiner, H. Marschall, and D. Bothe. Computational analysis of single rising bubbles influenced by soluble surfactant. *Journal of Fluid Mechanics*, 856:709–763, 2018.

[74] S.S. Ponoth and J.B. McLaughlin. Numerical simulation of mass transfer for bubbles in water. *Chemical Engineering Science*, 55:1237–1255, 2000.

[75] F. Ravera, M. Ferrari, and L. Liggieri. Adsorption and partitioning of surfactants in liquid-liquid systems. *Advances in Colloid and Interface Science*, 88:129–177, 2000.

[76] H. Rusche. *Computational fluid dynamics of dispersed two-phase flows at high phase fractions*. PhD thesis, Department of Mechanical Engineering, 2002.

[77] A. Sam, C. O. Gomez, and J. A. Finch. Axial velocity profiles of single bubbles in water/frother solutions. *International Journal of Mineral Processing*, 47:177–196, 1996.

[78] R. Sardeing, P. Painmanakul, and G. Hébrard. Effect of surfactants on liquid-side mass transfer coefficients in gas-liquid systems: A first step to modeling. *Chemical Engineering Science*, 61:6249–6260, 2006.

[79] R. Satapathy and W. Smith. The motion of single immiscible drops through a liquid. *Journal of Fluid Mechanics*, 10:561–570, 1960.

[80] scikit-learn developers (BSD License). "`https://scikit-learn.org/stable/modules/generated/sklearn.decomposition.PCA.html`", accessed March 15, 2019.

[81] M. Steinhausen. Numerical simulation of single rising bubbles influenced by soluble surfactant in the spherical and ellipsoidal regime. Master's thesis, TU Darmstadt, 2018.

[82] H. A. Stone. A simple derivation of the time-dependent convective-diffusion equation for surfactant transport along a deforming interface. *Physics of Fluids A: Fluid Dynamics*, 2(1):111–112, 1990.

[83] Y. Tagawa, S. Takagi, and Y. Matsumoto. Surfactant effects on path instability of a rising bubble. *Journal of Fluid Mechanics*, 738:124–142, 2014.

[84] S. Takagi, T. Ogasawara, M. Fukuta, and Y. Matsumoto. Surfactant effect on the bubble motions and bubbly flow structures in a vertical channel. *Fluid Dynamics Research*, 41(065003), 2009.

[85] F. Takemura. Adsorption of surfactants onto the surface of a spherical rising bubble and its effect on the terminal velocity of the bubble. *Physics of Fluids*, 17:048104 1–4, 2005.

[86] F. Takemura and Y. Yabe. Rising speed and dissolution rate of a carbon dioxide bubble in slightly contaminated water. *Journal of Fluid Mechanics*, 378:319–334, 1999.

[87] S. Tasoglu, U. Demirci, and M. Muradoglu. The effect of soluble surfactant on the transient motion of a buoyancy-driven bubble. *Physics of Fluids*, 20(4):040805, 2008.

[88] A. Tomiyama, I. Kataoka, I. Zun, and T. Sakaguchi. Drag coefficients of single bubbles under normal and micro gravity conditions. *JSME International Journal Seies B Fluids and Thermal Engineering*, 41(2):472–479, 1998.

[89] H. Tsuge and S. Hibino. The motion of single gas bubbles rising in various liquids. *Chemical Engineering*, 35(1):65–71, 1971.

[90] Z. Tuković and H. Jasak. Simulation of free-rising bubble with soluble surfactant using moving mesh Finite Volume/Area method. In *6th International Conference on CFD in Oil & Gas, Metallurgical and Process Industries SINTEF/NTNU*, Trondheim, Norway, 10-12 June 2008.

[91] Z. Tuković and H. Jasak. A moving mesh Finite Volume Interface Tracking method for surface tension dominated interfacial fluid flow. *Computers & Fluids*, 55:70–84, 2012.

[92] V. Ulaganathan. *Molecular Fundamentals of Foam Fractionation*. PhD thesis, Universität Potsdam, Potsdam, 2016.

[93] H. K. Versteeg and W. Malalasekera. *An Introduction to Computational Fluid Dynamics*. Pearson Education Limited, 1995-2007.

[94] P. S. Weber. *Modeling and Numerical Simulation of Multi-Component Single- and Two-Phase Fluid Systems*. PhD thesis, Technische Universität Darmstadt, 2016.

[95] A. Weiner and D. Bothe. Advanced subgrid-scale modeling for convection-dominated species transport at fluid interfaces with application to mass transfer from rising bubbles. *Journal of Computational Physics*, 347:261–289, 2017.

[96] A. Weiner, D. Hillenbrand, H. Marschall, and D. Bothe. Data-driven subgrid-scale modeling for convection-dominated concentration boundary layers. *Chemical Engineering & Technology*, 42(17):1349–1356, 2019.

[97] A. Weiner, J. Timmermann, C. Pesci, J. Grewe, M. Hoffmann, M. Schlüter, and D. Bothe. Experimental and numerical investigation of reactive species transport around a small rising bubble. *Chemical Engineering Science: X*, 1:100007, 2019.

[98] S Winnikow and BT Chao. Droplet motion in purified systems. *the Physics of Fluids*, 9(1):50–61, 1966.

[99] Y. Zhang and J. A. Finch. A note on single bubble motion in surfactant solutions. *Journal of Fluid Mechanics*, 429:63–66, 2001.

[100] Y. Zhang, J.B. McLaughlin, and J.A. Finch. Bubble velocity profile and model of surfactant mass transfer to bubble surface. *Chemical Engineering Science*, 56:6605–6616, 2001.

List of Figures

List of Tables

Acknowledgements

Firstly, I would like to express my sincere gratitude to my advisor Prof. Dieter Bothe for the possibility to do my Ph.D studies at his group, the helpful discussions and his immense knowledge which he is always willing to share with his students. I further like to thank Prof. Martin Oberlack for being my second supervisor.
Besides my advisors, I would like to thank Dr. Holger Maschall, for the introduction to the multiphase flows simulation world, his insightful comments and discussions, which encouraged me to pursue my objectives in this research field.
My sincere thanks also goes to Dr. Reinhard Miller and his group at the Max Plank Institute in Golm and Dr. Marcel Krzan from the Polish Academy of Sciences, who provided me with the experimental results. Without they precious contribution it would not have been possible to conduct part of this research.
I thank all my colleagues at the institute for Mathematical Modeling and Analysis for being always available to help, discuss and share coffee and fruit brakes. This time together was great. I also thank all my friends, in Darmstadt and in Italy, always being there to support me not only in the difficult but also in the gratifying moments of this path.
A special thank goes to Andre and to my family. Without their support, motivation and patience I would have never reached this objective.

Un grazie spaciale alla mamma e al papi, alla nonna Adele, alla Frenci, Diego, Michele e Mattia. Anche se sono lontana da casa non mi avete mai fatto mancare il vostro supporto e affetto, e le vostre visite a Darmstadt sono state la parte piú bella di questo viaggio di cui non conosco la prossima meta.